Thermo-Electrochemical Mechanisms of Lithium Ion Battery Assemblies for Human Space Flight Applications

A Dissertation

Presented to

the Faculty of the Materials Science and Engineering Program

University of Houston

In Partial Fulfillment

of the Requirements for the Degree

Doctor of Philosophy

in Materials Science and Engineering

by

William Quinn Walker

December 2016

Thermo-Electrochemical Mechanisms of Lithium Ion Battery Assemblies for Human Space Flight Applications

William Quinn Walker

Approved:

Chair of the Committee
Haleh Ardebili, Associate Professor,
Mechanical Engineering

Committee Members:

Jae-Hyun Ryou, Assistant Professor,
Mechanical Engineering

Kenneth White, Professor,
Mechanical Engineering

Dong Liu, Associate Professor,
Mechanical Engineering

Yashashree Kulkarni, Associate Professor,
Mechanical Engineering

Suresh K. Khator, Associate Dean,
Cullen College of Engineering

Pradeep Sharma, Program Director,
Materials Science and Engineering

Acknowledgements

I am forever indebted to the countless individuals who provided me with an endless amount of encouragement through my academic career at the University of Houston. Completion of the doctoral level academic requirements for the Materials Science and Engineering Program would not have been possible without such a supportive community.

First, I would like to express my deepest appreciation to my advisor Dr. Haleh Ardebili, Associate Professor of Mechanical Engineering at the University of Houston, for her spirited attitude, dedicated mentorship and academic support. Without Dr. Ardebili, the completion of this program and dissertation would not have been possible. Learning under Dr. Ardebili's leadership was truly a privilege. Dr. Ardebili takes every opportunity to provide the students in her group with a high quality education and to encourage them to continuously push the envelope of the scientific community.

Acknowledgement is given to various entities of the National Aeronautics and Space Administration (NASA). First, I would like to thank Johnson Space Center (JSC) for the award of the JSC Academic Fellowship, which was instrumental in the completion of this research. I would also like to directly recognize Dr. Christopher Iannello with the NASA Engineering and Safety Center (NESC), who provided project leadership, management and authorization for the accelerating rate calorimetry and thermal runaway studies presented in Chapter 5 of this dissertation. Special thanks is given to Steve Rickman, also with the NESC, who provided mentorship and expertise in understanding thermal runaway events. In addition, I would like to express my deepest appreciation to the NASA JSC Structural Engineering Division (ES) Thermal Design Branch (ES3) which served as my host organization throughout the duration of time spent on this research. My management and

colleagues in ES3 provided fundamental support, mentorship and leadership throughout the duration of the graduate program. Further acknowledgement is given to the JSC Propulsion and Energy Division (EP). EP continuously demonstrates leadership in battery assembly development and safety and it was a privilege to collaborate with their organization on the thermal runaway research.

Special thanks is also given to the members of Dr. Ardebili's battery research group; specifically Taylor Kelly, Mejdi Kammoun, Bahar Moradi, Mengying Yuan, Sean Berg and Sarah Adaryan. I wish to express that it was truly a privilege to work with these colleagues. It is exciting to see what comes next for my brilliant peers.

Last, but certainly not least, I would like to thank my family for their continuous support through the pursuit of academic success at the University of Houston. Completion of this program would not have been possible without a supportive family unit, which understands the rigorous nature of graduate level research and coursework. Thank you Abby, Mom, Dad, Megan and Brent for the sacrifices you made to help me achieve this dream.

Thermo-Electrochemical Mechanisms of Lithium Ion Battery Assemblies for Human Space Flight Applications

An Abstract

of a

Dissertation

Presented to

the Faculty of the Materials Science and Engineering Program

University of Houston

In Partial Fulfillment

of the Requirements for the Degree

Doctor of Philosophy

in Materials Science and Engineering

by

William Quinn Walker

December 2016

Abstract

Advanced energy storage and power management systems designed through rigorous materials selection, testing and analysis processes are essential to ensuring mission longevity and success for human space flight applications. Lithium ion (Li-ion) batteries provide superior performance characteristics, low mass and energy dense solutions. These features lead to the growing utilization of Li-ion technology for rockets, space exploration vehicles and satellites. Knowing that efficiency and survivability are influenced by temperature and that thermal safety concerns (i.e. thermal runaway) impede the utilization of Li-ion technology for human space flight applications, this dissertation focuses on the thermo-electrochemical mechanisms of Li-ion batteries. Test and analysis techniques developed here support the design of safe Li-ion battery assemblies.

Current finite element simulation methods support detailed analysis of thermo-electrochemical processes; however, said software packages do not maintain capabilities to incorporate the influence of thermal radiation driven orbital environments. In this dissertation, we couple existing thermo-electrochemical models of Li-ion battery local heat generation with specialized radiation analysis software, Thermal Desktop. The unique capability gained by employing Thermal Desktop is further demonstrated by simulating Li-ion battery thermal performance in example orbital environments exterior to a small satellite. Results provide demonstration of Li-ion battery thermo-electrochemical performance in space environments.

Experimental characterization of thermal runaway energy release with accelerated rate calorimetry supports safer thermal management systems. ‘Standard’ accelerated rate calorimetry setup provides means to measure the addition of energy exhibited through the

body of a Li-ion cell. This dissertation considers the total energy generated during thermal runaway as distributions between cell body and hot gases via inclusion of a unique secondary enclosure inside the calorimeter. This closed system not only contains the cell body and gaseous species, but also captures energy release associated with rapid heat transfer to the system unobserved by measurements taken on the cell body. An inverse relationship between state-of-charge and onset temperature is observed. Energy contained in the cell body and gaseous species are successfully characterized. Significant additional energy is measured with the heating of the secondary enclosure. Improved calorimeter apparatus including a secondary enclosure provides essential capability to measuring total energy release distributions during thermal runaway.

Table Contents

List of Figures

List of Tables

Chapter 1 Energy Storage for Space Flight Applications

1.1 Introduction to Advanced Energy Storage Devices

Increasing consumption of nonrenewable fuel and energy sources and the decreasing availability of said resources escalates a global energy crisis that drives a need for renewable energy, high efficiency energy consumption, transformation from reliance on non-renewable energy to renewable energy, and the incorporation of advanced energy storage technologies [1]. Utilization of advanced energy storage is seen in aerospace, automotive, industrial, medical, military, railway and space-exploration industries [2-4]. The leading advanced energy storage devices include batteries, capacitors and fuel cells; principal battery sub-categories include alkaline, lithium and lithium ion [5-7].

Two primary characteristics are typically used to describe advanced energy storage devices: energy density and power density. Energy density is the stored energy per unit volume (Wh L^{-1}) and power density is the amount of power per unit volume (W L^{-1}); note that these should not be confused with specific energy (Wh kg^{-1}) and specific power (W kg^{-1}). Both properties are significant for optimal storage but difficult to maximize simultaneously as high energy dense devices tend to be less power dense (i.e. batteries and fuel cells) while power dense devices exhibit lower energy densities (i.e. capacitors); this type of comparison is explored with Ragone plot (see Figure 1-1) which was originally developed by David V. Ragone to compare performance characteristics of battery assemblies developed for electric vehicles [8,9].

Advanced energy storage and power management systems are essential to mission longevity for all aerospace vehicles, spacecraft, rockets, satellites and associated equipment [10]. Energy production in space is limited by the finite quantity of constraining resources

and fuel supply is limited by the size of the storage tank and launch mass limits [10,11]. Battery energy is limited by cell capacity, storing power efficiency, available recharge resources (solar, mechanical, etc.) and overall service life. The efficiency of the power management system restricts the useful fuel and battery energy available operationally [10]. Resource replacement opportunities are not always available due to the cost and complexity involved with launching supplies.

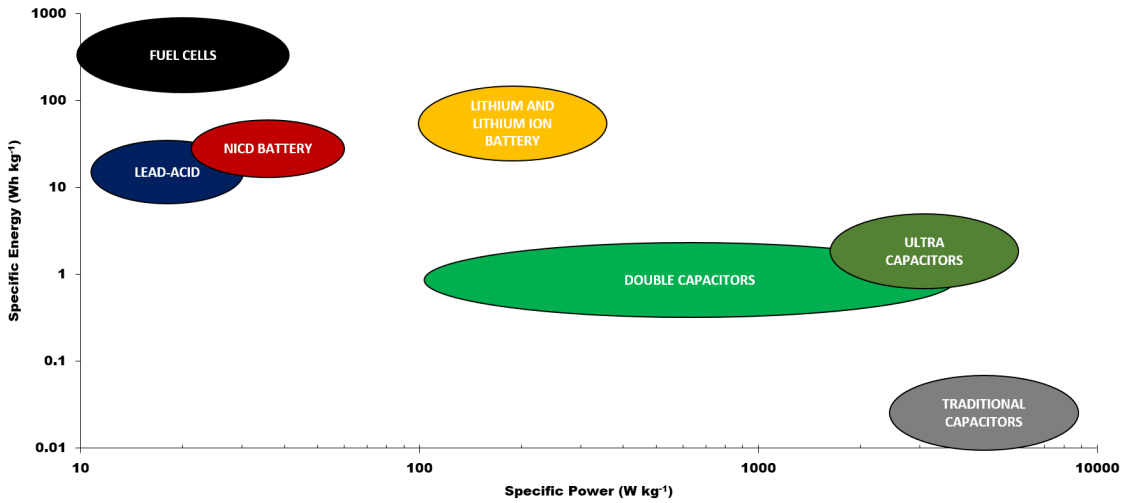

Figure 1-1 Image depicts a ragone plot which compares the specific energy (Wh kg^{-1}) and specific power (W kg^{-1}) characteristics of various leading advanced energy storage devices. This data was adapted from Winter and Brodd [5].

The exponential growth of the space industry further exemplifies the need for development of advanced energy storage technology for space exploration applications. Established government agencies include the National Aeronautics and Space Administration (NASA), the Russian Federal Space Agency (RFSA), the European Space Agency (ESA), the Japanese Aerospace Exploration Agency (JAXA) and the Canadian Space Agency (CSA); there are also some developing agencies such as the Indian Space Research Organization (ISRO) and the China National Space Administration (CNSA). The number of private industry competitors is growing rapidly with the increasing need for

small payload launch vehicles for satellites and science experiments. See representation of various established government space agencies and private industry competitors with Figure 1-2. The significance of the need for reliable advanced energy storage for space applications is magnified as the associated cost and risk increase significantly as compared to terrestrial applications; the average cost per pound to launch an object into orbit ranges between $10000 and $55000 United States Dollars (USD) depending on the payload capability of the launch vehicle [11].

Figure 1-2 **Image depicts the logos of relevant space and aerospace industry constituents which include (a) government agencies and (b) private industry competitors. This image does not indicate any preference or opinion of the author.**

Lithium ion (Li-ion) batteries provide superior, lightweight and energy dense solutions necessary for space exploration vehicles, technology and satellites [12-16]. Alkaline based nickel cadmium (NiCd), nickel-metal hydride (NiMH) and nickel hydrogen (NiH_2) batteries are traditionally used in aerospace, but these now face replacement with lighter and more efficient secondary (rechargeable) Li-ion battery systems which offer over double the performance for almost half the mass [14,17]. Li-ion batteries are popular for aerospace energy storage systems because the combined chemical compositions and material characteristics provide superior energy density and power density combinations, long shelf lives, large life cycle counts, the ability to operate in a wide array of thermal

environments, mass savings, reliable structural stability and effective management systems [14]. Cutchen et al. provided early evidence to the abilities of Li-ion batteries for space applications by providing research demonstrating the consistent performance of Li-ion batteries; testing considered extended periods of time (up to 10 years) and operation for wide temperature ranges (-40 °C to +70 °C) [18].

1.2 Lithium Ion Battery Fundamentals

Lithium ion batteries comprise of (a) the negative anode, (b) the positive cathode, (c) the ionically conductive and electrically insulative electrolytic material, (d) a thin polymer separator and (e) the current collectors [19]. The anode is typically carbon-based graphite or graphene, which consist of layered crystal structures that allow optimal intercalation and de-intercalation of the lithium ions; new research explores the use of Li metal anodes. Cathodes provide the lithium rich active material. The electrolyte is most often an organic liquid solution, but is also found in solid or gel forms. The current collectors are made of electrically conductive materials such as aluminum (Al) and copper (Cu). During the first few cycles of a new Li-ion battery, a passive layer of organic and inorganic electrolyte decomposition products develops across the anode to electrolyte interface; this is known as the solid electrolyte interphase (SEI) layer [20]. Although the SEI results in irreversible capacity loss, the presence of the SEI serves as a protective layer that prevents dendrite growth which reduces the overall risk of internal shorting [20].

Li-ion batteries function with electrochemical reactions, which are chemical reactions accompanied by electron flow. During discharge, Li ions flow from the anode to the cathode while simultaneously the anode is oxidized (i.e. the gives up electrons) and the cathode is reduced (i.e. receives the electrons). During charge, Li ions transfer back to the

anode, the cathode is oxidized and the anode is reduced. As an example, the half reactions for the discharge processes of a $LiCoO_2$ battery with a graphite anode (LiC_6) and hexafluorophosphate electrolyte ($LiPF_6$) are provided with Equation 1.1 through Equation 1.2 and the overall reaction is provided with Equation 1.3,

$$CoO_2 + Li^+ + e^- \leftrightarrow LiCoO_2, \quad (1.1)$$

$$LiC_6 \leftrightarrow Li^+ + e^- + C_6, \text{ and} \quad (1.2)$$

$$CoO_2 + LiC_6 \leftrightarrow LiCoO_2 + C_6. \quad (1.3)$$

A schematic describing the components of a Li-ion battery system, the movement of the Li ions and the transfer of electrons during discharge is provided with Figure 1-3. For charge, the flow of electrons and Li ions reverse.

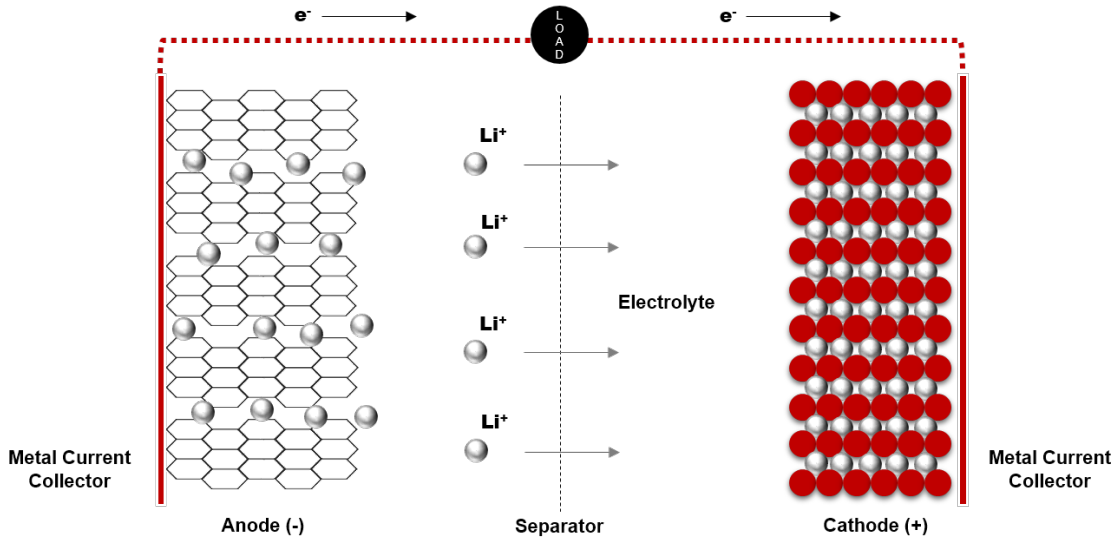

Figure 1-3 Schematic of Li-ion battery components and electrochemical processes for charge and discharge operations.

The most common types of Li-ion batteries include Lithium Cobalt Oxide ($LiCoO_2$), Lithium Manganese Cobalt Oxide ($LiMg_2O_4$), Lithium Nickel Manganese Cobalt Oxide ($LiNiMnCoO_2$ also referred to as NMC) and Lithium Iron Phosphate ($LiFePO_4$) [21]. Standard packaging of individual Li-ion cells come in the form of coin cells, cylindrical

cells, prismatic cells and pouch cells; some researchers are developing advanced materials and encapsulation techniques that support flexibility and stretchability.

1.3 Space Exploration Applications Utilizing Lithium Ion Batteries

The National Aeronautics and Space Administration (NASA) and private industry competitors utilize Li-ion technology extensively for space exploration applications. Some key examples include: (a) the James Webb Space Telescope, (b) Robonaut 2, (c) the SpaceX Dragon cargo vehicle, (d) the Orion Multi-Purpose Crew Vehicle, (e) the astronaut Extra-Vehicular Mobility Unit (EMU), (f) the International Space Station (ISS) and (g) the Curiosity rover; see Figure 1-4. Note that the Li-ion batteries focused on by this research specifically pertain to those used for the following *human* space flight applications: (a) the Li-ion EMU rechargeable battery assembly (LREBA), (b) the EMU long life battery (LLB) and (c) the battery backpack for Robonaut 2 (R2) [22-25].

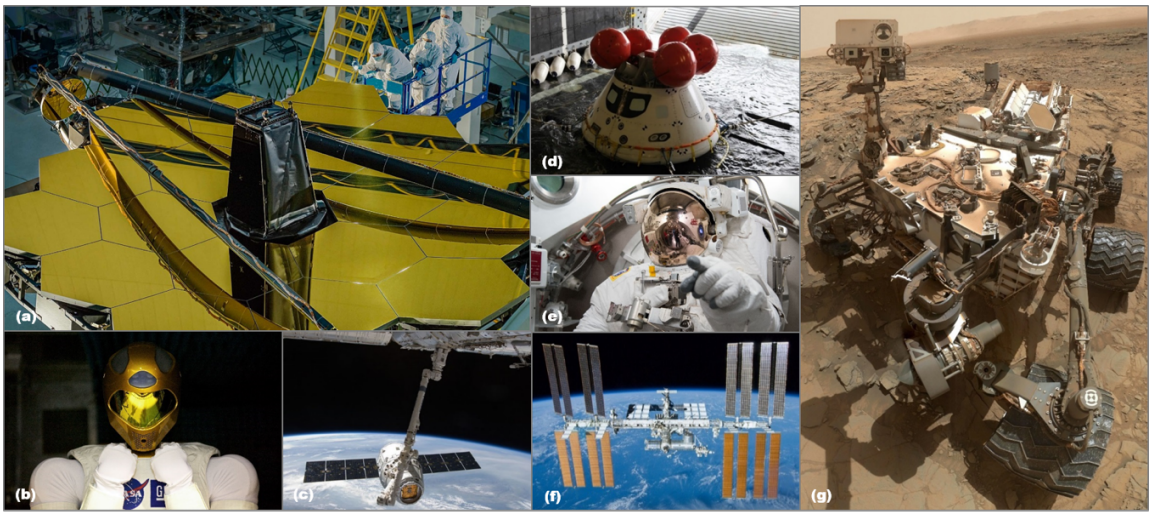

Figure 1-4 **Images of the following: (a) James Webb Space Telescope, (b) Robonaut 2, (c) SpaceX Dragon, (d) Orion Multi-Purpose Crew Vehicle, (e) Extra-Vehicular Mobility Unit, (f) International Space Station and (g) Curiosity Mars Rover.**

1.4 Thermal Challenges for Utilizing Lithium Ion Batteries for Human Space Flight

Despite their impressive performance characteristics, thermal safety concerns remain a challenge towards the complete reliance on Li-ion batteries for human space flight applications (e.g., overheating, off gassing, thermal runaway and propagation, fire and explosion) [26]. These concerns are magnified with the addition of complex and hostile space environments, which (a) increase the inherent danger associated with the technology and (b) increase the overall probability of catastrophic event. Battery design involving innovative materials selection, comprehensive testing and test-correlated computational analysis is the most effective means to developing safe and reliable Li-ion battery assemblies. This design process requires a fundamental understanding of Li-ion battery thermo-electrochemical mechanisms.

1.5 Overview of Dissertation

This research provides innovative test and analysis techniques for nominal operations and off-nominal scenarios (i.e. thermal runaway) that are essential to the design of safe Li-ion battery assemblies for human space flight applications.

Chapter 1 provides an introduction to the need for advanced energy storage devices for human space flight applications. Description is provided for why Li-ion batteries are the front running energy storage device for space applications. Fundamental aspects of electrochemistry are also discussed. Thermal issues of Li-ion batteries, which serve as the motivations for this research, are identified.

Chapter 2 provides a general energy balance of the Li-ion battery system derived from the first law of thermodynamics. The model was first developed by Sherfey and Brenner and later extensively expanded by Bernardi et al. [27,28]. This chapter provides an in depth

discussion of these models and their implications on thermo-electrochemical analysis in thermal radiation driven space environments. A brief literature review of studies incorporating these models is also provided.

Chapter 3 identifies that specialized software are needed for both electrochemical analysis and for thermal radiation analysis, but that a joint approach is required to predict Li-ion battery thermal performance in a space environment. A basic test-correlated thermo-electrochemical model of a large format Li-ion battery developed by Chen et al. [29] is recreated in space radiation analysis software Thermal Desktop. This served as a proof-of-concept study for Thermal Desktop's suitability for thermo-electrochemical analysis. Results discussed here are based on a publication in the Journal of Power Sources titled *Thermo-electrochemical analysis of lithium ion batteries for space applications using Thermal Desktop* [30].

Chapter 4 provides a validation-of-concept study, which builds from the results of Chapter 3 to develop a test-correlated Thermal Desktop model of the Robonaut 2 Li-ion battery assembly. This assembly consisted of 300 individual Boston Power Swing 5300 Li-ion cells. The battery assembly Thermal Desktop model is combined with a model of a simple satellite. Boundary conditions for various Earth orbital environments are defined and the resulting battery assembly thermal performance is simulated. This study provides demonstration of simulating Li-ion battery heat generation rates as a function of a thermal radiation driven orbital environment. Results discussed here are based on a publication in the Journal of Power Sources titled *Thermo-electrochemical evaluation of lithium ion batteries for space applications* [25].

Chapter 5 discusses the thermal safety concerns (i.e. thermal runaway and cell-to-cell propagation) associated with the utilization of Li-ion batteries. Thermal runaway event mechanisms are discussed and related to accelerating rate calorimetry testing of a statistically significant number of test articles. An understanding of the total energy release during thermal runaway is provided and a normalized energy release factor is developed to provided indication of expected total energy release of a general Li-ion cell based on the total stored electrochemical energy. Results discussed here are based on a publication in the Journal of Power Sources titled *Energy distributions exhibited by commercial lithium ion batteries used for human space flight applications* [31]. Acknowledgement is provided here to the NASA Engineering and Safety Center (NESC) and Dr. Christopher Iannello who provided project authorization, management and leadership. Acknowledgement is also given to the team at Thermal Hazard Technologies who conducted the experiments.

Chapter 6 provides overall conclusions for the research discussed in this dissertation and an overview of future research. Discussion is primarily oriented around the following: (1) the improvement of Thermal Desktop electrochemical simulation methods and (2) the utilization of solid polymer electrolyte for safer and thermally robust Li-ion battery assemblies for human space flight applications.

Chapter 2 Heat Generation Mechanisms during Lithium Ion Battery Charge and Discharge Operations

2.1 Temperature Dependence of Lithium Ion Batteries

Li-ion battery safety, performance and efficiency are largely influenced by the internal operating temperature of the cell and the ambient temperature of the environment [26,32,33]. Significantly lower cell capacities (Ah) are typically observed for low temperature operations (< 0 °C), while operation at excessively high temperatures (> 75 °C) could induce exothermic decomposition reactions that eventually lead to thermal runaway (see Chapter 5 for further discussion on thermal runaway). Li-ion battery efficiency and heat generation rates during charge and discharge are functions of the following factors: (a) the temperature of the ambient environment, (b) movement of ions and electrons, (c) electrode porosity, (d) the total potential, (e) the solid electrolyte interphase, (f) dendrite growth and (g) the thermophysical properties [26-28,32-37]. It is evident that thermal performance prediction capabilities are critical to the development of safe Li-ion battery assemblies for human space flight applications. Determining thermal performance in a radiation driven space environments first requires a general energy balance.

2.2 General Energy Balance

Beginning with the first law of thermodynamics, the total change in energy of the Li-ion cell (ΔE^{Tot}) is equal to the summation of the change in kinetic energy (ΔE^{Kin}), the change in potential energy (ΔE^{Pot}) and the change in internal energy (ΔU) as shown in Equation 2.1,

$$\Delta E^{Tot} = \Delta E^{Kin} + \Delta E^{Pot} + \Delta U. \tag{2.1}$$

The change in internal energy (ΔU) is the net energy based on the work done by the system and heat added to the system as shown with Equation 2.2,

$$\Delta U = W + Q. \tag{2.2}$$

Assuming no kinetic energy, potential energy or work are associated with the Li-ion cell (electrical work will be addressed later), Equation 2.1 is simplified to Equation 2.3 where the change in energy is a function of the heat flow into and out of the system,

$$\Delta E^{Tot} = Q. \tag{2.3}$$

The total heat associated with a Li-ion battery (Q_{Tot}) is the summation of the gain or loss of heat through the three primary heat transfer mechanisms of conduction ($Q_{Conduction}$), convection to the environment ($Q_{Convection}$), radiation to the environment ($Q_{Radiation}$) and all locally generated heat of a given cell (Q_{Cell}),

$$Q_{Tot} = Q_{Conduction} + Q_{Convection} + Q_{Radiation} + Q_{Cell}. \tag{2.4}$$

Convection, conduction and radiation are the three primary modes of heat transfer. Natural and forced convection refer to the heat transfer between solid and fluid mediums as a result of the motion of the fluid. Note that for space applications the effects of natural convection are neglected because space is a vacuum. When required for energy balance, convection is represented through Equation 2.5,

$$Q_{Convection} = hA(T_{Surface} - T_{Ambient}), \tag{2.5}$$

where, h is the convection coefficient (W m^{-2} °C^{-1}), A is the surface area of the interface between the system and the fluid medium (m^2), $T_{Surface}$ is the temperature of the surface (°C), and $T_{Ambient}$ is the temperature of the surrounding fluid (°C).

Conduction is the transfer of heat through solid and stagnant fluid mediums as represented by Equation 2.6,

$$Q_{Conduction} = kA\frac{dT}{dL}, \tag{2.6}$$

where, k is the thermal conductivity (W m^{-1} °C^{-1}), A is the surface area (m^2), dT represents the change in temperature between two linear points (°C) and dL represents the length of the conductive path (m). This represents that gain or loss of energy within the battery system and from the battery system to surrounding structures.

Radiation is the transfer of heat through electromagnetic waves between two bodies as shown through Equation 2.7,

$$Q_{Radiation} = \varepsilon\sigma AF(T_{Surface}^4 - T_{Ambient}^4), \tag{2.7}$$

where, ε is the surface emissivity of the radiating object, σ is the Stefan-Boltzmann Constant (W m^{-2} K^{-4}), A is the surface area (m^2), F is the view factor, $T_{Surface}$ is the temperature of the surface (K) and $T_{Ambient}$ is the temperature of the receiving surface or sink temperature (K). For radiation calculations, temperature is maintained in K for convenience due to the convention used with the Stefan-Boltzmann constant. Chen et al. report that radiation maintains a significant impact on the rate of cooling of a Li-ion cell [29]. Chen's study displayed that radiative heat transfer as a function of encasement surface optical properties attributes to 28-30% of the cooling a battery [29]. Gilmore discusses that solar and infrared radiation are the major drivers for environmental heating for all orbiting spacecraft and satellites thus instilling the importance of understanding this fundamental heat transfer mechanism for operations in space environments [38].

The overall energy balance addressing the heat required to increase the temperature of the Li-ion cell with known mass and specific heat capacity is represented as Equation 2.8,

$$m_{Cell}Cp_{Cell}\,dT = kA\frac{dT}{dL} + hA\left(T_{Surface} - T_{Ambient}\right) + \varepsilon\sigma AF\left(T_{Surface}^4 - T_{Ambient}^4\right) + Q_{Cell}, \tag{2.8}$$

where, T is temperature (°C), m_{Cell} is the mass of the cell (kg) and Cp_{Cell} is the specific heat capacity (J kg^{-1} °C^{-1}). Accurate characterization of Q_{Cell} is critical to the development of

effective thermal management systems designed to not only maintain acceptable temperatures during nominal operations but also to mitigate the disastrous effects of thermal runaway.

2.3 Models of Lithium Ion Battery Heat Generation Rates

Bernardi et al. discuss that Li-ion cells generate heat during charge and discharge operations due to electrochemical reactions, phase changes, mixing and electrical work [28]. Internal cell temperature and ambient temperature, combined with rates of charge and discharge, greatly influence the rate at which the Li-ion cell generates heat during operations. The rate of the local heat generated through the electrochemical processes of charge and discharge are commonly represented by an energy balance derived by Bernardi et al. [28] which was determined by using the first law of thermodynamics in the form shown with Equation 2.9 for an isobaric (constant pressure) Li-ion battery,

$$\frac{dH_{Tot}}{dt} = Q - IV, \tag{2.9}$$

where, H_{Tot} is the sum of the enthalpies, Q is the heat loss to the surroundings and IV represents the electrical work. Bernardi et al. [28] defines the enthalpy of reaction, enthalpy of mixing, phase change and heat capacity with Equations 2.10-2.13, respectively,

$$H_R = \sum_i I_i T^2 \frac{d\frac{U_{i,avg}}{T}}{dT}, \tag{2.10}$$

$$H_M = \sum_j \frac{d}{dt}\left(\int \sum_i c_{ij} R T^2 \frac{\partial}{\partial T} ln\left(\frac{y_{ij}}{y_{ij}^{avg}}\right) dv_j\right), \tag{2.11}$$

$$H_{PC} = \sum_{ij\neq m} \sum_i \left[\left(\Delta H^*_{ij\to m} - RT^2 \frac{d}{dT} \ln\left(\frac{\gamma_{i,m}^{avg}}{\gamma_{i,j}^{avg}}\right)\right)\frac{dn_{i,j}}{dt}\right], \text{ and} \tag{2.12}$$

$$H_{HC} = \frac{dT}{dt}\left[\sum_j \sum_i n^0_{i,j}\, c^{avg}_{pi,j} + \sum_i \frac{\int_v^t I_i dt}{n_i F} \Delta c_{pi} + \sum_{j,i\neq m} \sum_i \left(C^{avg}_{pi,j} - C^{avg}_{pi,m}\right)\left(n_{i,j} - n^0_{i,j}\right)\right]. \tag{2.13}$$

Bernardi et al. [28] discuss the energy balance in its final form by combining Equation 2.9 with Equations 2.10 through 2.13 to get the following form shown with Equation 2.14,

$$Q_{Cell} = IV + H_R - H_M - H_{PC} + H_{HC}. \quad (2.14)$$

For thermal analysis of heat generation during charge and discharge, phase change terms and enthalpy of mixing are generally neglected, as their thermal impact is minimal [28, 29, 39]. Phase change and mixing effects are negated with the assumption that there is only one electrochemical reaction in the battery cell (during normal operation phase change does not occur in Li-ion batteries and only one reaction occurs) [39]. The simplified form of the derivation by Bernardi et al. [28] commonly used for thermo-electrochemical analysis purposes is shown with Equation 2.15,

$$Q_{Cell} = I\left(V_{OC} - V_W - T\frac{\partial V_{OC}}{\partial T}\right), \quad (2.15)$$

where, I is the current (A), V_{OC} is the open circuit voltage (V), V_W working voltage (V), T is the temperature of the cell (°C) and $dV_{OC}\ dT^{-1}$ is the temperature coefficient representing the change in open circuit voltage with temperature (V $°C^{-1}$); $dV_{OC}\ dT^{-1}$ has magnitudes typically ranging between 10^{-3} to 10^{-4} [29, 40-42]. Bernardi et al. discuss that heating due to the irreversibility associated with electrical work (i.e. cell overpotential and ohmic losses) and with entropy change are contained in Equation 2.15 as represented with Equation 2.15a and Equation 2.15b, respectively [28],

$$Q_{Work} = I(V_{OC} - V_W), \text{ and} \quad (2.15a)$$

$$Q_{Entropy} = I\left(-T\frac{\partial V_{OC}}{\partial T}\right). \quad (2.15b)$$

Chen et al. explain that Equation 2.15 is efficient for overall temperature prediction and does not limit the ability to perform accurate thermal analysis despite its simplifications from Equation 2.14, and further uses Equation 2.15 to predict 3-D core temperatures for various discharge processes of a 185 Ah battery [29].

The use of Q_{Cell} based on the simplified Bernardi's equation for Ohmic heat generation (Equation 2.15) in Equation 2.8 yields a general energy balance for accurate temperature

predictions for charge and discharge operations of Li-ion batteries [29]. Simulations should incorporate the transient behavior of cell voltage and current rather than employing averaged values.

2.4 Literature Review on Thermo-Electrochemical Modeling

The characterization of the relationship between Li-ion battery heating and the electrochemical reactions primarily traces to models developed by Sherfey and Brenner in 1958 [27]. Newman and Tiedemann discuss the influence of electrode porosity in 1975 [37]. Bernardi et al. provide significant expansion to the Sherfey-Brenner model in 1985 [28]. The energy balance by Bernardi et al. incorporates the electrochemical reactions that occur as electrons and Li-ions flow, mixing enthalpies, and phase changes of Li-ion battery systems [28]. Numerous thermo-electrochemical modeling studies of Li-ion batteries, incorporating principles from Sherfey and Brenner, Newman and Tiedemann and Bernardi et al., have followed. Early studies that followed Bernardi's general energy balance focus on simple model development to help design electric vehicle Li-ion battery assemblies. Later studies concentrate on advanced multi-dimensional and multi-physics modeling techniques to develop a more comprehensive understanding of the thermo-electrochemical mechanisms.

2.4.1 Pre-Millennial Research (1990 to 1999)

Chen and Evans publish three early studies discussing the thermo-electrochemical performance of Li-ion batteries with solid polymer electrolyte [40-42]. These studies focused on the performance characteristics associated with stacks of cells configured to achieve the energy and power requirements for an electric vehicle [40-42]. These studies identified that airflow cooling may not necessarily be an effective means for cooling stacks of Li-ion cells due to the tendency to create non-uniform temperature profiles that lead to cell degradation

[40-42]. Chen and Evans also note that thermal management of large stacks of Li-ion cells may not be an issue as long as low discharge rates are maintained [40-42]. The later study also expanded the models to consider simulation of thermal runaway [42].

Baudry et al. provide a study of solid polymer electrolyte Li-ion batteries for electric vehicle applications which relates temperature, output power, internal resistance and energy expense due to inefficiencies [43]. This study noted that electric vehicles would waste approximately 6% of the total available power when starting the battery from room temperature (°C) to before the optimal temperature is achieved (40 °C) [43].

Rao and Newman provided modification to Bernardi's energy balance by calculating Li-ion battery heat generation based "enthalpy potentials" [39]. This study identified relationships between open circuit voltage and ohmic losses with respect to the electrolyte within the cathode material [39]. For constant-current discharge operations, this new method yields comparable results to Bernardi's energy balance. This is primarily because of the smooth open circuit potential curve that is observed with constant-current discharge. The new model by Rao and Newman offers more accurate results when considering "dynamic discharge" mechanisms which have varying open circuit voltage curves [39].

Hallaj et al. develop a test-correlated thermo-electrochemical model of a Sony 18650 cell for a range of C/6 to 1 C discharge rates and scale the same model up to represent cylindrical cells of a 10 Ah to 100 Ah capacities [44]. Less accuracy was observed for the 1 C discharge rate when compared to test data [44]. This study identified that excessive cooling rates may not be optimal due to the tendency to create temperature gradients within the individual cells and that more uniform bulk temperatures are observed as cooling mechanisms were reduced [44].

2.4.2 Early Millennial Research (2000 to 2009)

Newman et al. examine the error induced by electrode side reactions on the measurement of potential based on "concentration-cell measurements" or bulk electrolyte concentration [36]. Newman et al. note that this error subsequently influences the calculation of transference number and concentration gradients which are associated with the local heating due to mixing (i.e. local heating during relaxation when current is removed) [36].

Chen et al. developed a test-correlated three-dimensional simulation of a large format 185 Ah Li-ion battery for an electric vehicle. These simulations incorporate the cooling effects of convection and radiation to the ambient environment [29]. The model by Chen et al. examined the layered structure of cell stacks, the case of the battery pack, and the gaps between the elements. This study exemplified the importance of cooling through radiation, the effects of forced convection vs. natural convection, and the role of the metal encasement as a heat spreader [29].

Mills and Al-Hallaj focused not only on thermally analyzing Li-ion battery systems, but on managing the locally generated heat through phase change materials as a passive thermal management system [45]. Numerical thermo-electrochemical models displayed that for a pack of six Li-ion batteries, for safe operation in extreme conditions, the volume needed for an appropriate amount of phase change materials would need to double [45]. This demonstrated that improved properties of the composite could lead to a reduction in volume and mass (possibly through impregnating the material with expanded graphite) [45].

2.4.3 Recent Millennial Research (2010 to 2015)

Cai and White expand the COMSOL Multiphysics sample model of a Li-ion cell to include an energy balance for temperature calculations [46]. This short communication study

provides a method for using multiphysics software to simultaneously calculate Li-ion cell electrical and thermal performance [46]. Cai and White complete this process by including the temperature dependency to the models of diffusion coefficient, the reaction rate constants, the open circuit potential and the thermal conductivity of the electrolyte [46].

Kim et. al developed methods for modeling Li-ion battery thermal behavior during the charging phases through two dimensional finite element method simulations validated by experimental results [47]. The study determined the potential and current density distributions on the Li-ion battery electrodes as a function of the charging time [47]. The charging profile consisted of constant-current followed by constant-voltage charging [47]. This study was extremely useful as it outlined the necessary methods for hot spot identification near the current collectors [47].

Jeon and Baek develop a high fidelity thermo-electrochemical model of a cylindrical $LiCoO_2$ cell which distinctly represents the individual layers of the jellyroll region [48]. This study explores the impacts of higher discharge rates on the heat generated due to joule heating and entropy change; an overall range of C/2 to 5 C discharge rates are examined. The key findings of the study are that joule heating is significant for higher discharge rates and that entropy change was more significant for low discharge rates [48].

Chacko and Chung provide test-correlated thermo-electrochemical simulations of pouch format polymer Li-ion cells used for an electric vehicle battery assembly [49]. The goal of the model is to help develop suitable thermal management systems to maintain appropriate battery temperatures during all drive cycles [49]. Relationships were identified between periods of "repeated acceleration and deceleration" and temperature rise [49].

Sun et al. incorporate Bernardi's energy balance into a test-correlated, three-dimensional, thermo-electrochemical and computational fluid dynamics (CFD) model of an electric vehicle Li-ion battery assembly experiencing drive cycles [50]. One of the significant findings of the study is that these advanced modeling techniques may be used to optimize the geometry of the cooling system to reduce the temperature gradient induced on the cells by up to 70% [50].

Nieto et al. developed a thermal model in 2012 that represents the heat generation behavior of a large format 10.5 Ah Li-ion battery that is based on experimental measurements of internal resistance and entropic heat coefficients [33]. Depending on the discharge rate, this model predicted to the experimental results within 15-21% error.

Awarke et al. discuss the impacts of urban drive cycles in Europe on electric vehicle Li-ion battery thermo-electrochemical performance [51]. This study identified relationships between road vs. highway drive cycles and battery aging via employment of a sophisticated multiphysics analysis approach [51].

Lee et al. developed a numerical model which incorporates coupled electrical and electrochemical physics for a 20 Ah large format cylindrically wound set of Li-ion battery cells [52]. The interesting portion of these results is that because all components and materials of the battery were modeled individually, evaluation can occur at a layer-to-layer level. This allows the design to occur at multiple levels including (a) number and location of tabs, (b) thermal and electrical configuration and (c) performance and life [52].

Ye et al. developed numerical models which examined the electro-thermal life cycles of a Li-ion battery for various charge and discharge rates in relation to fading capacity with

time [53]. Understanding the reduction in capacity over time and accurately implementing this into thermal models is vital to the amount of accuracy the model holds.

This brief overview provides insight into the various topics of interest for the thermo-electrochemical analysis of Li-ion battery charge and discharge operations. Until recently, most of these studies did not incorporate the benefits of multi-dimensional finite element analysis software. Unfortunately, without implementing modern computer processing capability and specialized analysis software, it is not possible to analyze Li-ion battery thermo-electrochemical performance in the vast array of radiation driven space environments. Without advanced analysis techniques, the design of the battery for space exploration applications is significantly limited.

Chapter 3 Development of Simulation Techniques for Lithium Ion Battery Heat Generation in Thermal Desktop

3.1 Motivation for Coupling Thermo-Electrochemical Analysis Techniques with Thermal Radiation Analysis Software Thermal Desktop

Simulating the temperature dependent internal heating rates of Li-ion batteries in thermal radiation driven orbital environments is uniquely challenging as the environments are continuously changing; note that this research focuses on the environments associated with structures orbiting the Earth. For example, NASA reports that the International Space Station (ISS) travels in a Low Earth Orbit (LEO) at a velocity of 28,100 km hr^{-1} (17,500 mi hr^{-1}). Each 90 minutes orbit contains a period of time in direct view of the sun (hot period) and a period of time in the Earth's shadow (cold period) [38]. Surface temperatures of structures orbiting Earth can fluctuate between cold and hot extremes ranging from -250 °C to +250 °C depending on the current point in orbit, local attitude, surrounding structures, passive and active thermal control methods and more [38].

Li-ion batteries have a wide range of operating and storage temperatures when considering terrestrial applications (e.g. -40 °C to +70 °C) [18]. However, in thermal radiation driven space environments, these limits are rapidly exceeded without effective thermal management systems; e.g., temperatures easily drop below the lower limits due to radiation to deep space (-270 °C) and combinations of solar radiation, albedo, infrared fluxes and local heating lead to temperatures well beyond the upper limits (+250 °C) [38]. Any cell-to-cell temperature variations inside a Li-ion battery assembly also significantly influence the performance, reliability and life; uniform temperatures are preferable [54].

Cold temperatures beyond the lower storage and operating limits can permanently damage the capacity of the battery while combinations of environmental heating with Li-ion battery local heating could lead to elevated temperatures that induce thermal runaway [18]. Mission specific analysis, via tools such as Thermal Desktop, that consider combinations of environmental heating and local heat generation is necessary to develop safe and reliable Li-ion battery assemblies.

3.2 Factors Influencing Thermal Performance in Orbital Environments

This section provides a description of the parameters associated with thermal radiation driven orbital environments for Earth and the impact they have on Li-ion battery operating temperatures. The primary factors that come into consideration when determining the thermal performance of a Li-ion battery in orbital environments include [10, 38]:

- **Orbit type:** Low Earth Orbit (LEO), Geosynchronous Earth Orbit (GSO), Geostationary Earth Orbit (GEO), Medium Earth Orbit (MEO), etc.
- **Local attitude:** Yaw (z-rotation), pitch (y-rotation) and roll (x-rotation) of the orbiting structure
- **Orbital velocity:** The velocity of the orbiting structure which will partially dictate how much time is spent in and out of the direct view of the sun
- **Beta angle:** the angle between the solar vector (i.e. the vector pointing towards the sun) and its projection onto the orbit plane
- **Solar flux:** the intensity of the incoming radiation energy from the sun
- **Albedo:** the solar energy reflected from Earth and its atmosphere
- **Infrared flux:** the heating from the Earth in the form of long-wave radiation

- **Surrounding structures:** all of the structures and components of an orbiting system contribute to the overall radiation network (e.g., view factor to the sun and Earth, shading, etc.) and also create conduction paths
- **Active thermal control systems:** pump and flow controlled thermal management systems (e.g., cold plates and loop heat pipes)
- **Passive thermal control systems:** thermophysical and optical property controlled thermal management systems (e.g., surface coatings, insulation blankets, etc.)

Thermophysical properties considered with any thermal analysis are thermal conductivity (W m^{-1} $ºC^{-1}$), specific heat capacity (J kg^{-1} $ºC^{-1}$) and density (kg m^{-3}). These properties, combined with local heating effects and the environment, determine how quickly or slowly orbiting structures change temperature in the space environment. For Li-ion batteries, the specific heat capacity and density of the jellyroll materials (i.e. materials inside the encasement) greatly dictate the transient nature of the thermal assessment of a Li-ion battery [29]. Conduction, which is controlled by these material properties, is the transfer of heat through the solids (and/or semisolids) of the battery system and at the mounting locations to the primary structure in orbit. The rate at which energy is gained or lost at this contact location is dependent on how well the objects are in contact; i.e. how much thermal resistance exists (conductance).

Optical properties include surface absorbance (α) and emissivity (ε). Controlling these properties affects how well the surfaces of the orbiting structure absorbs and emits thermal energy. Utilizing experimentally measured optical properties in analysis is essential when considering the impact these properties play when combined with solar radiation, albedo, infrared fluxes, etc. For example, if a given Li-ion battery assembly has an encasement

coating with a low emissivity (e.g., 0.03), surface temperatures can quickly exceed +250 °C, whereas the same encasement with a higher emissivity (e.g., clear anodized aluminum 0.87 [38]), surface temperatures may not exceed +80 °C [10, 38]. Radiation is not considered a major driver of battery thermal control for terrestrial applications, but in space, radiation is the primary form of passive thermal control. Chen et al. reports that even in convective environments, controlling surface optics of the encasement can attribute to 28-30% of the cooling of a battery [29]. The surface optical properties of the surrounding structures and the specific mounting location of the orbiting object also contribute to determining the effects of the thermal environment as these objects provide shading (or no shading) which increase or decrease the thermal energy experienced by the system.

Zero gravity and vacuum environments also contribute. Microgravity, often referred to as zero-gravity (0-G), and vacuum environments indicate that natural convection will not be present to cool the system [38]. The effects of vacuum and 0-G could alter the movement of ions, electronics and other species, which would not only affect the efficiency of the battery, but can also affect the rate at which local heating occurs.

Some of the key parameters discussed in this section are demonstrated in Figure 3-1.

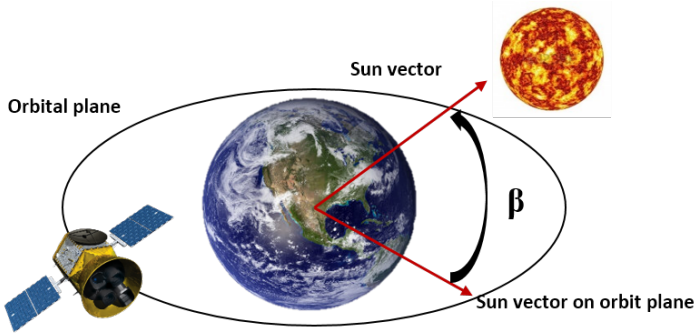

Figure 3-1 **Image displays a satellite orbiting the Earth. The following components are a radiation driven space environment are captured: (a) orbit plane, (b) beta angle, (c) solar flux, (d) infrared heating and (e) albedo.**

3.3 Orbital Simulation Software Packages

Li-ion battery analysis with software designed to incorporate the complexities of thermo-electrochemical reactions that occur throughout charge and discharge operations helps design suitable systems to maintain the integrity of the battery throughout its lifecycle. Examples of these software packages include COMSOL Multiphysics, CD Adapco Battery Design Studio and CD Adapco Battery Simulation Module [46,55]. Though powerful for battery design applications, these software suites do not currently offer options to thoroughly simulate radiation driven space environments. Likewise, software capable of simulating space radiation, such as Cullimore & Ring Technologies (CRTech) Thermal Desktop (TD) and Systems Improved Numerical Differencing Analyzer (SINDA), Thermal Radiation Analyzer System (TRASYS), Siemen's NX Space Systems Thermal (SST) and Thermal Synthesizer System (TSS), are not immediately ready to include thermo-electrochemical processes of Li-ion batteries. A joint approach is required.

To ensure the success of orbit bound Li-ion batteries, we develop Li-ion battery temperature prediction techniques for thermal radiation driven space environments by integrating proven numerical thermo-electrochemical models of battery reactions derived through energy balance equations with CRTech's Thermal Desktop to provide an intuitive coupling of thermal radiation analysis and thermo-electrochemical modeling techniques.

Thermal Desktop is a graphical user interface (GUI) integrated into AutoCAD with built in tools that allow analysts to provide thermal definition as the model is constructed. When radiation analysis is necessary, Thermal Desktop engages a tool named RadCAD to generate what the software refers to as radiation conductors (Radks). After the thermal model is completed, Thermal Desktop writes a SINDA language code which is exported

to SINDA to solve for transient and steady state solutions. For orbital analysis, Thermal Desktop allows the analyst to define orbit specific boundary conditions and the number of points in orbit that should be considered; i.e. separate sets of radks and SINDA code are created for each point in orbit to account for the transient effects of the changing thermal environment. Figure 3-2 displays Thermal Desktop representation of an example orbital sequence for a simple satellite model.

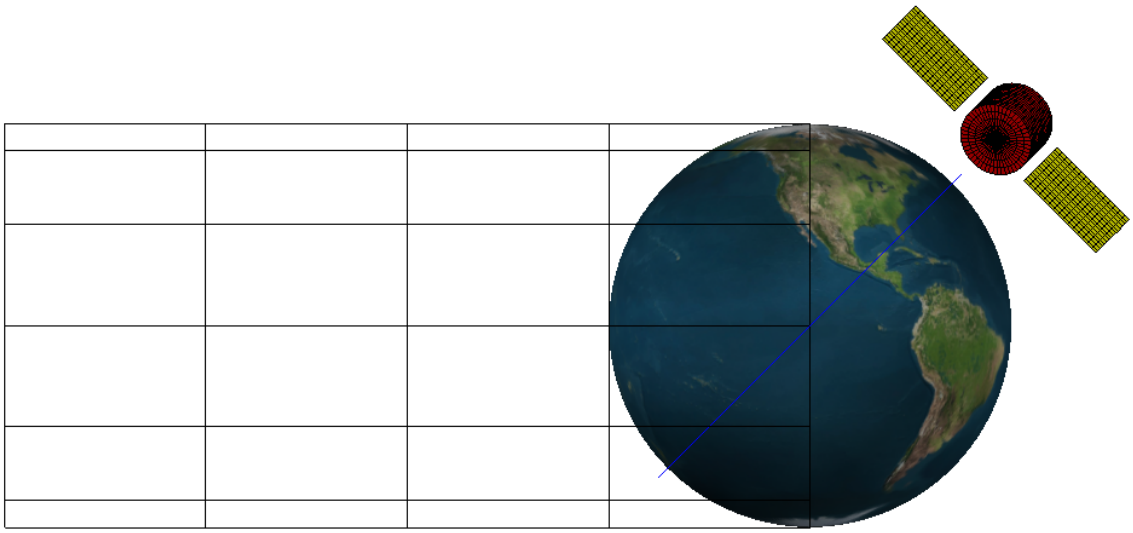

Figure 3-2 Example sequence of a satellite orbiting the Earth in the thermal analysis software Thermal Desktop.

Once validated, this combination of radiation analysis and thermo-electrochemical simulation techniques will allow the charge and discharge heat generation rates of the Li-ion battery simulation to be a function of temperature for any set of orbital conditions. In that, once modeling techniques are not limited to user-defined environmental conditions and pre-defined local heat generation rates, the thermo-electrochemical performance of the Li-ion battery becomes an accurate function of the orbital model.

3.4 Thermal Desktop Model Development

Chen et al. [29] provide a test-correlated thermo-electrochemical simulation of a large format 185 Ah Li-ion battery under constant-current discharge conditions. Simulation conditions include a 60 minutes discharge at 185 A (1 C), a 30 minutes discharge at 370 A (2 C), and a 20 minutes discharge at 555 A (3 C). The ambient temperature for the Li-ion battery assembly is 26.85 ºC (300 K). Each discharge rate is considered in a natural convection environment and the 3C discharge rate is considered in various forced convection environments. The heat transfer coefficient for the forced convection studies ranged from 20 W m^{-2} ºC^{-1} to 300 W m^{-2} ºC^{-1}. Radiation to the ambient temperature is also included in all calculations. The study by Chen et al. [29] is recreated in Thermal Desktop as a baseline evaluation to determine the suitability of the software package for thermo-electrochemical analysis. The following sections discuss the discretization of the Li-ion battery assembly geometries, the development of local heating through SINDA logic statements, thermophysical properties, surface optical properties, contact regions, the institution of environmental parameters and the test case matrix.

3.4.1 Geometry Development and Assigned Material Properties

The geometries of the 185 Ah Li-ion battery assembly are displayed in Figure 3-3. The Thermal Desktop model is divided into four sub-models to individually represent (a) the aluminum encasement that serves as the heat spreader, (b) the core region (i.e. the jellyroll materials) and (c) the contact layer of liquid electrolyte between the encasement and the core region. The basic geometries displayed in Figure 3-3 are imported into Thermal Desktop where discretization and thermal definition are provided.

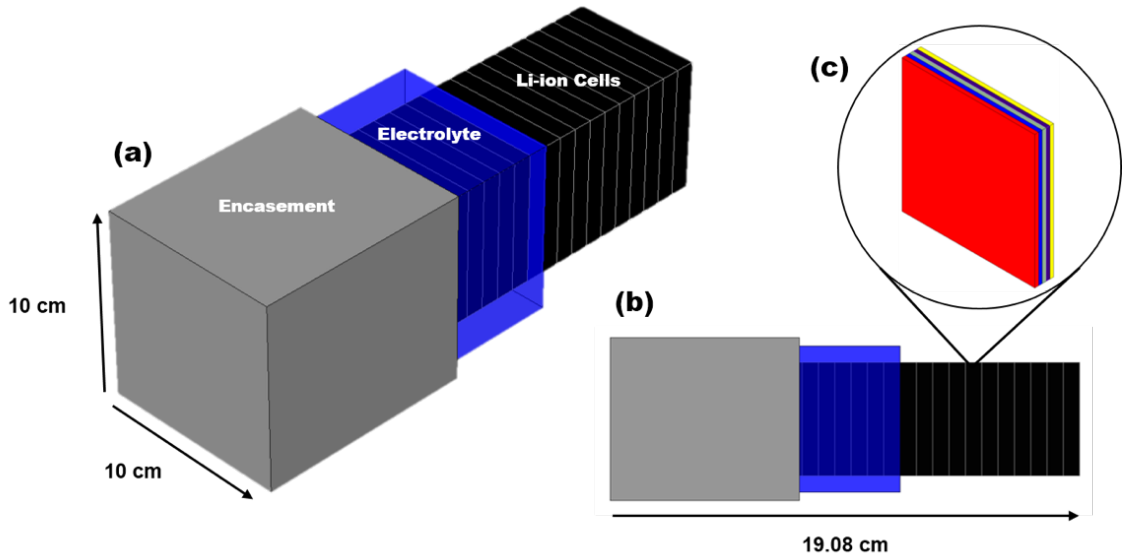

Figure 3-3 **Large format 185 Ah Li-ion battery where: (a) an isometric view of the battery, (b) the side view of the battery and (c) a breakdown of the cell layup. Geometries and dimensions adapted from Chen et al. [29].**

The aluminum encasement is represented with six surfaces (1233 nodes total) that are assigned a thickness of 0.07 cm; Al 6061-T6 thermophysical properties and an exterior surface emissivity of 0.25 are assigned per the specification by Chen et al. [29]. The liquid electrolyte region is represented with an additional six surfaces (1233 nodes total) that are assigned a thickness of 0.05 cm; the electrolyte thermophysical properties are based on those provided by Chen et al. [29]. A single block (125 nodes total) is used to represent the Li-ion cells that make up the core region; the thermophysical properties of the core region are averaged properties representing the lump mass of all of the individual Li-ion cells. Anisotropic thermal conductivity of 28.3 W m^{-1} °C^{-1} in the x-direction and 3.3 W m^{-1} °C^{-1} in the y and z-directions is implemented to take into account the thermal resistance between the cell materials [29].

3.4.2 Development of SINDA Logic Statements to Represent Ohmic Heating

Each of the 125 core region nodes are assigned a local heat load (W) via SINDA logic statements that are defined with variable symbols expression of Bernardi's energy balance

(Equation 2.15). To apply the heating rate correctly, we established temperature dependent heat loads to each of the 125 core region nodes. Each heat load is multiplied by a proportionality factor to take into account the percent volume of the core region that each node represents. The total volume of the core region is 1908 cm^3, or approximately 125 individual blocks of 15.3 cm^3.

The transient profiles of open circuit and working voltages (V_{OC} and V_W) used in Thermal Desktop are based on experimental data by Chen et.al. [29]. The experimentally determined curves for the 185 Ah Li-ion battery for 1 C, 2 C and 3 C discharge rates are represented in Figure 3-4 as a function of voltage vs. depth-of-discharge (DOD). Because Thermal Desktop works with heat loads as functions of time rather than DOD, arrays of these curves with respect to time are developed based on the following:

- 1 C: 60 minutes discharge time at 185 A constant current
- 2 C: 30 minutes discharge time at 370 A constant current
- 3 C: 20 minutes discharge time at 555 A constant current

The resulting temperature profiles from Chen's natural convection experiments are displayed with Figure 3-5 and forced convection experiments with Figure 3-6. Comparing the two figures with Figure 3-4 demonstrates the direct relationship between local heating rate, the magnitude of the V_{OC} and V_W difference and cell temperature. Larger differences between V_{OC} and V_W lead to increased heating rates. This is the reason for the elevated heating rates at the beginning and end of discharge.

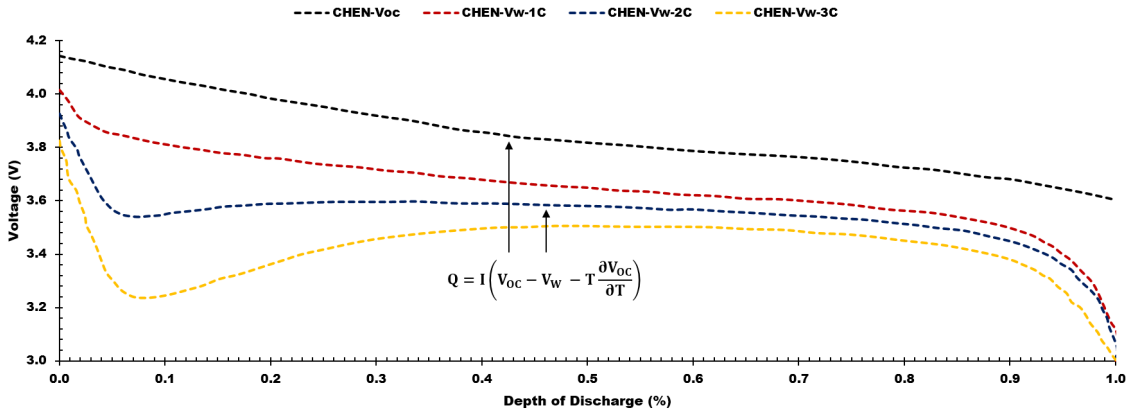

Figure 3-4 **V_{OC} and V_W profiles for constant-current discharge for the following: (a) 1 C rate, (b) 2 C rate and (c) 3 C rate. The data is adapted from Chen et al. [29].**

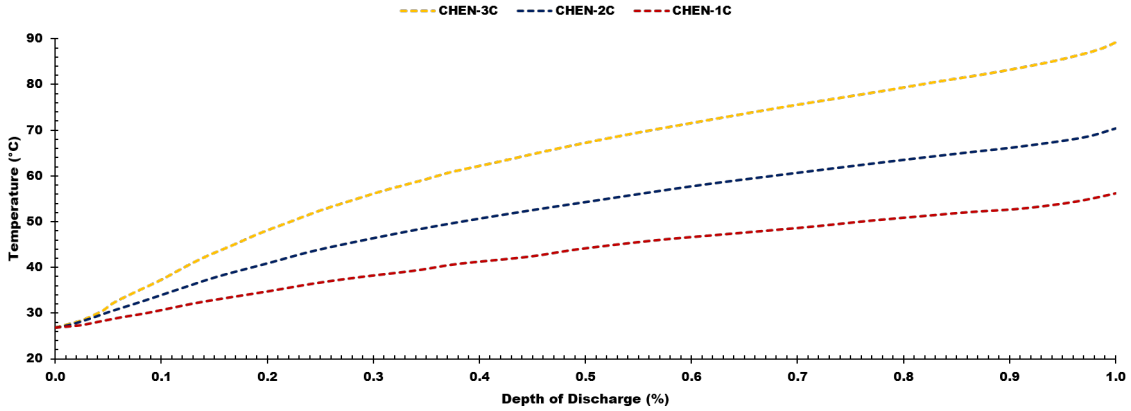

Figure 3-5 **Natural convection environment temperature profiles for the following: (a) 1 C rate, (b) 2 C rate and (c) 3 C rate. The data is adapted from Chen et al. [29].**

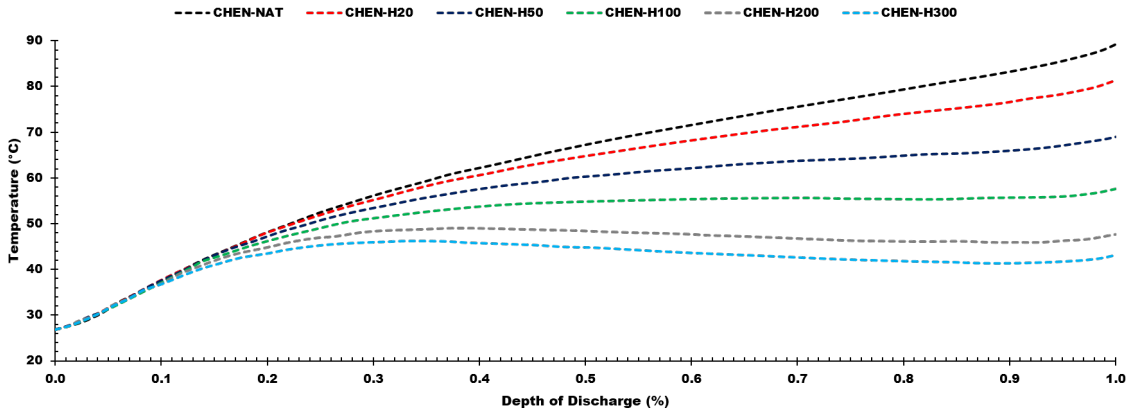

Figure 3-6 **Temperature profiles for constant-current 3 C rate discharge in forced convection environments ranging from 20 W m^{-2} $^oC^{-1}$ to 300 W m^{-2} $^oC^{-1}$. The data is adapted from Chen et al. [29].**

3.4.3 Establishing Convection and Radiation to the Boundary Temperature

The external surfaces of the encasement are bounded with a radiation and convection network with a temperature of 26.85 ºC (300 K). Radiation calculations are handled with Thermal Desktop's RadCAD utility. The convective environment is established by connecting the exterior encasement surfaces to a separate boundary node via a conductor defined with a heat transfer coefficient (W m^{-2} ºC^{-1}). Location dependent heat transfer coefficients ranging between 5 W m^{-2} ºC^{-1} to 10.6 W m^{-2} ºC^{-1} are used for natural convection calculations and constant values ranging between 20 to 300 W m^{-2} ºC^{-1} are used for forced convection [29].

3.4.4 Definition of Contact Region

Two locations of contact are defined in the Thermal Desktop model: (1) between the encasement bottom and the top of the contact region solids and (2) between the bottom of the contact region and the top of the core region block. Chen et.al. noted that thermal resistance between all contacting surfaces was negligible because the electrolytic solution surrounded the core and was filled to all edges of the encasement [29]. In Thermal Desktop, an arbitrarily high conductance of 3000 W m^{-2} ºC^{-1} is assumed to minimize thermal resistance at the interfaces between the simulation geometries.

3.4.5 Completed Thermal Desktop Model

The completed Thermal Desktop model, shown with Figure 3-7, is created with Thermal Desktop native objects and consists of 2592 nodes divided between four submodels (i.e. the encasement, the electrolyte and the core region). Table 3-1 describes all dimensions, battery properties, material properties and environmental characteristics used for the

Thermal Desktop model in recreation of the work by Chen et al. [29]. The Thermal Desktop model development process is described with Figure 3-8.

Table 3-1 Physical characteristics and material properties for the Thermal Desktop model of the 185 Ah Li-ion battery. Data adapted from Chen et al. [29].

Characteristic	Value	Unit
Total battery dimensions	19.32 x 10.24 x 10.24	cm x cm x cm
Thickness of the case	0.07	cm
Thickness of the electrolytic layer	0.05	cm
Core region dimensions	19.08 x 10 x 10	cm x cm x cm
Individual cell dimensions	0.0636 x 10 x 10	cm x cm x cm
Thickness of the Al foil	0.002	cm
Thickness of the Cu foil	0.0014	cm
Thickness of the cathode	0.014	cm
Thickness of the anode	0.0116	cm
Theoretical capacity	185	Ah
Surrounding temperature	29.85	°C
Initial temperature	300	°C
Properties, carbon electrode	1347.3 | 1437.4 | 1.04	kg m^{-3} | J kg^{-1} $°C^{-1}$ | W m^{-1} $°C^{-1}$
Properties, $LiCoO_2$ electrode	2328.5 | 1269.2 | 1.58	kg m^{-3} | J kg^{-1} $°C^{-1}$ | W m^{-1} $°C^{-1}$
Properties, Al foil	2702.0 | 903.0 | 238	kg m^{-3} | J kg^{-1} $°C^{-1}$ | W m^{-1} $°C^{-1}$
Properties, Cu foil	8933.0 | 385.0 | 398	kg m^{-3} | J kg^{-1} $°C^{-1}$ | W m^{-1} $°C^{-1}$
Properties, polymer separator	1008.9 | 1978.2 | 0.33	kg m^{-3} | J kg^{-1} $°C^{-1}$ | W m^{-1} $°C^{-1}$
Properties, Al-2024	700.0 | 477.0 | 14.6	kg m^{-3} | J kg^{-1} $°C^{-1}$ | W m^{-1} $°C^{-1}$
Properties, electrolyte	1129.9 | 2055.0 | 0.60	kg m^{-3} | J kg^{-1} $°C^{-1}$ | W m^{-1} $°C^{-1}$

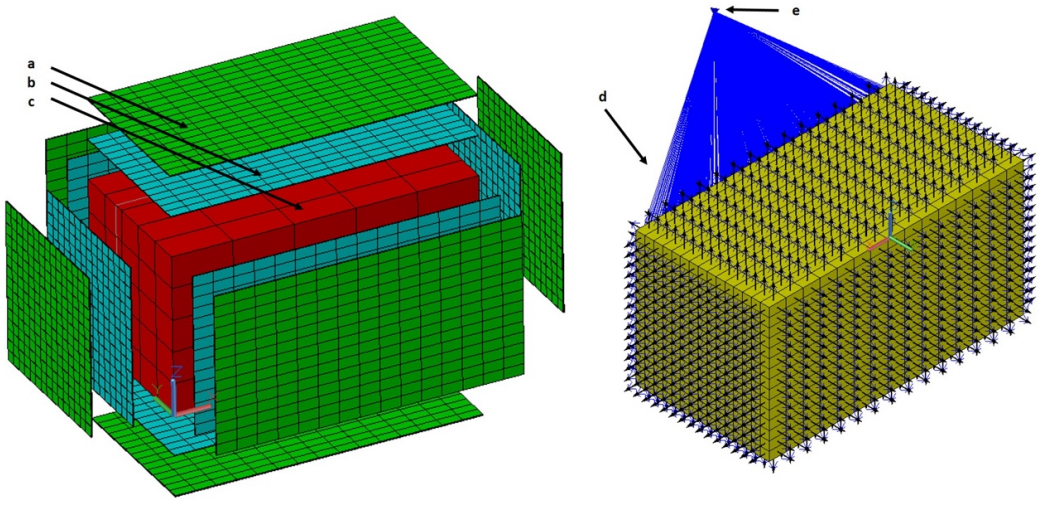

Figure 3-7 Image displays the Thermal Desktop model which simulates the 185 Ah battery discussed by Chen et al. [29].

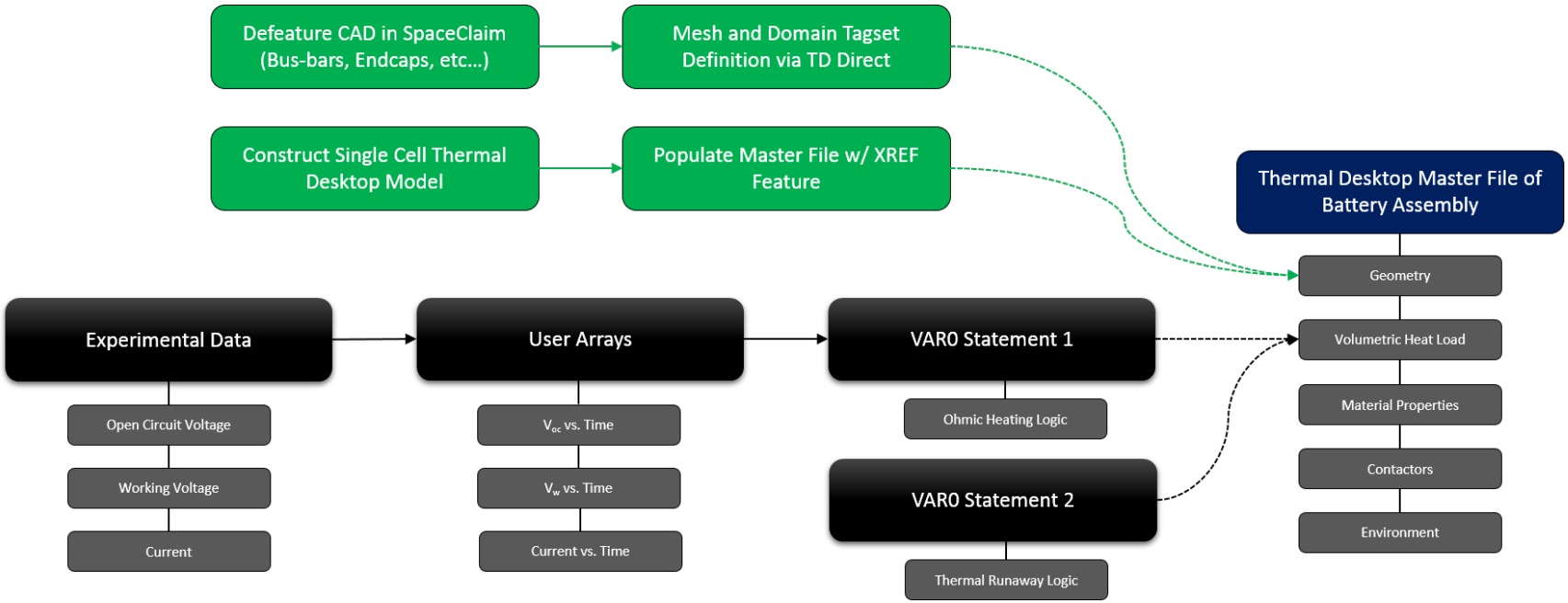

Figure 3-8 Process flow diagram describing the simulation of Li-ion battery local heat generation in Thermal Desktop.

3.4.6 Analysis of Three Specific Cases

Three cases are analyzed in this study; Case 1 (replication study), Case 2 (model improvement) and Case 3 (parametric study). For Case 1, an exact replication of the study by Chen et al. [29] is conducted which utilizes the same V_{OC} and V_W profiles, boundary conditions and Bernardi's energy balance for local heating. Case 2 sought to improve the model with the implementation SINDA logic to update the local temperature assigned to the heating logic for each of the 125 Qs after each iteration of the transient solution. With said logic implemented, as the local temperature updates per iteration, the Q per node varies as a function of depth-of-discharge and temperature. The effects were expected to be small because the local temperature is multiplied against $dV_{OC}\ dT^{-1}$, which is an e-4 variable. Case 3 provides a small parametric study to observe the effects of different combinations core region ρ and c_p. The ρ and c_p utilized by Chen et al. did not account for the fact that an electrolytic layer also exists between the two electrodes which could affect the transient thermal response of the Li-ion battery assembly. Table 3-2 describes all test cases analyzed.

3.5 Results and Discussion

For Case 1, an exact replication of the study by Chen et al. [29] was created in Thermal Desktop. SINDA logic is implemented to update the Q applied to each core region node after each iteration of the transient solution; i.e. the SINDA logic updates the open circuit potential and working voltage used to determine Q through depth of discharge. A constant 26.85 °C (300 K) value was applied to the temperature term of Bernardi's equation for Q. The Thermal Desktop boundary conditions were driven by convection and radiation to a 26.85 °C (300 K) sink temperature. This variation of the model was executed for the three discharge rates (1 C to 3 C) and six convection rates (natural to 300 W m^{-2} $°C^{-1}$). The

Thermal Desktop predictions compared to the test data from Chen et al. [29] for the 1 C to 3 C discharge rates in a natural convection environment are displayed with Figure 3-9. The Thermal Desktop results for 3 C discharge in the forced convection environments are compared to the test data by Chen et al. [29] with Figure 3-10.

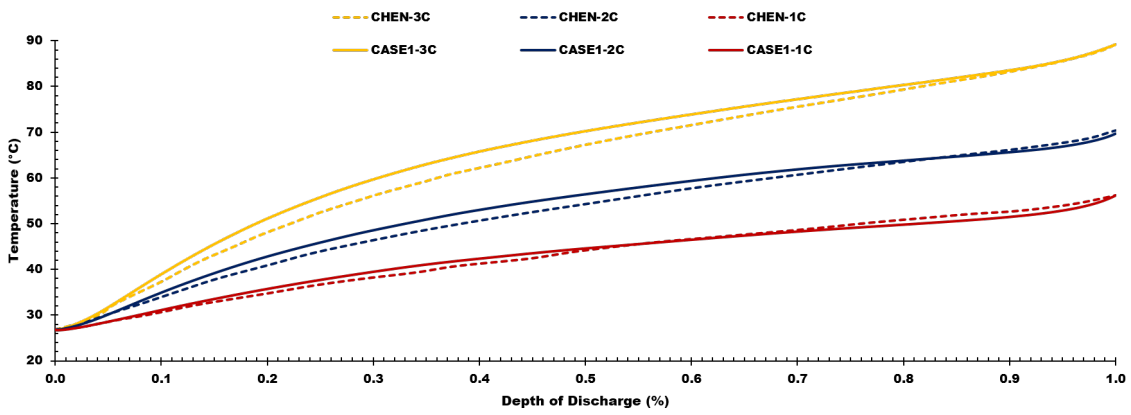

Figure 3-9 Case 1 Thermal Desktop results for a large format 185.3 Ah Li-ion battery compared to the test data by Chen et al. for natural convection [29].

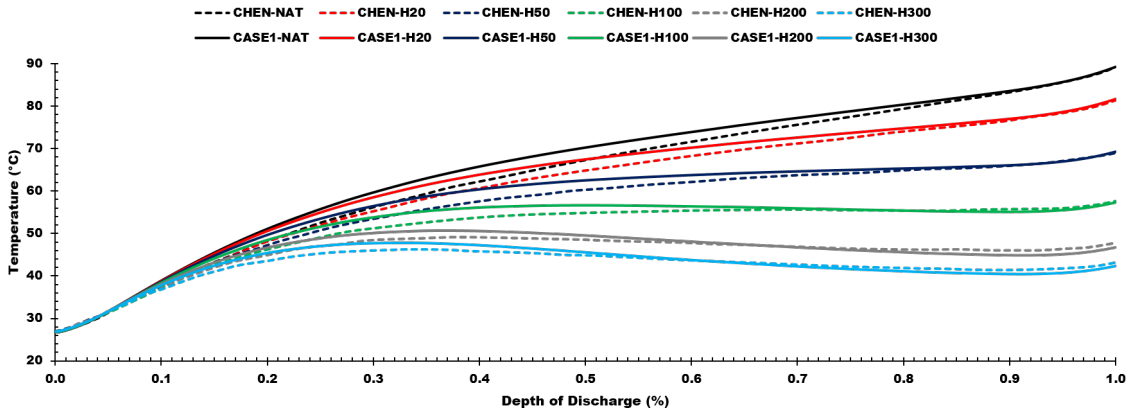

Figure 3-10 Case 1 Thermal Desktop results for a large format 185.3 Ah Li-ion battery compared to the test data by Chen et al. for various forced convection environments [29].

The results of the Thermal Desktop simulation for Case 1 closely follow the transient temperature profiles and the end of cycle profiles provided by Chen et al. [29]. The hot spot location for the Thermal Desktop simulation is in the middle for the x-axis direction and towards the bottom in the z-axis direction; i.e. the center of the stack of cells along the

length of battery assembly and towards the bottom of the cell where less cooling effects occur. The temperature gradient in is symmetric in the y-direction; i.e. the width of the Li-ion battery assembly. The Al encasement, which serves as a heat spreader, is significantly cooler than the core region. As put by Chen et al., this is a result of the high specific heat capacity and thermal conductivity of Al and the direct interaction of the encasement with the cooling environment [29]. These results are in direct agreement with the Chen et al. [29]. Isothermal images of the core region throughout the discharge duration for the 3 C rate in a natural convection environment are provided with Figure 3-11. The Case 1 results, compared to Chen et al., demonstrate that Thermal Desktop has the capability to accurately simulate Li-ion battery local heat generation through discharge.

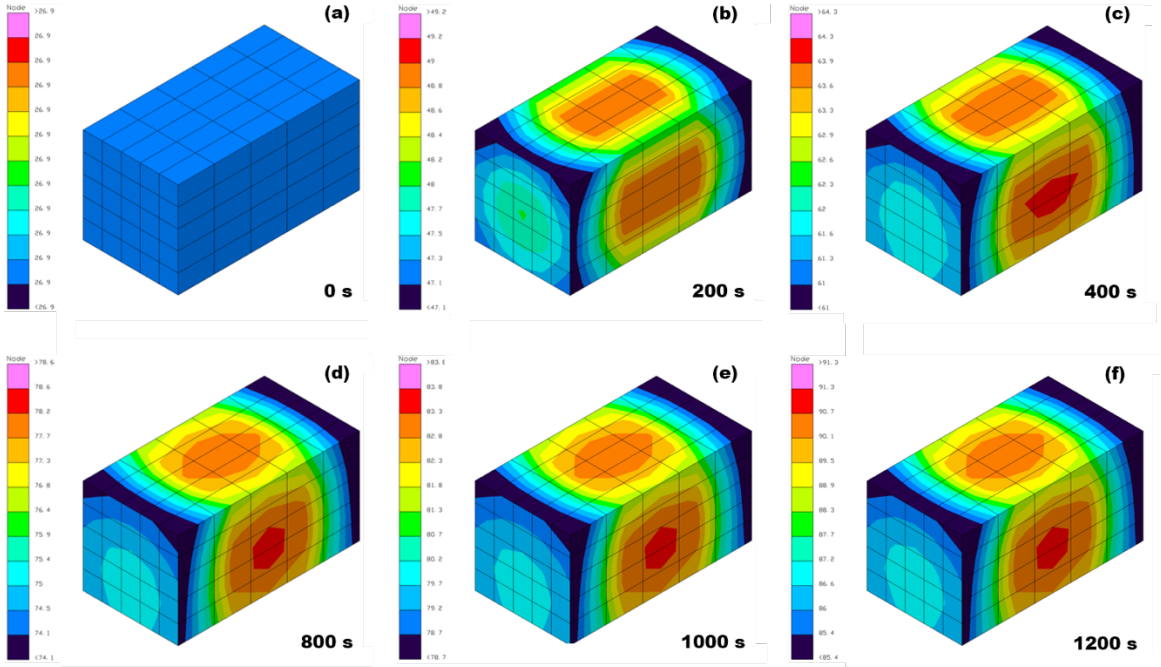

Figure 3-11 **Isothermal image of the core region results for a 3 C discharge rate in a natural convection environment for the following timesteps: (a) 0 s, (b) 200 s, (c) 400 s, (d) 800 s, (e) 1000 s and (f) 1200 s.**

Case 2 analyses sought to improve the model, which assumed a constant 26.85 °C (300 K) for the temperature term in the Q logic statements. SINDA logic was programmed here to update the Q of each core region node after every iteration of Thermal Desktop's solving process based on changes in open circuit potential, working voltage and local node temperature through depth of discharge. This variation of the model was executed for all discharge rates and convection combinations as with Case 1. The transient temperatures are provided with Figure 3-12 (natural convection) and Figure 3-13 (forced convection).

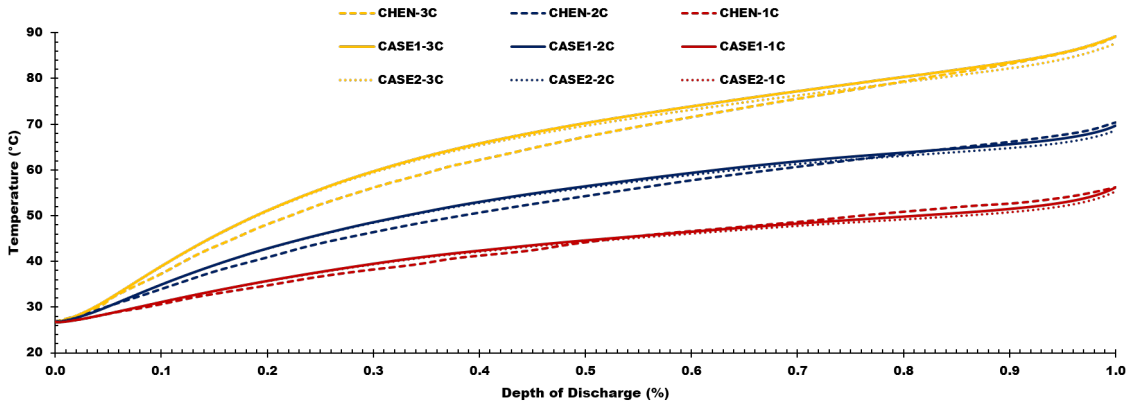

Figure 3-12 Case 1 and Case 2 Thermal Desktop results for a large format 185.3 Ah Li-ion battery compared to the test data by Chen et al. for natural convection [29].

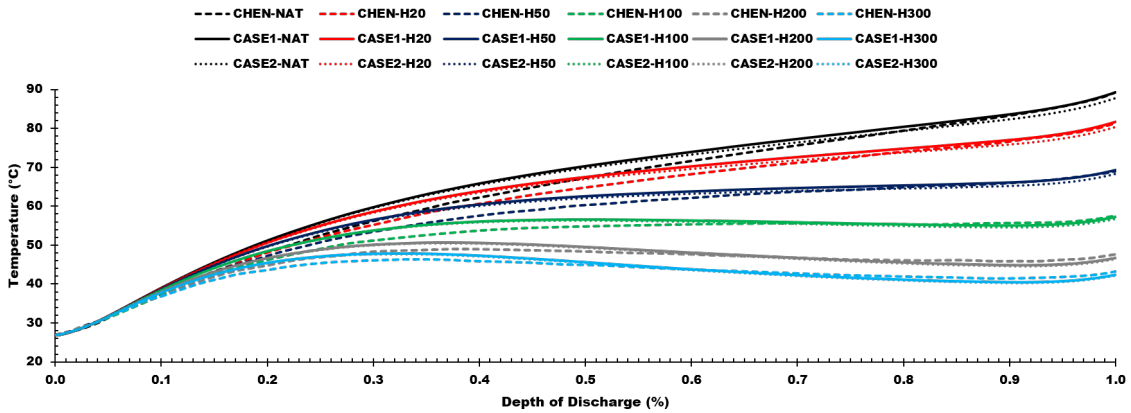

Figure 3-13 Case 1 and Case 2 Thermal Desktop results for a large format 185.3 Ah Li-ion battery compared to the test data by Chen et al. for various forced convection environments ranging from 20 W m^{-2} °C^{-1} to 300 W m^{-2} °C^{-1} [29].

The results indicate that for the temperature profile at the end of cycle transient for all discharge cases were approximately 0.5 °C to 1 °C lower than the model without the updating temperature term. It is observed that this lower temperature profile appears to be highly sensible, as it decreases the total voltage that the current is multiplied against. For a general sink temperature analysis, the model assumption by Chen et al. [29] would make for a more conservative assessment. The reader should note that this is partially an effect of the Li-ion battery interacting with a constant 26.85 °C (300 K) sink temperature via radiation and convection. The effects of a higher local temperature in non-symmetric locations through the entirety of depth-of-discharge, due to combinations of solar radiation, infrared fluxes, albedo and shading, could drastically alter the transient profile by more than just a few degrees Celsius. The isothermal profile through depth-of-discharge could also be completely different as well. The authors recognize that the effects of a per iteration update to the entropy term has a small overall effect; however, this study simply recommends that this parameter not be neglected, but considered a combined effect with orbital heating. Also, recall that Jeon and Baek identified that the entropy term has a greater effect on the heating associated with lower discharge rates [48].

Case 3 is conducted because Chen et al. [29] did not assume an electrolytic layer between the electrodes of the individual cells when calculating the core region volumetric material properties. This circumstance presented the question: what is the effect on the thermal profile as a result of error related calculations in core region specific heat capacity? Standard specific heat capacity testing includes the entire cell; i.e. the testing includes the metal encasement and is not a direct measure of the individual cell jellyroll region materials. Because cell jellyroll materials are often proprietary in nature, it is difficult to

ascertain the actual value of the specific heat capacity. For Case 3, six combinations of core region specific heat capacities are considered: (a) 15% C_p reduction, (b) 10% C_p reduction, (c) 5% C_p reduction, (d) 5% C_p increase, (e) 10% C_p increase, (f) 15% C_p increase. These different property combinations are considered for a constant 3 C discharge rate of the 185.3 Ah Li-ion battery in a 26.85 °C (300 K) natural convection environment. The results are provided with Figure 3-14.

These analyses explore the effects that are caused by incorrect calculation of the combined material properties. The results in Figure 3-14 exemplify the importance of determining the correct core region specific heat capacity. Overestimating core region c_p results in lower predicted temperatures while underestimating results in higher predicted temperatures. Future work might consider the error associated with incorrect calculation of core region thermal conductivity in the x-direction.

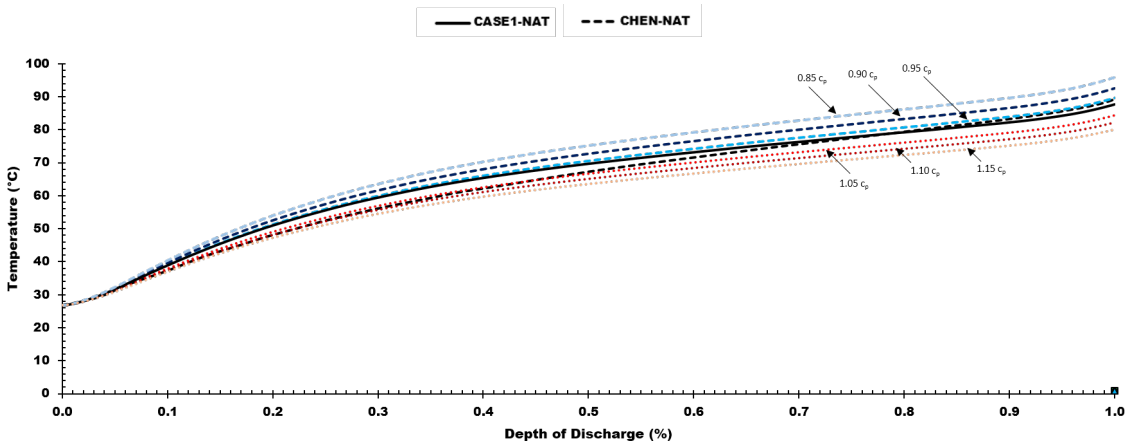

Figure 3-14 Thermal Desktop results compared to results by Chen et al. for the large format 185.3 Ah Li-ion battery at a 3 C discharge rate in a natural convection environment [29]. These results examine the effects of varied core region c_p.

3.6 Thermal Desktop Model Development Conclusions

We validated the capability of thermal radiation analysis software Thermal Desktop to perform basic thermo-electrochemical analyses based on energy balance developed by Bernardi et al. [28]. The studies are based on test results of a large format 185 Ah Li-ion battery by Chen et al. [29]. An overview of the test case matrix that results are provided for is given in Table 3-2.

Table 3-2 Comprehensive test case matrix for the Thermal Desktop analysis of the large format 185 Ah Li-ion battery discussed by Chen et al. [29].

Case ID	Type	Rate (C)	Time (s)	I (A)	h (W m^{-2} °C^{-1})
1	Case 1	3	1200	555	Natural
2	Case 1	2	1800	370	Natural
3	Case 1	1	3600	185	Natural
4	Case 1	3	1200	555	20 (Forced)
5	Case 1	3	1200	555	50 (Forced)
6	Case 1	3	1200	555	100 (Forced)
7	Case 1	3	1200	555	200 (Forced)
8	Case 1	3	1200	555	300 (Forced)
9	Case 2	3	1200	555	Natural
10	Case 2	2	1800	370	Natural
11	Case 2	1	3600	185	Natural
12	Case 2	3	1200	555	20 (Forced)
13	Case 2	3	1200	555	50 (Forced)
14	Case 2	3	1200	555	100 (Forced)
15	Case 2	3	1200	555	200 (Forced)
16	Case 2	3	1200	555	300 (Forced)
17	Case 3	3 C discharge, natural convection, 0.85% specific heat, actual density			
18	Case 3	3 C discharge, natural convection, 0.90% specific heat, actual density			
19	Case 3	3 C discharge, natural convection, 0.95% specific heat, actual density			
20	Case 3	3 C discharge, natural convection, 1.05% specific heat, actual density			
21	Case 3	3 C discharge, natural convection, 1.10% specific heat, actual density			
22	Case 3	3 C discharge, natural convection, 1.15% specific heat, actual density			

In summary, Case 1 results displayed an accurate replication of the temperature profiles provided by Chen et al. for all discharge and convection combinations. This supports the use of Thermal Desktop for coupled thermal radiation and thermo-electrochemical analysis of Li-ion batteries. The minimal deviation from experimental results would easily be encompassed by the recommended predicted +11 °C margin for test correlated thermal models as recommended by both the Gilmore Satellite Thermal Control Handbook and the

Department of Defense Standard Practice Product Verification Requirements for Launch, Upper Stage, and Space Vehicles (MIL-STD-1540D) section for thermal model margin for spacecraft hardware [38,56].

Case 2 identified the impact of updating the local temperature term when calculating core region heating rates. This case revealed that for less extreme sink temperatures and heat fluxes, the change in heat generation is minimal, but that combination with space environments could greatly affect the thermal profile.

Case 3 results display the impact of error when calculating core region specific heat capacity and that minimal error here could have a detrimental effect on temperature predictions (e.g., the prediction of temperatures lower or higher than what the Li-ion battery will actually experience). Underestimating the specific heat capacity might lead analysts to develop an insufficient thermal management system.

Chapter 4 Simulation of Robonaut 2 Lithium Ion Battery Assembly Heat Generation in Thermal Radiation Driven Orbital Environments

4.1 Introduction to the Robonaut 2 Lithium Ion Battery Assembly

The Thermal Desktop technique discussed in the previous section is employed and improved to support NASA by developing a test correlated thermo-electrochemical model of the Li-ion battery power system for humanoid robot Robonaut 2 which utilizes 300 Boston Power Swing 5300 (BP-5300) Li-ion cells in the form of a backpack. A single BP-5300 cell is displayed with Figure 4-1. R2 is currently on the International Space Station (ISS) and receives power through a tether; Figure 4-2. Building from the previous study which considered discharge operations only, this test-correlated Thermal Desktop model precisely simulates BP-5300 cell temperatures as a function of combinations of environments and self-heating rates during both charge and discharge operations.

Figure 4-1 Image of a Boston Power Swing 5300 Li-ion cell; the cell maintains a 5300 mAh capacity and is approximately double the size of the standard 18650 cell.

A vertical approach to battery pack model development is also presented by expanding a test validated cell level model into a 300 cell system level battery model. One goal for R2 is the use of the humanoid robot in the vacuum of space external to the ISS to support astronauts during extra vehicular activities. As a demonstration of the newly developed

Thermal Desktop modeling capability, the R2 battery model is combined with another Thermal Desktop model of a satellite to simulate thermal performance for a hypothetical EVA exterior to an orbiting structure in a thermal radiation driven orbital environment. The combined results of this study yield necessary validation that Thermal Desktop is suitable for thermo-electrochemical analysis and safe design of Li-ion battery assemblies operating in thermal radiation driven space environments.

Table 4-1 Boston Power Swing 5300 lithium ion cell characteristics adapted from the manufacturer provided datasheet [57].

Characteristic	Value	Unit
Cell dimensions	1.92 x 3.73 x 6.48	cm^3
Cell mass	93.5	g
Cell volume	46.4	cm^3
Theoretical capacity	5.3	Ah
Nominal energy	19.3	Wh
Gravimetric density	2.07e5	Wh g^{-1}
Volumetric energy density	5.90e2	Wh L^{-1}
Cycle life	3.00e3	Cycles
Operating temperature range	-20 to +60	°C
Storage temperature range	-40 to +70	°C

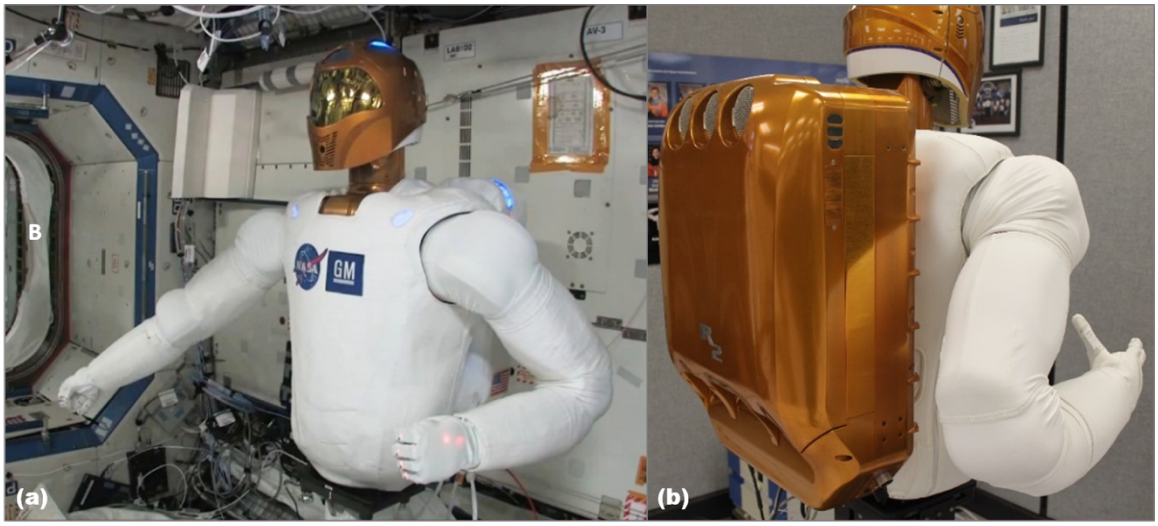

Figure 4-2 Images of (a) Robonaut 2 on the ISS where power is received through a tether and (b) the battery backpack which will soon add further mobility capabilities to the humanoid robot. NASA receives credit for image 4-2a.

4.2 Thermal Testing of the Boston Power Swing 5300 Lithium Ion Cell

Ground testing is conducted to provide a thermal characterization of the BP-5300 Li-ion cell necessary for model correlation. Thermal Desktop models of the space flight hardware are correlated to test data at which point the software is used to simulate thermal performance in a space environment. Experimental methods include thermocouple measurement, voltage control measurement and current control measurement during charge-discharge operations for varied C-rates in a ~22.0 °C (± 2.5 °C) natural convection environment. The constant current charge and discharge C-rates include 2.0 C, 1.0 C, 0.7 C and 0.5 C. Results for rates below 0.5 C are not reported as they are driven by the environment temperature only. Figure 4-3 details the thermal test configuration.

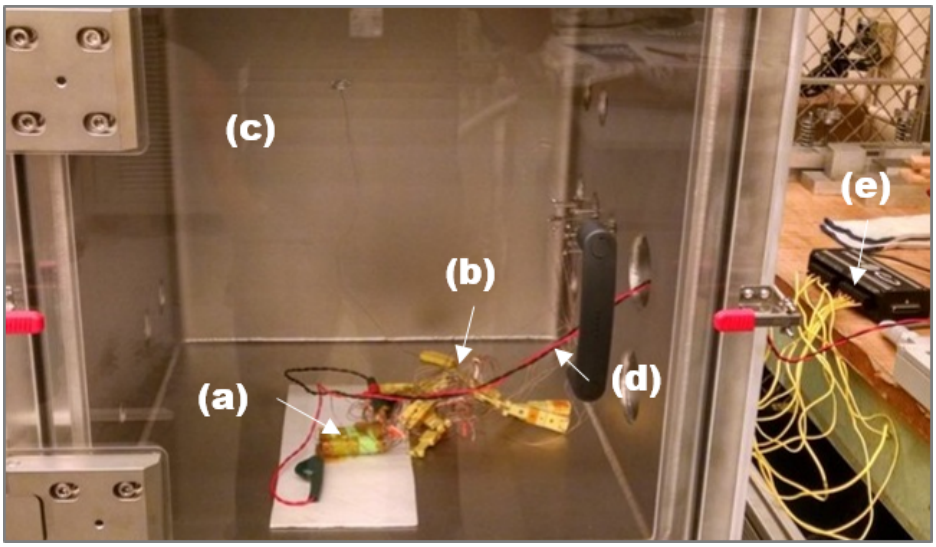

Figure 4-3 Configuration for the BP-5300 thermal testing where: (a) is the test article, (b) displays the thermocouples, (c) shows the safety chamber, (d) shows the external circuit lines and (e) shows the data acquisition device.

The transient voltage vs. time and temperature vs. time results for the charging of the BP cell are displayed in Figure 4-4 and Figure 4-5, respectively. The transient voltage vs. time and temperature vs. time results for the discharging of the BP cell are displayed in Figure 4-6 and Figure 4-7, respectively.

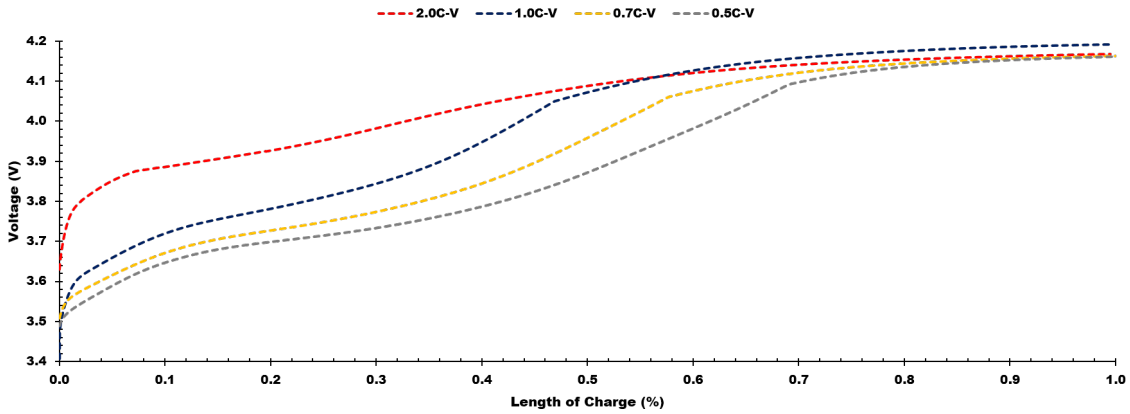

Figure 4-4 **Charging voltage vs. time for the Boston Power Swing 5300 Li-ion cell at (a) 2 C, (b) 1 C, (c) 0.7 C and (d) 0.5 C.**

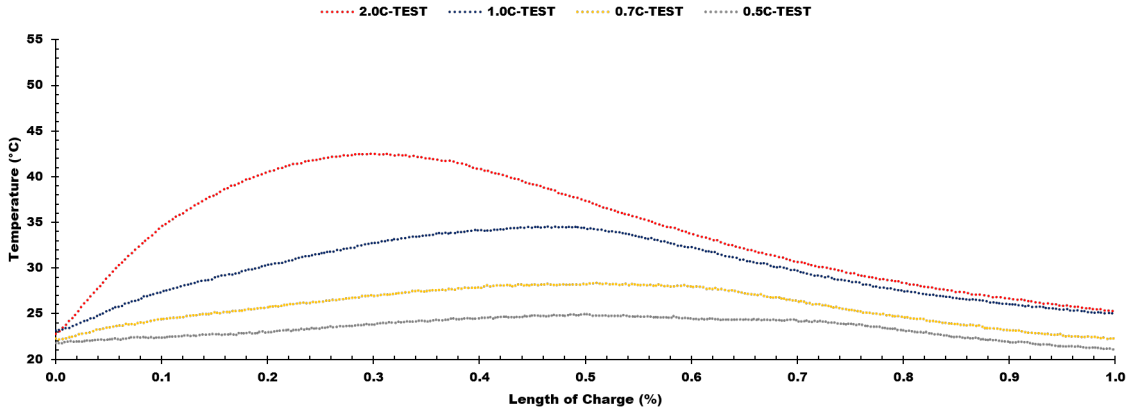

Figure 4-5 **Temperature vs. time for the charging of a Boston Power Swing 5300 Li-ion cell at (a) 2 C, (b) 1 C, (c) 0.7 C and (d) 0.5 C.**

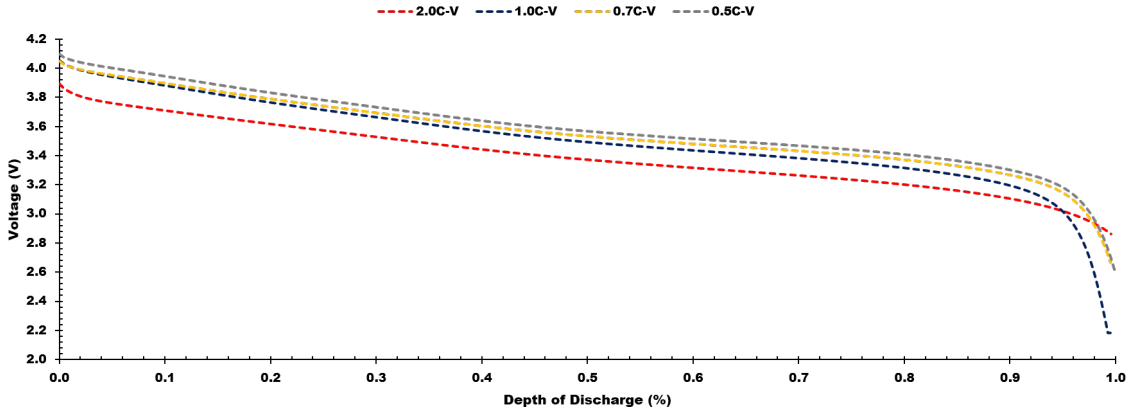

Figure 4-6 **Discharge voltage vs. time for the Boston Power Swing 5300 Li-ion cell at (a) 2 C, (b) 1 C, (c) 0.7 C and (d) 0.5 C.**

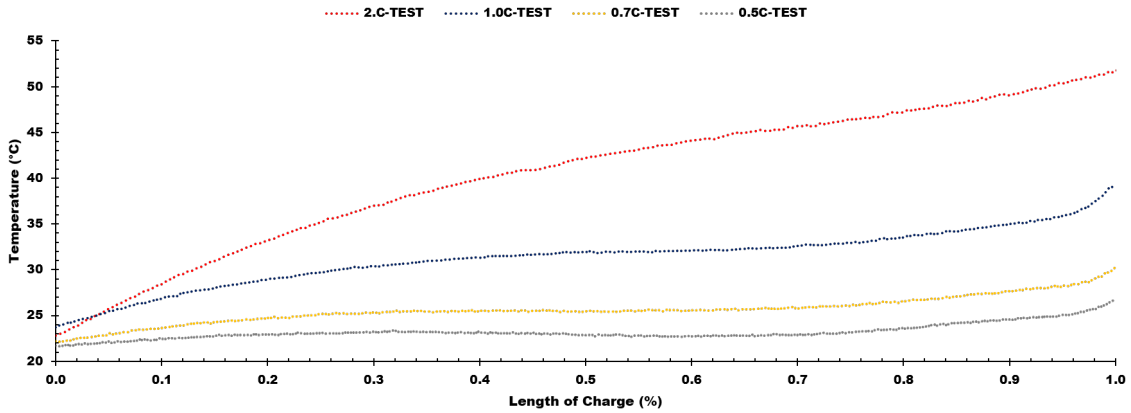

Figure 4-7 Temperature vs. time for the discharging of a Boston Power Swing 5300 Li-ion cell at (a) 2 C, (b) 1 C, (c) 0.7 C and (d) 0.5 C.

4.3 Robonaut 2 Battery Assembly Thermal Desktop Model Development

Development of a test correlated thermo-electrochemical Thermal Desktop model of the R2 battery is completed with a vertical approach. Each cell in the 300 cell battery pack functions uniformly (i.e. each cell nominally experiences the same charge and discharge currents and voltages at all times); therefore a detailed Thermal Desktop model of a single cell is first developed for correlation to experimental results.

4.3.1 Geometries and Material Properties

Thermal Desktop native cylindrical and brick geometries are used to directly simulate the physical makeup of the cell. Based on manufacturer recommendation for thermal modeling, the Li-ion cell and encasement are simulated as a single solid object with volumetrically averaged thermophysical properties to account for the aluminum casing, cathode, anode, separator and electrolytic materials.

Thermophysical properties considered are thermal conductivity, density and specific heat capacity. Thermal conductivity is applied anisotropically with 1.7 W cm^{-1} $°C^{-1}$ applied in the y and z directions and 0.02 W cm^{-1} $°C^{-1}$ in the x direction; the x direction experiences thermal resistivity as a result of the alternating layers of Li-ion cell materials. Density is

set at 2.3 g cm^{-3} to ensure 93 g per cell and 0.6 J g^{-1} $°C^{-1}$ specific heat capacity is applied. Note that these properties are best estimates based on model response and that actual manufacturer values remain unknown due to proprietary constraints. The experimentally measured optical properties of the casing, thermal absorbance (α) and emittance (ε), are 0.42 and 0.88, respectively. The α measurements are taken with a LPSR-300 spectro-reflectometer and ε measurements with an ET-100 reflectometer.

To represent the entire R2 battery, the cell model is expanded into 5 cartridges of 60 cells per cartridge (300 cells total). To create the individual cartridges, the single cell model is multiplied to create a 3 by 20 array with 0.042 cm spacing between all sides. The positive and negative side copper (Cu) bus bars and G-10 structural plates are constructed and placed on each side of a given cartridge. To construct the entire R2 battery pack the cartridge level model was multiplied as a 5 by 1 array horizontally and placed inside an aluminum encasement. Figure 4-8 displays the (a) final Thermal Desktop model of the single BP-5300 Li-ion cell, (b) the radiation-convection network active surfaces for a single cell and (c) the final Thermal Desktop model of the 300 cell R2 Li-ion battery assembly. A summary of the properties applied to the model are provided in Table 4-2.

Table 4-2 Thermal Desktop model thermophysical and optical properties.

Property	Value	Unit
Al thermal conductivity	1.67	W cm^{-1} $°C^{-1}$
Al specific heat capacity	0.89	J g-1 $°C^{-1}$
Al density	2.77	g cm^{-3}
Cell thermal conductivity (aniso)	1.70, 0.02, 0.02 x, y, z	W cm^{-1} $°C^{-1}$
Cell specific heat capacity	0.60	J g-1 $°C^{-1}$
Cell density	2.28	g cm^{-3}
Cell absorbance/emissivity	0.42/0.88	-
Cu thermal conductivity	3.98	W cm^{-1} $°C^{-1}$
Cu specific heat capacity	0.39	J g-1 $°C^{-1}$
Cu density	8.93	g cm^{-3}
G-10 thermal conductivity	0.29	W cm^{-1} $°C^{-1}$
G-10 specific heat capacity	1.46	J g-1 $°C^{-1}$
G-10 density	1.80	g cm^{-3}

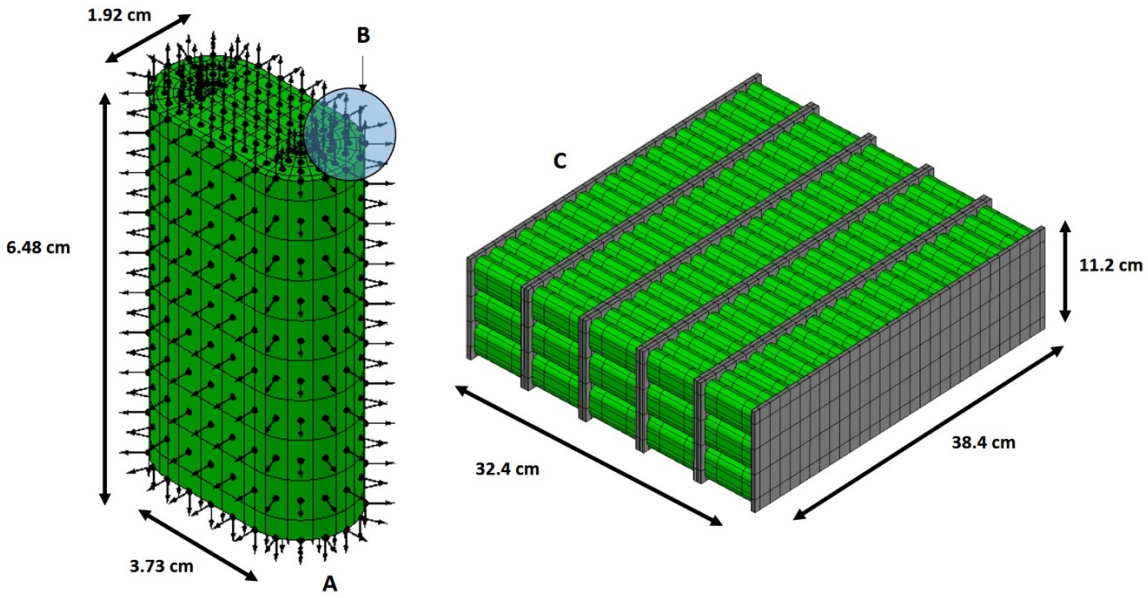

Figure 4-8 Displays (a) the Thermal Desktop model of a single cell, (b) visualization of the radiation-convection network applied to active external surfaces and (c) the final 300 cell Thermal Desktop model of the R2 battery

Following geometry development and provision of thermal definition, the Ohmic heat generation for charge and discharge operations is incorporated into the model (Q_{Cell}) for each C-rate. Q_{Cell} is set to be a function of V_{OC}, V_W, T_{Cell}, $T_{Ambient}$ and capacity by instituting Fortran language VAR0 statements via the same methods as with the previous study (refer to Figure 3-8 for a complete description of the process).

4.3.2 Thermal Model Test Correlation

The Thermal Desktop temperature predictions compared to experimental data are presented for charge and discharge C-rates of 2.0 C, 1.0 C, 0.7 C and 0.5 C in an ~22.0 °C (±2.5 °C) natural convection environment. Analysis shows that the maximum temperature occurs at the center of the cell and cools towards the edges due to the anisotropy of the overall thermal conductivity. Figure 4-9 and Figure 4-10 compare the Thermal Desktop temperature predictions (solid lines) to the experimental data (dashed lines) for the charge and discharge experiments at 2.0 C, 1.0 C, 0.7 C and 0.5 C. The peak charging temperatures

are approximately 43 °C, 35 °C, 27 °C, and 25 °C for the 2.0 C, 1.0 C, 0.7 C, and 0.5 C cases, respectively. The peak discharging temperatures are approximately 52 °C, 39 °C, 30 °C, and 27 °C for the 2.0 C, 1.0 C, 0.7 C, and 0.5 C cases, respectively. The results for all cases compared to Thermal Desktop predictions exemplify excellent correlation. The accuracy of the predictions, compared to the test data, demonstrates Thermal Desktop's suitability for general thermo-electrochemical analysis. Though thermal radiation environments exterior to orbiting structures cannot be directly tested without the use of expensive thermal vacuum chambers and/or elaborate test apparatuses (hence ground testing in ambient environments), confidence in orbital results is still ascertained by first correlating the model to ground-test data prior analysis; once the functionality is test-validated, the only parameter that changes with orbital analysis is the highly complex environmental effects. With assurance in charge and discharge operations simulations as a function of Q_{Cell} logic statements, accurate orbital analysis is possible.

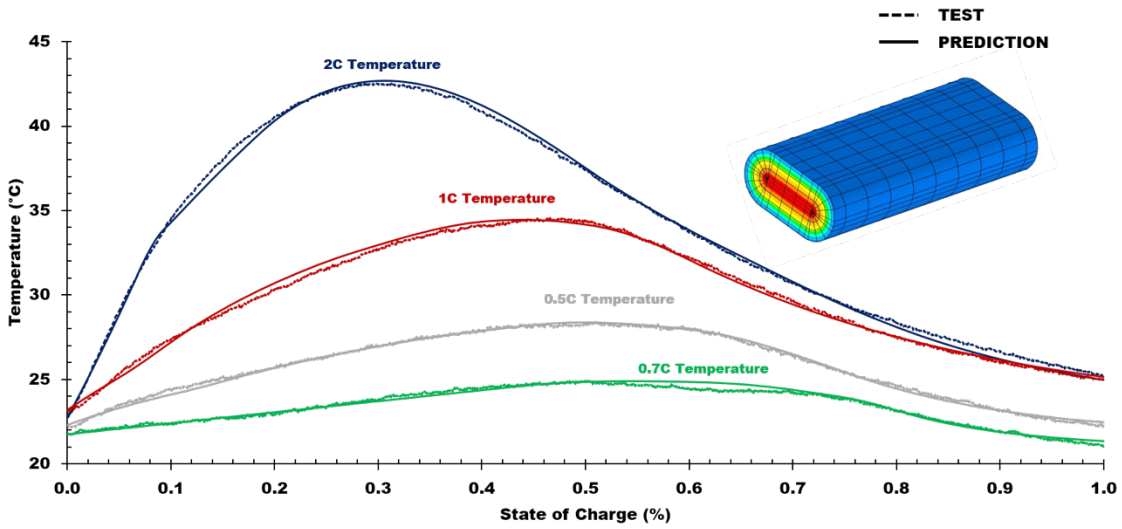

Figure 4-9 Comparison of the model vs. experiment temperature vs. time for the charging of a BP-5300 Li-ion cell at (a) 2 C, (b) 1 C, (c) 0.7 C and (d) 0.5 C.

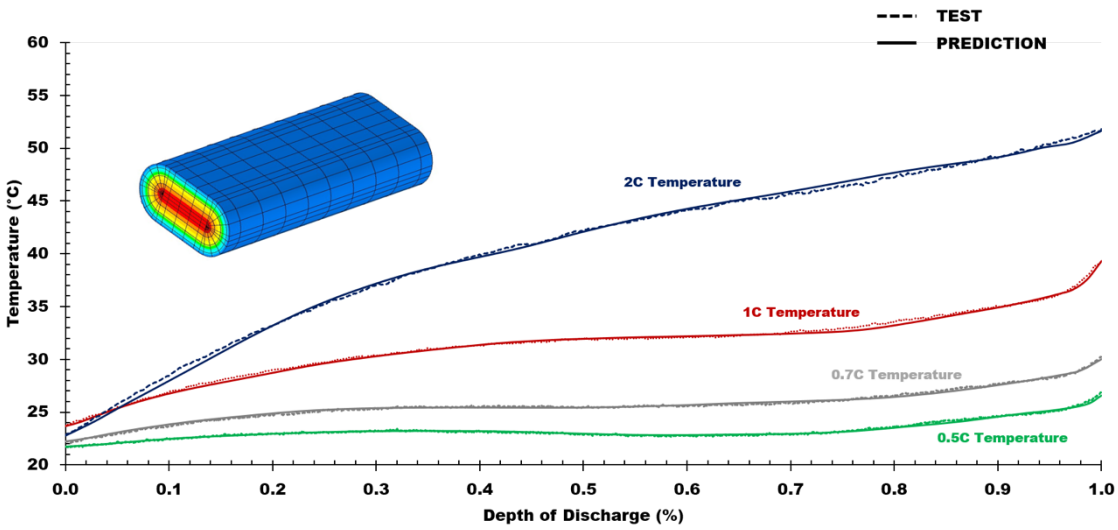

Figure 4-10 Comparison of the model vs. experiment temperature vs. time for the discharge of a BP-5300 Li-ion cell at (a) 2 C, (b) 1 C, (c) 0.7 C and (d) 0.5 C.

4.4 Simulation of Robonaut 2 Lithium Ion Battery Assembly Thermo-electrochemical Performance in Radiation Driven Orbital Environments

Thermal Desktop analysis is one option used for payload, vehicle and hardware thermal certification for the ISS. Developers can determine the thermal viability of a given design by combining their own model with a Thermal Desktop model of the entire ISS vehicle for environment simulation. Due to certain restrictions, ISS Thermal Desktop model generated results and images cannot be included in this study. However, as a demonstration of the unique modeling capability gained by using Thermal Desktop and the necessary analysis prior to any EVA, the R2 battery pack model is incorporated into a sample satellite Thermal Desktop model for orbital simulations. Though the satellite is not a direct representation of the ISS, it does represent similar components; orbiting mechanical body, sun tracking solar panels, varied optical properties, shading due to surrounding bodies and large temperature gradients influenced by attitude, orbit, albedo, infrared planet shine and solar flux.

The thermal model geometries of the satellite are displayed in Figure 4-11a. To simulate R2 battery discharge thermal performance for a hypothetical 5 hour EVA (i.e. 18000

seconds, 0.2 C discharge), the R2 battery model is imported and placed exterior to the satellite structure (Figure 4-11b) and orbital parameters are defined (e.g., 0 beta as shown in Figure 4-11c). Note that this simulation negates shading that would occur due to the presence of the R2 body.

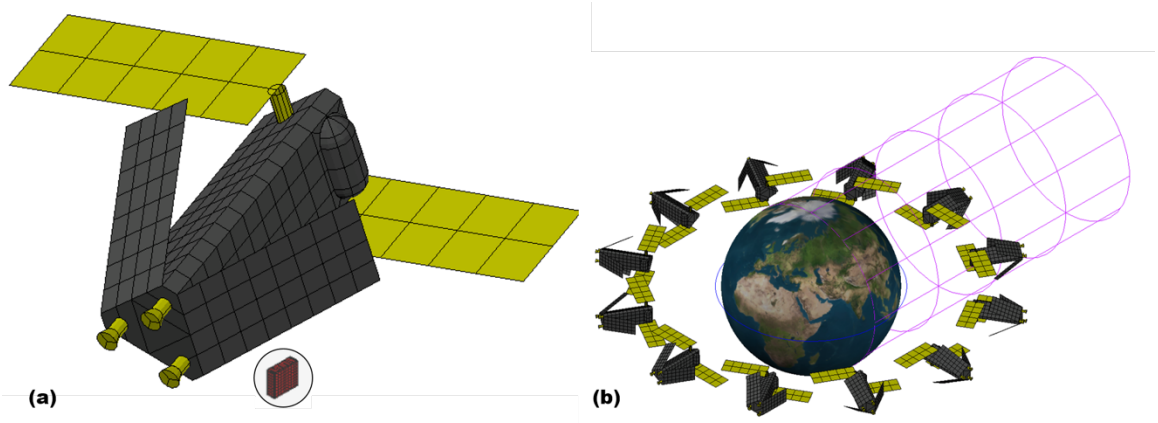

Figure 4-11 **Images representing the (a) sample satellite Thermal Desktop model, (b) incorporation of the R2 battery pack model exterior to the satellite, and (c) definition of orbital parameters for radiation simulation.**

The combined R2 battery and sample satellite model parameters are set to define low Earth orbit thermal environments for -75°, 0° and +75° solar betas, 398.2 km altitude, 0.13 W cm^{-2} solar flux, 0.02 W cm^{-2} and an albedo of 0.2 (see all orbital parameters detailed in Table 4-3) [10, 38, 58]. Radks are generated for 12 orbital positions per beta angle configuration to capture the change in solar environment throughout orbit. The model is initialized with all node temperatures starting at 0 °C and the Q_{Cell} logic is set to simulate a 0.2 C discharge. Thermal Desktop generates the final input file which is exported and solved in SINDA.

Table 4-3 **Environment and orbital parameters for the EVA simulations [10, 38, 58].**

Property	Value	Unit
Beta angle	-75, 0, +75	°
Altitude	398.2	km
Solar flux	0.13	W cm^{-2}
Albedo	0.40	-
Infrared planet shine	0.02	W cm^{-2}

Results from the hypothetical EVA assessment are presented in two forms; (1) transient plots of battery temperatures through discharge (Figure 4-12 through Figure 4-17) and (2) isothermal images of the system at the point when the largest delta between the coldest and warmest cells occurs (Figure 4-18 through Figure 4-20).

For Figure 4-12 through Figure 4-17 the following is illustrated; (i) the thermal profile spread of all 300 cells (shaded area) between the absolute coldest and warmest cells, (ii) an image representing the orbital configuration at the starting position, (iii) an image of the entire battery and (iv) similar transient thermal profiles of the battery encasement. The transient plots display expected continuous temperature fluctuation of the R2 battery backpack driven by the combination of infrared radiation, solar radiation and Ohmic heating as the hypothetical satellite orbits the Earth.

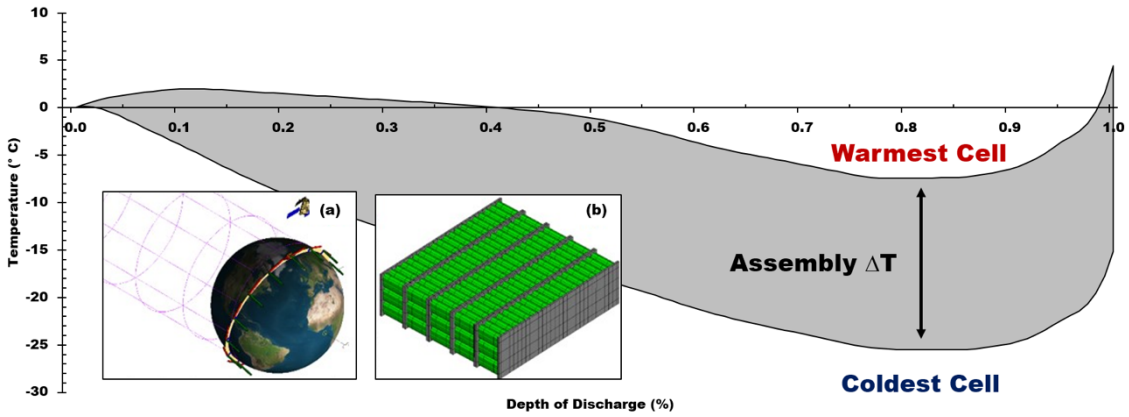

Figure 4-12 **R2 battery assembly thermal performance for -75° beta where: (a) represents the orbital configuration at time zero and (b) is an image of the battery.**

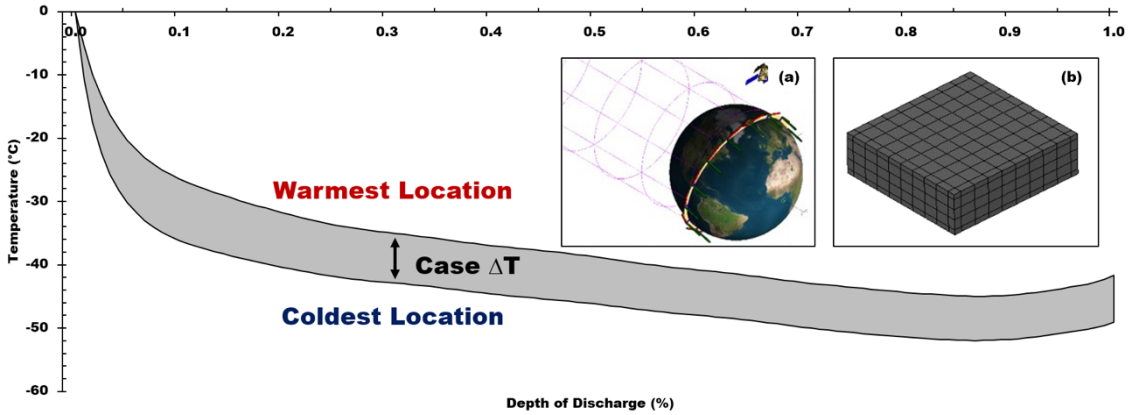

Figure 4-13 R2 battery encasement thermal performance for -75° beta where: (a) represents the orbital configuration at time zero and (b) is the encasement.

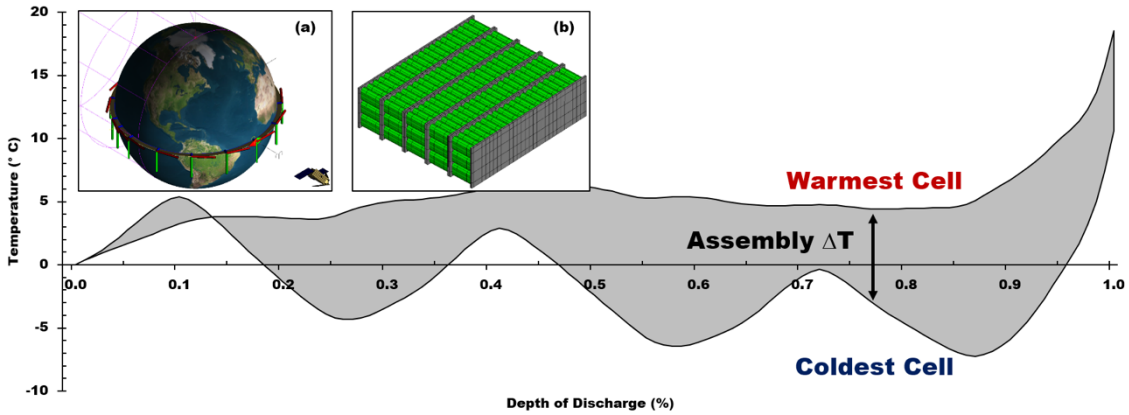

Figure 4-14 R2 battery assembly thermal performance for 0° beta where: (a) represents the orbital configuration at time zero and (b) is an image of the battery.

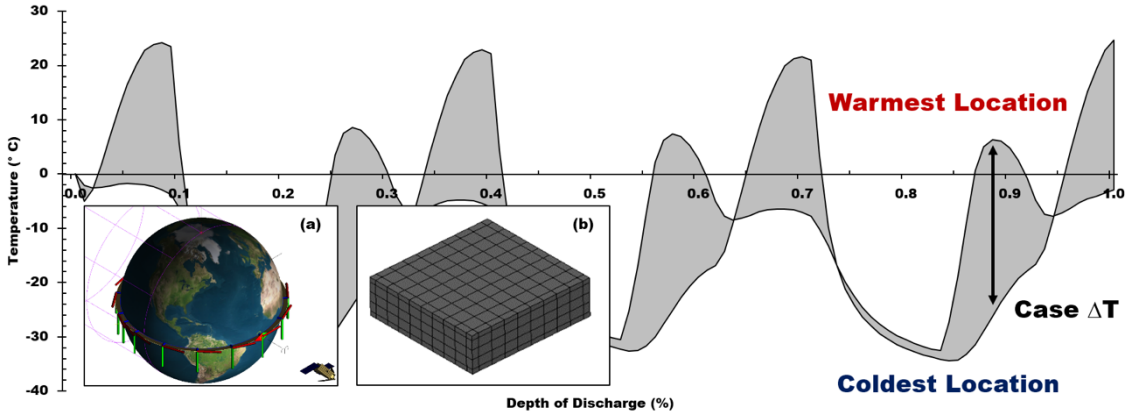

Figure 4-15 R2 battery encasement thermal performance for 0° beta where: (a) represents the orbital configuration at time zero and (b) is the encasement.

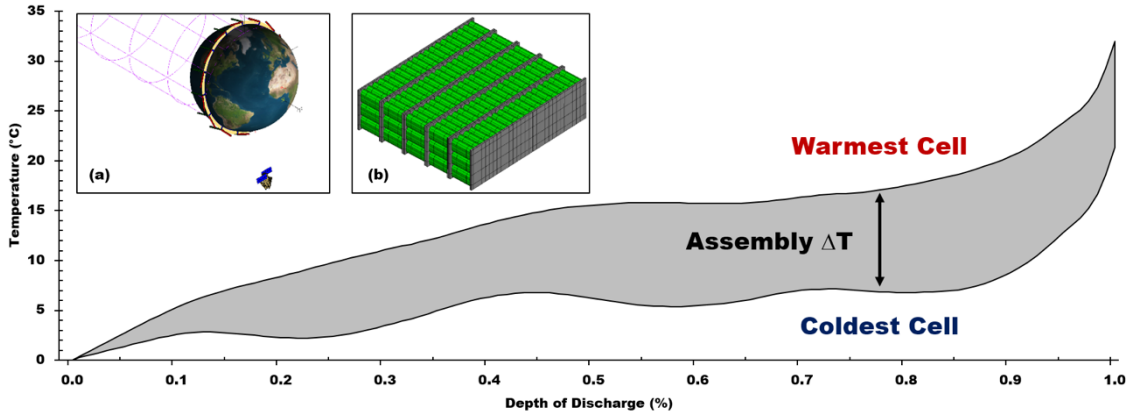

Figure 4-16 **R2 battery assembly thermal performance for +75° beta where: (a) represents the orbital configuration at time zero and (b) is an image of the battery.**

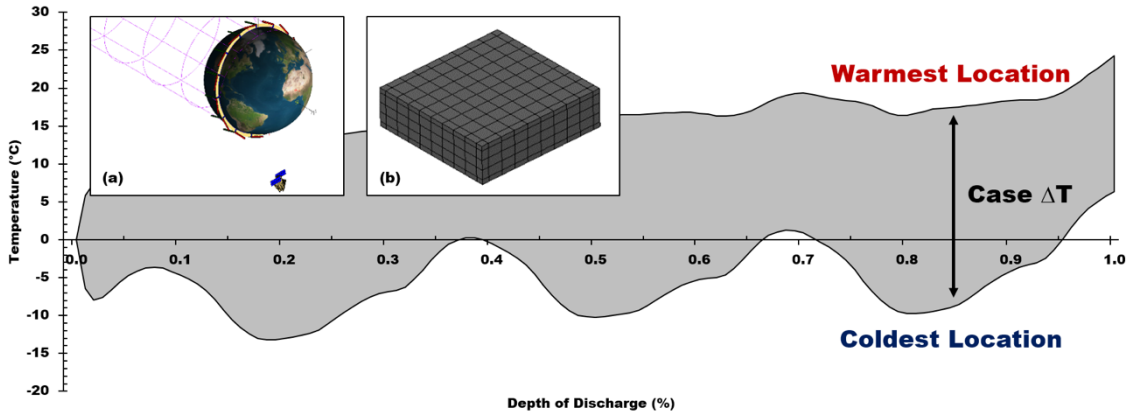

Figure 4-17 **R2 battery encasement thermal performance for +75° beta where: (a) represents the orbital configuration at time zero and (b) is the encasement.**

The three isothermal images of the satellite displayed in Figure 4-18 through Figure 4-20 (left images) provide example of the large temperature distribution a single large orbiting structure may experience at any given point in the orbit (e.g., -84 °C to +33 °C for the -75 beta environment). Note that maximum/minimum temperatures and the magnitude of the temperature distribution are also subject to change based on mass, thermophysical properties and surface optical properties.

The isothermal images battery cells shown in Figure 4-18 through Figure 4-20 (right images) consistently display non-uniform heating on objects as small as the R2 battery backpack as a function of orbit. The transient plots of the encasement temperatures (Figure

4-13, Figure 4-15 and Figure 4-17) demonstrate the more drastic effects of direct exposure to the environment.

For the -75° beta orbit, at 80% discharge, the minimum cell temperature is -25 °C and the maximum cell temperature is -2 °C yielding a 23 °C delta. For the 0° beta orbit, at 87% discharge, the minimum cell temperature is -7 °C and the maximum cell temperature is 6 °C yielding a 13 °C delta. For the +75° beta orbit, at 57% discharge, the minimum cell temperature is 6 °C and the maximum cell temperature is 16 °C yielding a 10 °C delta (a 10 °C delta is also observed at 85% discharge). Understanding and preventing non-uniform heating is imperative because these factors can adversely affect the lifespan of the cell and the overall cell capacity [54]. All orbital results are organized in Table 4-4.

Table 4-4 Orbital simulation results at the point of the maximum temperature delta. The table includes cell and satellilte maximum and minimum temperatures at the point of the maximum temperature delta.

Orbit	Cell Max T	Cell Min T	Satellite Max T	Satellite Min T	DOD
-75 Beta	-2 °C	-25 °C	+31 °C	-84 °C	80 %
0 Beta	+6 °C	-7 °C	+6 °C	-82 °C	87 %
+75 Beta	+16 °C	+6 °C	+34 °C	-72 °C	57 %

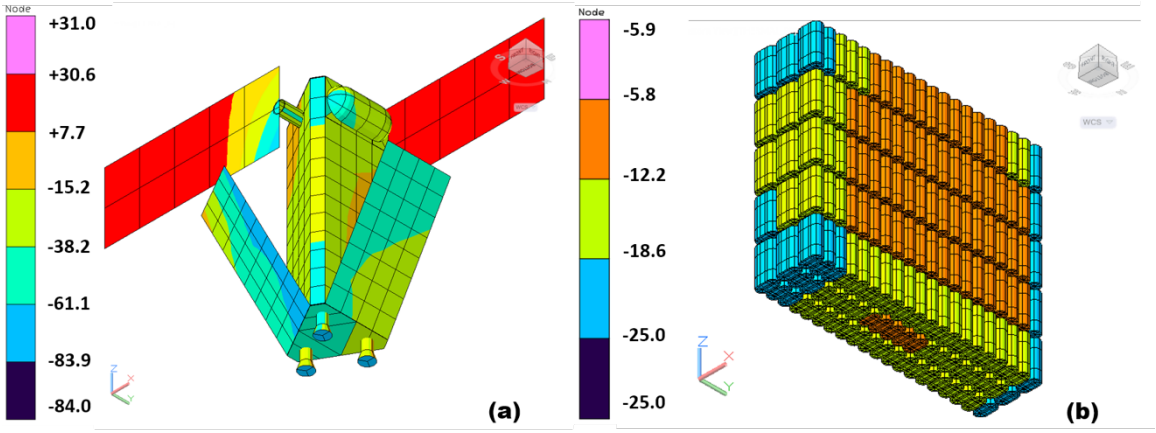

Figure 4-18 **Isothermal images of the satellite and the battery pack at the point when the largest delta between coldest and warmest cells occurs for the -75° beta case.**

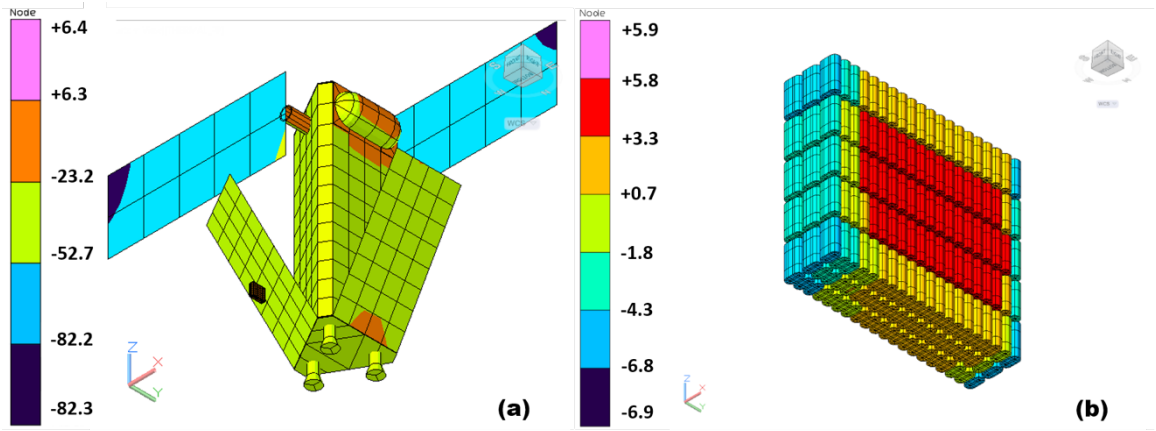

Figure 4-19 **Isothermal images of the satellite and the battery pack at the point when the largest delta between coldest and warmest cells occurs for the 0° beta case.**

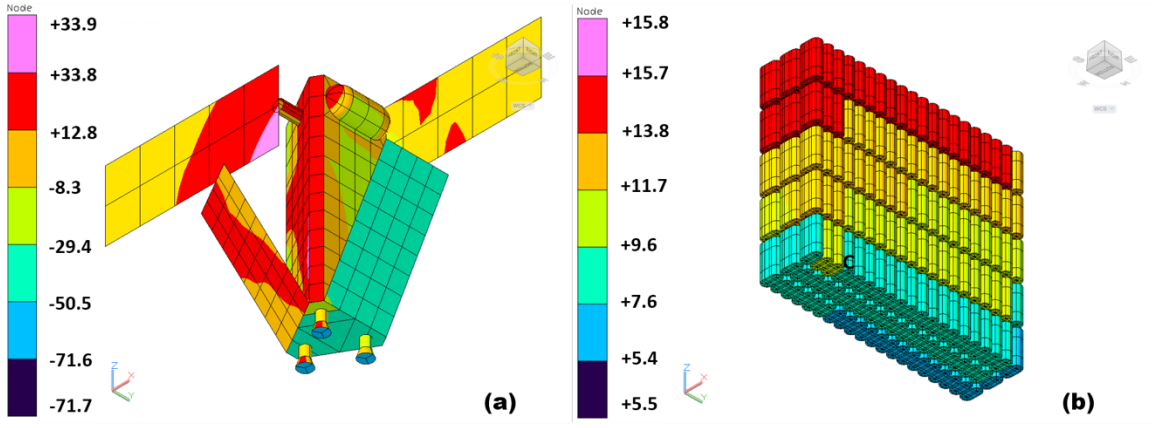

Figure 4-20 **Isothermal images of the satellite and the battery pack at the point when the largest delta between coldest and warmest cells occurs for the +75° beta case.**

Using this joint thermo-electrochemical and orbital radiation analysis technique, R2 designers can identify acceptable combinations of EVA locations exterior to the ISS, orbital parameters (dependent on time of the year) and battery discharge rates to accomplish predefined tasks. Reliability and cell efficiency are preserved by implementing this analysis technique prior to robotic activities by minimizing thermal environment caused permanent degradation and efficiency losses. Environmental heating induced thermal runaway can also be prevented by predefining conditions that would yield an exceedance of acceptable cell operating temperatures (i.e. conditions that would cause cell temperatures to reach the 100 °C to 200 °C threshold discussed previously). Opportunity for project cost reduction is presented by supporting a passive thermal control approach to battery thermal performance (i.e. using the environment and passive thermal design to maintain acceptable battery temperatures); though some form of active control is typically required for permanently mounted components, the need for ATCS can possibly be avoided through pre-mission analysis for non-permanent applications like R2. Thermal performance of passively controlled exterior batteries is subject to change based on location on the orbiting structure, time of the year, beta, altitude, infrared fluxes, solar radiation and other related parameters. To ensure that the design of a battery is robust enough for extreme space environments, analysis with a joint thermo-electrochemical approach similar to the technique presented by this study is highly recommended.

4.5 Robonaut 2 Thermal Desktop Model Conclusions

Advanced energy storage and power management systems designed through rigorous materials selection, testing and analysis processes are essential to ensuring mission longevity and success for space exploration applications. A test-correlated Thermal

Desktop model is developed to support NASA R2 design requirements, to provide confidence in the R2 battery thermal performance and safety and to demonstrate suitability of Thermal Desktop for thermo-electrochemical analysis of passively controlled Li-ion batteries designed to function in thermal radiation driven environments.

The cell level model accurately predicts BP Swing 5300 temperatures for 2.0 C, 1.0 C, 0.7 C and 0.5 C charge-discharge operations based on direct comparison to experimental data. The R2 battery pack model combined with a satellite model for example thermal radiation environment analysis demonstrates the unique capability gained by utilizing Thermal Desktop for thermo-electrochemical analysis. With the added capability of simulating charging processes and the demonstration discharge operations in orbit, this study provides necessary validation that this Thermal Desktop technique is a suitable for thermo-electrochemical analysis and necessary for thermal design of batteries designed for space applications. Performing thermo-electrochemical analysis in software capable of simulating radiation driven environments provides the opportunity for safe, reliable and passively controlled Li-ion battery systems.

Chapter 5 Energy Distributions Exhibited during Thermal Runaway of Commercial Lithium Ion Batteries used for Human Space Flight Applications

5.1 Thermal Safety Concerns Associated with Lithium Ion Batteries

Despite the technological maturity of Li-ion batteries, thermal runaway failures become more common with the increasing use of these advanced energy storage devices. Thermal runaway has caused airplanes, buses, taxis, other vehicles, hover boards and various mobile devices to catch fire or explode [59]. As a result, safety concerns related to thermal runaway and subsequent cell-to-cell propagation impede the use of these cells for human space flight applications. Global interest in thermal runaway safety concerns was renewed following the Boeing 787 Dreamliner incident in which the aircraft's novel Li-ion battery used for auxiliary power experienced a short circuit induced thermal runaway failure [60]. The event occurred on January 7th, 2013 while the vehicle was still on the tarmac, crew and passengers were not on board and no one on the cleaning and maintenance team was injured [60].

Preventing and mitigating the disastrous effects of thermal runaway and cell-to-cell propagation are critical to ensuring astronaut safety for human space flight applications. This portion of the dissertation focuses on characterizing the total energy release associated with the thermal runaway behavior of three Li-ion cells used for human space flight applications: (a) Boston Power Swing 5300, (b) Samsung 18650-26F and (c) MoliCel 18650-J. The characteristics of these three cells are described in detail with Table 5-1.

As discussed in Chapter IV, Boston Power Swing 5300 (BP-5300) cells are selected to power R2 in the form of a battery backpack on board the ISS in the near future. R2 is a

humanoid robot designed to demonstrate robotic activity in a microgravity environment and to assist astronauts by conducting routine maintenance activities. The BP-5300 cells are slightly more than double the size, mass and power of the other 18650 cells considered in this study and employ an aluminum can rather than the traditionally used stainless steel. The BP-5300 can is prismatic in shape with rounded edges. An open environment (non-ARC) thermal runaway event of a BP-5300 cell, conducted at the NASA Johnson Space Center (JSC) Energy Systems Test Area (ESTA) facility is presented in Figure 5-1. Thermal runaway is induced here by applying 163 W to the cell via patch heater. The figure displays the test article at the following points of interest: (a) prior to heater instrumentation, (b) when smoke is first observed, (c) when smoke generation rates significantly increase, (d) moments before runaway occurs, (e) the instant that runaway occurs, (f) still heating from decomposition reactions following explosion, (g) when maximum temperature of 492 °C is achieved, (h) following a portion of the cool down period, (i) is an image of the R2 battery backpack that will contain 300 BP-5300 cells.

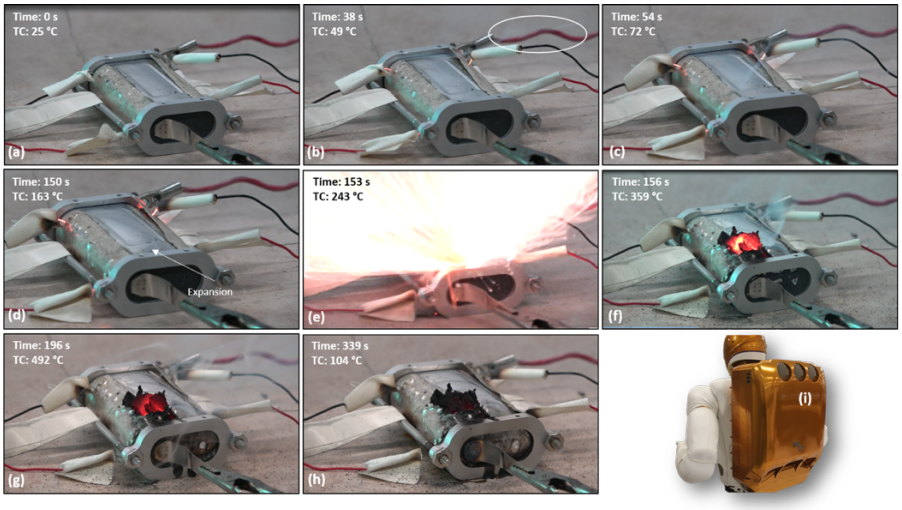

Figure 5-1 Images of a BP-5300 Li-ion cell throughout an open atmosphere patch heater induced thermal runaway event.

Astronauts are able to work in hostile space environments with the support of an EMU which provides power, mobility, communication and life support systems [22-24]. NASA works to update EMU power systems with new Li-ion battery assemblies designed to safely mitigate the effects of thermal runaway and to prevent cell-to-cell propagation while also maintaining strict power requirements. The nickel metal hydride (NiMH) Rechargeable EVA Battery Assembly (REBA) will be replaced with the Li-ion Rechargeable EVA Battery Assembly (LREBA) [22-24]. The LREBA design incorporates 45 Samsung 18650-26F cells [22-24]. The EMU Li-ion Long Life Battery (LLB) replaced the silver-zinc (Ag-Zn) Increased Capacity Battery (ICB) in 2011 [61]. The LLB assembly consists of 80 MoliCel 18650-J cells [22-24]. Figure 5-2 displays the following: (a) an image, taken from the ISS Cupola Observational Module, of the EMU attached to an astronaut performing an EVA, (b) an image of a Samsung 18650-26F cell the moment thermal runaway occurs during non-ARC testing and (c) an image of a MoliCel 18650-J cell the moment thermal runaway occurs during non-ARC testing.

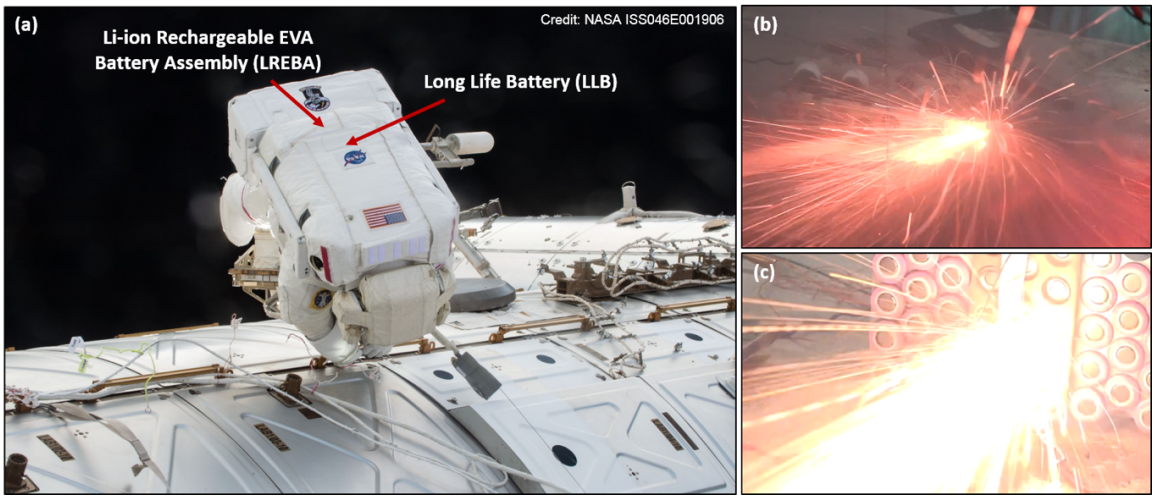

Figure 5-2 **The extravehicular mobility unit provides power, mobility, communications and life support systems to astronauts while performing EVAs exterior to the ISS in hostile space environment.**

Table 5-1 Characteristics for, (a) Boston Power Swing 5300, (b) Samsung 18650-26F and (c) MoliCel 18650-J [57, 62-67]

Characteristic	Boston Power Swing 5300 [57,62,63]	Samsung 18650-26F [63-65]	MoliCel 18650-J [63,66,67]
Nominal Capacity	5300 mAh	2600 mAh	2370 mAh
Nominal Voltage	3.65 V	3.70 V	3.76 V
Maximum Charge Voltage	4.2 V	4.2 V	4.2 V
Electrochemical Energy at 100% SOC	19.35 Wh (69.66 kJ)	9.62 Wh (34.63 kJ)	8.91 Wh (32.08 kJ)
Volumetric Energy Density	490 Wh/L	510 Wh/L	517 Wh/L
Gravimetric Energy Density	207 Wh/kg	191 Wh/kg	187 Wh/kg
Operating Temp. (Charge)	-20 to +60 °C	0 to +45 °C	0 to +45 °C
Operating Temp. (Discharge)	-40 to +70 °C	-20 to +60 °C	-20 to +60 °C
Storage Temp.	-40 to +60 °C	-20 to +25 °C	-20 to +60 °C
Cathode Material	$LiNiO_2$	CoO, MnO_2, NiO	$LiCoO_2$, LiNiMnCo
Anode Material	Graphite	Carbon	Graphite Carbon Black
Cell Mass	93.5 gm	47.0 gm	48.0 gm
Cell Specific Heat Capacity	1.3 kJ kg^{-1} K^{-1}	0.85 kJ kg^{-1} K^{-1}	0.85 kJ kg^{-1} K^{-1}
Cell Can Material	Aluminum	Mild Steel	Mild Steel

5.2 Thermal Runaway Mechanisms

Li-ion utilization for any application requires understanding of thermal runaway mechanisms and the resulting energy release into the surroundings. This information is critical when designing safe thermal management systems, which should mitigate the effects of thermal runaway and prevent cell-to-cell propagation. Thermal runaway is characterized by heat generation within a cell at a rate that is faster than what can be dissipated to the surroundings.

Thermal runaway can be caused by (a) overheating (thermal failure), (b) electrochemical failure (such as overcharge) or (c) mechanical failure (such as crushing) [26,59,68-72]. Common abusive test methods to induce thermal runaway include application of a controlled heat load via heat gun or patch heater (thermal failure), uniform radiative heating (thermal failure), nail penetration (mechanical failure), intentional self-induced shorting mechanism (electrical failure) and overcharge (electrical failure) [73-77].

5.3 Literature Review of Lithium Ion Battery Thermal Runaway

5.3.1 Pre-Millennial Research (1990-1999)

Hallaj et al. provide experiments and analysis to support the design of power systems for electric vehicles [44]. Part of this study focused on thermal runaway via ARC experiments. Hallaj et al. note an inverse relationship between state-of-charge and capacity and it is noticed that voltage drop corresponds to when the ARC temperature approaches the melting temperature of the separator material [44].

Richard and Dahn utilize ARC experiments to provide necessary data to develop mathematic models of SEI and anode decomposition reaction rates; these models are later expanded by other studies to include cathode decomposition and electrolyte

decomposition, boiling and vaporization [78,79]. This pair of studies by Richard and Dahn identified relationships between self-heating rate, Li content, electrolyte composition, surface area and initial temperature [78,79].

5.3.2 Early Millennial Research (2000-2009)

Hatchard et al. develop mathematic models of thermal runaway which expand Richard and Dahn's models to include the decomposition of the cathode material [72]. Hatchard et al. identify that thermal runaway testing is expensive to cell manufacturers and that design costs are reduced when implementing thermal runaway kinetics based analysis [76]. The model is test correlated to $LiCoO_2$ MoliCel 18650 test data [72]. Lastly it was shown that the model produced acceptable results for cells of different sizes and electrode material [72].

Gnanaraj et al. utilize ARC and differential scanning calorimetry (DSC) to examine the thermal stability of various electrolytes at elevated temperatures [80]. This study identifies endothermic reactions for $LiPF_6$ combinations which occur prior to the exothermic reactions that lead to the thermal runaway event [80].

Spotnitz and Franklin develop detailed chemical models and estimated heating of thermal runaway due based on a survey of available literature [73]. Specifically, this study focuses on thermal runaway behavior due to abuse mechanisms including (a) overcharge, (b) nail penetration, (c) crushing, (d) over-temping and (e) short-circuit [73]. These models identify that binder materials do not play a significant role in thermal runaway [73].

Roth et al., in collaboration with Sandia National Laboratories, report early examination of the thermal behavior and generated gases of 18650 cells experiencing thermal runaway [81,82]. ARC and DSC are used to characterize the 18650 cells during thermal runaway [81,82]. These studies focus on the thermal runaway behavior associated with two combinations of

Li-ion batteries: (1) $LiNi_xCo_xO_2$ and (2) $LiNi_xCo_xAl_xO_2$ [81,82]. This study demonstrated a positive relationship between aging and the exothermic reactions; in that, aged electrode materials lead to less severe reactions during thermal runaway [81,82].

Doughty et al. manipulate 18650 cells with various additives and examine the thermal runaway behavior via ARC and gas chromatography (GC); in some cases lower thermal runaway temperatures were identified [83]. This study used innovative testing methods to examine the flammability by establishing an spark system that ignites the vented effluence if a flammable material is present [83]. Doughty et al. demonstrate that certain additives can reduce the overall flammability of the effluence [83]. This study also identified the presence of CO, CO_2 and various hydrocarbons in the generated gases [83].

Ohsaki et al. perform examine the thermal runaway behavior associated with the overcharging of a small format $LiCoO_2$ Li-ion battery [74]. This study identifies similar gaseous products as Doughty et al. (i.e. CO, CO_2 and various hydrocarbons) [74,83]. Specifically, this study identified that the reactions associated with the over-lithiated carbon anode are what lead to the thermal runaway reaction for overcharge [74].

Abraham et al. conduct thermal runaway experiments which lead to a detailed understanding of the progression of events that lead to the ultimate destruction of the cell [84]. Similar gaseous products are observed as discussed by Doughty et al. and Ohsaki et al. [74,83,84]. The study uses "accelerating rate calorimetry… microscopy, spectroscopy and diffraction techniques" to analyze the runaway event [84]. Interesting findings are discussed regarding the behavior of the separator material at elevated temperatures and the surface compounds and structures that are formed on the electrode surfaces [84].

Kim et al. provide expansion to the models by Richard and Dahn and Hatchard et al. by introducing the models of the electrolyte decomposition and then expanding the models for multi-dimensional analysis [85]. This expansion was key to identifying the movement of heat through the cell from the point of origination (i.e. hot spot) [85]. The study identifies differences in when the multi-dimensional model predicts thermal runaway vs. the original 0-dimension "lump" models [85]. Also, it was noted that smaller Li-ion batteries dissipate heat more quickly than larger cells which sometimes results in these batteries not achieving thermal runaway under similar conditions that induce runaway for larger cells [85].

Spotnitz et al. utilize the models of thermal runaway to examine the thermal behavior of battery packs for small electronic devices should a single cell undergo thermal runaway [86]. The general findings identified a relationship between likelihood of cell-to-cell propagation with the heat of reaction and convective heat transfer coefficient [86]. Spotnitz et al. also suggest that the reason in-field thermal runaway incidents are increasing is due to the increased heat-of-reaction that is associated with the modern cells that are more energy dense [86].

5.3.3 Recent Millennial Research (2010-2015)

Jhu et al. perform a pair of studies which perform ARC testing of Sony, Sanyo, Samsung and LG 18650 cells and report expected maximum temperatures, peak system pressures and cell body heating rates [87,88]. This study was of particular interest as it reports the expected energy release at varying states-of-charge [87,88].

Wang et al. provide one of the most widely referenced papers regarding thermal runway which provides detailed description of in-field incidents, thermal runaway mechanisms, modeling studies and the various safety mechanisms built into then different components

of the Li-ion cell [59]. Though new insight is not provided, this study provides a comprehensive review of studies on the topics of thermal runaway testing and analysis.

Lu et al. provide studies performing ARC testing of $LiCoO_2$ cells in a format conducive to determining the TNT equivalent of the explosive event; varied states-of-charge are examined with alongside the appropriate respective amount of TNT [89]. Results here regarding maximum temperature and pressures observed during the experiments are in agreement with other values found in literature [89].

Nagasubramanian and Fenton, in collaboration with Sandia National Laboratories, consider the development of safe Li-ion batteries by implementing non-flammable electrolyte materials [90]. This study found that introducing flame-retardant materials to the electrolyte had a minimal impact to the thermal runaway response [90]. Non-flammable ionic liquids were also discussed, but Nagasubramanian and Fenton point out that this option is not desirable due to the poor low temperature performance of these materials [90].

Feng et al. explore extended volume (EV) ARC testing of large format $LiNi_xCo_xMn_xO_2$ Li-ion batteries exposed to high temperatures; experiments in this study are terminated prior to achieving thermal runaway to analyze battery performance post-exposure [91]. Feng et al. noted up to 20% losses in capacity after cells achieve temperatures of 120 ºC [91]. A separate of ARC experiments are performed which examine the thermal resistance throughout the thermal runaway event [92]. Feng et al. observe a significant rise in resistance and report that it is most likely due to the breakdown of the separator material [92].

5.4 Characterizing Heat Generation during Thermal Runaway

The generation of heat within the cell can be caused by solid electrolyte interphase (SEI) exothermic decomposition reactions and exothermic reactions between the electrodes and

the liquid electrolyte [72, 78, 79, 85]. Additionally, high internal pressure can be created within the cell by vaporization and decomposition of the liquid electrolyte [93, 94]. The Arrhenius behavior of these reactions eventually leads to a point of instability which results in cell rupture and the remaining chemical and electrical energy are rapidly released from the cell to its surroundings as heat through the cell body and hot ejecta [72, 78, 79, 85]. Clearly, the total energy release of a Li-ion cell experiencing thermal runaway, and the subsequent thermal profile, is a function of the rates of the exothermic decomposition reactions [72, 78, 79, 85]. Richard and Dahn conducted ARC experiments that provided the groundwork to formulating mathematic models of the SEI and anode decomposition rates; the Arrhenius-form equations are as follows [78,79],

$$\frac{dx_{SEI}}{dt} = -A_{SEI} x_{SEI} \exp\left(\frac{-E_{SEI}}{k_b T}\right) \text{ and} \tag{5.1}$$

$$\frac{dx_a}{dt} = -A_a x_a \exp\left(\frac{-z}{z_0}\right) \exp\left(\frac{-E_a}{k_b T}\right), \tag{5.2}$$

where x_{SEI} is the amount of lithium containing species in the SEI, A_{SEI} is a frequency factor (s^{-1}), E_{SEI} is the activation energy of the SEI reaction (J), k_b is the Boltzmann constant (J K^{-1}), T is temperature (K), x_a is the amount of lithium intercalated within the anode, A_a is a frequency factor (s^{-1}) and E_a is the activation energy of the anode reaction (J). The ($-z/z_0$) term is introduced to account for the increases in SEI layer thickness (z) relative to the initial thickness (z_0); the rate of increase is characterized by the following equation [78,79],

$$\frac{dz}{dt} = A_a x_a \exp\left(\frac{-z}{z_0}\right) \exp\left(\frac{-E_a}{k_b T}\right). \tag{5.3}$$

Hatchard et al. [72] recognized that cathode materials can react exothermically via two distinct mechanisms: (i) the oxidized cathode materials can react exothermically with the electrolyte and (ii) the cathode materials can decompose and emit oxygen which reacts

exothermically with the electrolyte. This observation resulted in the expansion of the models to include the cathode decomposition rate with the following equation [72],

$$\frac{dx_c}{dt} = A_c x_c (1 - x_c) \exp\left(\frac{-E_c}{k_b T}\right), \tag{5.4}$$

where x_c is the amount of lithium intercalated within the cathode, A_c is a frequency factor (s^{-1}) and E_c is the activation energy for the cathode reaction (J).

Understanding that elevated temperatures greater than 200 °C can lead to the exothermic decomposition of the electrolyte, Kim et al. provided further development of the mathematic models as shown in the following equation [85],

$$\frac{dY_e}{dt} = -A_e Y_e \exp\left(\frac{-E_e}{k_b T}\right), \tag{5.5}$$

where Y_e is the fraction of electrolyte in the liquid phase, A_e is a frequency factor (s^{-1}) and E_e is the activation energy for the electrolyte decomposition reaction (J). The combination of the models represented by Equation 5.1 through Equation 5.5 capture the rates of decomposition for the SEI, anode, cathode and electrolyte, respectively.

The combination of the models shown by Equation 5.1 through Equation 5.5 capture the rates of decomposition for the SEI, anode, cathode and electrolyte, respectively. The resulting heat generation that causes the temperature of the cell to rise due to the exothermic decomposition reactions may then be understood with Equations 5.6-5.10 [72,78,79,85],

$$\frac{dQ_{SEI}}{dt} = -m_{SEI}\, h_{SEI}\, \frac{dx_{SEI}}{dt}, \tag{5.6}$$

$$\frac{dQ_a}{dt} = -m_a\, h_a\, \frac{dx_a}{dt}, \tag{5.7}$$

$$\frac{dQ_c}{dt} = m_c\, h_c\, \frac{dx_c}{dt}, \text{ and} \tag{5.8}$$

$$\frac{dQ_e}{dt} = -m_e\, h_e\, \frac{dx_e}{dt}, \tag{5.9}$$

where $dQ_{SEI}\ dt^{-1}$ is the heat added due to the decomposition of the SEI (W), h_{SEI} is the heat of the SEI reactions (J g^{-1}), m_{SEI} is the mass of the SEI (g), $dQ_a\ dt^{-1}$ is the heat added due to the decomposition of the anode (W), m_a is the mass of the anode (g), h_a is the heat of anode reactions (J g^{-1}), $dQ_c\ dt^{-1}$ is the heat added due to the decomposition of the cathode (W), m_c is the mass of the cathode (g), h_c is the heat of the cathode reactions (J g^{-1}), $dQ_e\ dt^{-1}$ is the heat added due to the decomposition of the electrolyte (W), m_e is the mass of the electrolyte (g) and h_e is the heat of the electrolyte reactions (J g^{-1}).

Expanding from Richard and Dahn's original model, the temperature rise of the cell due to the exothermic decomposition reactions is characterized as follows [72, 78,79, 85],

$$\frac{dT}{dt} = \frac{h_{SEI}}{c_p}\left|\frac{dx_{SEI}}{dt}\right| + \frac{h_a}{c_p}\left|\frac{dx_a}{dt}\right| + \frac{h_c}{c_p}\left|\frac{dx_c}{dt}\right| + \frac{h_e}{c_p}\left|\frac{dY_e}{dt}\right|, \tag{5.10}$$

where c_p is the specific heat capacity of the battery, h_{SEI} is the heat of the SEI reactions, h_a is the heat of anode reactions, h_c is the heat of the cathode reactions, and h_e is the heat of the electrolyte reactions. Multi-physics simulation quantification of total energy release that is associated with SEI, anode, cathode and electrolyte decomposition reactions combined with comprehensive experimental data gathered here will help provide further insight into the total energy release distribution exhibited during thermal runaway [93,94].

5.4.1 COMSOL Model of Heat Generation

Coman et al. uses COMSOL Multiphysics to introduce an expansion to the models with a 0-D simulation of an 18650 format $LiCoO_2$ cell experiencing thermal runaway which: (i) includes the boiling, venting and decomposition of the electrolyte and (ii) accounts for the rapid release of stored electrochemical energy [93,94]. The method developed by Coman et al. using the ordinary differential equation (ODE) solver in COMSOL is recreated here to provide example of the expected thermal runaway profile based on the models alone. The

necessary parameters, as indicated by Equation 5.1 through Equation 5.10, are defined in Table 5-2. The COMSOL model setup is a 0-D simulation with the general mass and specific heat capacity of an 18650 Li-ion cell represented. The ambient temperature is initialized to 20 ºC and set to increase at a rate of 2 ºC min^{-1}. The temperature of the cell responds to the ambient temperature via radiation and natural convection.

The temperature profile generated is shown with Figure 5-3; the Li-ion cell experiences thermal runaway after approximately 4200 seconds and has a peak temperature approaching 1400 ºC. This result is in agreement with the models developed by Coman et al. and with the test results by Golubkov et al. [93-95]. This temperature profile is better understood after examining (a) the change in lithium content for the anode, cathode and SEI, (b) the fraction of electrolyte remaining in the liquid phase and (c) the release of electrochemical energy based on the state-of-charge. These transient response of these parameters due to the slow heating of the environment is displayed with Figure 5-4. Eventually a point of instability is reached and all remaining Li is consumed via exothermic reactions and all remaining electrochemical energy is released (i.e. the state-of-charge term drops). Detailed electrolyte analysis, such as that performed by Coman et al. [93, 94], require the calculation of the remaining electrolyte in the liquid phase to track the vaporization processes. The model accurately simulates the vaporization processes, which begin prior to the runaway event. This parameter is also captured by Figure 5-4. The energy release into the system is captured with Figure 5-5 and the resulting temperature rate vs. temperature profile is shown with Figure 5-6.

Table 5-2 Parameters defined in COMSOL Multiphysics for 0-D simulation of thermal runaway of an 18650 format $LiCoO_2$ Li-ion cell; the simulations were largely a recreation of the work by Coman et al. [72, 93,94, 95].

Term	Value	Description
Aa	1.67E12 1/s	Frequency Factor, Anode
Ac	6.67E11 1/s	Frequency Factor, Cathode
Aec	1.67E10 1/s	Frequency Factor, Electrochemical
Aelec	1.0E12 1/min	Frequency Factor, Electrolyte
Asei	1.67E13 1/s	Frequency Factor, SEI
Ea	2.24E−19 J	Activation Energy, Anode
Ec	2.03E−19 J	Activation Energy, Cathode
Eec	2.07E−19 J	Activation Energy, Electrochemical
Eelec	1.75E-19 J	Activation Energy, Electrolyte
Esei	2.24E−19 J	Activation Energy, SEI
Ha	1.71E6 J/kg	Enthalpy, Anode
Hc	3.14E5 J/kg	Enthalpy, Cathode
Hec	1.75E6 J/kg	Enthalpy, Electrochemical
Helec	1.55 J/kg	Enthalpy, Electrolyte
Hsei	2.57E5 J/kg	Enthalpy, SEI
JELLCp	830 J/(kg·K)	Specific Heat Capacity, Jellyroll
JELLRho	2914 kg/m³	Density, Jellyroll
ma	0.0081 kg	Mass, Anode
mc	0.0183 kg	Mass, Cathode
melec	4.6E-3 kg	Mass, Electrolyte
Tinit	293.15 K	Initial Temperature
Trate	0.03 K/s	Ambient Heating Rate
Xai	0.75	Initial Li Content, Anode
Xci	0.04	Initial Li Content, Cathode
Xeleci	1	Initial Liquid Electrolyte
Xseii	0.15	Initial Li Content, SEI
XSoCi	0.8	Initial SoC
Xzi	0.033	Initial Z Factor, SEI
Z1	0.00364 m²	Area, Cell Body Surfaces
Z2	0.8	Surface Emissivity
Z3	5.0 W/(m²·K)	Convection Coefficient
Z4	1.38E−23 J/K	Boltzmann Constant
Z5	5.67E−8 kg/(s³·K⁴)	S-Boltzmann Constant
Z6	1.52E−5 m³	Volume Cell

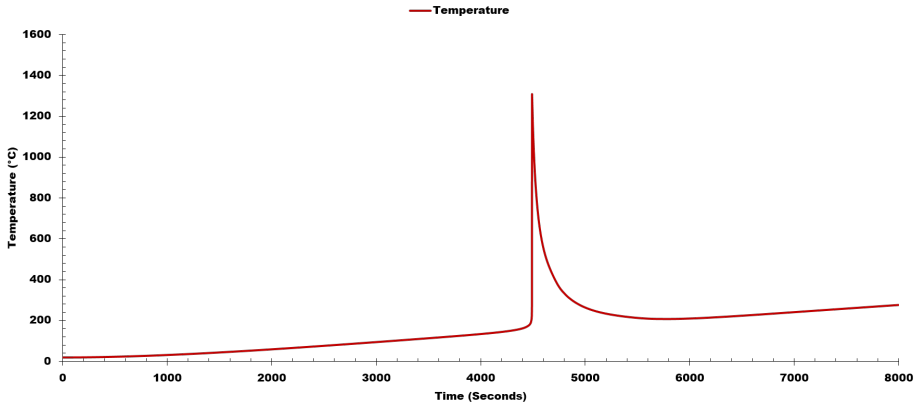

Figure 5-3 **Simulated temperature profile of a $LiCoO_2$ Li-ion cell induced into thermal runaway by increasing the environment temperature at a rate of 2 ºC min^{-1}. The results are in agreement with Coman et al. and Golubkov et al. [93-95].**

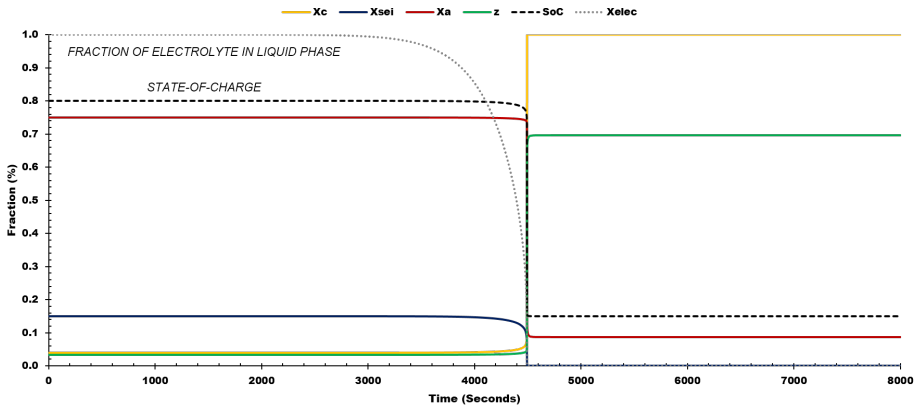

Figure 5-4 **Simulated thermal runaway lithium consumption rates, electrolyte vaporization rate and state-of-charge for a $LiCoO_2$ Li-ion cell. The results are in agreement with Coman et al. and Golubkov et al. [93-95].**

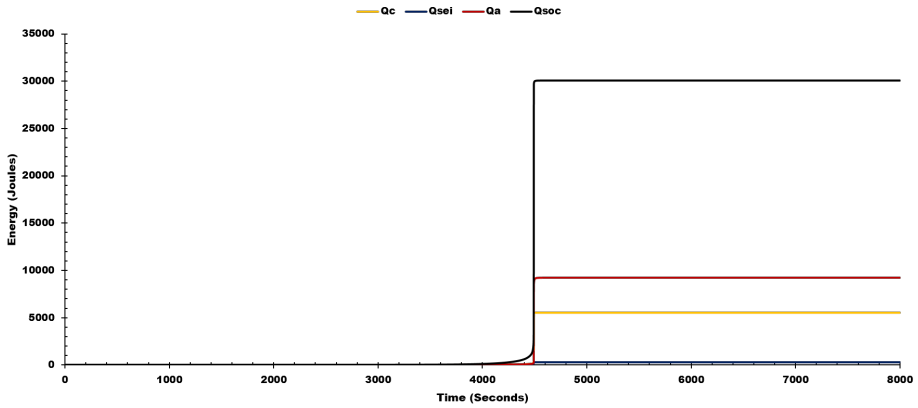

Figure 5-5 **Simulated heating profile of a $LiCoO_2$ Li-ion cell induced into thermal runaway by increasing the environment temperature at a rate of 2 ºC min^{-1}. The results are in agreement with Coman et al. and Golubkov et al. [93-95].**

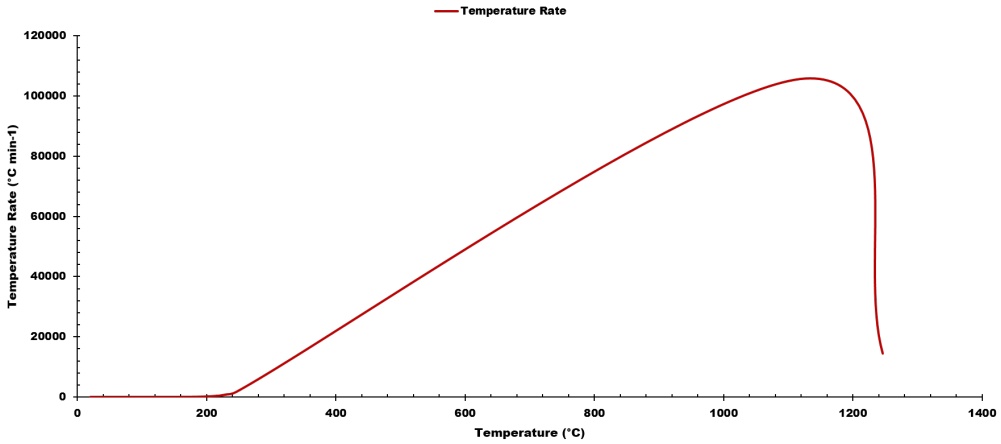

Figure 5-6 Simulated temperature rate vs. temperature profile of a $LiCoO_2$ Li-ion cell. The results are in agreement with Coman et al. and Golubkov et al. [93-95].

COMSOL Multiphysics provides an excellent vehicle for simulating thermal runaway mechanisms based on the exothermic chemical reactions which drive the event. Here a 0-D model of an 18650 format LiCoO2 Li-ion cell is developed in COMSOL Multiphysics in replication of work published by Coman et al. [93,94]. The actual models used in the simulations are based on the work by Richard and Dahn, Hatchard et al. and Kim et al. [72,78,79,85]. The simulations are in direct agreement with Coman's COMSOL results and with Golubkov's test results [93-95]. The model developed provides a unique tool to utilize to re-analyze the accelerated rate calorimetry (ARC) testing conducted recently by Sandeep et al. [31]. We can now examine the total energy release of the event as a fraction of energy introduced by the anode, cathode, SEI, electrolyte and electrochemical components.

One significant area for improvement to the models would be to account for the degradation and melting of the internal materials. The simulated peak temperatures are far above the melting point of some of the cell components. Another area of interest is that experimental results indicate that the simulated jellyroll temperature (over 1000 ºC) is unrealistically high. This is possible due to a number of reasons which include: (a) the movement of heat away from the cell via ejecta material is not being simulated correctly,

(b) simulations drive the chemical reactions to 100% completion which may not happen on an experimental basis and (c) the degradation and melting of internal components are not accurately represented in the simulations.

5.5 Accelerated Rate Calorimetry Methods

Using heat-wait-seek methodology, quasi-adiabatic accelerated rate calorimetry (ARC) experiments provide the ability to measure self-heating rates of a sample throughout high energy and explosive events (i.e. Li-ion cell experiencing thermal runaway) [96, 100]. This study focuses on improved ARC experiments designed to capture total thermal runaway energy release distributions between the cell body and hot gases via placement of the cell inside a uniquely designed secondary enclosure; this pressure sealed canister not only contains the cell body and hot gases, but also captures energy release associated with rapid heat transfer to the canister walls unobserved by measurements taken on the cell body.

Experiments are conducted with commercial Li-ion cells that NASA plans to use for various human space flight applications. The Boston Power Swing 5300, Samsung 18650-26F and MoliCel 18650-J Li-ion cells are tested in triplicate inside the secondary enclosure, referred to hereafter as the canister, in both closed (pressure sealed) and open (secondary canister lid off) form at 100% and 50% SOC. The three commercial cells are characterized in Table 5-1 [57,62-67]. Note that the closed canister tests are the primary experiments and that the open configuration testing is meant for comparison purposes. The improved ARC experiments yield temperature and pressure measurements in a format that facilitates accurate calculation of total energy release distributions.

Accelerated rate calorimetry experiments employ a heat-wait-seek methodology where the system is heated via external power which results in the slow radiative heating of the

interior sample [96, 100]. After short increments power is removed and the sample temperature is monitored for indication of self-heating that exceeds 0.02 °C min^{-1}. If self-heating is not detected another increment of power is applied thus raising the system to higher temperatures (typically +5 °C). This cycle is repeated until self-heating is detected; the sample temperature at this moment is referred to as onset temperature [96, 100]. After self-heating begins, the ARC system changes modes to match the ARC chamber wall temperature to the sample temperature to preserve a quasi-adiabatic condition [96, 100].

5.5.1 Quasi-Adiabatic Environment and Phi Correction Factor

ARC methods provide close to adiabatic conditions essential for determining onset temperature and self-heating rates of a sample [96, 100]. True adiabatic environments are theoretical and cannot occur in a laboratory environment [96, 100]. The two primary sources of error are the (a) thermal inertia of the system (i.e. the heat lost from the sample to its direct surroundings) and (b) the overall loss of heat from the test apparatus to the environment [96, 100]. A secondary container inside the ARC system is recommended to provide means to mitigate the error associated with thermal inertia; the intent of this recommendation should not be confused with the purpose of this study's sealed canister which is designed to contain the cell and hot gases in a format conducive to energy calculations. Error observed in ARC data is corrected with the phi-factor which is a proportionality constant relating the temperature rise of the container and the temperature rise that would have occurred in the sample were there no heat loss to the container [96, 100].

5.5.2 Improved ARC Experiment

Though useful in determining onset temperature and cell body heating rates during runaway, 'standard' ARC apparatus alone does not readily provide necessary features to

directly measure the total energy distribution exhibited during the thermal runaway event. Thermal runaway energy distributions are not isolated to cell body, as energy release is also in the form of hot gases and rapid heat transfer to the surroundings.

The solution presented here is a pressure sealed secondary canister constructed with stainless steel designed for measurement of cell body temperature, canister temperature, gaseous material temperature and canister pressure during the high energy and pressure event; each variable listed is required information for calculating total energy distribution. The canister mass is 1.96 kg with a specific heat capacity of 0.5 kJ kg^{-1} K^{-1}. Carefully designed cell holders are incorporated inside the canister to prevent movement of the cell and to ensure an open path for the vented products. Due to the BP-5300 cell's propensity to eject jellyroll materials during runaway events, a small steel strap is installed over the top of the cell and holder. Figure 5-7 details the improved ARC apparatus.

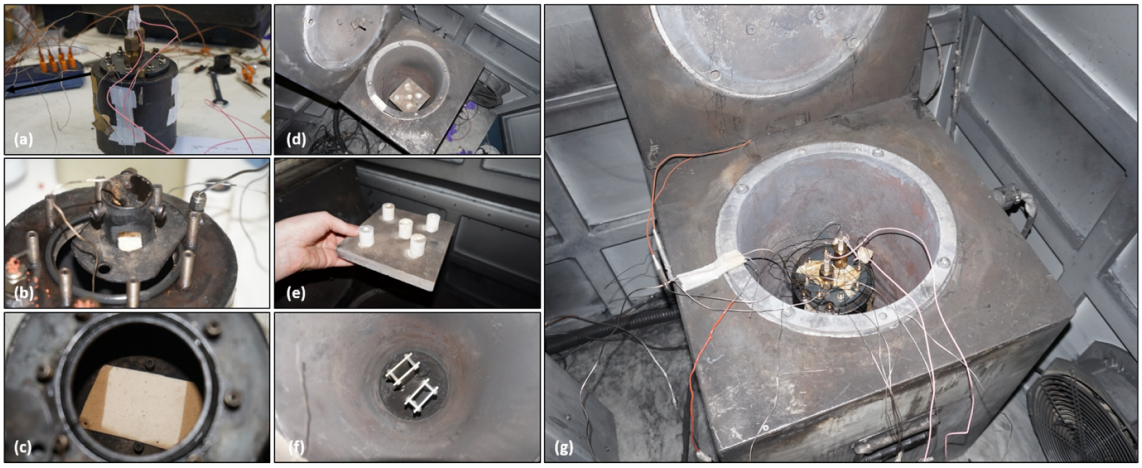

Figure 5-7 **Images of the following: (a) the secondary canister, (b) the cell holder, (c) the canister interior, (d) the empty ARC vessel, (e) the ceramic insulator, (f) the stand inside the ARC vessel and (g) the final apparatus.**

5.6 Improved ARC Experiment Results and Energy Calculations

The Boston Power Swing 5300, Samsung 18650-26F and MoliCel 18650-J Li-ion cells are tested in triplicate inside the canister in both closed and open form at 100% and 50% SOC. Transient data is collected throughout each experiment for temperature, pressure inside the secondary canister, cell voltage and ARC system power; pre and post-test mass measurements are also taken to determine the overall mass loss experienced by the cell.

Figure 5-8 through Figure 5-25 displays transient temperature, pressure, voltage and temperature rate profiles for one set of the closed configuration experiments; note that comprehensive documentation of the same plots for each of the 36 experiments is found in the appendices. The experiments include (i) Boston Power Swing 5300 @ 100% SOC, (ii) Samsung 18650-26F @ 100% SOC, (iii) MoliCel 18650-J @ 100% SOC, (iv) Boston Power Swing 5300 @ 50% SOC, (v) Samsung 18650-26F @ 50% SOC and (vi) MoliCel 18650-J @ 50% SOC. The individual experiments are labeled with a [manufacturer – identification number – canister configuration] format where a "BP" prefix indicates Boston Power, "S" prefix indicates Samsung, "M" prefix indicates MoliCel, the middle number indicates the individual identification number, a "C" suffix indicates closed canister configuration and an "O" suffix indicates open canister configuration.

Each temperature and pressure vs. time plot captures the entire experiment and provides annotation at the moments that the cell loses thermal stability and the system achieves peak temperatures and pressures. Voltage drop is compared to onset temperature. Note that the brief pressure loss observed with the 100% SOC Boston Power cell occurs because the rise in pressure, due to the rapid generation of hot gases, encroaches on the 20 bar design limit of the canister. All peak values are annotated on the figure for the respective tests.

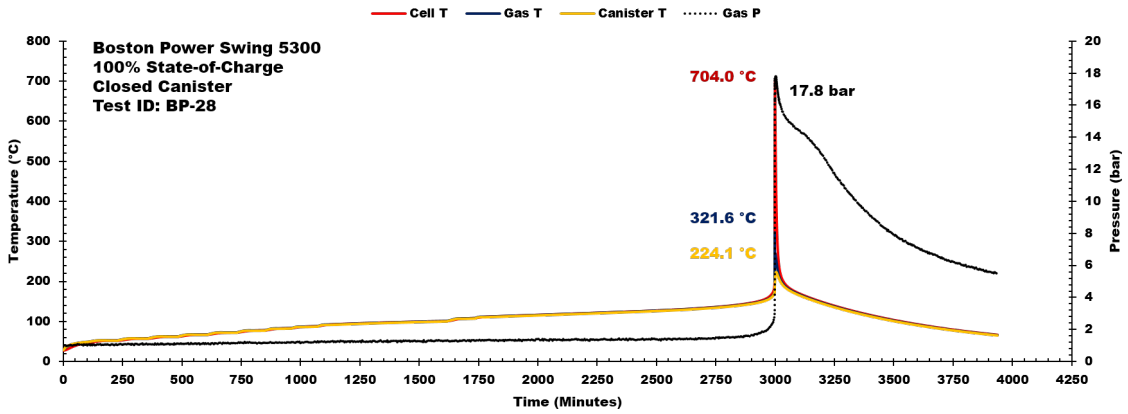

Figure 5-8 BP-5300 ARC data for the 100% SOC closed canister configuration (BP28). Data includes the following: (a) cell temperature, (b) gas temperature, (c) average canister temperature and (d) pressure.

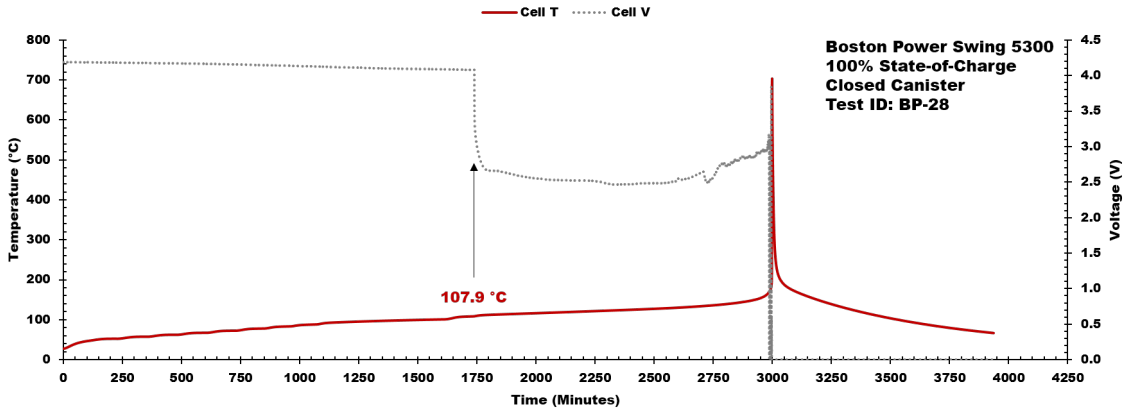

Figure 5-9 BP-5300 ARC data for the 100% SOC closed canister configuration (BP28). Data includes the following: (a) voltage and (b) temperature. The annotation compares onset temperature to voltage drop.

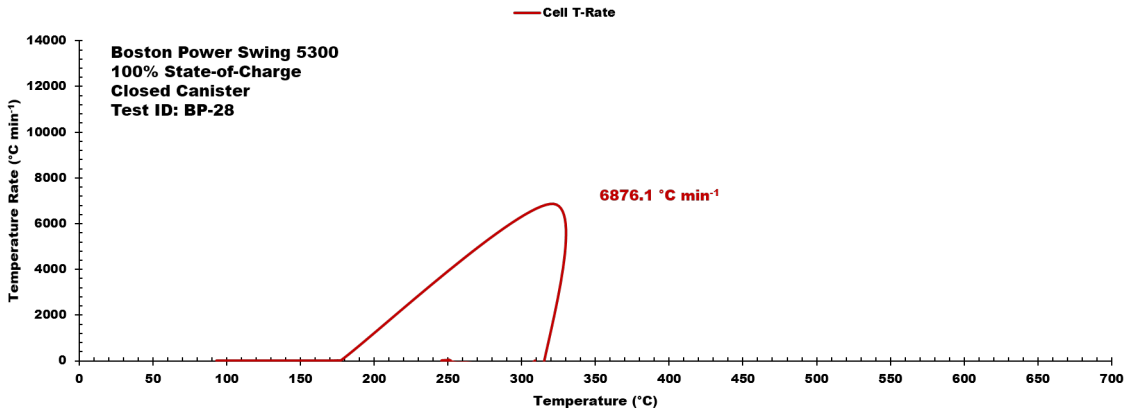

Figure 5-10 BP-5300 ARC data for the 100% SOC closed canister configuration (BP28). Data presented includes the temp. rate vs. temperature.

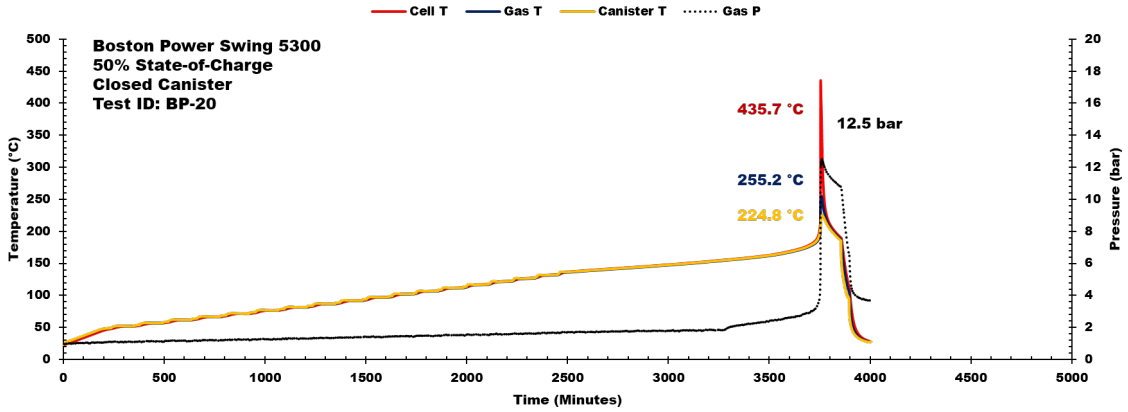

Figure 5-11 BP-5300 ARC data for the 50% SOC closed canister configuration (BP20). Data includes the following: (a) cell temperature, (b) gas temperature, (c) average canister temperature and (d) pressure.

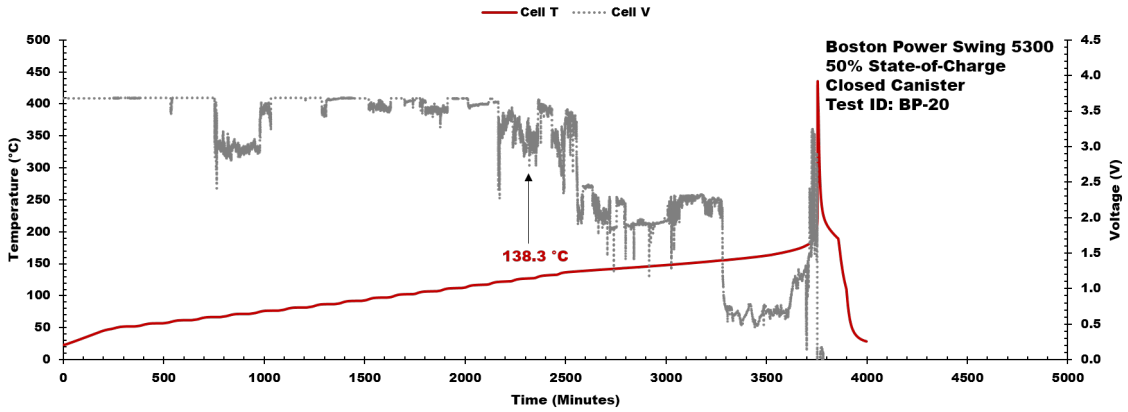

Figure 5-12 BP-5300 ARC data for the 50% SOC closed canister configuration (BP20). Data includes the following: (a) voltage and (b) temperature. The annotation compares onset temperature to voltage drop.

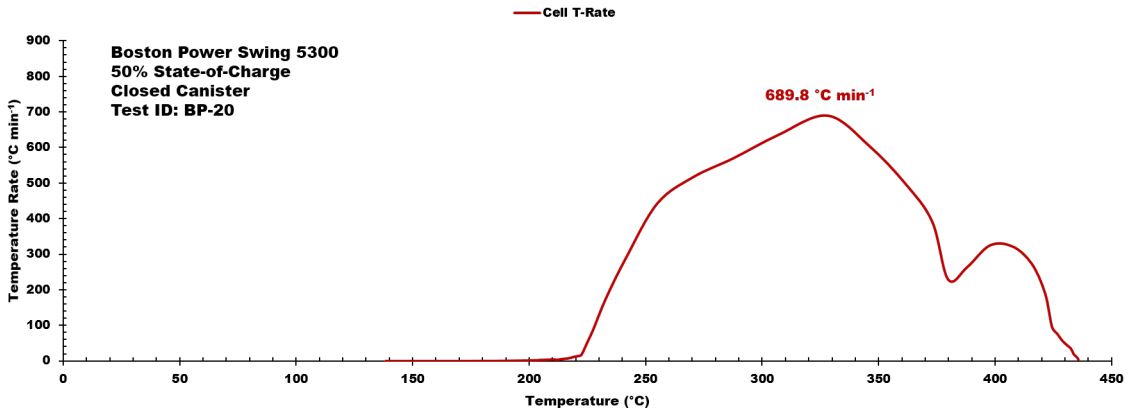

Figure 5-13 BP-5300 ARC data for the 50% SOC closed canister configuration (BP20). Data presented includes temp. rate vs. temperature.

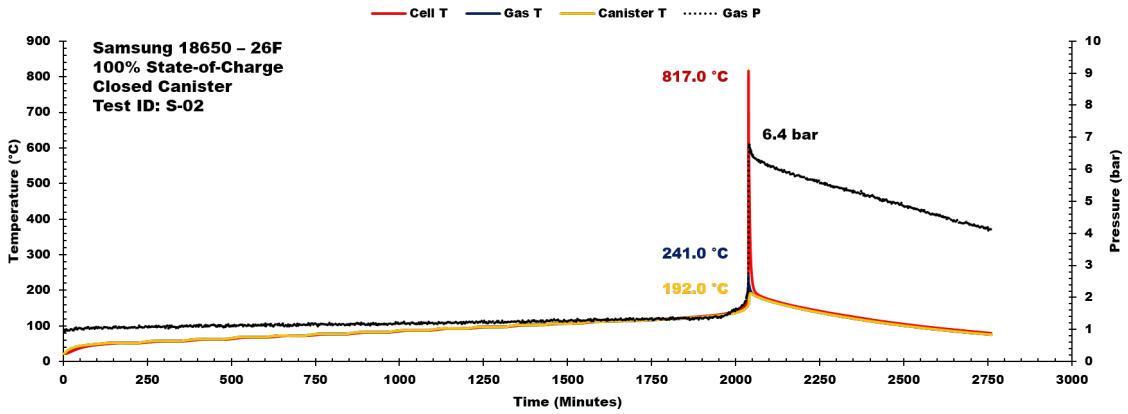

Figure 5-14 Samsung 18650-26F ARC data for the 100% SOC closed canister configuration (S02). Data includes the following: (a) cell temperature, (b) gas temperature, (c) average canister temperature and (d) pressure.

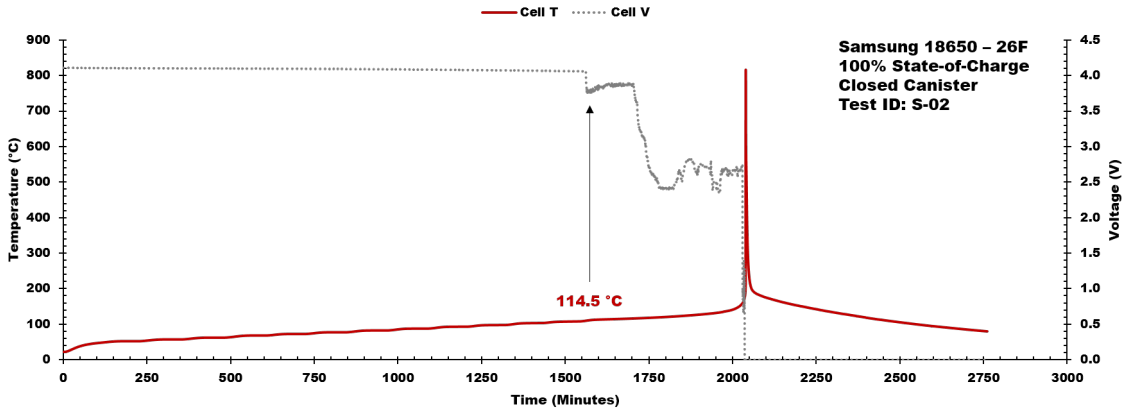

Figure 5-15 Samsung 18650-26F ARC data for the 100% SOC closed canister configuration (S02). Data includes the following: (a) voltage and (b) temperature. The annotation compares onset temperature to voltage drop.

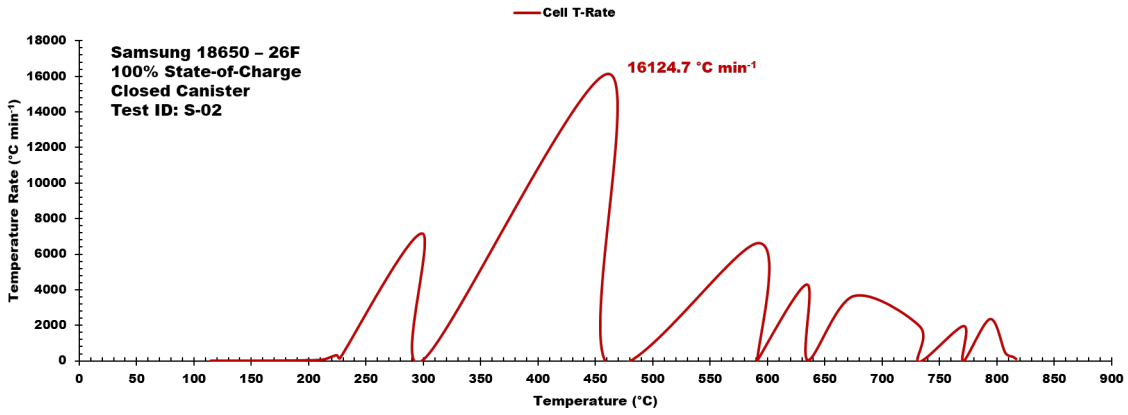

Figure 5-16 Samsung 18650-26F ARC data for the 100% SOC closed canister configuration (S02). Data presented includes temp. rate vs. temperature.

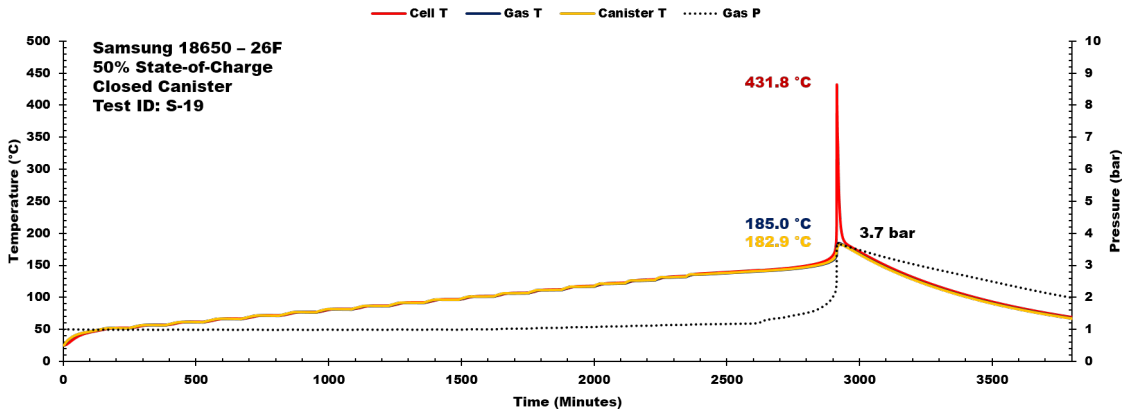

Figure 5-17 Samsung 18650-26F ARC test data for the 50% SOC closed canister configuration (S19) including the following: (a) cell temperature, (b) gas temperature, (c) average canister temperature and (d) pressure.

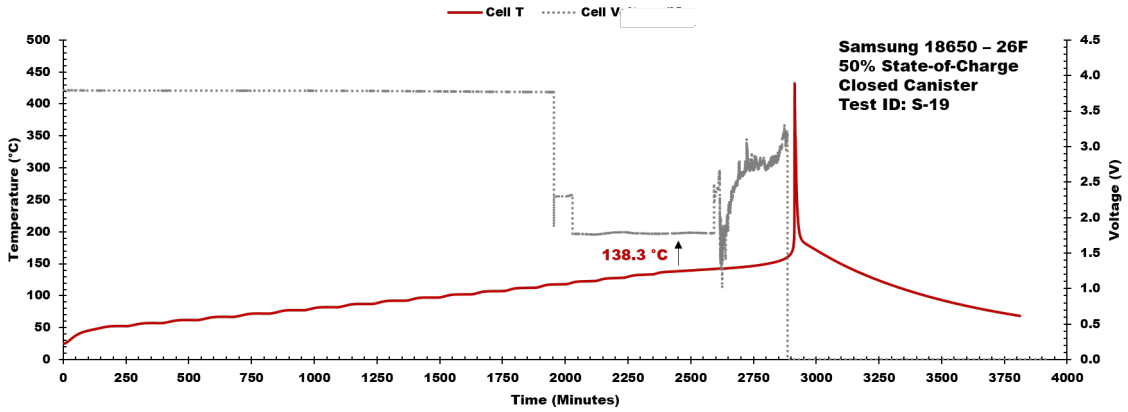

Figure 5-18 Samsung 18650-26F ARC data for the 50% SOC closed canister configuration (S19). Data includes the following: (a) voltage and (b) temperature. The annotation compares onset temperature to voltage drop.

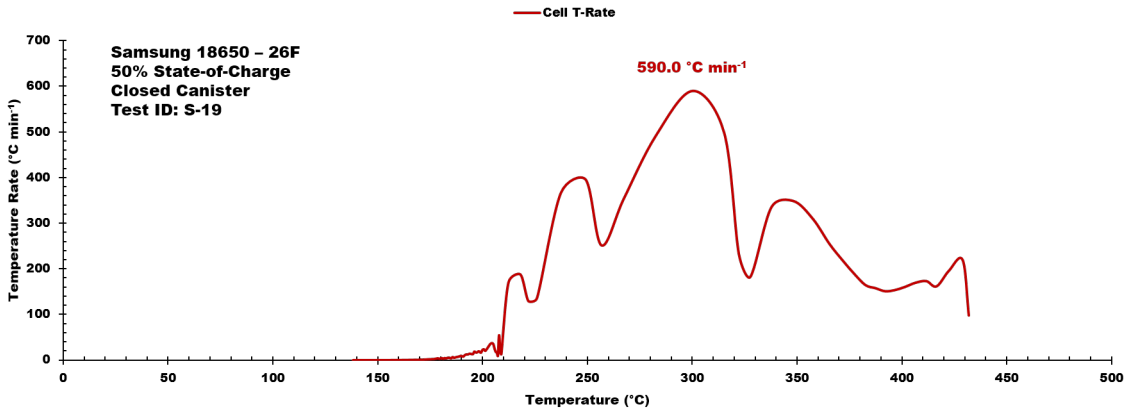

Figure 5-19 Samsung 18650-26F ARC data for the 50% SOC closed canister configuration (S19). Data presented includes temp. rate vs. temperature.

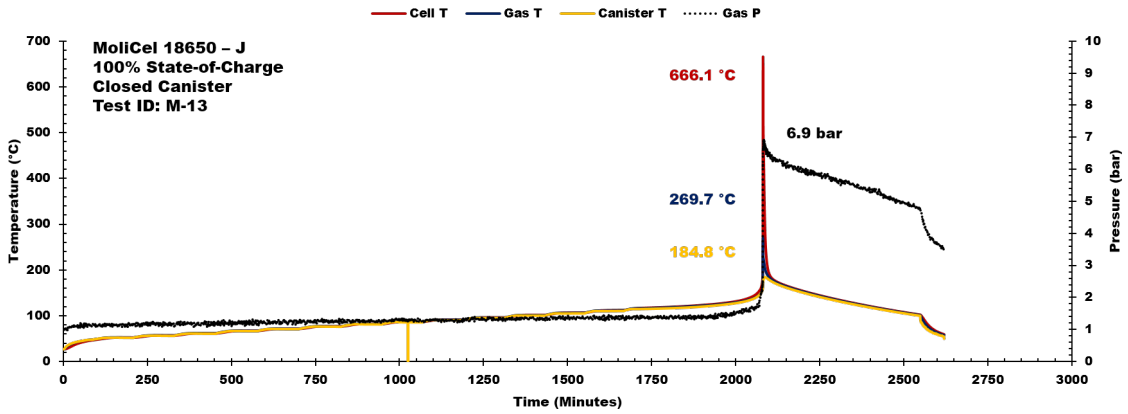

Figure 5-20 MoliCel 18650-J ARC data for the 100% SOC closed canister configuration (M13). Data presented includes the following: (a) cell temperature, (b) gas temperature, (c) average canister temperature and (d) pressure.

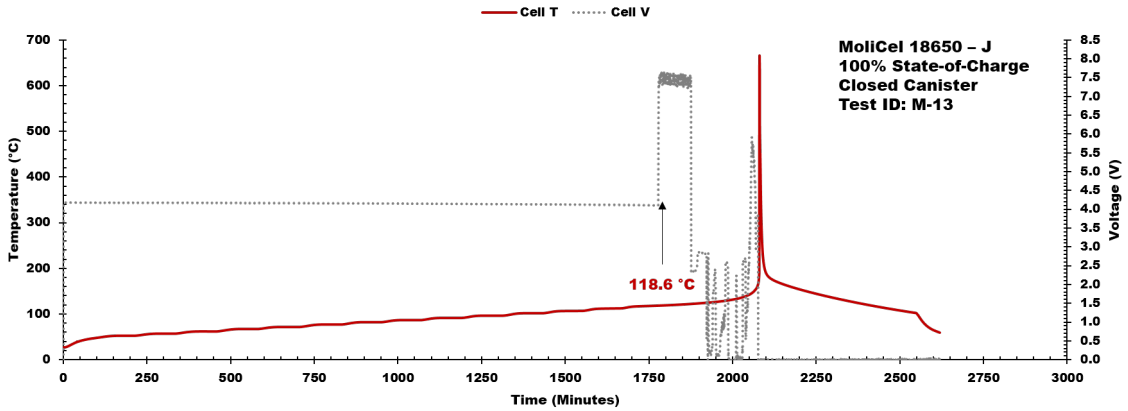

Figure 5-21 MoliCel 18650-J ARC data for the 100% SOC closed canister configuration (M13). Data presented includes the following: (a) voltage and (b) temperature. The annotation compares onset temperature to voltage drop.

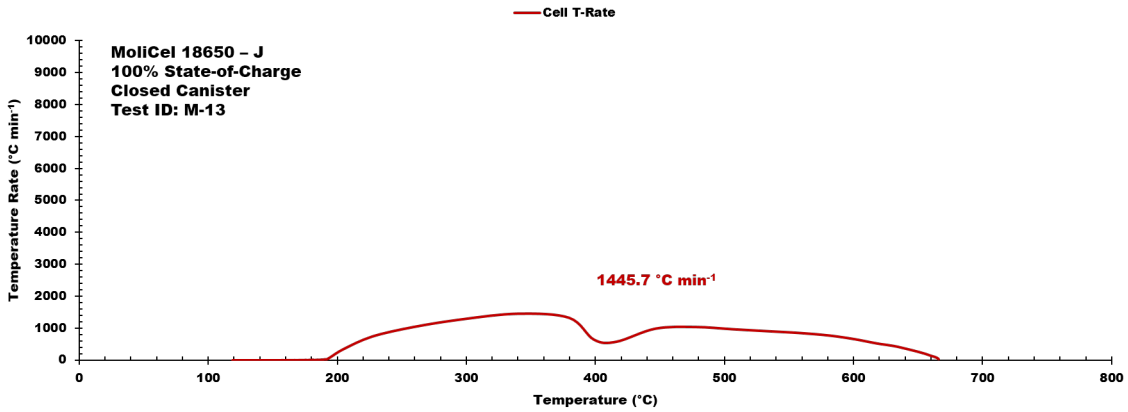

Figure 5-22 MoliCel 18650-26F ARC data for the 100% SOC closed canister configuration (M13). Data presented includes temp. rate vs. temperature.

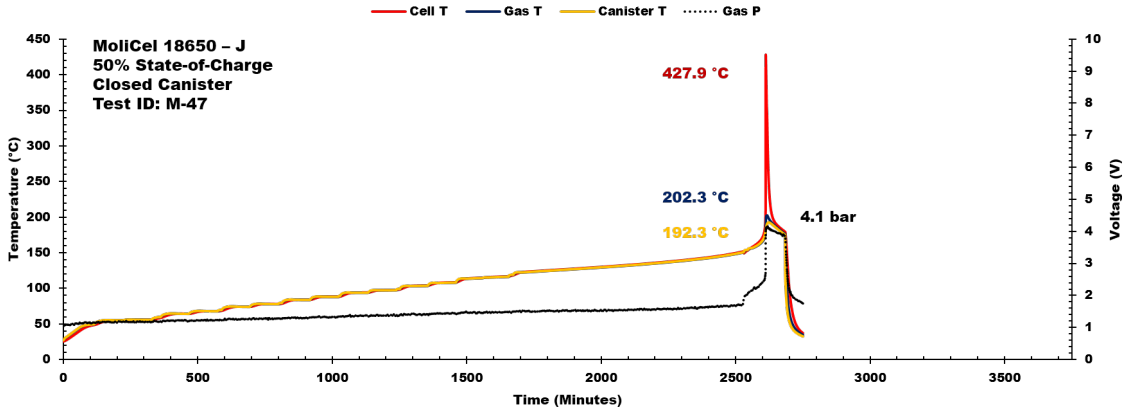

Figure 5-23 MoliCel 18650-J ARC data for the 50% SOC closed canister configuration (M47). Data presented includes the following: (a) cell temperature, (b) gas temperature, (c) average canister temperature and (d) pressure.

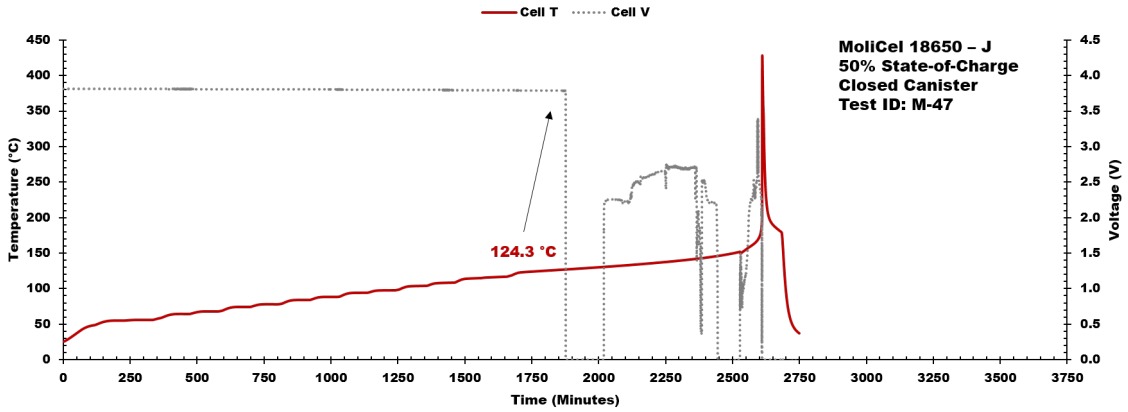

Figure 5-24 MoliCel 18650-J ARC data for the 50% SOC closed canister configuration (M47). Data presented includes the following: (a) voltage and (b) temperature. The annotation compares onset temperature to voltage drop.

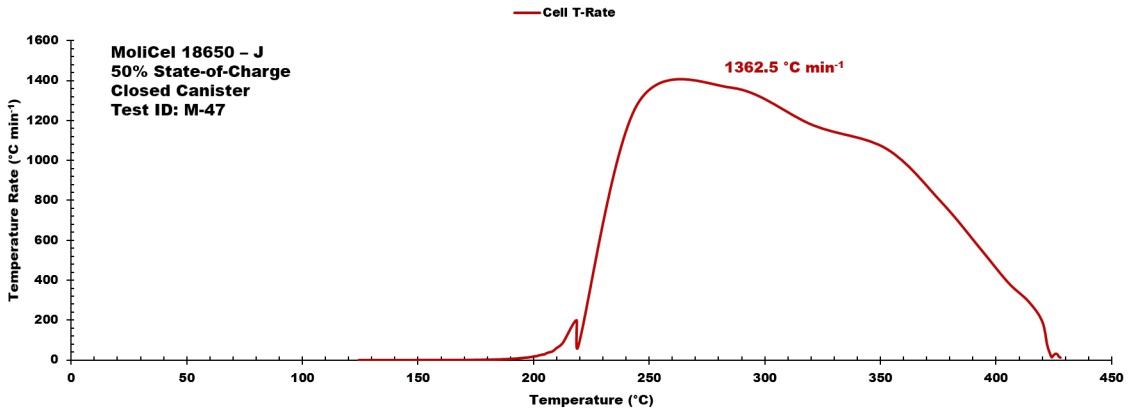

Figure 5-25 MoliCel 18650-26F ARC data for the 50% SOC closed canister configuration (M47). Data presented includes temp. rate vs. temperature.

Boston Power cell body maximum temperatures exhibited during 100% SOC experiments are typically lower than the 18650 cells; cell body maximum temperatures for 50% SOC experiments are all comparable. It is possible that this response is due to the overall higher mass of the BP cell and the manufacturer utilization of an aluminum cell can (stainless steel cans are used with the Samsung and MoliCel 18650 cells). Additionally, the lower temperatures may be a result of the BP cell safety features which allow the cell to vent at lower pressures.

For all cells, an inverse relationship between SOC and onset temperature is observed; 50% SOC resulted in higher onset temperatures while 100% SOC yielded lower onset temperatures. This finding is in agreement with studies performed by Golubkov et al. which observes similar relationship for 18650 cells at various states-of-charge; notably, experiments by Golubkov et al. observe a much lower onset temperature of 60 °C for cells overcharged to 150% SOC [95].

Comparison of cell mass loss and the pressure profiles for the closed configuration experiments indicates that the quantity of gaseous material generated during the Boston Power runaway events is higher than for the Samsung and MoliCel cells. This response is expected considering the difference in mass and capacity of the BP cell and the 18650 cells. Predictable ranges for onset temperature, maximum temperatures and peak canister pressure are observed when comparing all experiments; see Figure 5-26 and Figure 5-27 which compare onset temperature, maximum cell body temperature and peak canister pressure for the closed canister configuration with cells charged to 100% and 50%, respectively. Table 5-3 summarizes the averages of cell mass loss, peak system pressure, onset temperature and maximum cell body temperature for each test configuration.

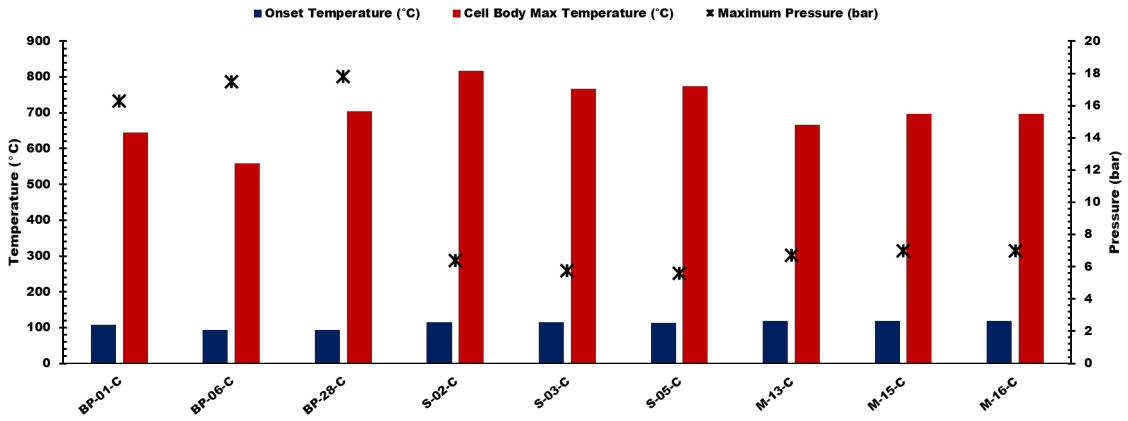

Figure 5-26 **Comparison of individual experiment measurements of onset temperature, maximum cell body temperature and maximum canister pressure for the closed configuration 100% state-of-charge.**

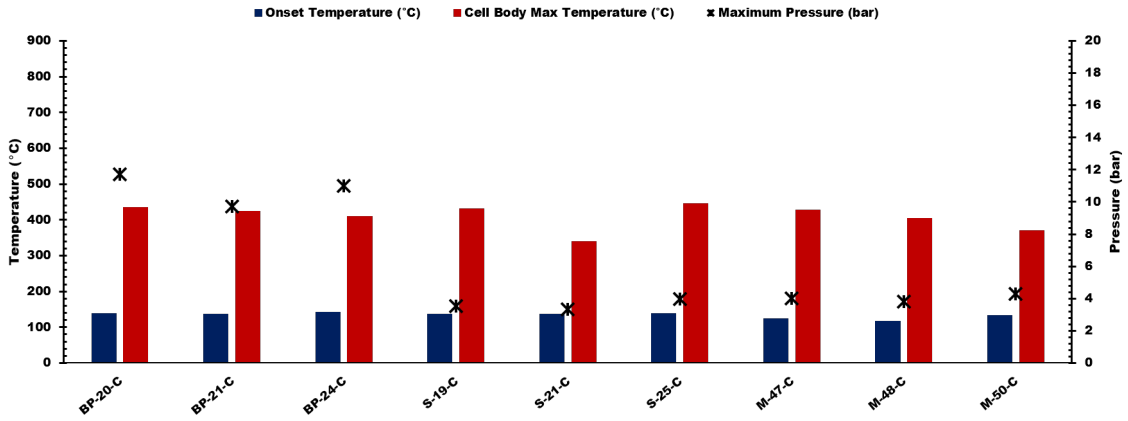

Figure 5-27 **Comparison of individual experiment measurements of onset temperature, maximum cell body temperature and maximum canister pressure for the closed configuration 50% state-of-charge.**

5.6.1 Energy Calculations

Known mass and specific heat capacity, combined with transient temperature profiles, are used to calculate the heating rates of the cell body, hot gases and canister throughout the durations of the ARC experiments; see Equation 5.11,

$$\dot{Q} = \frac{mc_p(T_2 - T_1)}{t_2 - t_1}, \tag{5.11}$$

where $\dot{Q}$ is heating rate (kW), m is the mass (kg), c_p is the specific heat capacity (kJ kg^{-1} $°C^{-1}$), T_2 is the current temperature (°C), T_1 is the temperature at the previous timestep (°C), t_2 is the current timestep (s) and t_1 is the previous timestep (s). The heating rate profiles are

integrated, following the trapezoidal rule, to determine total energy release per component; See Equation 5.12,

$$E_{Total} = \int_{t_{Start}}^{t_{End}} \dot{Q}\, dt, \tag{5.12}$$

where E_{Total} is the total energy (kJ), t_{Start} at the start of energy addition (s) and t_{End} is the time-stamp at the end of energy addition (s). E_{Total} is determined individually for the cell body, gaseous species and the canister; the totals of these three calculations yield total energy release due to the thermal runaway event.

Primary assumptions for the calculations include: (a) cell body and gaseous material energy calculations only consider the time between onset temperature and cell body maximum temperature, (b) gaseous material composition is carbon dioxide and (c) canister energy calculations are performed using the average of the thermocouples on the vessel and only consider the time between the moment ARC heaters shutoff and maximum average canister temperature.

Gaseous species energy calculations incorporate changes in specific heat, density and mass per timestep by combining experimentally gathered pressure and temperature data with the National Institute of Standards and Technology (NIST) Reference Fluid Thermodynamic and Transport Properties (REFPROP) Database Version 9.1 excel plugin. The primary reaction product from thermal runaway of an 18650 cell are carbon dioxide (CO_2), carbon monoxide (CO) and various hydrocarbons [74,83]. The NIST REFPROP calculated material properties of CO_2 provides sufficient approximation for energy calculations. Considering the relatively low mass of the gaseous species, combined with measured temperature rise inside the canister, minimal associated energy addition is expected throughout the duration of the experiment. Sampling the gaseous species and

determining exact composition prior to input into NIST REFPROP is recommended for future studies.

The sum of the energy for the cell body, gaseous species and canister yields the total calculated energy release to the system due to the thermal runaway event. Figure 6 compares the energy release distributions between the cell body, the canister and the hot gases for the three cells. Note that the slightly lower energy totals for test articles BP09 and BP25 are primarily due to partial jellyroll ejections which resulted in lower cell body temperature measurements; though it is also possible that the respective experiments simply released less energy than the other Boston Power experiments for reasons detailed in the experiment variance discussion previously. The total energy release of a BP cell thermal runaway event is approximately double the energy release of the 18650 cells due to the increased mass and cell capacity.

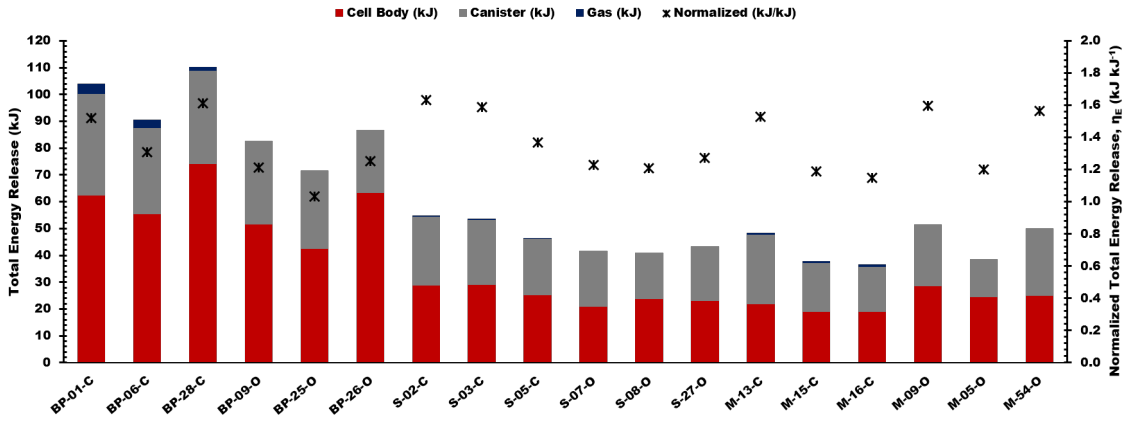

Figure 5-28 Comparison of energy release distributions and the normalized energy release factor for the BP-5300, Samsung 18650-26F and MoliCel 18650-J Li-ion cells for the 100% state-of-charge closed and open configurations.

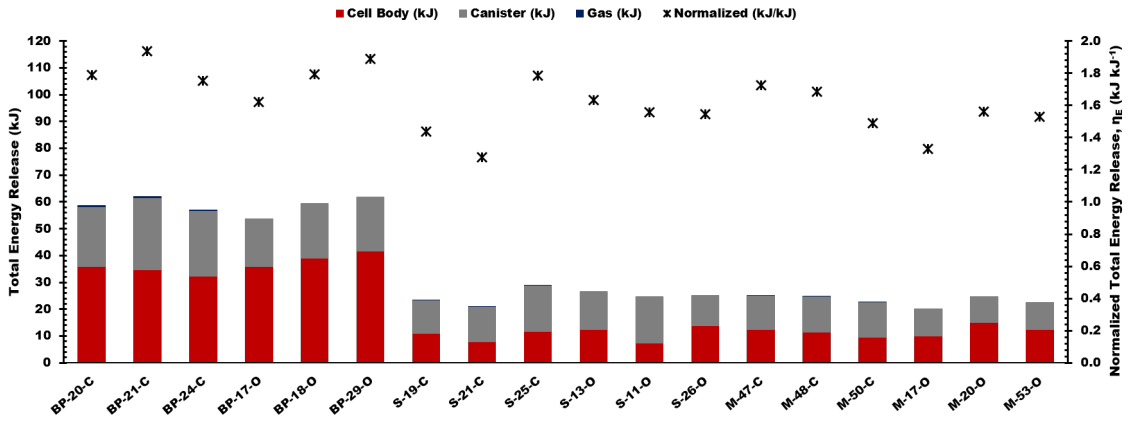

Figure 5-29 Comparison of energy release distributions and the normalized energy release factor for the BP-5300, Samsung 18650-26F and MoliCel 18650-J Li-ion cells for the 50% state-of-charge closed/open configurations.

Gaseous material energy is minimal. The fraction of energy observed with the canister mass is 45-55% of the total energy released in all experiments. The average 100% SOC total energy release is 98.6 kJ for the Boston Power cells, 47.0 kJ for the Samsung cells and 44.2 kJ for the MoliCel cells. These values are greater than the electrochemical energy stored in the cells at full charge, which are 19.4 Wh (69.7 kJ), 9.6 Wh (34.6 kJ) and 8.9 Wh (32.1 kJ), respectively. The average 50% SOC total energy release is 59.3 kJ for the Boston Power cells, 25.0 kJ for the Samsung cells and 23.4 kJ for the MoliCel cells; again the values are greater than the stored electrochemical energy.

The electrochemical energy stored in a Li-ion battery is determined and limited by specific oxidation and reduction reactions within the electrodes. However, during thermal runaway at elevated temperatures, other reactions occur, such as decomposition of the anode, decomposition of the cathode, self-reaction of salt with electrolyte, and combustion of the solvent [97,98]. These reactions can liberate more energy than that stored as electrochemical energy [99]. For example, decomposition reactions (without solvent combustion) in an 18650-size cell can produce 29 to 49 kJ. When solvent combustion reactions are included (which need additional oxygen from the ambient air) the total energy

liberated ranges from 119 to 175 kJ. In the improved ARC experiments discussed in this study, oxygen access is limited. Therefore, decomposition reactions could be expected to be similar to the lower estimates of 29 to 49 kJ. The average of this energy range (39 kJ) is larger than the electrochemical energy content of the 18650 cells in this study, which range from 32 to 35 kJ.

A dimensionless factor, η_E, characterized as total energy release (kJ) normalized by the stored electrochemical energy (kJ), is proposed to provide insight into general thermal runaway responses of Li-ion cells of similar chemistry (refer to anode/cathode combinations listed in Table 5-1). The stored electrochemical energy for each cell is measured from cycles performed prior to runaway testing rather than using nameplate energy from the manufacturers. The ability to develop η_E is highly reliant on a statistically significant number of test articles for each manufacturer and SOC combination. For all 100% SOC experiments, regardless of manufacturer, the average η_E is 1.4; the absolute η_E range observed when comparing all 100% experiments is 1.0 to 1.6. For all 50% SOC experiments, regardless of manufacturer, the average η_E is 1.6; the absolute η_E range observed when comparing all 50% experiments is 1.3 to 1.9. See the individual experiment η_E markers provided with Figure 5-28 and Figure 5-29.

Total energy release presented here is significantly higher than values published for Samsung 18650, Sanyo 18650, Sony 18650 and various custom 18650 cells tested in similar quasi-adiabatic calorimetry apparatus [81,87-89]. This comparison provides significant new insight into the expected total energy release of commercial Li-ion cells and also demonstrates that cell body measurements alone are not sufficient for total energy calculations. Overlooking the large fraction of energy release observed via the improved

ARC apparatus, or with the proposed η_E, may result in the design of an insufficient thermal management system. These findings suggest that the total energy release into the system is greater than the electrochemical energy stored in the cells and that normalized energy release factors can be used to accurately approximate total energy release of the Li-ion cell prior to design phases of battery assemblies. The averages of all of the results are provided with Table 5-3 and an executive summary of all results is provided with Table 5-4.

5.6.2 Expected Variance in Results and Calculations

Variance in the experimental measurements and in the subsequent energy calculations is observed across the board. This is expected due to the following reasons: (a) loss of quasi-adiabatic condition following the runaway event, (b) runaway event responses are never exactly the same, (c) differences in cell can materials exist and (d) variances in cell chemistries influence the exothermic decomposition reactions. The standard deviation for each of the measured variables for each test configuration is documented in Table 5-5.

The primary source of deviation in the energy calculations is due to the differences in the peak temperature measured by the thermocouple on the cell body. Because 45-55% of the energy release is measured through the cell body, these differences can significantly influence the total energy release calculation. Note that there is only one temperature measurement on the cell. Finegan et al. provides infrared videography which demonstrates non-uniform cell body temperatures during thermal runaway [75]. An area for improvement is to increase the number of temperature measurements on the trigger cell, which may reveal a closer overall response on an experiment-to-experiment basis.

Table 5-3 Averages of experiment measurements and resulting energy calculations for the Boston Power Swing 5300, Samsung 18650-26F and MoliCel 18650-J Li-ion cells.

Item	Boston Power Swing 5300		Samsung 18650-26F		MoliCel 18650-J	
	100% [4]	50%	100%	50%	100%	50%
Cell Body Mass Loss	24.0 gm	15.5 gm	9.8 gm	4.4 gm	8.4 gm	4.6 gm
Max Pressure [1,2]	17.2 bar	10.8 bar	5.9 bar	3.6 bar	6.9 bar	4.0 bar
Onset Temperature	93.4 °C	126.7 °C	111.4 °C	131.0 °C	113.9 °C	122.2 °C
Cell Body Max Temperature [3]	618.6 °C	429.4 °C	786.4 °C	410.8 °C	742.6 °C	416.3 °C
Cell Body Energy	63.8 kJ	36.4 kJ	25.0 kJ	10.6 kJ	22.9 kJ	11.7 kJ
Canister Body Energy	32.1 kJ	22.2 kJ	21.6 kJ	14.3 kJ	20.6 kJ	11.6 kJ
Gas Energy [5]	2.7 kJ	0.7 kJ	0.4 kJ	0.1 kJ	0.7 kJ	0.1 kJ
Total Energy Release	98.6 kJ	59.3 kJ	47.0 kJ	25.0 kJ	44.2 kJ	23.4 kJ
Normalized Energy Release Factor, η_E [6]	1.4	1.8	1.4	1.5	1.4	1.6

[1] *Conversion factor of 1 bar = 100000 Pa*

[2] *Max pressure average does not include open canister configuration; measurement of pressure increase is only possible with the closed canister configuration.*

[3] *Two of the open configuration 100% SOC BP experiments resulted in a partially ejected jellyroll thus reducing overall maximum temperature achieved; cell body max temperature average excludes these two data points.*

[4] *Though the two experiments which resulted in ejected jellyrolls reduced maximum temperature achieved, it was still possible to determine approximate energy release in these cases; therefore the individual energy calculations are considered in the averages presented by this table.*

[5] *Gas energy calculations require pressure measurements and are subsequently only based on closed canister configuration data points.*

[6] *The dimensionless η_E factor is total calculated energy release (kJ) normalized by electrochemical energy (kJ)*

Table 5-4 Test case matrix and executive summary of results.

Test ID	SOC	Type	Post-Charge Voltage (V)	Stored Electrochemical Energy (kJ)	Cell Mass Loss (gm)	Max Pressure (bar)	Cell Onset Temperature (°C)	Cell Max Temperature (°C)	Cell Body Energy (kJ)	Canister Body Energy (kJ)	Gas Energy (kJ)
BP01	100%	Closed	4.18	68.41	19.80	16.30	108.30	644.70	62.21	38.05	3.73
BP06	100%	Closed	4.18	69.17	21.40	17.50	93.90	558.80	55.37	32.23	2.91
BP28	100%	Closed	4.19	68.50	20.90	17.80	93.90	704.00	74.18	34.66	1.52
BP09	100%	Open	4.20	68.20	27.70	N/A	77.30	499.20	51.50	31.10	N/A
BP25	100%	Open	4.17	69.52	25.51	N/A	77.40	451.30	42.50	29.20	N/A

Table 5-4 (Continued)

BP26	100%	Open	4.19	68.28	28.70	N/A	77.60	566.70	63.30	23.50	N/A
BP20	50%	Closed	3.68	32.93	16.27	11.70	138.30	435.70	35.71	22.26	0.90
BP21	50%	Closed	3.68	32.07	14.67	9.70	138.20	425.00	34.46	27.08	0.56
BP24	50%	Closed	3.68	32.61	14.76	11.00	143.50	410.60	32.12	24.52	0.59
BP17	50%	Open	3.68	33.18	16.00	N/A	113.58	409.89	35.67	18.09	N/A
BP18	50%	Open	3.68	33.20	15.37	N/A	113.42	436.32	38.84	20.67	N/A
BP29	50%	Open	3.68	32.83	16.21	N/A	112.94	458.88	41.63	20.36	N/A
S02	100%	Closed	4.08	33.62	8.38	6.38	114.50	816.90	28.66	25.79	0.45
S03	100%	Closed	4.15	33.83	8.15	5.75	114.20	766.60	28.88	24.41	0.38
S05	100%	Closed	4.16	33.99	8.93	5.58	113.70	775.00	25.04	21.12	0.34
S07	100%	Open	4.17	33.91	11.23	N/A	107.70	711.90	20.86	20.77	N/A
S08	100%	Open	4.17	33.87	11.41	N/A	114.10	847.20	23.79	17.16	N/A
S27	100%	Open	4.17	34.05	10.80	N/A	104.00	800.60	22.95	20.42	N/A
S19	50%	Closed	3.78	16.21	4.56	3.55	138.10	431.80	10.94	12.29	0.05
S21	50%	Closed	3.78	16.39	3.70	3.34	138.20	340.90	7.70	13.18	0.08
S25	50%	Closed	3.78	16.28	4.68	3.96	138.40	447.10	11.68	17.26	0.11
S26	50%	Open	3.80	16.23	4.89	N/A	123.70	481.80	13.63	11.49	N/A
S11	50%	Open	3.79	15.84	5.34	N/A	124.00	325.70	7.32	17.36	N/A
S13	50%	Open	3.76	16.25	5.10	N/A	123.40	437.30	12.39	14.18	N/A
M13	100%	Closed	4.17	31.70	7.90	6.80	118.60	666.10	21.77	26.03	0.65
M15	100%	Closed	4.18	31.81	8.26	7.00	118.60	673.20	18.79	18.42	0.61
M16	100%	Closed	4.15	31.87	8.08	7.00	119.10	696.40	18.98	16.75	0.91
M05	100%	Open	4.15	32.00	8.47	N/A	113.40	794.20	24.43	14.03	N/A
M09	100%	Open	4.17	32.29	9.11	N/A	118.90	804.10	28.50	23.00	N/A
M54	100%	Open	4.18	32.07	8.39	N/A	94.30	798.30	25.00	25.19	N/A
M47	50%	Closed	3.81	14.61	4.81	4.00	124.30	427.90	12.26	12.84	0.09
M48	50%	Closed	3.80	14.85	4.48	3.80	118.30	404.30	11.33	13.48	0.19

Table 5-4 (Continued)

M50	50%	Closed	3.81	15.17	4.62	4.30	134.20	371.60	9.41	13.06	0.12
M53	50%	Open	3.81	14.70	5.03	N/A	108.90	458.30	12.30	10.20	N/A
M17	50%	Open	3.81	15.22	4.03	N/A	123.20	388.20	9.82	10.44	N/A
M20	50%	Open	3.80	15.78	4.89	N/A	124.10	447.50	14.92	9.74	N/A

Table 5-5 Standard deviation for experimentally measured parameters, calculated energy release distributions, total energy release and normalized total energy release.

Item	**Boston Power Swing 5300**				**Samsung 18650-26F**				**MoliCel 18650-J**			
	Closed		**Open**		**Closed**		**Open**		**Closed**		**Open**	
	100%	**50%**	**100%**	**50%**	**100%**	**50%**	**100%**	**50%**	**100%**	**50%**	**100%**	**50%**
Cell Body Mass Loss (gm)	0.82	0.90	1.63	0.10	0.40	0.53	0.31	0.77	0.18	0.17	0.34	0.44
Max Pressure (bar)	0.79	1.01	N/A	N/A	0.42	0.32	N/A	N/A	0.17	0.25	N/A	N/A
Onset Temperature (°C)	8.31	3.03	1.77	0.33	0.40	0.15	5.11	0.30	0.29	8.03	12.91	8.53
Cell Body Max Temperature (°C)	73.0	12.60	57.98	24.52	26.95	57.41	68.73	80.42	17.49	28.27	4.97	37.74
Cell Body Energy (kJ)	9.52	1.82	10.43	2.98	2.16	2.12	1.51	3.34	1.67	1.45	2.21	2.55
Canister Body Energy (kJ)	2.92	2.41	3.96	1.41	2.40	2.65	1.99	2.94	4.94	0.33	5.91	0.35
Gas Energy (kJ)	1.12	0.19	N/A	N/A	0.05	0.03	N/A	N/A	0.17	0.05	N/A	N/A
Total Energy Release (kJ)	10.13	2.48	7.79	4.22	6.06	4.16	1.25	0.99	6.50	1.45	7.18	2.20
Normalized Energy Release Factor, η_E	0.16	0.10	0.12	0.14	0.14	0.26	0.03	0.05	0.21	0.13	0.22	0.13

5.7 Total Energy Release Conclusions

Li-ion batteries provide low mass and energy dense solutions necessary for space exploration, but thermal safety concerns impede the utilization of Li-ion technology for human space flight applications. Experimental characterization of thermal runaway energy release with accelerated rate calorimetry prior to battery pack development supports safer thermal management systems. This study, which improves the 'standard' ARC apparatus, considers the total energy generation as a distribution between the cell body, hot gaseous species and rapid conduction and radiation to the system via the employment of a pressure sealed secondary canister.

Inverse relationship between SOC and onset temperature is observed. Energy associated with hot gases is minimal; however, the energy measured with the canister mass due to rapid conduction and radiation is significant. Average 100% SOC total energy release during thermal runaway is 98.6 kJ for the Boston Power cells, 47.0 kJ for the Samsung cells and 44.2 kJ for the MoliCel cells. Average 50% SOC total energy release is 59.3 kJ for the Boston Power cells, 25.0 kJ for the Samsung cells and 23.4 kJ for the MoliCel cells. The total energy release is greater than the electrochemical energy.

Regardless of manufacturer or SOC combination, predictable ranges for maximum temperature, peak pressure and total energy release are observed; this study uses these ranges to develop η_E which can approximate total energy release for cells of similar chemistry as discussed here. Improved ARC apparatus including a secondary enclosure provides essential capability for experimentally determining the total energy release distribution of thermal runaway.

Acknowledgement is given to the NASA Engineering and Safety Center (NESC) and Dr. Christopher Iannello who provided project authorization, management and leadership for the ARC testing studies. These experiments were part of an overall NASA effort to better understand thermal runaway events in pursuit of designing safe battery assemblies for human space flight applications. Special thanks and acknowledgement also goes to the team at Thermal Hazard Technology who conducted the testing.

Chapter 6 Conclusions and Future Work

6.1 Thermo-Electrochemical Analysis of Lithium Ion Batteries with Thermal Desktop

We evaluated the capability of thermal radiation analysis software Thermal Desktop to perform basic thermo-electrochemical analyses by coupling energy balance models developed by Bernardi et al. [28] with the Thermal Desktop solution process. A proof-of-concept study is provided which is based on the test-correlated simulations of a large format 185 Ah Li-ion battery by Chen et al [29].

The first series of results displays that the Thermal Desktop model provides accurate replication of the temperature profiles provided by Chen et al. [29] for all discharge and convection combinations. The minimal deviation from experimental results would easily be encompassed by the recommended predicted +11 °C margin for test correlated thermal models as recommended by both the Gilmore Satellite Thermal Control Handbook and the Department of Defense Standard Practice Product Verification Requirements for Launch, Upper Stage, and Space Vehicles (MIL-STD-1540D) section for thermal model margin for spacecraft hardware [38, 56].

The second series of analysis identifies the impact of updating the local temperature term when calculating Li-ion battery core region heating rates. These results demonstrate that for less extreme sink temperatures and heat fluxes, the change in heat generation is minimal, but that combination of local heating and space environments could greatly affect the thermal profile.

The third set of results display the impact of error when calculating core region specific heat capacity and that minimal error here could have a detrimental effect on temperature predictions (e.g., the prediction of temperatures lower or higher than what the Li-ion

battery will actually experience). Underestimating the specific heat capacity might lead analysts to develop an insufficient thermal management system.

The results obtained through this study support the use of Thermal Desktop for coupled thermal radiation and thermo-electrochemical analysis of Li-ion batteries. Though the study did not directly examine space environments, it provides proof-of-concept that Thermal Desktop is suitable Li-ion battery analysis.

6.2 Simulation of Robonaut 2 Lithium Ion Battery Assembly in Thermal Radiation Driven Orbital Environments

A test-correlated Thermal Desktop model is developed to support NASA R2 design requirements, to provide confidence in the R2 battery thermal performance and safety and to demonstrate suitability of Thermal Desktop for thermo-electrochemical analysis of passively controlled Li-ion batteries designed to function in thermal radiation driven environments.

The cell level model accurately predicts BP Swing 5300 temperatures for 2.0 C, 1.0 C, 0.7 C and 0.5 C charge and discharge operations based on direct comparison to experimental data. The R2 battery pack model combined with a satellite model for example thermal radiation environment analysis demonstrates the unique capability gained by utilizing Thermal Desktop for thermo-electrochemical analysis. With the added capability of simulating charging processes and the demonstration of discharge operations in orbit, this study provides necessary validation that the Thermal Desktop technique is suitable for thermo-electrochemical analysis and necessary for thermal design of safe Li-ion batteries intended for human space flight applications. Performing thermo-electrochemical analysis

in software capable of simulating radiation driven environments provides the opportunity for safe, reliable and passively controlled Li-ion battery systems.

6.3 Energy Distributions Exhibited during Thermal Runaway of Commercial Lithium Ion Batteries used for Human Space Flight Applications

Li-ion batteries provide low mass and energy dense solutions necessary for space exploration, but thermal safety concerns impede the utilization of Li-ion technology for human space flight applications. Experimental characterization of thermal runaway energy release with accelerated rate calorimetry (ARC) prior to battery pack development supports safer thermal management systems. This study, which improves the 'standard' ARC apparatus, considers the total energy generation as a distribution between the cell body, hot gaseous species and rapid conduction and radiation to the system via the employment of a pressure sealed secondary canister.

Inverse relationship between SOC and onset temperature is observed. Energy associated with hot gases is minimal; however, the energy measured with the canister mass due to rapid conduction and radiation is significant. Average 100% SOC total energy release during thermal runaway is 98.6 kJ for the Boston Power cells, 47.0 kJ for the Samsung cells and 44.2 kJ for the MoliCel cells. Average 50% SOC total energy release is 59.3 kJ for the Boston Power cells, 25.0 kJ for the Samsung cells and 23.4 kJ for the MoliCel cells. The total energy release is greater than the electrochemical energy.

Regardless of manufacturer or SOC combination, predictable ranges for maximum temperature, peak pressure and total energy release are observed; this study uses these ranges to develop η_E which can approximate total energy release for cells of similar chemistry as discussed here. Improved ARC apparatus including a secondary enclosure

provides essential capability for experimentally determining the total energy release distribution of thermal runaway.

Results and insights from this study provide valuable inputs for developing a complete characterization of the thermal runaway event. A diagram describing the characterization and influencing variables of thermal runaway is developed to describe the complex event (see Figure 6-1). This diagram provides the following categories: (a) failure mechanisms, (b) decomposition reactions, (c) environment influences, (d) system impacts, (e) cell level architecture, (f) time specific parameters, (g) experimental methods and (h) event characterization. Each category is described with the following general statements:

(a) Thermal, mechanical, electrochemical and electrical abuse failure mechanisms can lead to elevated temperatures high enough to initiate exothermic decomposition reactions.

(b) Exothermic decomposition reactions initiate following elevated temperatures or internal shorting. Self-heating is initiated when the cell generates heat at a rate greater than the rate of dissipation. Eventually, stability is lost and explosion occurs.

(c) Environmental influences, such as atmospheric composition, temperature and pressure can influence the thermal runaway event. These parameters play a significant role in relationship to the combustion behavior associated with the thermal runaway event.

(d) The thermal performance, observed during the event, is directly influenced by surrounding structures, heat paths and thermal control methods.

(e) Individual cell level architecture must be understood in relationship to thermal runaway. Relevant influencing parameters include the specific chemistry of the

electrode/electrolyte materials, the overall capacity, safety features (e.g., charge interrupt devices), the cell case material and overall geometry and mass.

(f) Time-specific parameters may play a role. Specifically, what is the state-of-charge and age of the cell at the time of the event? Also, was the battery in operation or standby mode at the time of the event? Was this an experiment or a field occurrence?

(g) Experimental methods utilized to understand thermal runaway include accelerating rate calorimetry, x-ray, infrared videography, post mortem assessments and chemical species analysis.

(h) Numerous variables may be considered to characterize the actual event. These variables include temperature, pressure, heating rate, temperature rate, voltage drop, total energy release, gas generation, combustion effects, mass loss and the overall length of the runaway event.

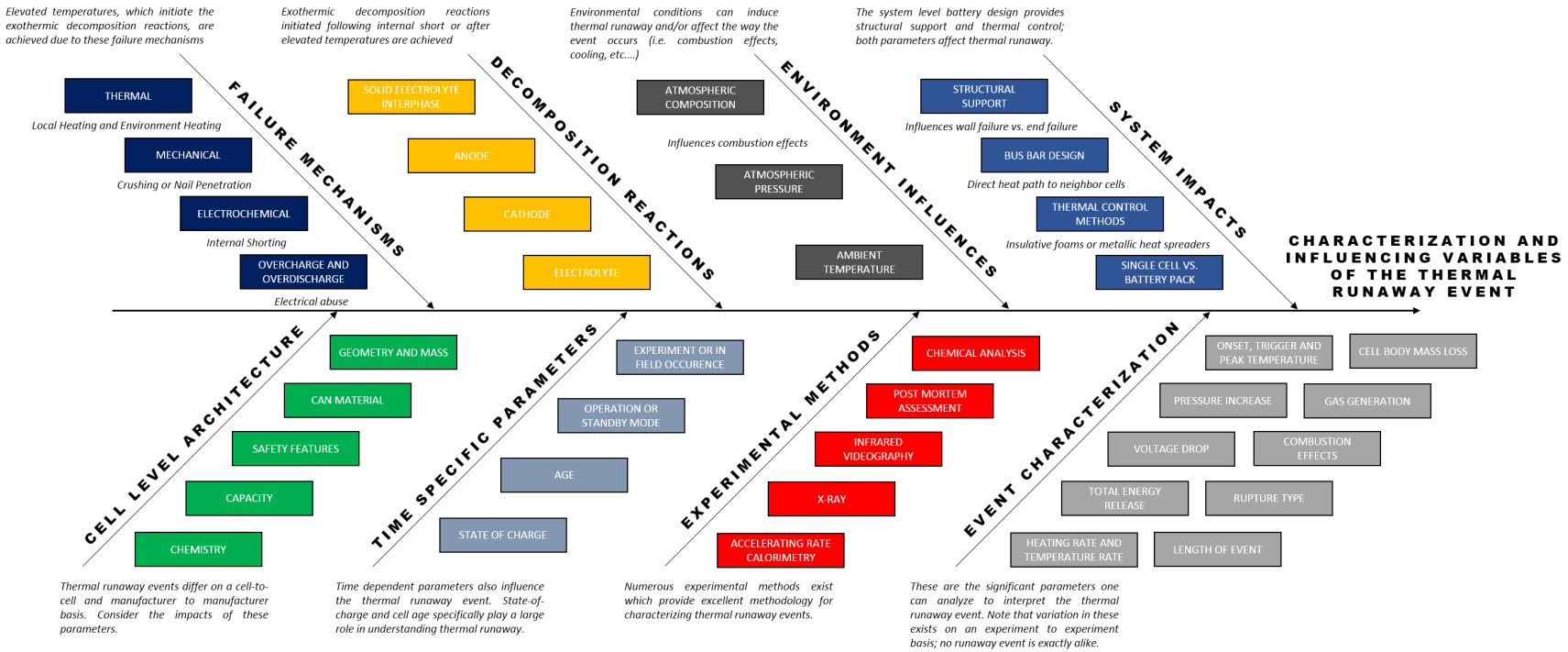

Figure 6-1 **Fishbone diagram describing the characterization and influencing variables of the thermal runaway event with the following primary categories: (a) failure mechanims, (b) decomposition reactions, (c) environment influences, (d) system impacts, (e) cell level architecture, (f) time specific parameters, (g) experimental methods and (h) event characterization.**

6.4 Future Work

Two aspects of the work described by this dissertation are in focus for future work. First, the Thermal Desktop analysis techniques seeks final improvements to (1) further reduce necessary user input in the analysis technique by implementing logic which allows Thermal Desktop to calculate voltage (and subsequently the updated heat load) throughout operations and (2) incorporate accurate thermal runaway logic into the Thermal Desktop simulation which correctly represents the total energy release and approximate distribution of said energy. The second aspect of future work focuses on determining the safety improvements to the Li-ion battery when incorporating a solid polymer electrolyte.

6.4.1 Thermal Desktop Model Improvement: Simulation of Charge and Discharge

The Thermal Desktop model lacks the ability to solve for state-of-charge or depth-of-discharge, and subsequently working voltage, alongside the thermal calculation; this requires user input of voltage arrays based on test data. Implementation of logic statements, which reflect available accurate models of battery electrochemical processes, will allow the simulation to calculate state-of-charge or depth-of-discharge and voltage as a function of temperature. With this improvement, the Thermal Desktop model could accurately simulate Li-ion battery electrical performance and the resulting internal heating rates as a function of the thermal radiation driven orbital environment.

Another method to accomplish the task would be to test the Li-ion battery assembly throughout a range of thermal environments. Voltage vs. time arrays would be constructed for each temperature considered. These arrays are then combined into bivariate arrays that are a function of state-of-charge or depth-of-discharge and temperature. Similar logic as discussed for Chapter III and Chapter IV would update the heat load as a function of the

bivariate arrays. Though the simulation would still be a function of user input for electrical calculations, the improved analysis would accurately determine the influence of the orbital environment on the local heating rate.

6.4.2 Thermal Desktop Model Improvement: Thermal Runaway Simulations

Thermal runaway logic is in development to improve the Thermal Desktop technique's ability to support safe Li-ion battery design. Two options are available: (1) use the Thermal Desktop differential equation solver (DIFFEQ) to solve the thermal runaway mechanism ODEs described in Chapter V or (2) create logic statements that induce a heat load on the jellyroll for a short time period if a user defined "trigger" temperature is achieved.

Challenges exist for Option 1 because the differential equation solver with Thermal Desktop is not equipped to handle the Arrhenius (exponential) terms associated with thermal runaway mechanisms. Re-calculation of timestep per iteration leads to an increasingly small timestep that eventually crashes the model. Also, note that the large number of parameters requiring manipulation to fit the temperature profile of the simulation to test data (recall Table 5-2) may indicate that this type of thermal runaway simulation is impractical for orbital analysis.

Option 2 is feasible by instituting logic statements defining an applied heat load that is only induced if a certain trigger temperature is achieved. The total heat load and the length of time the heat load is applied are the primary considerations. Logic should also include statements to prevent the event from happening again (i.e. when the cell cools off to the trigger temperature after the first thermal runaway event).

As a demonstration, a uniform logic statement is applied to control thermal runaway for twelve 18650-format Li-ion cells. The parameters defined a 10-second release of 3500 W

if a jellyroll achieves a trigger temperature of 135 °C. 35 W heater power is applied to an interior cell to induce runaway. The intent of the example is to demonstrate single cell thermal runaway and to show the code functioning for cell-to-cell propagation. The visibility of the cell cans is turned off and only the jellyroll materials are visible. Note that the simulation only includes the cells (no interstitial materials). Heat transfers to the neighbor cells and to the environment via radiation only. Figure 6-2 displays the results of the demonstration.

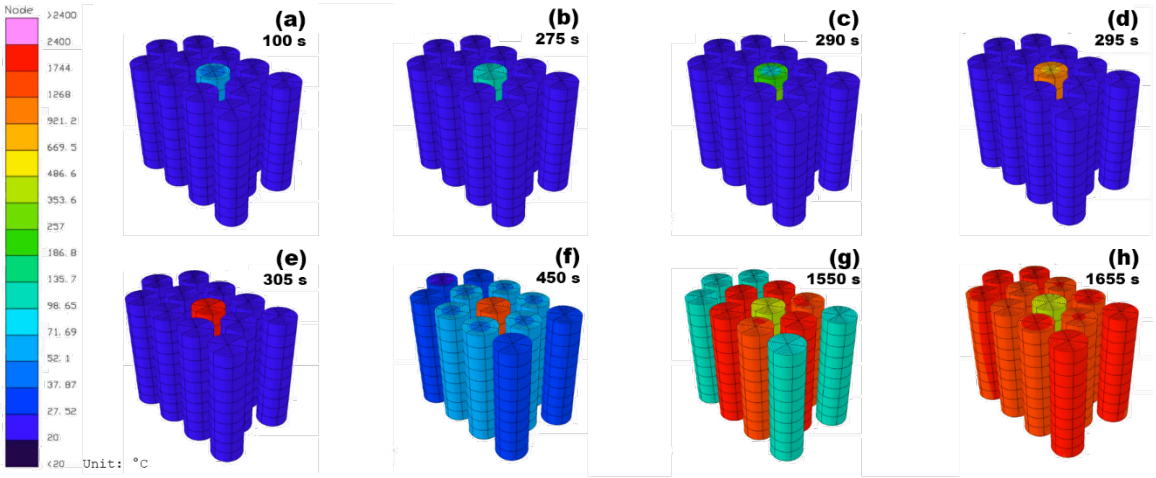

Figure 6-2 **Image displays twelve 18650 format Li-ion cells. The first cell triggers after approximately 100 s and the energy propagates and causes each immediate neighbor cell to trigger after approximately 1550 s.**

This method may prove more practical for Li-ion battery design purposes with respect to orbital analysis as the thermal runaway logic statements are able to run concurrently with the local heat generation logic without causing time-step problems. However, with utilization of this method, all insight into the decomposition of the cell materials is lost.

6.4.3 Safety Characteristics Associated with Solid Polymer Electrolyte

The results of Chapter V identify that the total energy release associated with electrolyte material is minimal. This does not mean that Li-ion battery safety cannot be improved with

respect to the electrolyte. Most Li-ion cells utilize an organic liquid electrolyte, which is highly toxic, flammable and can cause harm. As a cell approaches thermal runaway, the electrolyte boils and eventually vaporizes; the chemicals released during this process are also toxic. Understanding the vaporization of the liquid electrolyte is also compounded when considering combustion effects. The result of this in combination with other hot ejecta materials requires designers to include venting systems or similar safety features to prevent harm should a thermal runaway event occur. Solid polymer electrolyte (SPE) may provide enhanced safety characteristics for Li-ion batteries.

Charge and discharge performance for a freshly constructed coin cell are displayed with Figure 6-3. The active cathode material is $LiCoO_2$ and the anode is graphite. A solid polymer electrolyte consisting primarily of polyethylene oxide (PEO) is used here in the place of a traditional organic liquid electrolyte. The solid electrolyte consists of 65% kMw PEO, 22% kMw PEO and 13% lithium perchlorate ($LiClO_4$). Each of the coin cell components are cut to 1 cm^2 pieces.

The new cell charges to a maximum voltage of 4.2 V and discharges for approximately 9.7 hours with a constant current of 0.01 mA. The cell discussed her maintains a capacity per surface area of 0.097 mAh cm^{-2} which falls in the overall expected range of 0.16 mAh cm^{-2} to 0.2 mAh cm^{-2}. With a mass of 0.00293 kg, the specific energy is 0.319 Wh kg^{-1}. This specific energy is lower than other Li-ion cells, but this is due to the increased mass and internal resistance associated with the utilization of a solid polymer electrolyte.

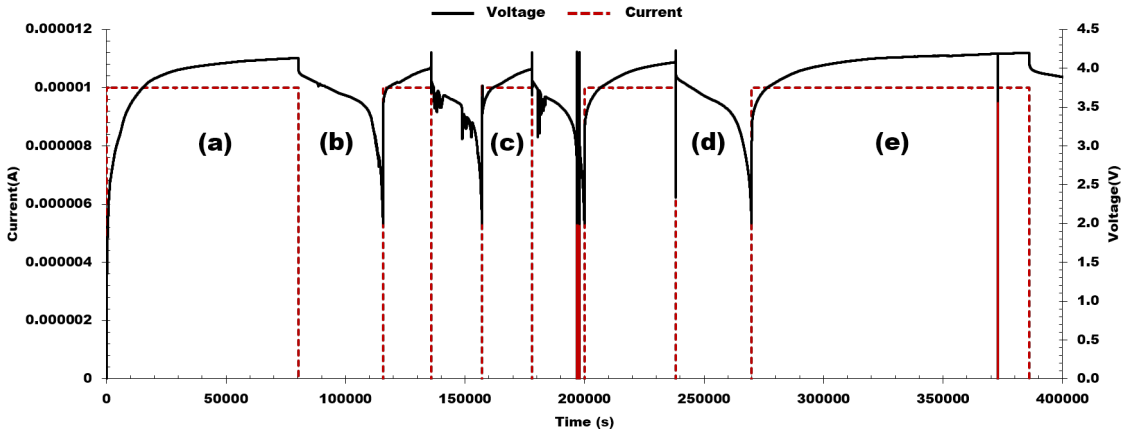

Figure 6-3 The image displays cycle results for a SPE $LiCoO_2$ Li-ion coin cell. The following are demonstrated: (a) the first charge, (b) the first discharge, (c) a period of stabilization, (d) another discharge and (e) final charge.

With a solid polymer electrolyte, possibly consisting primarily of combinations of PEO and $LiClO_4$ as discussed here, the safety of the battery is improved by removing the organic liquid electrolyte. This would also remove the possibility of the vaporized electrolyte influencing the combustion behavior of the runaway event. Questions pertaining to thermal runaway and solid polymer electrolyte should be addressed such as:

- Can we improve the Li-ion battery safety characteristics because toxic gases are not released during thermal runaway?
- Can we improve the Li-ion battery by reducing the amount of mass loss and ejected material that is typically associated with the electrolyte?
- What is the effect of solid polymer electrolyte, if any, on the combustion behavior associated with thermal runaway?
- Can we improve the models by Richard and Dahn, Hatchard et al. and Kim et al. [72, 78, 79, 85] by developing the models defining the thermal runaway behavior of solid polymer electrolyte?

Other benefits are also associated with solid polymer electrolyte such as (a) there is not a performance reducing SEI layer and (b) the physical nature of the solid polymer electrolyte reduces the risks of internal shorting by preventing the electrodes from touching. Some disadvantages are also associated with the solid polymer electrolyte such as higher internal resistance, lower specific capacity and interface challenges. Continued progress will help determine if the safety features associated with solid polymer electrolyte outweigh the relevant disadvantages.

References

1 Jacobson, M. Z. & Delucchi, M. A. "Providing all Global Energy with Wind, Water, and Solar Power, Part I: Technologies, Energy Resources, Quantities and Areas of Infrastructure, and Materials". *Energy Policy* **39**, 1154-1169, (2011).

2 Pistoia, G. Lithium Ion Batteries: Advances and Applications. (Elsevier, 2014).

3 Franco, A. Rechargeable Lithium Batteries: From Fundamentals to Applications. (Woodhead Publishing, 2015).

4 Jha, A. R. Next-Generation Batteries and Fuel Cells for Commercial, Military, and Space Applications. (CRC Press, 2012).

5 Winter, M. & Brodd, R. "What are Batteries, Fuel Cells, and Supercapacitors?". *Chemical Reviews* **104**, 4245-4270, (2004).

6 Chalk, S. G. & Miller, J. "Key Challenges and Recent Progress in Batteries, Fuel Cells, and Hydrogen Storage for Clean Energy Systems". *Journal of Power Sources* **159**, 73-80, (2006).

7 Groger, O., Gasteiger, H. A. & Suchsland, J. P. "Review-Electromobility: Batteries or Fuel Cells". *Journal of The Electrochemical Society* **163**, A2605-A2622, (2015).

8 Ragone, D. V. "Review of Battery Systems for Electrically Powered Vehicles". *Society of Automotive Engineers International*, (1968).

9 Lee, S. C. & Jung, W. Y. "Analogical Understanding of the Ragone plot and a New Categorization of Energy Devices". *Energy Procedia* **88**, 526-530, (2016).

10 Griffin, M. D. & French, J. R. Space Vehicle Design. (AIAA, 1991).

11 McCleskey, C. M., Zapata, E. & Rhodes, R. E. "An Analysis and Review of Measures and Relationships in Space Transportation Affordability". (2014).

12 Fellner, J. P., Loeber, G. J., Vukson, S. P. & Riepenhoff, C. A. "Lithium-Ion Testing for Spacecraft Applications". *Journal of Power Sources* **119-121**, 911-913, (2003).

13 Sone, Y., Ooto, H., Yamamoto, M., Eguro, T., Sakai, S., Yoshida, T., Takahashi, K., Uno, M., Hirose, K., Tajima, M. & Kawaguchi, J. I. "Storage of a Lithium-Ion Secondary Battery Under Micro-Gravity Conditions". *Journal of Power Sources* **181**, 149-154, (2008).

14 Uno, M., Ogawa, K., Takeda, Y., Sone, Y., Tanaka, K., Mita, M. & Saito, H. "Development and On-Orbit Operation of Lithium-Ion Pouch Battery for Small Scientific Satellite “REIMEI”". *Journal of Power Sources* **196**, 8755-8763, (2011).

15 Liu, D., Wang, H., Peng, Y., Xie, W. & Liao, H. "Satellite Lithium-Ion Battery Remaining Cycle Life Prediction with Novel Indirect Health Indicator Extraction". *Energies* **6**, 3654-3668, (2013).

16 Sone, Y. "Charge/Discharge Performance of Lithium-Ion Secondary Cells Under Microgravity Conditions: Lessons Learned from Operation of Interplanetary Spacecraft Hayabusa". *Electrochimica Acta* **100**, 358-363, (2013).

17 Marsh, R. A., Vukson, S. P., Surampudi, S., Ratnakumar, B. V., Smart, M. C., Manzo, M. & Dalton, P. J. "Li Ion Batteries for Space Applications". *Journal of Power Sources* **97-98**, 25-27, (2011).

18 Cutchen, J. T., Baldwin, A. R. & Levy, S. C. "A Preliminary Evaluation of Lithium Batteries for Extended Life Continuous Operation Applications". *Journal of Power Sources* **14**, 167-172, (1985).

19 Armand, M. & Tarascon, J. M. "Building Better Batteries". *Nature* **451**, 652-657, (2008).

20 Verma, P., Maire, P. & Novák, P. "A Review of the Features and Analyses of the Solid Electrolyte Interphase in Li-ion Batteries". *Electrochimica Acta* **55**, 6332-6341, (2010).

21 Kraytsberg, A. & Ein-Eli, Y. "Higher, Stronger, Better... A Review of 5 Volt Cathode Materials for Advanced Lithium-Ion Batteries". *Advanced Energy Materials* **2**, 922-939, (2012).

22 Darcy, E. "COTS Lithium Ion Cells - How Rugged are New Designs". *NASA Aerospace Battery Workshop.* (2012).

23 Darcy, E. "Thermal Runaway Severity Reduction Assessment for EVA Lithium Ion Batteries". *NASA Aerospace Battery Workshop.* (2014).

24 Darcy, E. "Challenges with Achieving >180 Wh/kg Lithium Ion Battery Modules that Don't Propagate Thermal Runaway or Emit Flames-Sparks". *The Battery Conference.* (2015).

25 Walker, W., Yayathi, S., Shaw, J. & Ardebili, H. "Thermo-Electrochemical Evaluation of Lithium-Ion Batteries for Space Applications". *Journal of Power Sources* **298**, 217-227, (2015).

26 Bandhauer, T. M., Garimella, S. & Fuller, T. F. "A Critical Review of Thermal Issues in Lithium-Ion Batteries". *Journal of The Electrochemical Society* **158**, R1, (2011).

27 Sherfey, J. M. & Brenner, A. "Electrochemical Calorimetry". *Journal of The Electrochemical Society* **105**, 665-672, (1958).

28 Bernardi, D., Pawlikowski, E. & Newman, J. "A General Energy Balance for Battery Systems". *Journal of The Electrochemical Society* **132**, 5-12, (1985).

29 Chen, S. C., Wan, C. C. & Wang, Y. Y. "Thermal Analysis of Lithium-Ion Batteries". *Journal of Power Sources* **140**, 111-124, (2005).

30 Walker, W. & Ardebili, H. "Thermo-Electrochemical Analysis of Lithium Ion Batteries for Space Applications Using Thermal Desktop". *Journal of Power Sources* **269**, 486-497, (2014).

31 Yayathi, S., Walker, W., Doughty, D. H. & Ardebili, H. "Energy Distributions Exhibited during Thermal Runaway of Commercial Lithium Ion Batteries used for Human Spaceflight Applications". *Journal of Power Sources*, (2016).

32 Gu, W. B. & Wang, C. Y. "Thermal-Electrochemical Modeling of Battery Systems". *Journal of The Electrochemical Society* **147**, 2910-2922, (2000).

33 Nieto, N., Diaz, L., Gastelurrutia, J., Alava, I., Blanco, F., Carlos Ramos, J. & Rivas, A. "Thermal Modeling of Large Format Lithium-Ion Cells". *Journal of The Electrochemical Society* **160**, A212-A217, (2012).

34 Doyle, M. & Newman, J. "Modeling the Performance of Rechargeable Lithium-Based Cells - Design Correlations for Limiting Cases". *Journal of Power Sources* **54**, 46-51, (1995).

35 Doyle, M. & Newman, J. "Comparison of Modeling Predictions with Experimental Data from Plastic Lithium Ion Cells". *Journal of The Electrochemical Society* **143**, 1890-1903, (1996).

36 Newman, J., Thomas, K. E., Hafezi, H. & Wheeler, D. R. "Modeling of Lithium-Ion Batteries". *Journal of Power Sources* **119-121**, 838-843, (2003).

37 Newman, J. & Tiedemann, W. "Porous-Electrode Theory with Battery Applications". *AiChE Journal* **21**, 25-41, (1975).

38 Gilmore, D. Satellite Thermal Control Handbook. (The Aerospace Corporation Press, 1994).

39 Rao, L. & Newman, J. "Heat-Generation Rate and General Energy Balance for Insertion Battery Systems". *Journal of The Electrochemical Society* **144**, 2697-2704, (1997).

40 Chen, Y. & Evans, J. W. "Heat Transfer Phenomena in Lithium-Polymer-Electrolyte Batteries for Electric Vehicle Application". *Journal of The Electrochemical Society* **140**, 1833-1838, (1993).

41 Chen, Y. & Evans, J. W. "Three-Dimensional Thermal Modeling of Lithium-Polymer Batteries under Galvenostatic Discharge and Dynamic Power Profile". *Journal of The Electrochemical Society* **141**, (1994).

42 Chen, Y. & Evans, J. W. "Thermal Analysis of Lithium-Ion Batteries". *Journal of The Electrochemical Society* **143**, 2708-2712, (1996).

43 Baudry, P., Neri, M., Gueguen, M. & Lonchampt, G. "Electro-Thermal Modeling of Thermal Polymer Lithium Batteries for Starting Period and Pulse Power". *Journal of Power Sources* **54**, 393-396, (1995).

44 Hallaj, S. A., Maleki, H., Hong, J. S. & Selman, J. R. "Thermal Modeling and Design Considerations of Lithium-Ion Batteries". *Journal of Power Sources* **83**, 1-8, (1999).

45 Mills, A. & Al-Hallaj, S. "Simulation of Passive Thermal Management System for Lithium-Ion Battery Packs". *Journal of Power Sources* **141**, 307-315, (2005).

46 Cai, L. & White, R. E. "Mathematical Modeling of a Lithium Ion Battery with Thermal Effects in COMSOL Inc. Multiphysics (MP) Software". *Journal of Power Sources* **196**, 5985-5989, (2011).

47 Kim, U. S., Yi, J., Shin, C. B., Han, T. & Park, S. "Modelling the Thermal Behaviour of a Lithium-Ion Battery during Charge". *Journal of Power Sources* **196**, 5115-5121, (2011).

48 Jeon, D. H. & Baek, S. M. "Thermal Modeling of Cylindrical Lithium Ion Battery during Discharge Cycle". *Energy Conversion and Management* **52**, 2973-2981, (2011).

49 Chacko, S. & Chung, Y. M. "Thermal Modelling of Li-Ion Polymer Battery for Electric Vehicle Drive Cycles". *Journal of Power Sources* **213**, 296-303, (2012).

50 Sun, H., Wang, X., Tossan, B. & Dixon, R. "Three-Dimensional Thermal Modeling of a Lithium-Ion Battery Pack". *Journal of Power Sources* **206**, 349-356, (2012).

51 Awarke, A., Jaeger, M., Oezdemir, O. & Pischinger, S. "Thermal Analysis of a Li-Ion Battery Module Under Realistic EV Operating Conditions". *International Journal of Energy Research* **37**, 617-630, (2013).

52 Lee, K.-J., Smith, K., Pesaran, A. & Kim, G.-H. "Three Dimensional Thermal-, Electrical-, and Electrochemical-Coupled Model for Cylindrical Wound Large Format Lithium-Ion Batteries". *Journal of Power Sources* **241**, 20-32, (2013).

53 Ye, Y., Saw, L. H., Shi, Y., Somasundaram, K. & Tay, A. A. O. "Effect of Thermal Contact Resistances on Fast Charging of Large Format Lithium Ion Batteries". *Electrochimica Acta* **134**, 327-337, (2014).

54 Tie, S. F. & Tan, C., W. "A Review of Energy Sources and Energy Management System in Electric Vehicles". *Renewable and Sustainable Energy Reviews* **20**, 82-102, (2013).

55 Damblanc, G., Hartridge, S., Spotnitz, R. & Imaichi, K. *Society of Automotive Engineers of Japan Annual Congress* (2011).

56 USAF. Vol. FSE1810 (AMSC, 1999).

57 *Boston Power Swing 5300 Data Sheet*. (Boston Power, 2015).

58 Wang, K., Li, J., Cui, Z., Wang, N., Sun, Q. & Cheng, L. "Operations of the Thermal Control System for Alpha Magnetic Spectrometer Electronics Following the Beta Angle of the International Space Station". *Nuclear Instruments and Methods in Physics Research Section A: Accelerators, Spectrometers, Detectors and Associated Equipment* **11**, 235-244, (2014).

59 Wang, Q., Ping, P., Zhao, X., Chu, G., Sun, J. & Chen, C. "Thermal Runaway Caused Fire and Explosion of Lithium Ion Battery". *Journal of Power Sources* **208**, 210-224, (2012).

60 Boeing 787 Battery Report. (National Transportation and Safety Board, Boston, Massachusetts, 2013).

61 Russell, S. P., Elder, M. A., Williams, A. G. & Dembeck, J. *American Institute of Aeronautics and Astronautics Space 2010* (AIAA, Anaheim, Ca, 2010).

62 *Boston Power Swing 5300 Material Safety Data Sheet*. (Boston Power, 2015).

63 *Determining the Specific Heat Capacity of a Battery Pack: Illustrative Example and Description Method*. (Thermal Hazard Technology, 2015).

64 *Samsung 18650 Material Safety Datasheet*. (Samsung, 2015).

65 *Samsung 18650 Data Sheet*. (Samsung, 2015).

66 *Molicel 18650 Safety Data Sheet*. (MoliCel, 2015).

67 *MoliCel 18650 Datasheet*. (MoliCel, 2015).

68 Lopez, C. F., Jeevarajan, J. A. & Mukherjee, P. P. "Experimental Analysis of Thermal Runaway and Propagation in Lithium-Ion Battery Modules". *Journal of The Electrochemical Society* **162**, A1905-A1915, (2015).

69 Balakrishnan, P. G., Ramesh, R. & Prem Kumar, T. "Safety Mechanisms in Lithium-Ion Batteries". *Journal of Power Sources* **155**, 401-414, (2006).

70 Lisbona, D. & Snee, T. "A Review of Hazards Associated with Primary Lithium and Lithium-Ion Batteries". *Process Safety and Environmental Protection* **89**, 434-442, (2011).

71 Yuan, Q., Zhao, F., Wang, W., Zhao, Y., Liang, Z. & Yan, D. "Overcharge Failure Investigation of Lithium-Ion Batteries". *Electrochimica Acta* **178**, 682-688, (2015).

72 Hatchard, T. D., MacNeil, D. D., Basu, A. & Dahn, J. R. "Thermal Model of Cylindrical and Prismatic Lithium-Ion Cells". *Journal of The Electrochemical Society* **148**, A755, (2001).

73 Spotnitz, R. & Franklin, J. "Abuse Behavior of High-Power, Lithium-Ion Cells". *Journal of Power Sources* **113**, 81-100, (2003).

74 Ohsaki, T., Kishi, T., Kuboki, T., Takami, N., Shimura, N., Sato, Y., Sekino, M. & Satoh, A. "Overcharge Reaction of Lithium-Ion Batteries". *Journal of Power Sources* **146**, 97-100, (2005).

75 Finegan, D. P., Scheel, M., Robinson, J. B., Tjaden, B., Hunt, I., Mason, T. J., Millichamp, J., Di Michiel, M., Offer, G. J., Hinds, G., Brett, D. J. & Shearing, P.

R. "In-Operando High-Speed Tomography of Lithium-Ion Batteries During Thermal Runaway". *Nature Communications* **6**, 6924, (2015).

76 Hatchard, T. D., Trussler, S. & Dahn, J. R. "Building a “Smart Nail” for Penetration Tests on Li-Ion Cells". *Journal of Power Sources* **247**, 821-823, (2014).

77 Feng, X., Sun, J., Ouyang, M., Wang, F., He, X., Lu, L. & Peng, H. "Characterization of Penetration Induced Thermal Runaway Propagation Process Within a Large Format Lithium ion Battery Module". *Journal of Power Sources* **275**, 261-273, (2015).

78 Richard, M. N. & Dahn, J. R. "Accelerating Rate Calorimetry Study on the Thermal Stability of Lithium Intercalated Graphite in Electrolyte - I. Experimental". *Journal of The Electrochemical Society* **146**, 2068-2077, (1999).

79 Richard, M. N. & Dahn, J. R. "Accelerating Rate Calorimetry Study on the Thermal Stability of Lithium Intercalated Graphite in Electrolyte - II. Modeling the Results and Predicting Differential Scanning Calorimetry Curves". *Journal of The Electrochemical Society* **146**, 2078-2084, (1999).

80 Gnanaraj, J. S., Zinigrad, E., Asraf, L., Gottlieb, H. E., Sprecher, M. & Aurbach, D. "The Use of Accelerating Rate Calorimetry (ARC) for the Study of Thermal Reactions of Li-Ion Battery Electrolyte Solutions". *Journal of Power Sources* **119**, 794-798, (2003).

81 Roth, E. P. & Doughty, D. H. "Thermal Abuse Performance of High-Power 18650 Li-Ion Cells". *Journal of Power Sources* **128**, 308-318, (2004).

82 Roth, E. P., Crafts, C. C., Doughty, D. H. & McBreen, J. Advanced Technology Development Program for Lithium Ion Batteries - Thermal Abuse Performance of

18650 Lithium Ion Cells. (Sandia National Laboratories, Albuquerque, New Mexico, 2004).

83 Doughty, D. H., Roth, E. P., Crafts, C. C., Nagasubramanian, G., Henriksen, G. & Amine, K. "Effects of Additives on Thermal Stability of Li Ion Cells". *Journal of Power Sources* **146**, 116-120, (2005).

84 Abraham, D. P., Roth, E. P., Kostecki, R., McCarthy, K., MacLaren, S. & Doughty, D. H. "Diagnostic Examination of Thermally Abused High-Power Lithium-Ion Cells". *Journal of Power Sources* **161**, 648-657, (2006).

85 Kim, G.-H., Pesaran, A. & Spotnitz, R. "A Three-Dimensional Thermal Abuse Model for Lithium-Ion Cells". *Journal of Power Sources* **170**, 476-489, (2007).

86 Spotnitz, R. M., Weaver, J., Yeduvaka, G., Doughty, D. H. & Roth, E. P. "Simulation of Abuse Tolerance of Lithium-Ion Battery Packs". *Journal of Power Sources* **163**, 1080-1086, (2007).

87 Jhu, C. Y., Wang, Y. W., Wen, C. Y., Chiang, C. C. & Shu, C. M. "Self-Reactive Rating of Thermal Runaway Hazards on 18650 Lithium-Ion Batteries". *Journal of Thermal Analysis and Calorimetry* **106**, 159-163, (2011).

88 Jhu, C. Y., Wang, Y. W., Shu, C. M., Chang, J. C. & Wu, H. C. "Thermal Explosion Hazards on 18650 Lithium Ion Batteries with a VSP2 Adiabatic Calorimeter". *Journal of Hazardous Materials* **192**, 99-107, (2011).

89 Lu, T.-Y., Chiang, C.-C., Wu, S.-H., Chen, K.-C., Lin, S.-J., Wen, C.-Y. & Shu, C.-M. "Thermal Hazard Evaluations of 18650 Lithium-Ion Batteries by an Adiabatic Calorimeter". *Journal of Thermal Analysis and Calorimetry* **114**, 1083-1088, (2013).

90 Nagasubramanian, G. & Fenton, K. "Reducing Li-Ion Safety Hazards Through Use of Non-Flammable Solvents and Recent Work at Sandia National Laboratories". *Electrochimica Acta* **101**, 3-10, (2013).

91 Feng, X., Sun, J., Ouyang, M., He, X., Lu, L., Han, X., Fang, M. & Peng, H. "Characterization of Large Format Lithium Ion Battery Exposed to Extremely High Temperature". *Journal of Power Sources* **272**, 457-467, (2014).

92 Feng, X., Fang, M., He, X., Ouyang, M., Lu, L., Wang, H. & Zhang, M. "Thermal Runaway Features of Large Format Prismatic Lithium Ion Battery Using Extended Volume Accelerating Rate Calorimetry". *Journal of Power Sources* **255**, 294-301, (2014).

93 Coman, P. T., Rayman, S. & White, R. E. "A 0-D Model of Venting During Thermal Runaway in a 18650 Lithium Cobalt Oxide Lithium Ion Cell". (2015).

94 Coman, P. T., Rayman, S. & White, R. E. "A Lumped Model of Venting During Thermal Runaway in a Cylindrical Lithium Cobalt Oxide Lithium-Ion Cell". *Journal of Power Sources* **307**, 56-62, (2016).

95 Golubkov, A. W., Scheikl, S., Planteu, R., Voitic, G., Wiltsche, H., Stangl, C., Fauler, G., Thaler, A. & Hacker, V. "Thermal Runaway of Commercial 18650 Li-Ion Batteries with LFP and NCA Cathodes – Impact of State of Charge and Overcharge". *Royal Society of Chemistry Advances* **5**, 57171-57186, (2015).

96 *The Phi Correction in Accelerating Rate Calorimetry: Technical Information Note 22*. (Thermal Hazard Technology, 2015).

97 Barnett, B., Sriramulu, S., Stringfellow, R., Ofer, D., Takata, R. & Oh, B. "How to Mitigate/Prevent Safety Incidents in Lithium Ion Cells and Batteries". *26th International Battery Seminar and Exhibit.* (2009).

98 Sriramulu, S. & Stringfellow, R. Internal Short Circuits in Lithium Ion Cells for PHEVs. (TIAX LLC, TIAX LLC, 2014).

99 Doughty, D. H. & Pesaran, A. A. *National Renewable Energy Laboratory* (NREL, 2012).

100 *Thermal Hazard Technology: Accelerating Rate Calorimetry Brochure*. (Thermal Hazard Technology, 2015).

Appendix A1: Boston Power Swing 5300 ARC Data (100%-C)

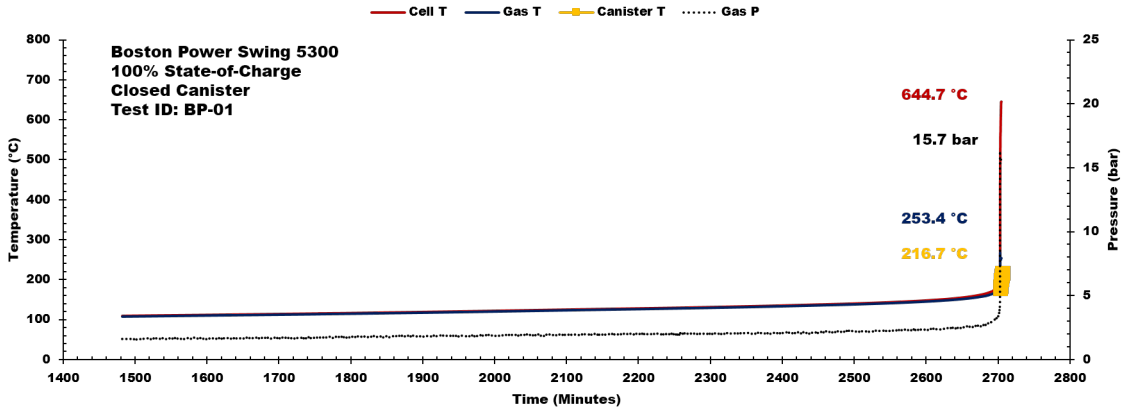

Figure A1-1 BP-5300 ARC data used for energy calculations for the 100% SOC closed canister configuration (BP01). Data presented includes the following: (a) cell temperature, (b) gas temperature, (c) average canister temperature and (d) pressure.

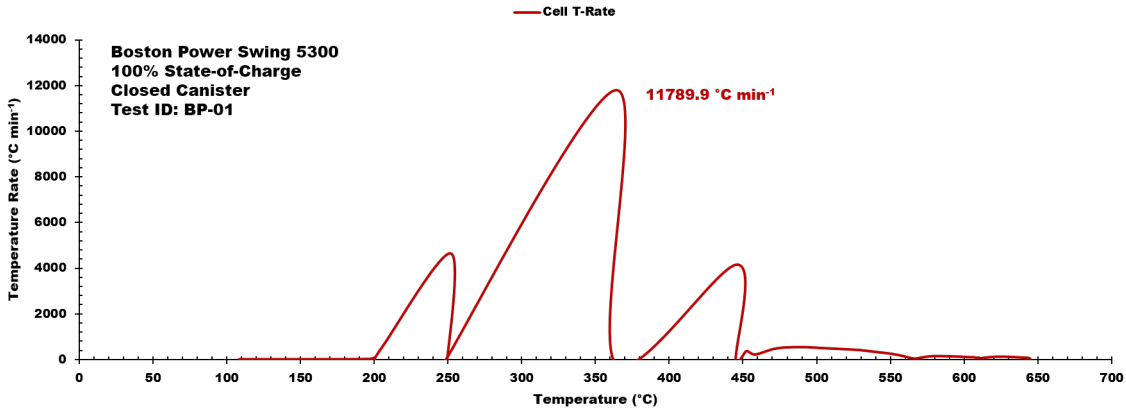

Figure A1-2 BP-5300 ARC data used for energy calculations for the 100% SOC closed canister configuration (BP01). Temp. rate vs temperature profile is displayed.

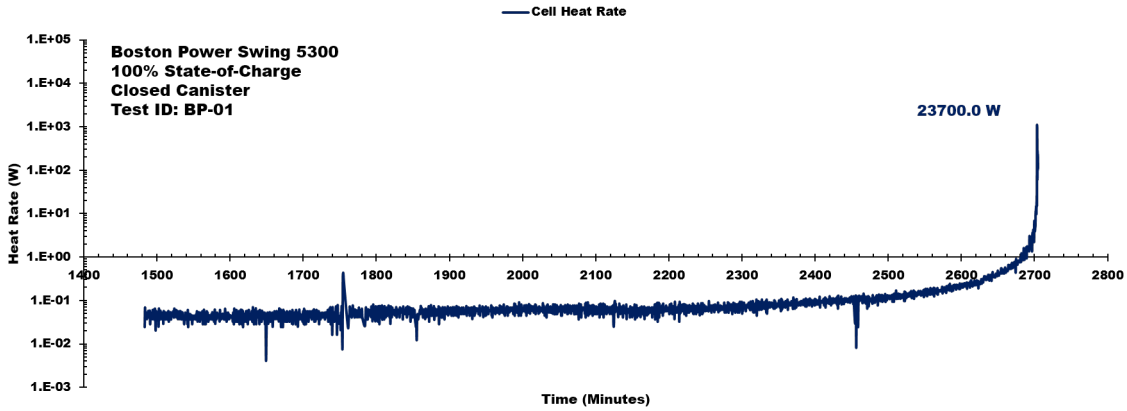

Figure A1-3 BP-5300 ARC data used for energy calculations for the 100% SOC closed canister configuration (BP01). Cell body heat rate profile is displayed.

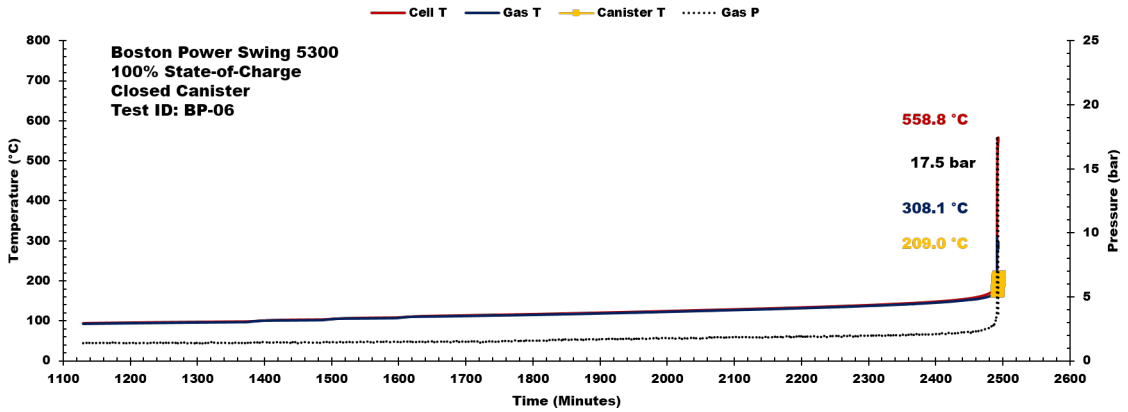

Figure A1-4 BP-5300 ARC data used for energy calculations for the 100% SOC closed canister configuration (BP06). Data presented includes the following: (a) cell temperature, (b) gas temperature, (c) average canister temperature and (d) pressure.

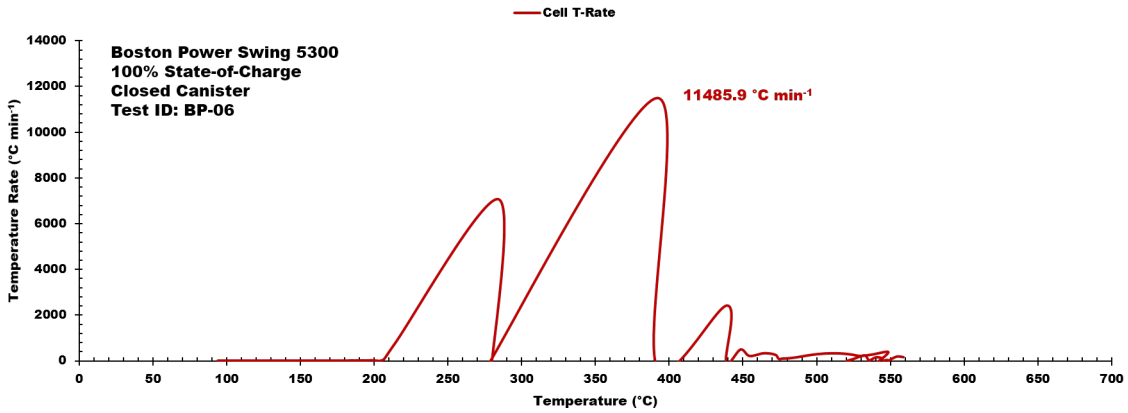

Figure A1-5 BP-5300 ARC data used for energy calculations for the 100% SOC closed canister configuration (BP06). Temp. rate vs temperature profile is displayed.

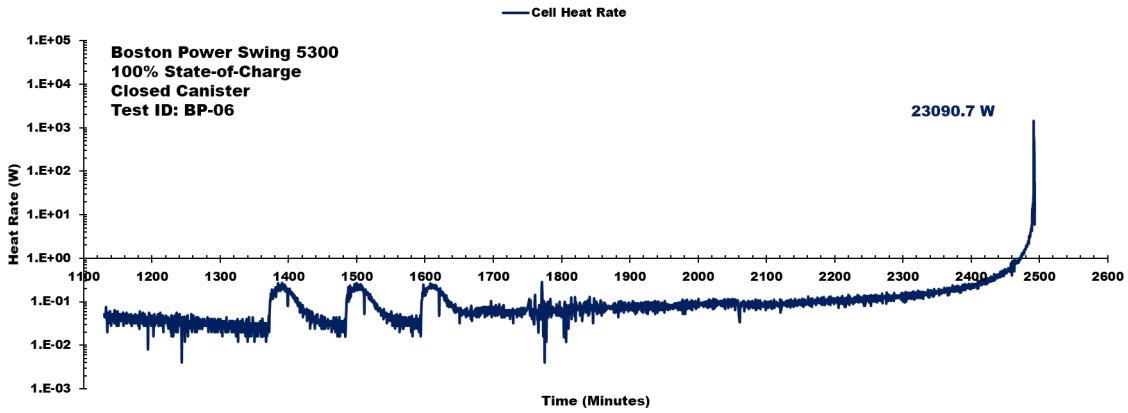

Figure A1-6 BP-5300 ARC data used for energy calculations for the 100% SOC closed canister configuration (BP06). Cell body heat rate profile is displayed.

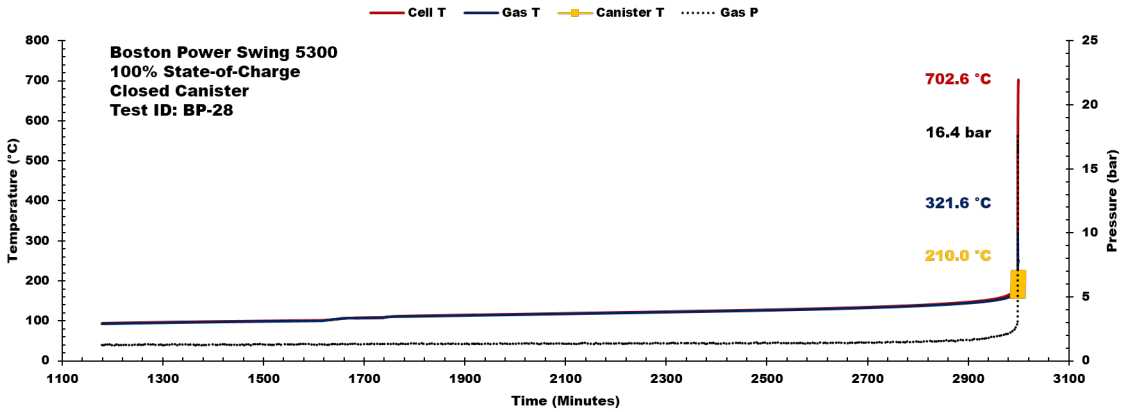

Figure A1-7 BP-5300 ARC data used for energy calculations for the 100% SOC closed canister configuration (BP28). Data presented includes the following: (a) cell temperature, (b) gas temperature, (c) average canister temperature and (d) pressure.

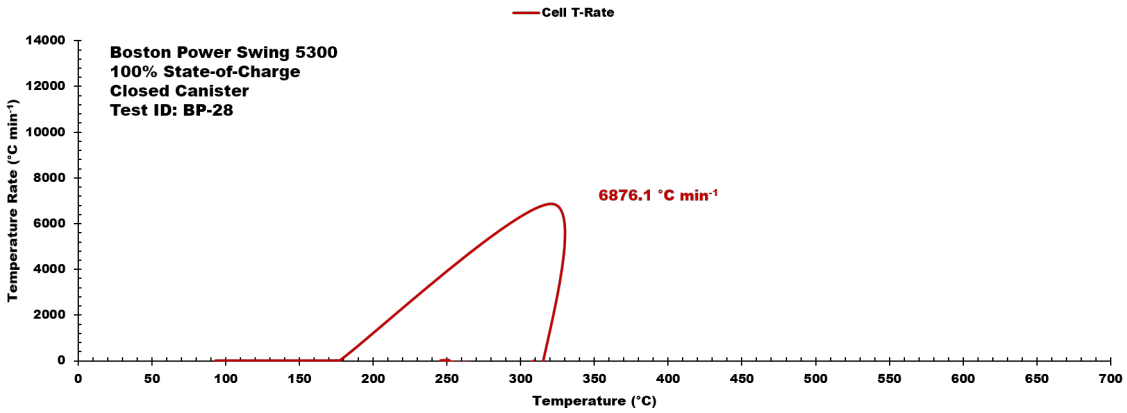

Figure A1-8 BP-5300 ARC data used for energy calculations for the 100% SOC closed canister configuration (BP28). Temp. rate vs temperature profile is displayed.

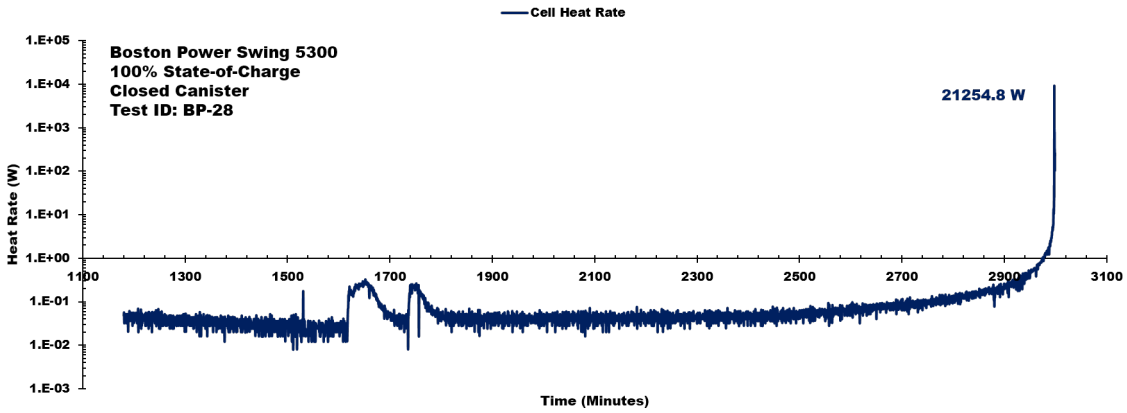

Figure A1-9 BP-5300 ARC data used for energy calculations for the 100% SOC closed canister configuration (BP28). Cell body heat rate profile is displayed.

Appendix A2: Boston Power Swing 5300 ARC Data (50%-C)

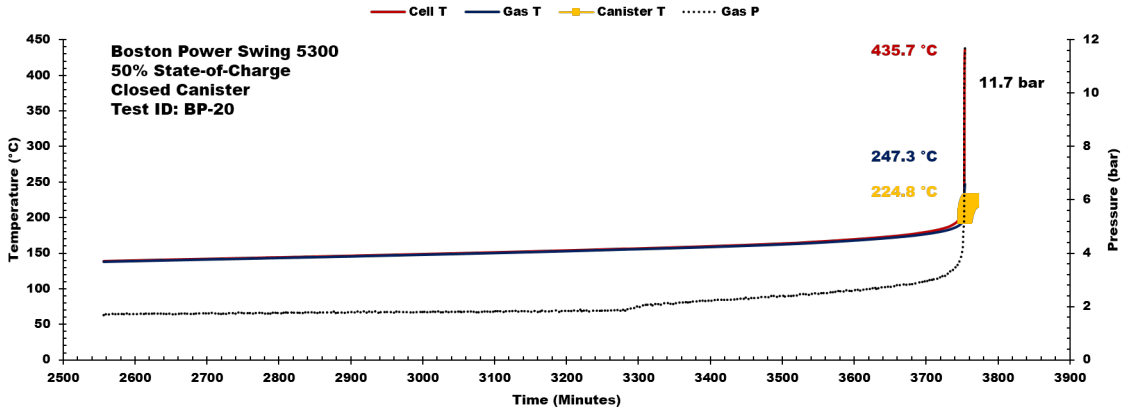

Figure A2-1 BP-5300 ARC data used for energy calculations for the 50% SOC closed canister configuration (BP20). Data presented includes the following: (a) cell temperature, (b) gas temperature, (c) average canister temperature and (d) pressure.

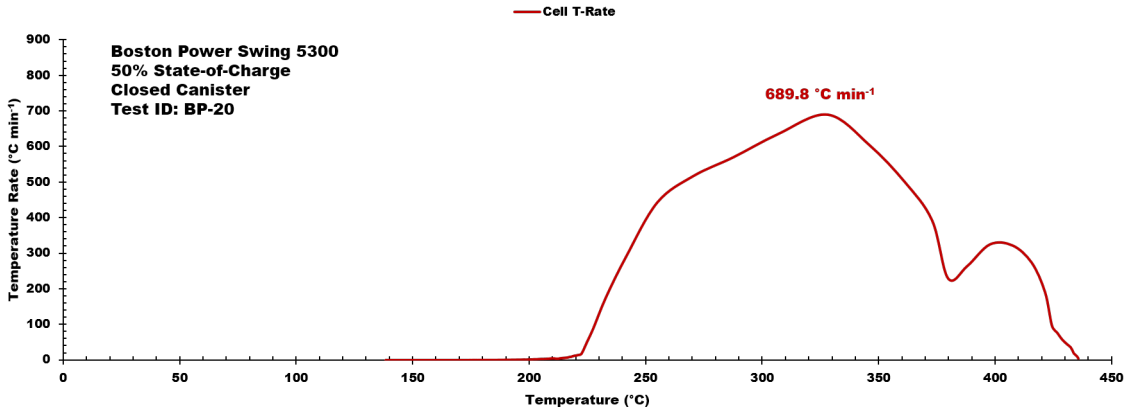

Figure A2-2 BP-5300 ARC data used for energy calculations for the 50% SOC closed canister configuration (BP20). Temp. rate vs. temperature profile is displayed.

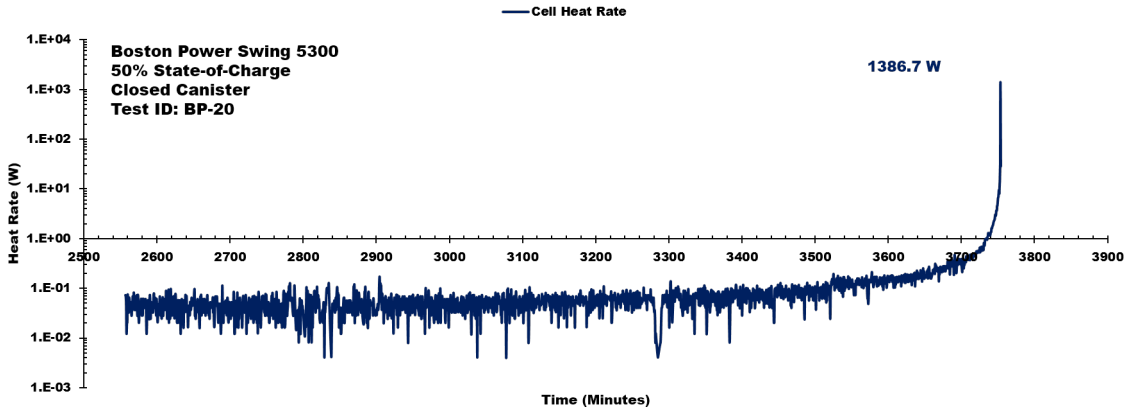

Figure A2-3 BP-5300 ARC data used for energy calculations for the 50% SOC closed canister configuration (BP20). Cell body heat rate profile is displayed.

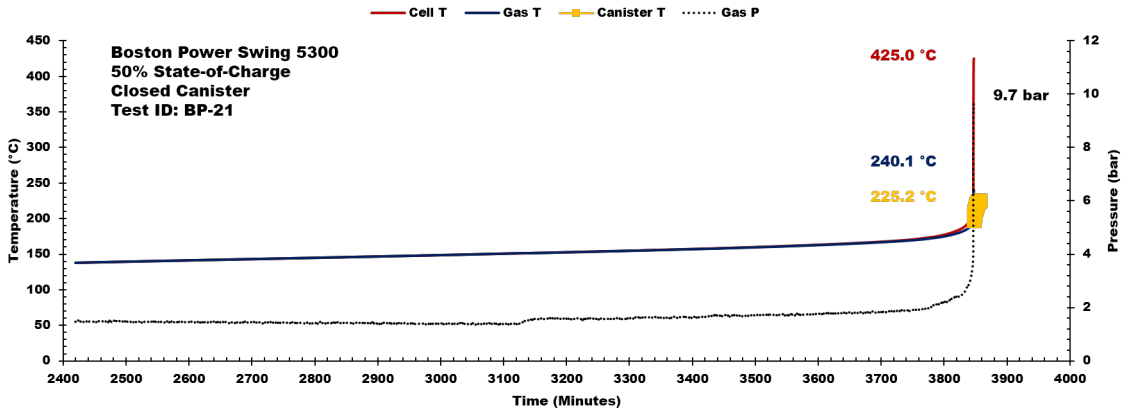

Figure A2-4 BP-5300 ARC data used for energy calculations for the 50% SOC closed canister configuration (BP21). Data presented includes the following: (a) cell temperature, (b) gas temperature, (c) average canister temperature and (d) pressure.

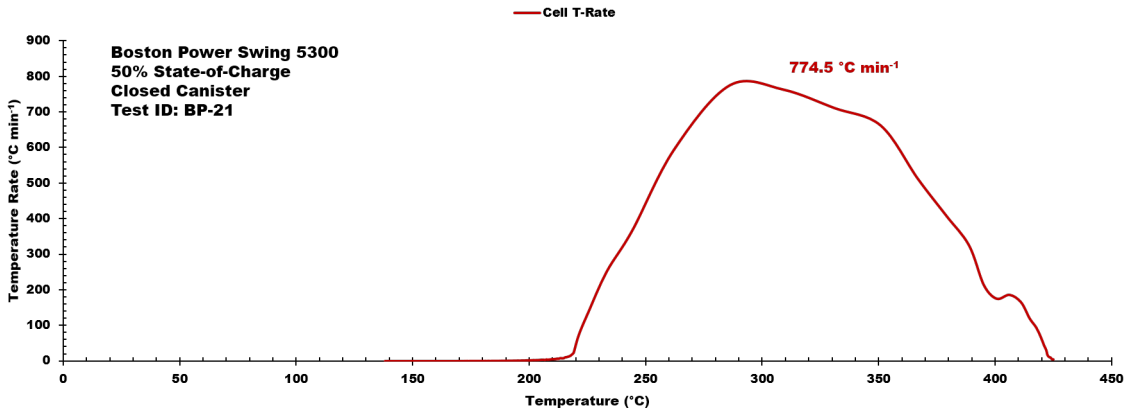

Figure A2-5 BP-5300 ARC data used for energy calculations for the 50% SOC closed canister configuration (BP21). Temp. rate vs. temperature profile is displayed.

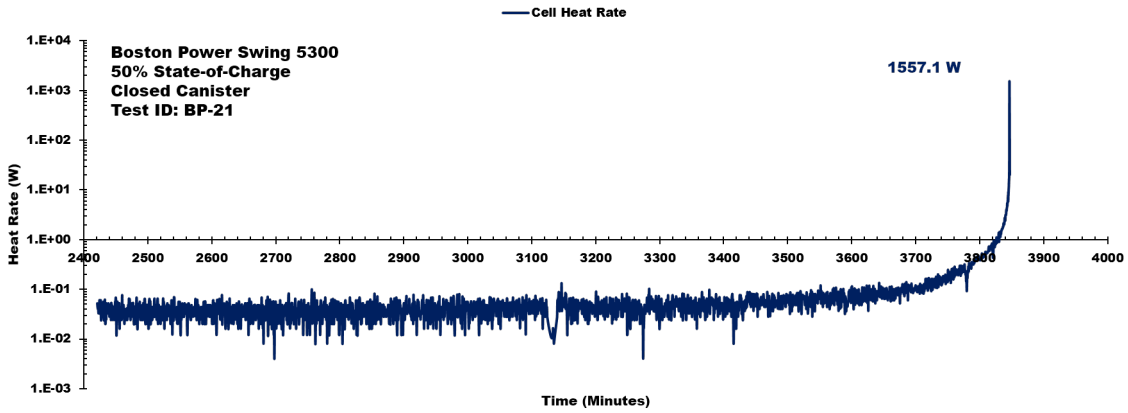

Figure A2-6 BP-5300 ARC data used for energy calculations for the 50% SOC closed canister configuration (BP21). Cell body heat rate profile is displayed.

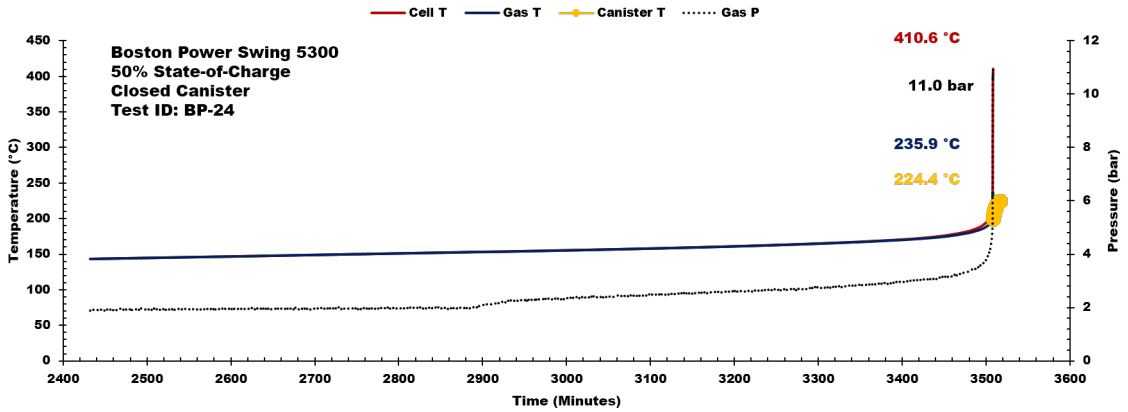

Figure A2-7 BP-5300 ARC data used for energy calculations for the 50% SOC closed canister configuration (BP24). Data presented includes the following: (a) cell temperature, (b) gas temperature, (c) average canister temperature and (d) pressure.

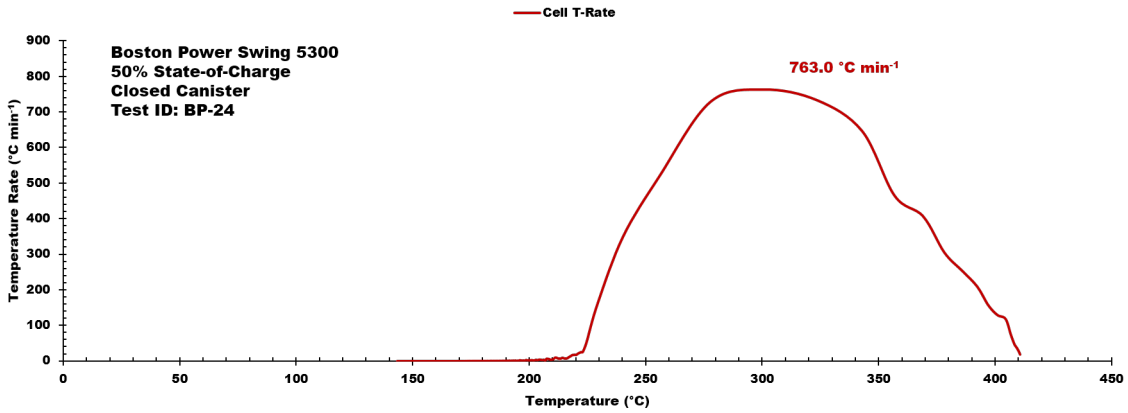

Figure A2-8 BP-5300 ARC data used for energy calculations for the 50% SOC closed canister configuration (BP24). Temp. rate vs. temperature profile is displayed.

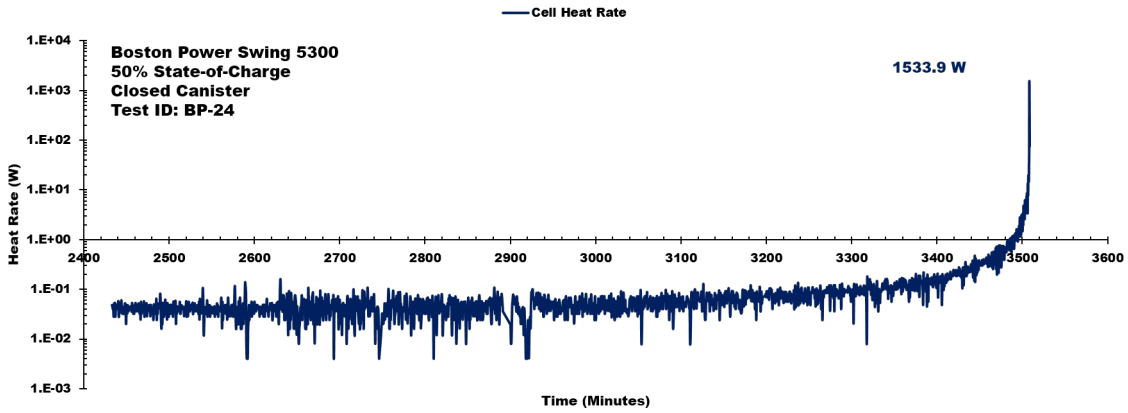

Figure A2-9 BP-5300 ARC data used for energy calculations for the 50% SOC closed canister configuration (BP24). Cell body heat rate profile is displayed.

Appendix A3: Boston Power Swing 5300 ARC Data (100%-O)

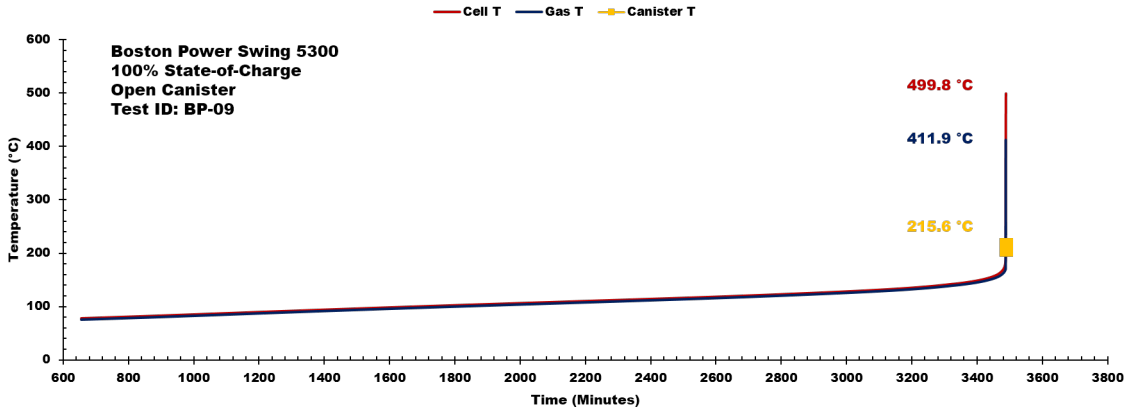

Figure A3-1 BP-5300 ARC data used for energy calculations for the 100% SOC open canister configuration (BP09). Data presented includes the following: (a) cell temperature, (b) gas temperature and (c) average canister temperature.

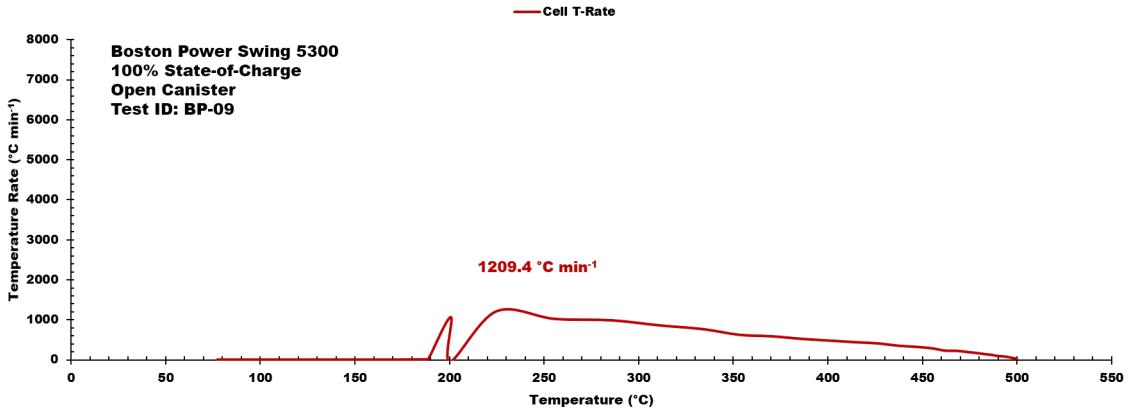

Figure A3-2 BP-5300 ARC data used for energy calculations for the 100% SOC open canister configuration (BP09). Temp. rate vs. temperature profile is displayed.

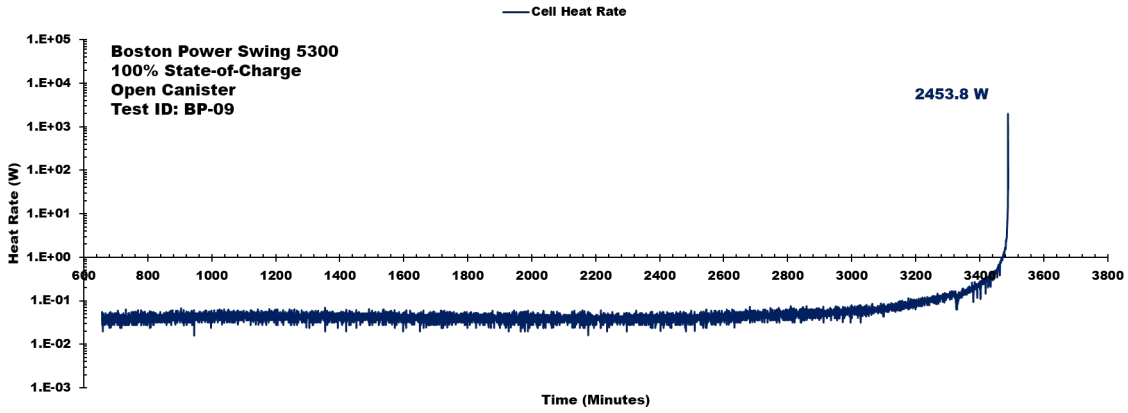

Figure A3-3 BP-5300 ARC data used for energy calculations for the 100% SOC open canister configuration (BP09). Cell body heat rate profile is displayed.

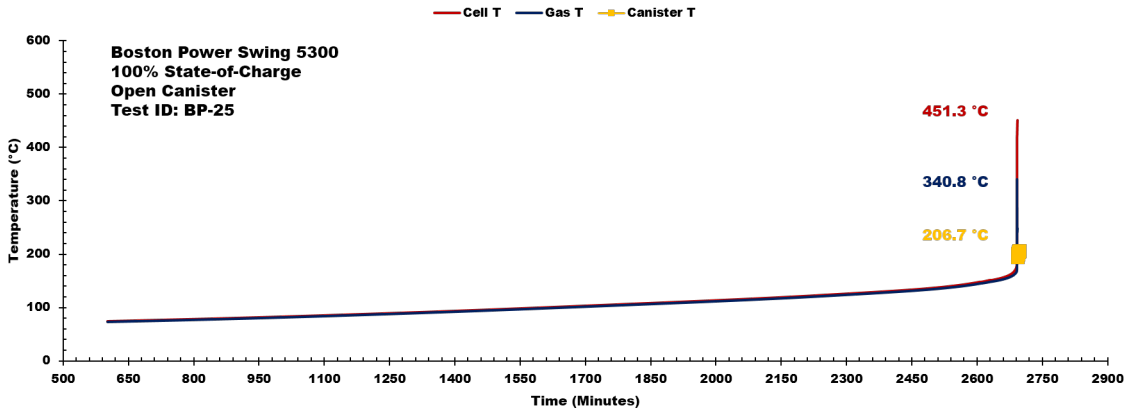

Figure A3-4 BP-5300 ARC data used for energy calculations for the 100% SOC open canister configuration (BP25). Data presented includes the following: (a) cell temperature, (b) gas temperature and (c) average canister temperature.

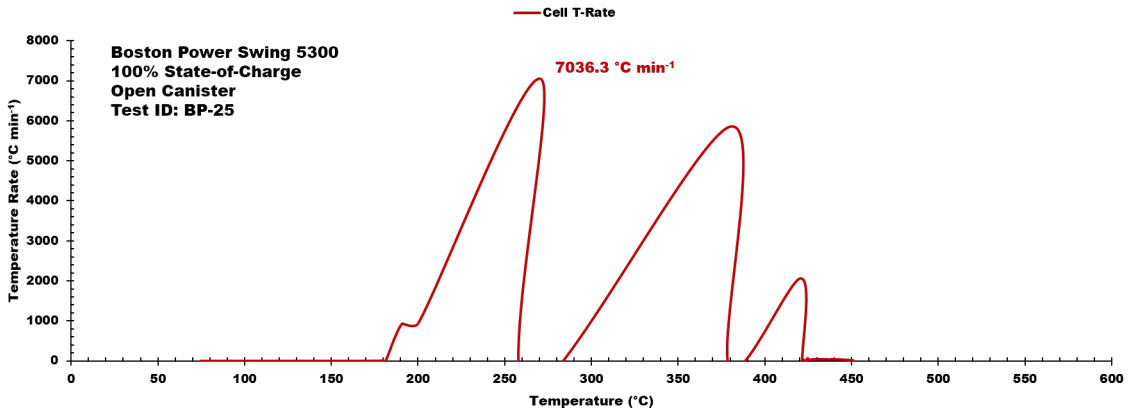

Figure A-5 BP-5300 ARC data used for energy calculations for the 100% SOC open canister configuration (BP25). Temp. rate vs. temperature profile is displayed.

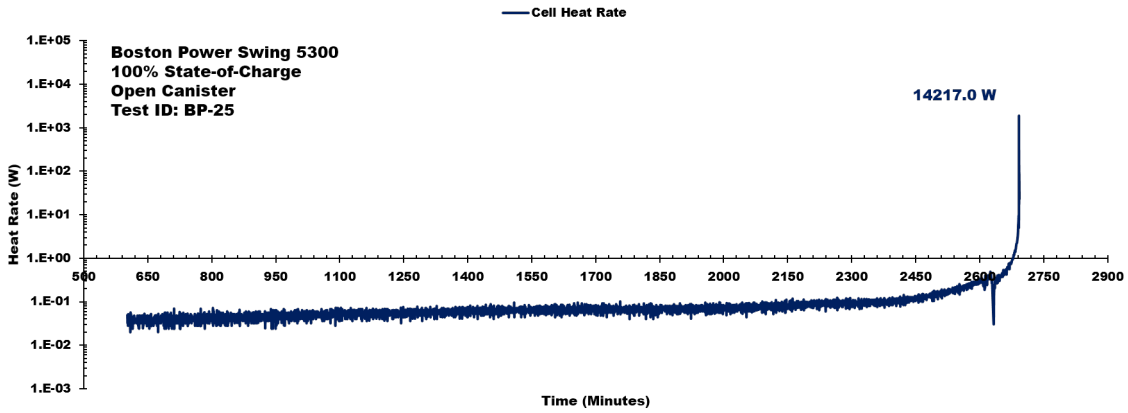

Figure A3-6 BP-5300 ARC data used for energy calculations for the 100% SOC open canister configuration (BP25). Cell body heat rate profile is displayed.

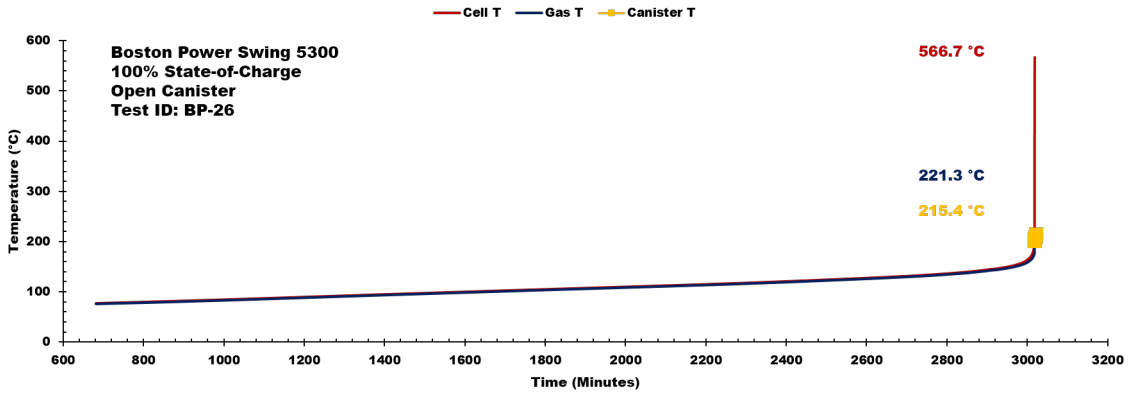

Figure A3-7 BP-5300 ARC data used for energy calculations for the 100% SOC open canister configuration (BP26). Data presented includes the following: (a) cell temperature, (b) gas temperature and (c) average canister temperature.

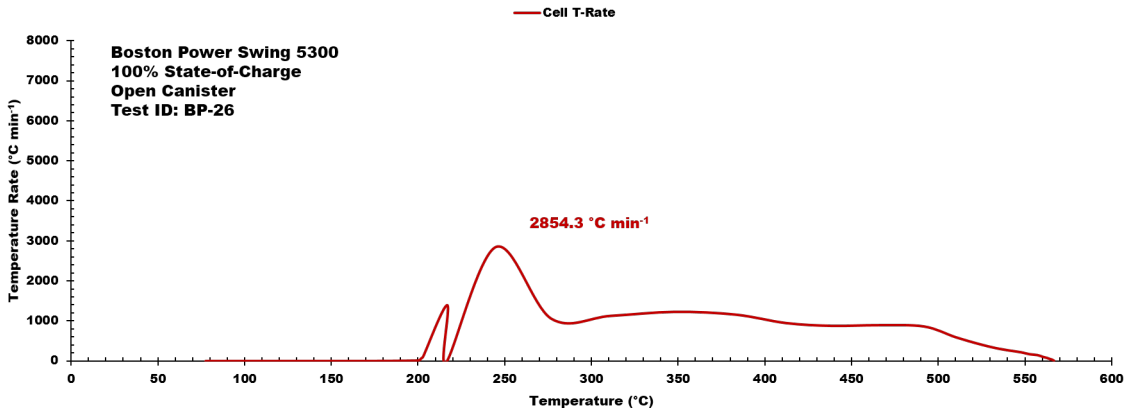

Figure A3-8 BP-5300 ARC data used for energy calculations for the 100% SOC open canister configuration (BP26). Temp. rate vs. temperature profile is displayed.

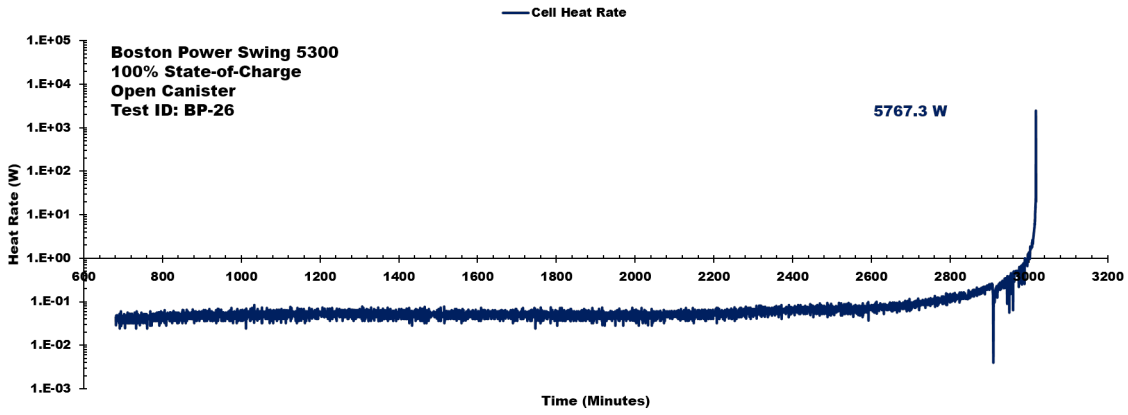

Figure A3-9 BP-5300 ARC data used for energy calculations for the 100% SOC open canister configuration (BP26). Cell body heat rate profile is displayed.

Appendix A4: Boston Power Swing 5300 ARC Data (50%-O)

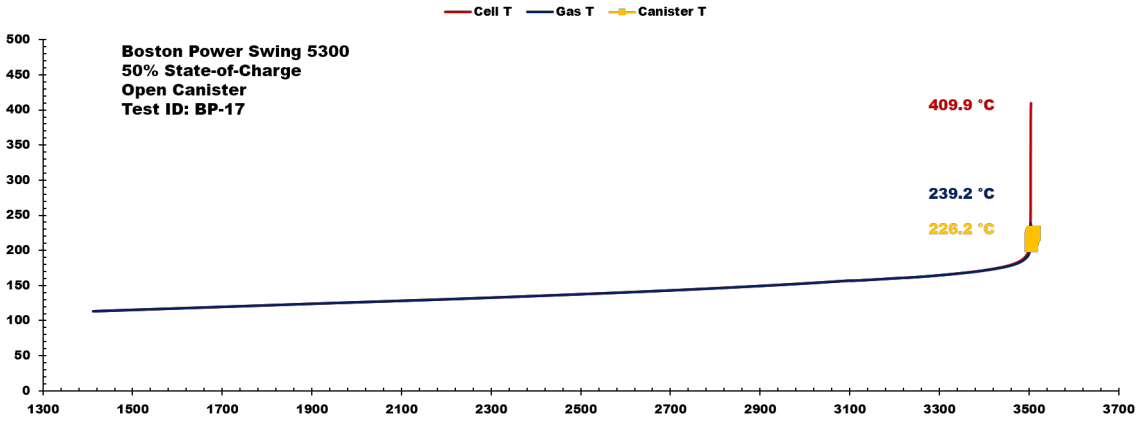

Figure A4-1 BP-5300 ARC data used for energy calculations for the 50% SOC open canister configuration (BP17). Data presented includes the following: (a) cell temperature, (b) gas temperature and (c) average canister temperature.

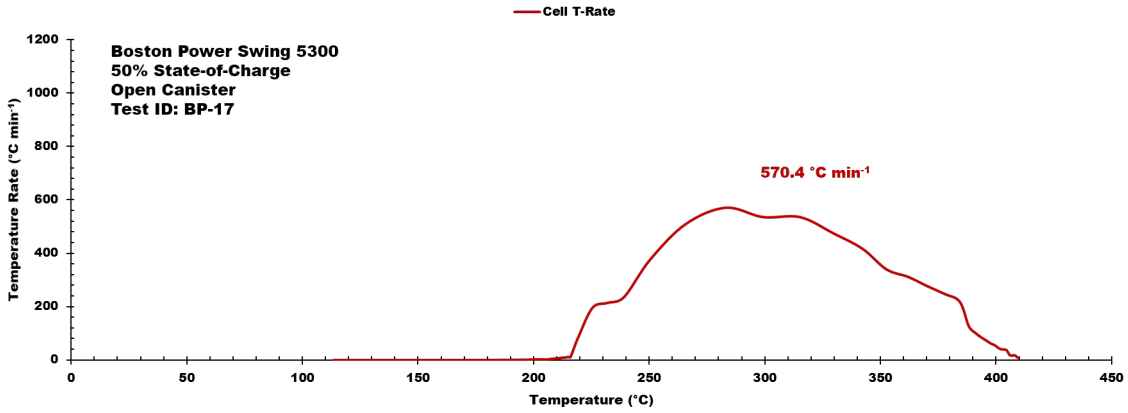

Figure A4-2 BP-5300 ARC data used for energy calculations for the 50% SOC open canister configuration (BP17). Temp. rate vs. temperature profile is displayed.

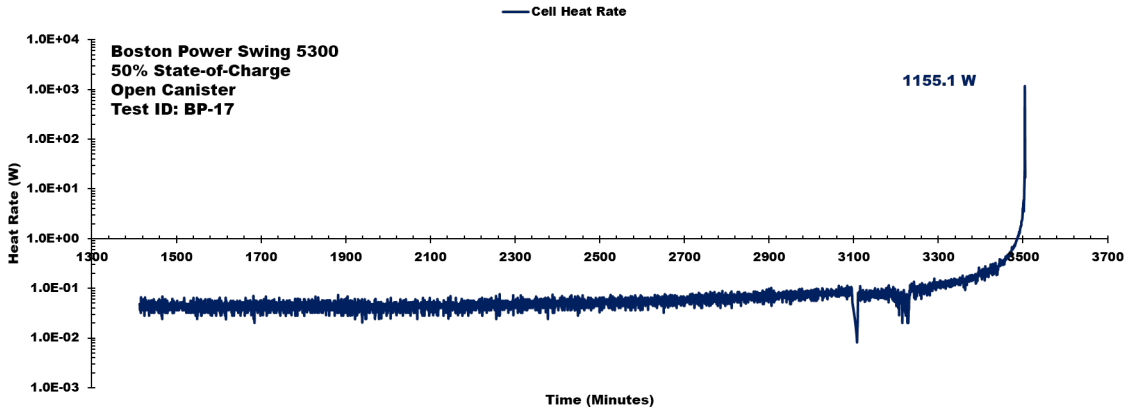

Figure A4-3 BP-5300 ARC data used for energy calculations for the 50% SOC open canister configuration (BP17). Cell body heat rate profile is displayed.

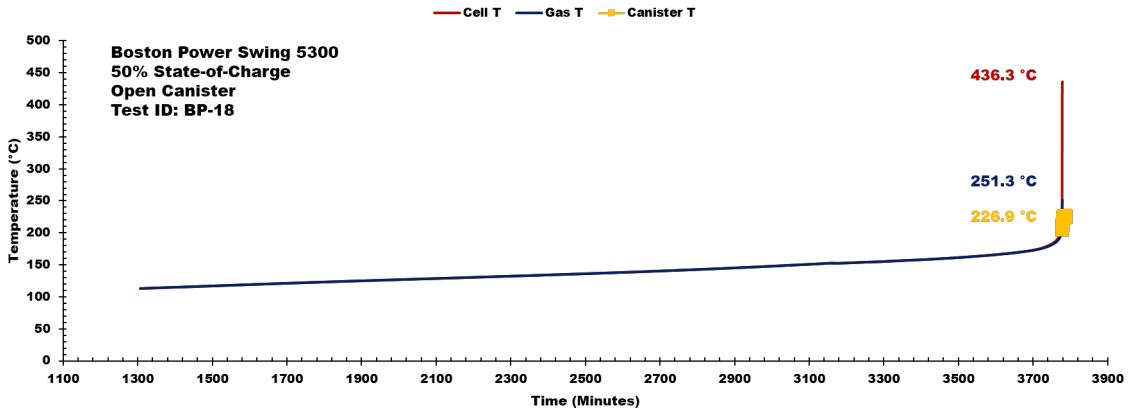

Figure A4-4 BP-5300 ARC data used for energy calculations for the 50% SOC open canister configuration (BP18). Data presented includes the following: (a) cell temperature, (b) gas temperature and (c) average canister temperature.

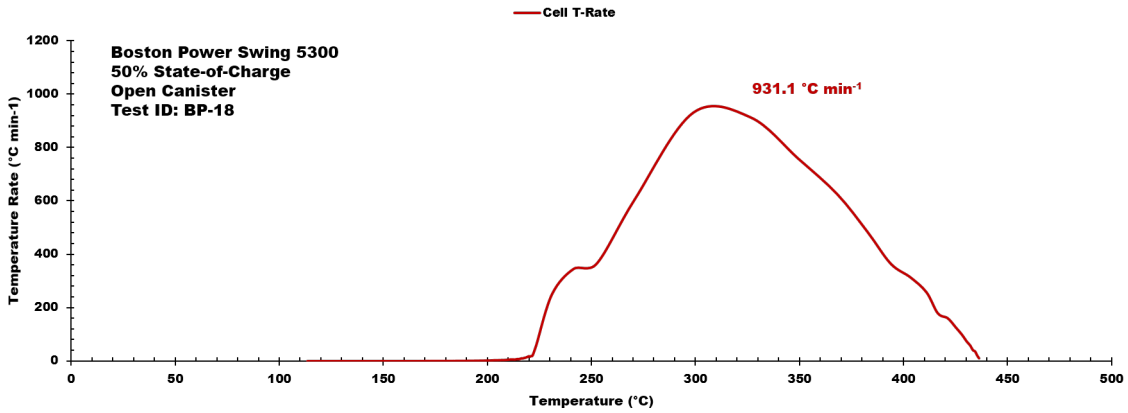

Figure A4-5 BP-5300 ARC data used for energy calculations for the 50% SOC open canister configuration (BP18). Temp. rate vs. temperature profile is displayed.

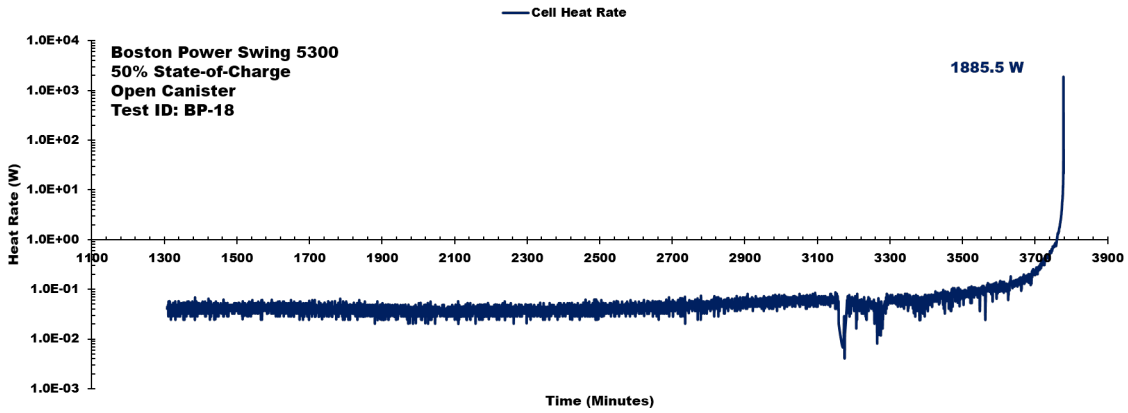

Figure A4-6 BP-5300 ARC data used for energy calculations for the 50% SOC open canister configuration (BP18). Cell body heat rate profile is displayed.

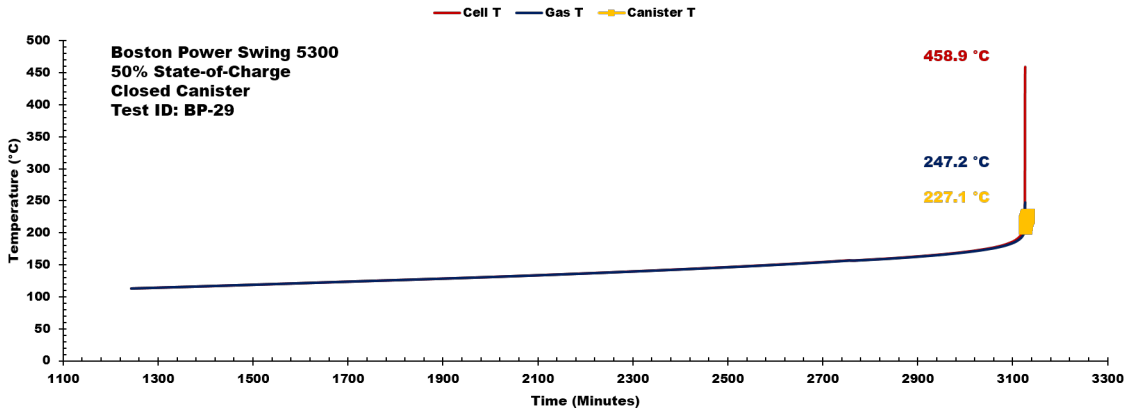

Figure A4-7 BP-5300 ARC data used for energy calculations for the 50% SOC open canister configuration (BP29). Data presented includes the following: (a) cell temperature, (b) gas temperature and (c) average canister temperature.

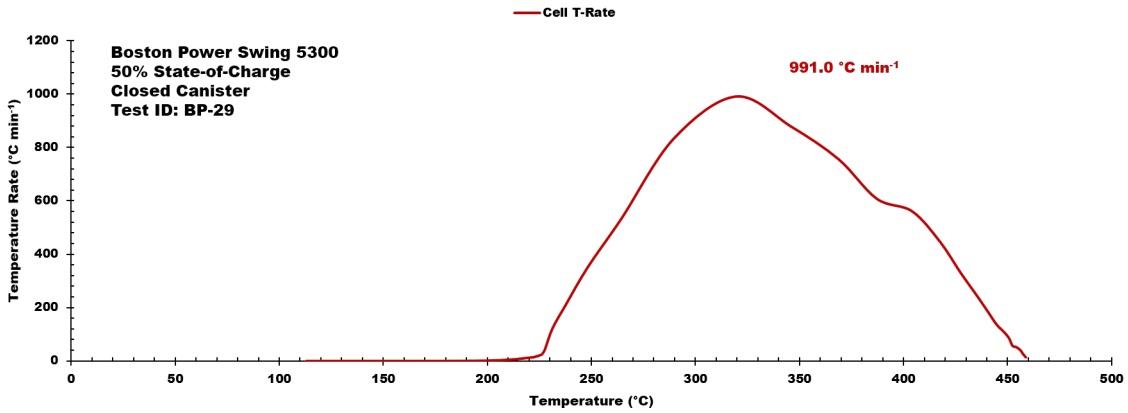

Figure A4-8 BP-5300 ARC data used for energy calculations for the 50% SOC open canister configuration (BP29). Temp. rate vs. temperature profile is displayed.

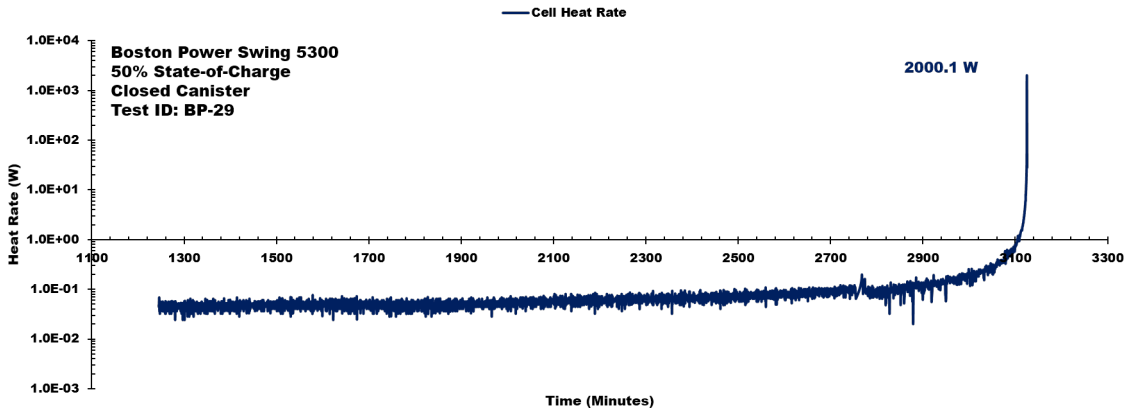

Figure A4-9 BP-5300 ARC data used for energy calculations for the 50% SOC open canister configuration (BP29). Cell body heat rate profile is displayed.

Appendix B1: Samsung 18650-26F ARC Data (100%-C)

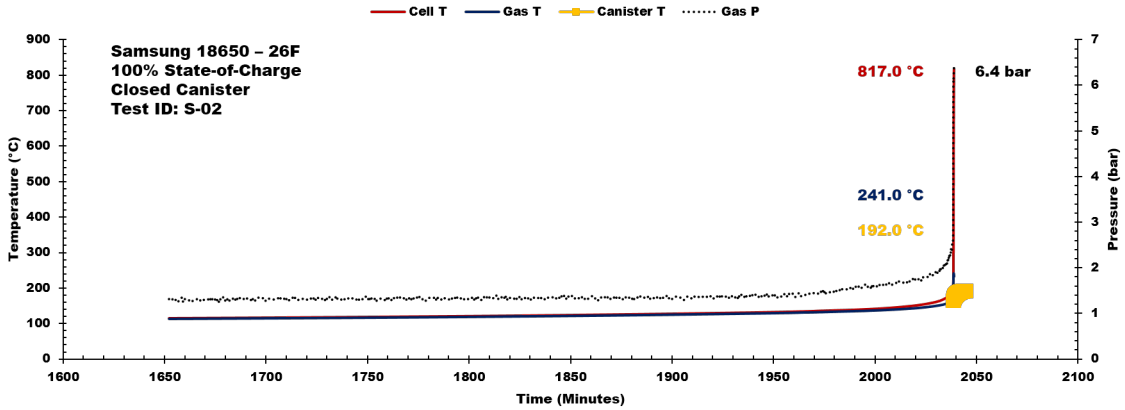

Figure B1-1 Samsung 18650-26F ARC test data used for energy calculations for the 100% SOC closed canister configuration (S02). Data presented includes the following: (a) cell temperature, (b) gas temperature, (c) average canister temperature and (d) pressure.

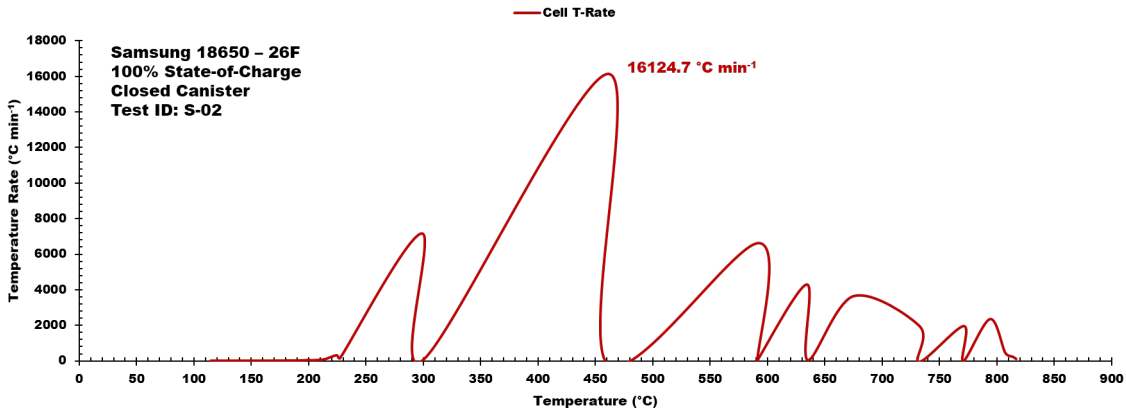

Figure B1-2 Samsung 18650-26F ARC test data used for energy calculations for the 100% SOC closed canister configuration (S02). Temp. rate vs. temperature profile is displayed.

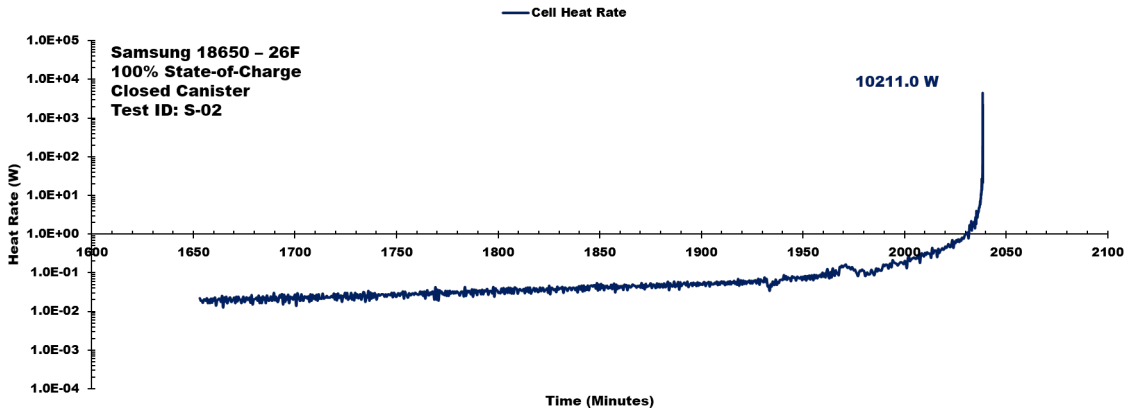

Figure B1-3 Samsung 18650-26F ARC test data used for energy calculations for the 100% SOC closed canister configuration (S02). Cell body heat rate profile is displayed.

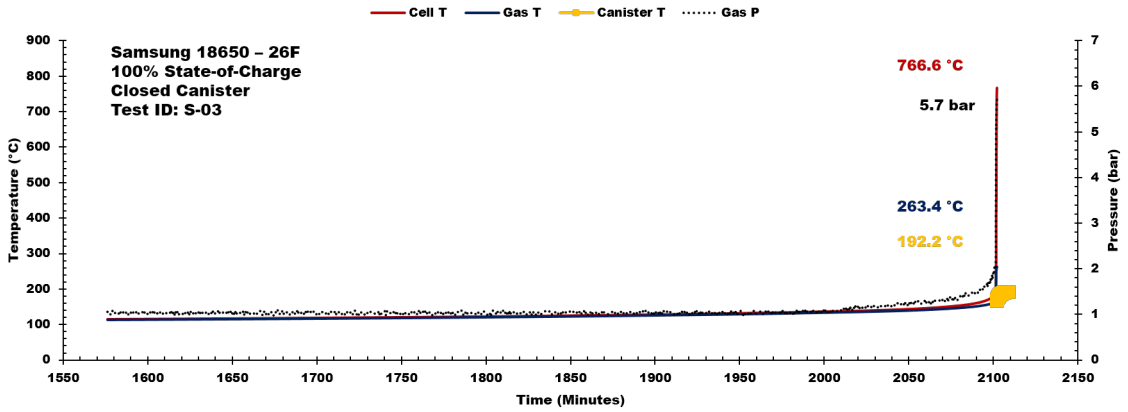

Figure B1-4 **Samsung 18650-26F ARC test data used for energy calculations for the 100% SOC closed canister configuration (S03). Data presented includes the following: (a) cell temperature, (b) gas temperature, (c) average canister temperature and (d) pressure.**

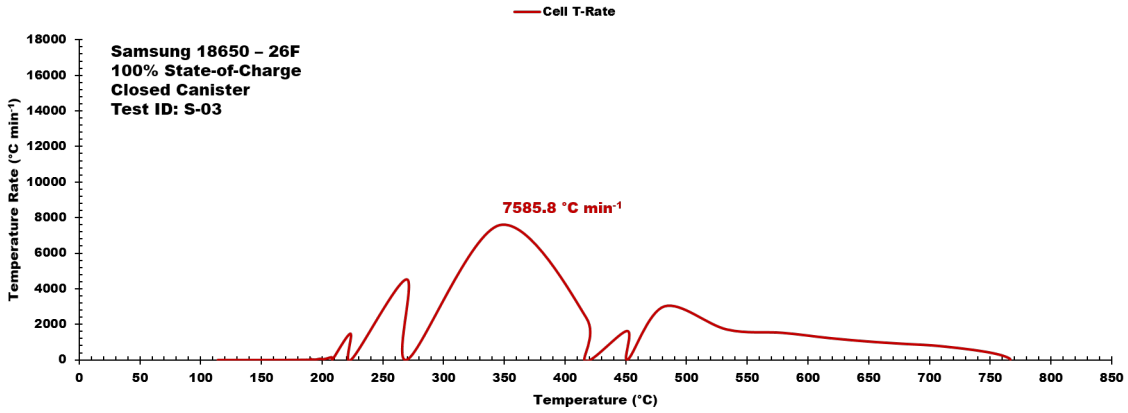

Figure B1-5 **Samsung 18650-26F ARC test data used for energy calculations for the 100% SOC closed canister configuration (S03). Temp. rate vs. temperature profile is displayed.**

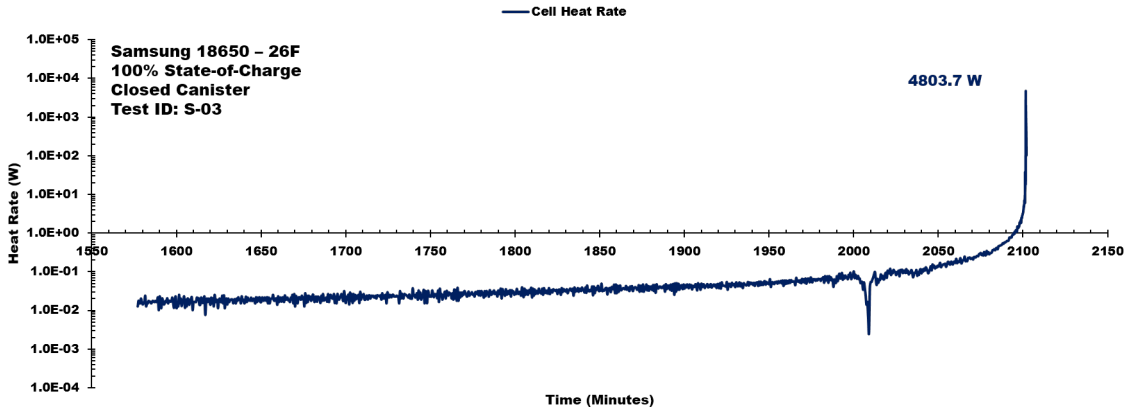

Figure B1-6 **Samsung 18650-26F ARC test data used for energy calculations for the 100% SOC closed canister configuration (S03). Cell body heat rate profile is displayed.**

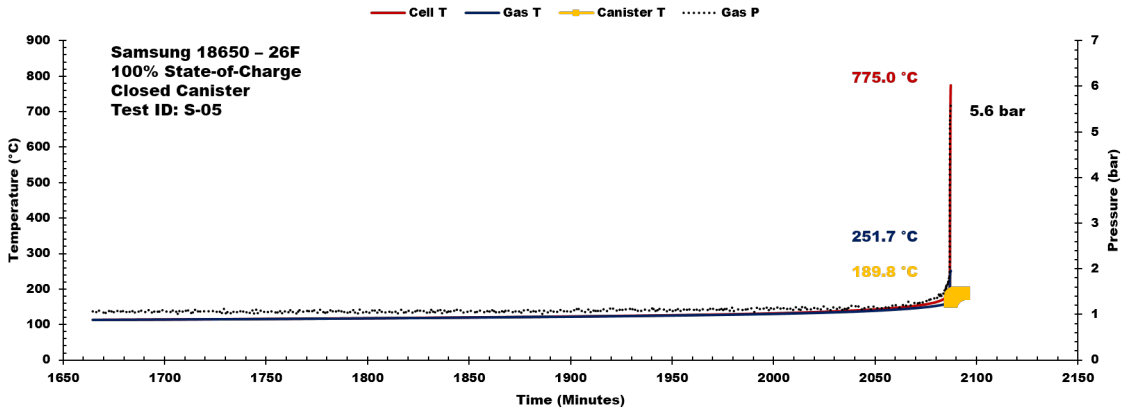

Figure B1-7 **Samsung 18650-26F ARC test data used for energy calculations for the 100% SOC closed canister configuration (S05). Data presented includes the following: (a) cell temperature, (b) gas temperature, (c) average canister temperature and (d) pressure.**

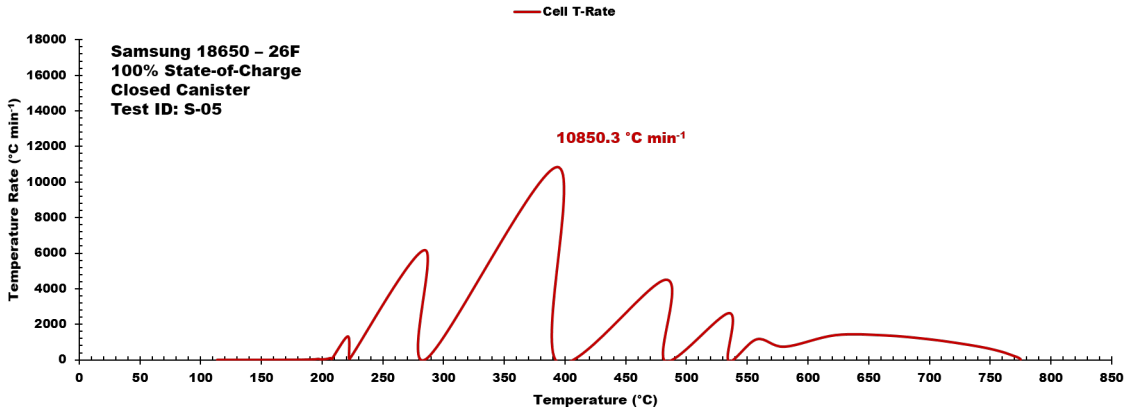

Figure B1-8 **Samsung 18650-26F ARC test data used for energy calculations for the 100% SOC closed canister configuration (S05). Temp. rate vs. temperature profile is displayed.**

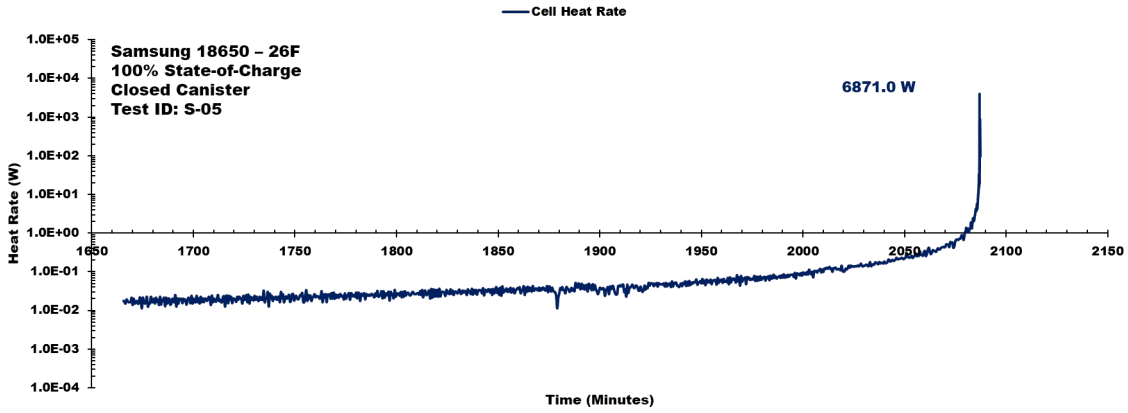

Figure B1-9 **Samsung 18650-26F ARC test data used for energy calculations for the 100% SOC closed canister configuration (S05). Cell body heat rate profile is displayed.**

Appendix B2: Samsung 18650-26F ARC Data (50%-C)

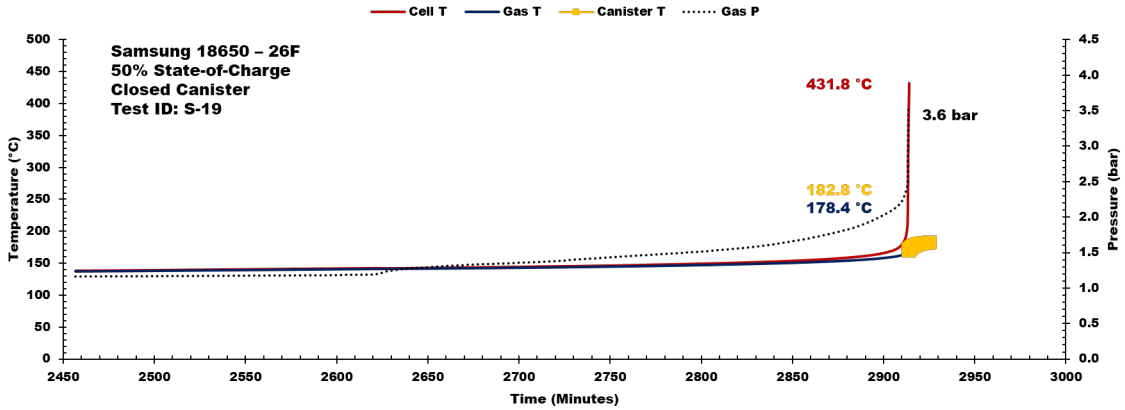

Figure B2-1 Samsung 18650-26F ARC test data used for energy calculations for the 50% SOC closed canister configuration (S19). Data presented includes the following: (a) cell temperature, (b) gas temperature, (c) average canister temperature and (d) pressure.

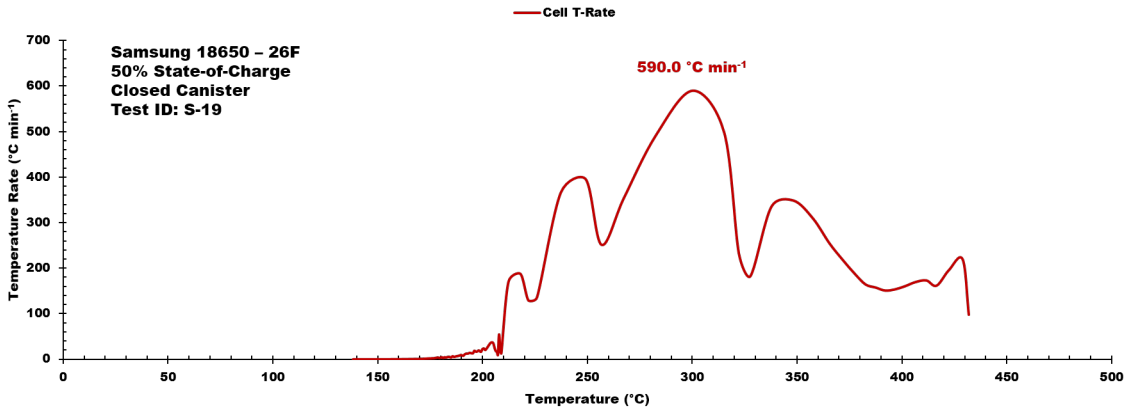

Figure B2-2 Samsung 18650-26F ARC test data used for energy calculations for the 50% SOC closed canister configuration (S19). Temp. rate vs. temperature profile is displayed.

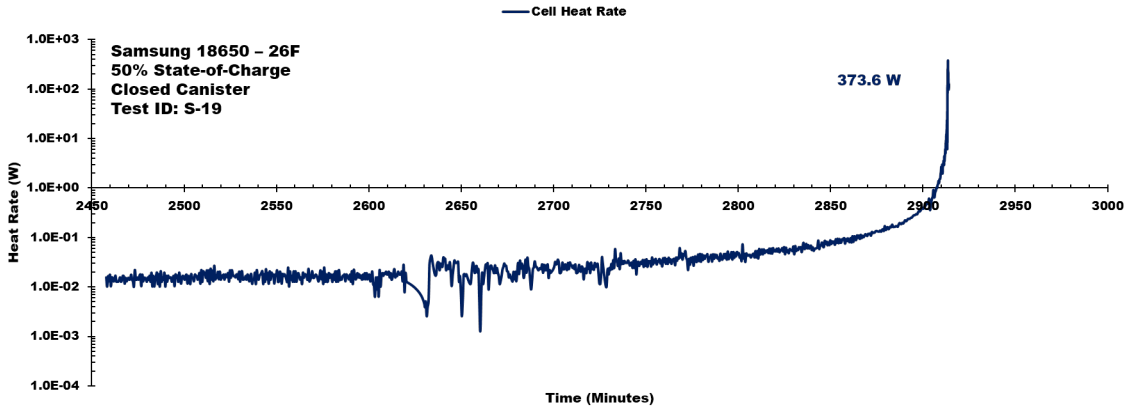

Figure B2-3 Samsung 18650-26F ARC test data used for energy calculations for the 50% SOC closed canister configuration (S19). Cell body heat rate profile is displayed.

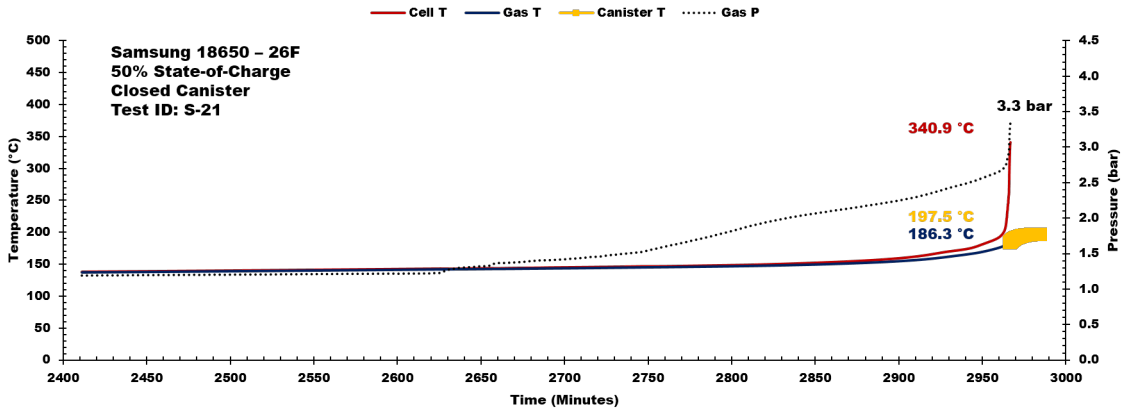

Figure B2-4 Samsung 18650-26F ARC test data used for energy calculations for the 50% SOC closed canister configuration (S21). Data presented includes the following: (a) cell temperature, (b) gas temperature, (c) average canister temperature and (d) pressure.

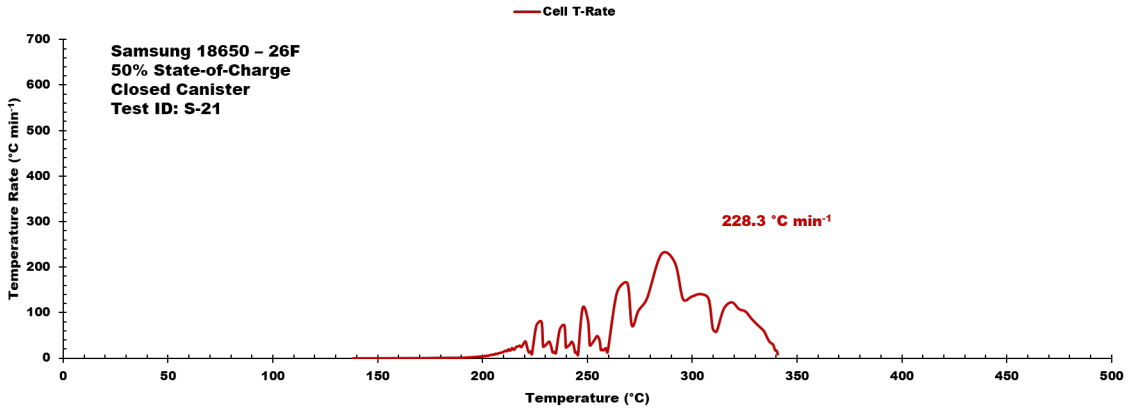

Figure B2-5 Samsung 18650-26F ARC test data used for energy calculations for the 50% SOC closed canister configuration (S21). Temp. rate vs. temperature profile is displayed.

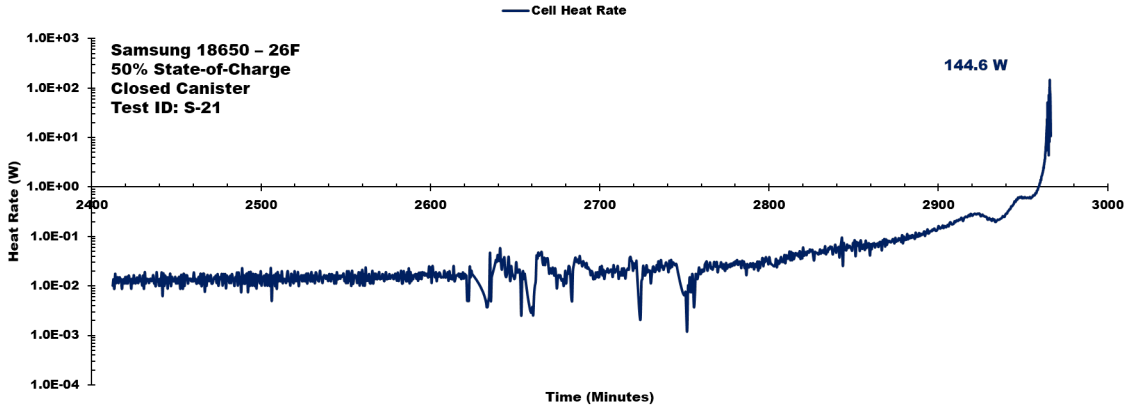

Figure B2-6 Samsung 18650-26F ARC test data used for energy calculations for the 50% SOC closed canister configuration (S21). Cell body heat rate profile is displayed.

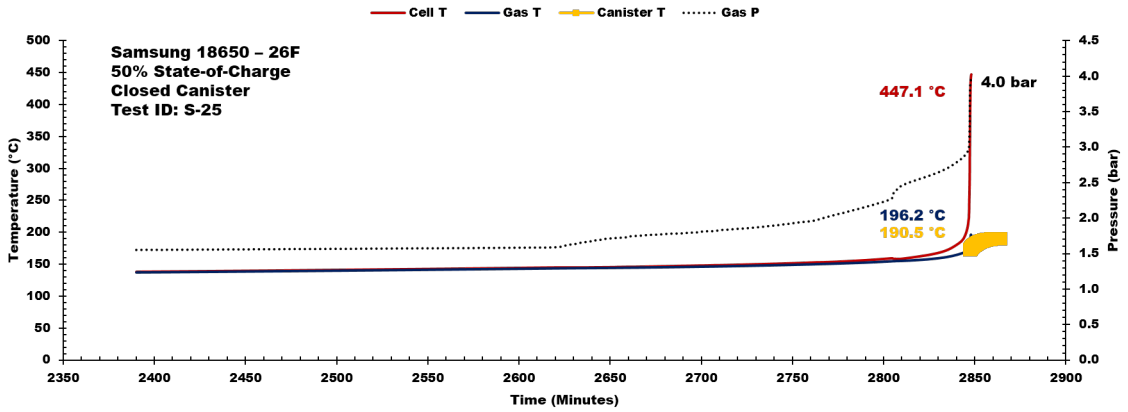

Figure B2-7 **Samsung 18650-26F ARC test data used for energy calculations for the 50% SOC closed canister configuration (S25). Data presented includes the following: (a) cell temperature, (b) gas temperature, (c) average canister temperature and (d) pressure.**

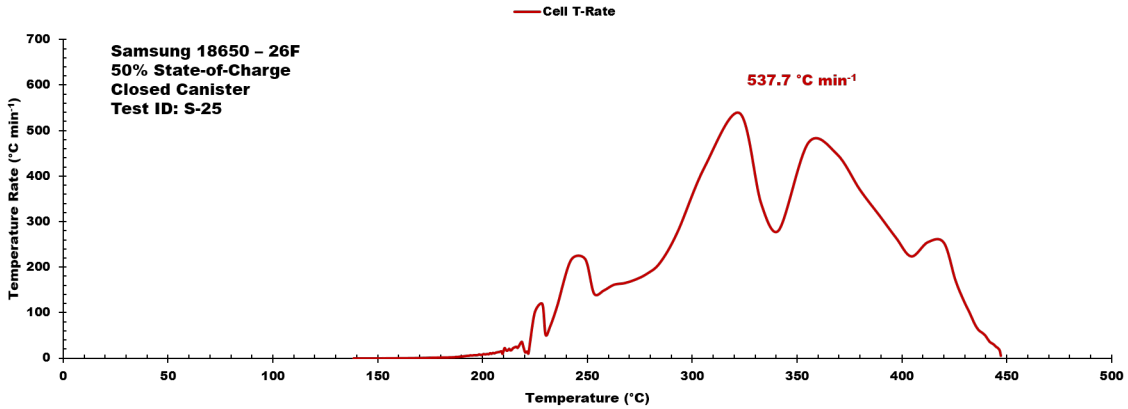

Figure B2-8 **Samsung 18650-26F ARC test data used for energy calculations for the 50% SOC closed canister configuration (S25). Temp. rate vs. temperature profile is displayed.**

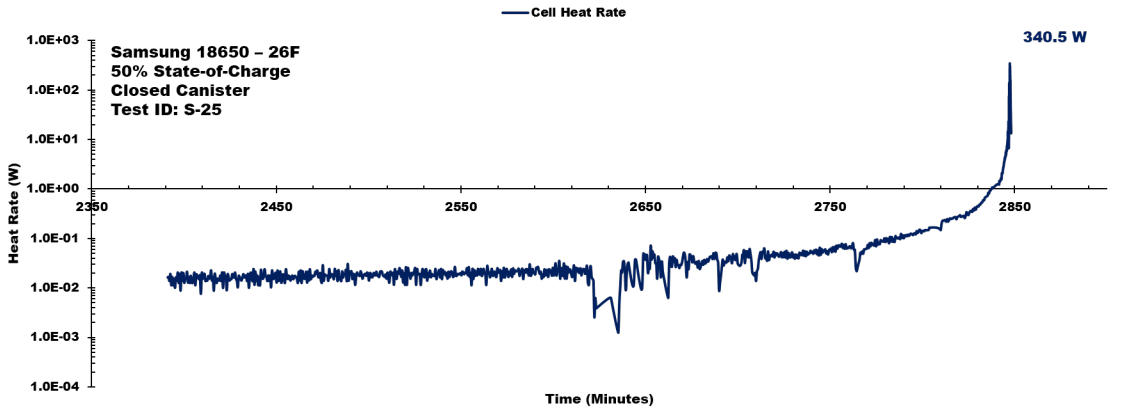

Figure B2-9 **Samsung 18650-26F ARC test data used for energy calculations for the 50% SOC closed canister configuration (S25). Cell body heat rate profile is displayed.**

Appendix B3: Samsung 18650-26F ARC Data (100%-O)

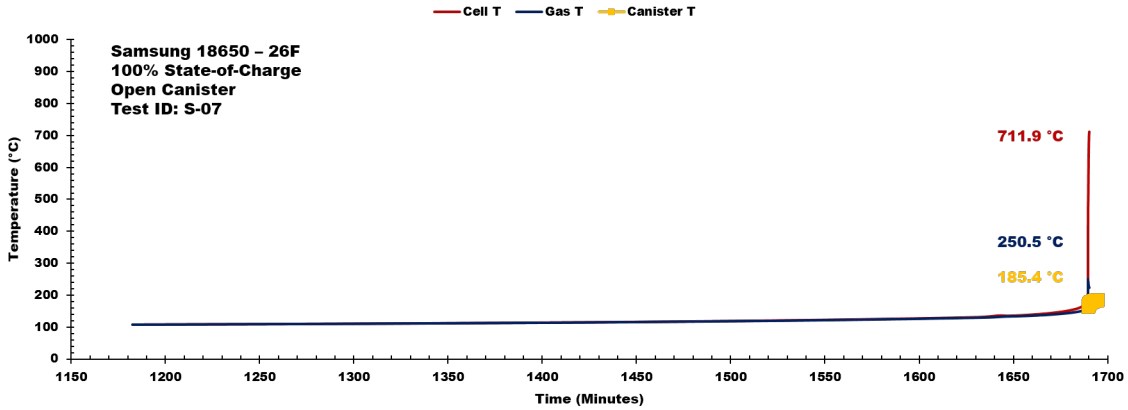

Figure B3-1 Samsung 18650-26F ARC test data used for energy calculations for the 100% SOC open canister configuration (S07). Data presented includes the following: (a) cell temperature, (b) gas temperature and (c) average canister temperature.

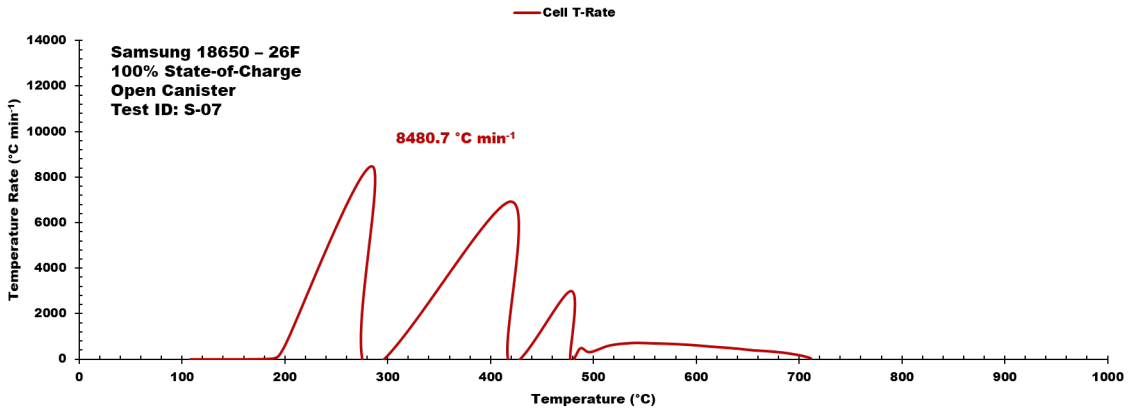

Figure B3-2 Samsung 18650-26F ARC test data used for energy calculations for the 100% SOC open canister configuration (S07). Temp. rate vs. temperature profile is displayed.

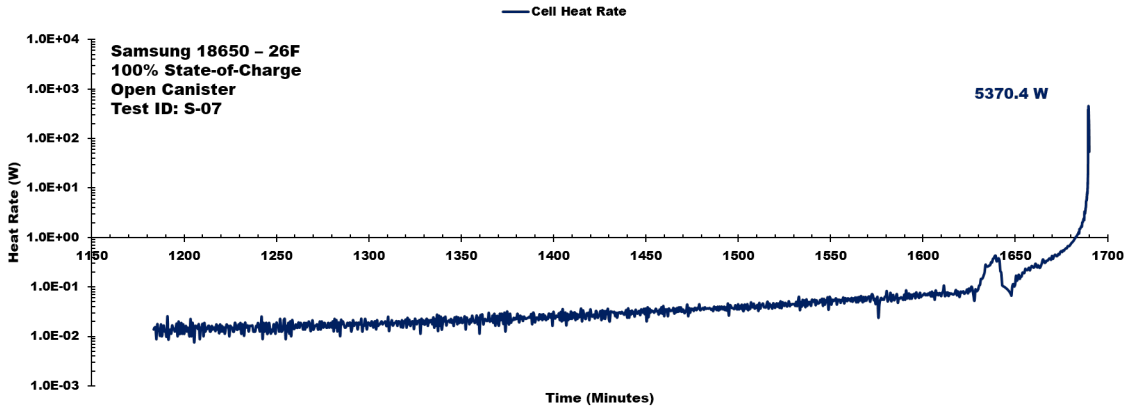

Figure B3-3 Samsung 18650-26F ARC test data used for energy calculations for the 100% SOC open canister configuration (S07). Cell body heat rate profile is displayed.

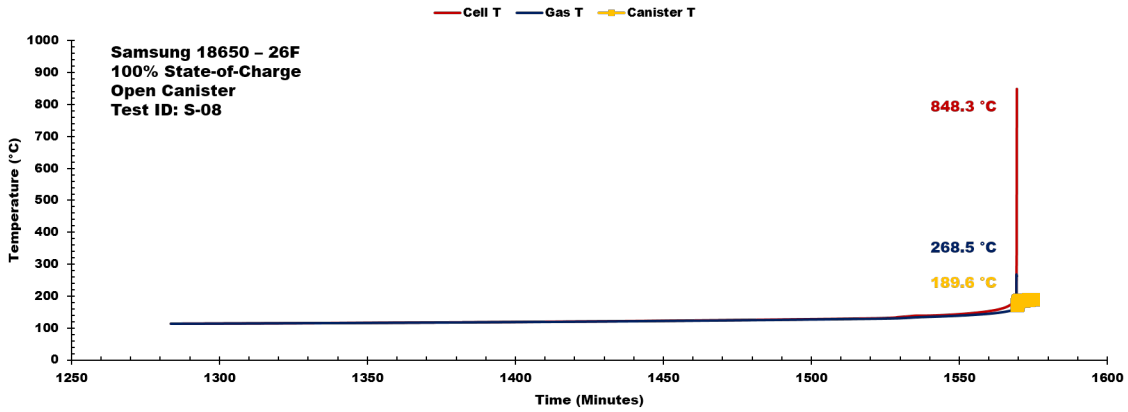

Figure B3-4 **Samsung 18650-26F ARC test data used for energy calculations for the 100% SOC open canister configuration (S08). Data presented includes the following: (a) cell temperature, (b) gas temperature and (c) average canister temperature.**

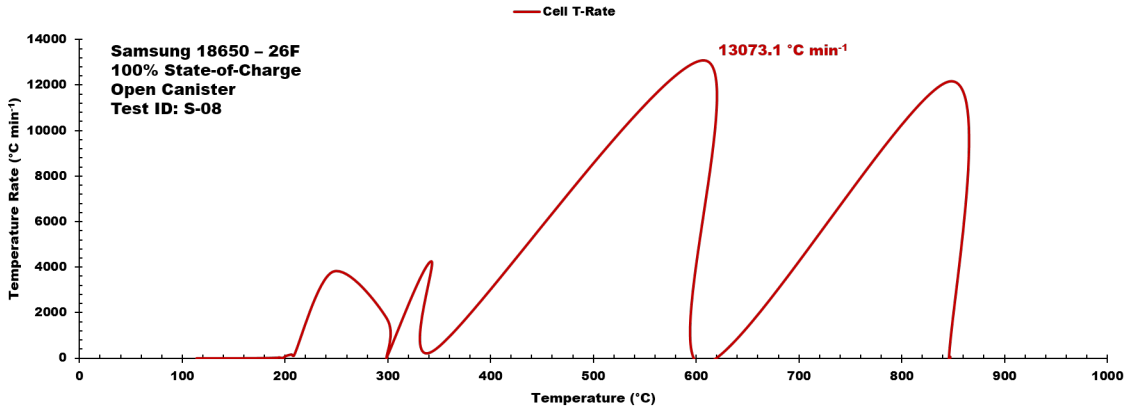

Figure B3-5 **Samsung 18650-26F ARC test data used for energy calculations for the 100% SOC open canister configuration (S08). Temp. rate vs. temperature profile is displayed.**

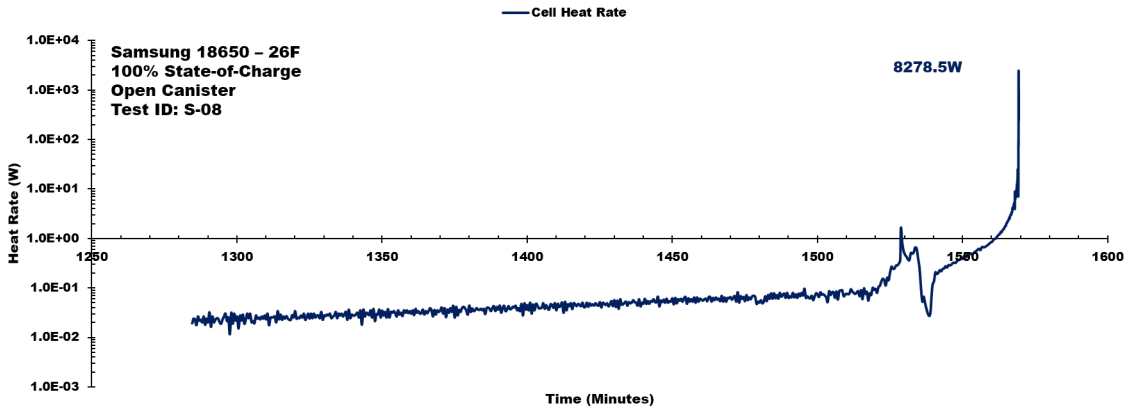

Figure B3-6 **Samsung 18650-26F ARC test data used for energy calculations for the 100% SOC open canister configuration (S08). Cell body heat rate profile is displayed.**

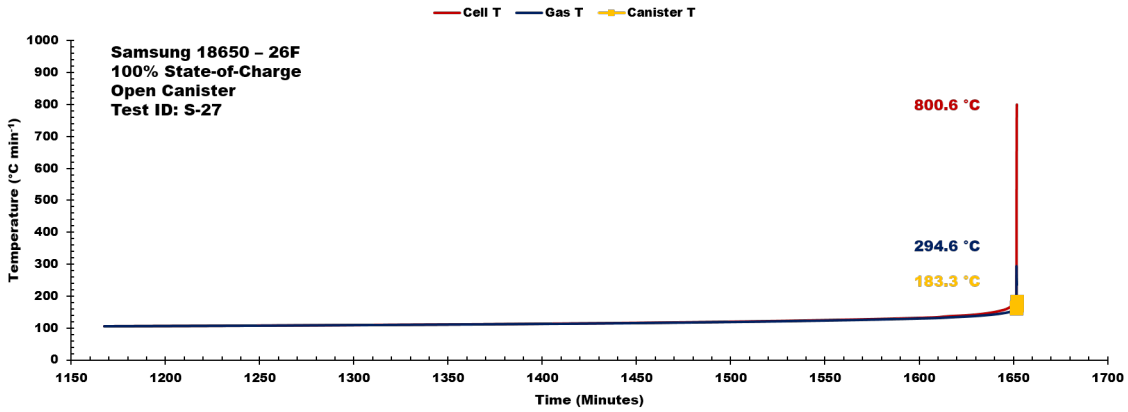

Figure B3-7 Samsung 18650-26F ARC test data used for energy calculations for the 100% SOC open canister configuration (S27). Data presented includes the following: (a) cell temperature, (b) gas temperature and (c) average canister temperature.

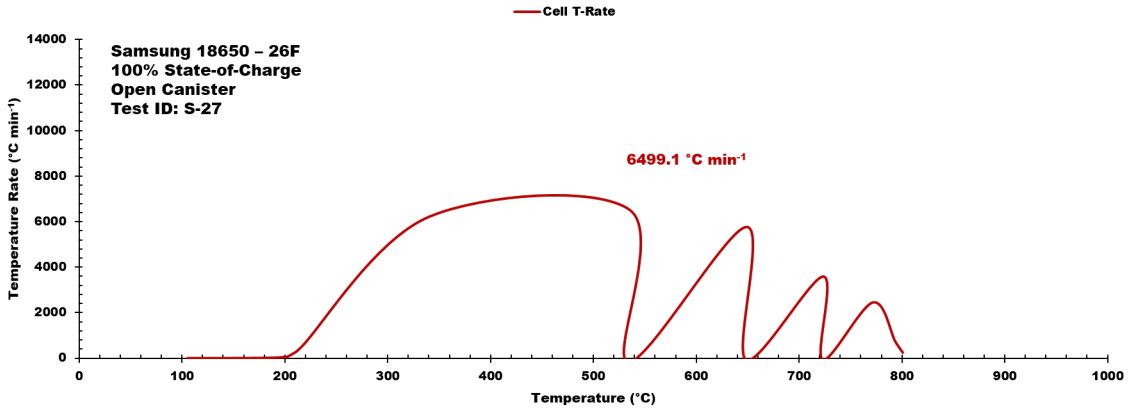

Figure B3-8 Samsung 18650-26F ARC test data used for energy calculations for the 100% SOC open canister configuration (S27). Temp. rate vs. temperature profile is displayed.

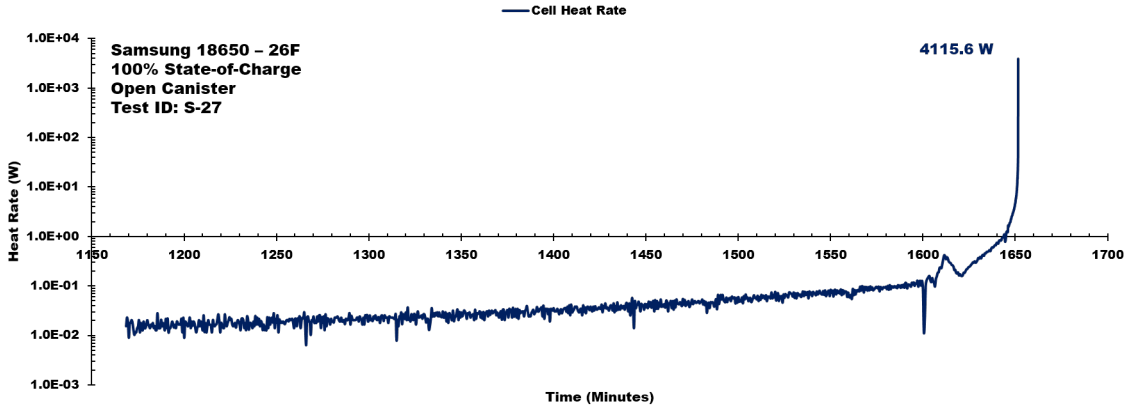

Figure B3-9 Samsung 18650-26F ARC test data used for energy calculations for the 100% SOC open canister configuration (S27). Cell body heat rate profile is displayed.

Appendix B4: Samsung 18650-26F ARC Data (50%-O)

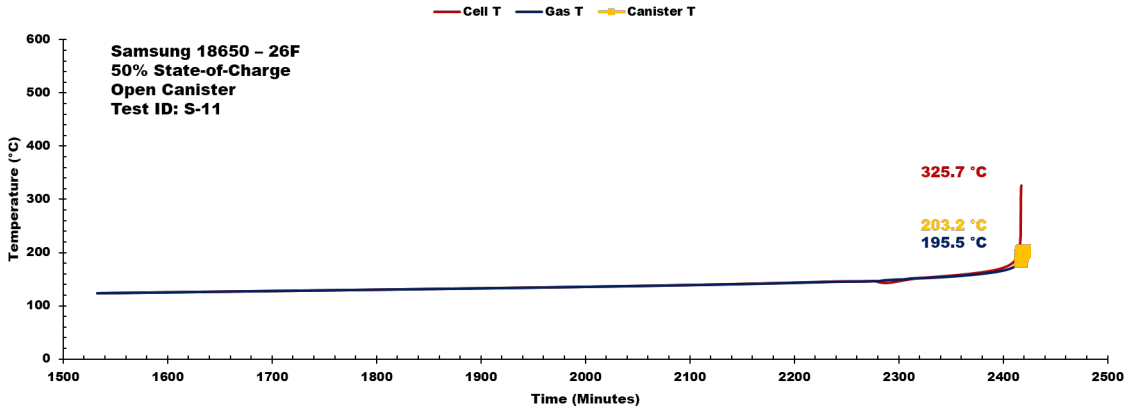

Figure B4-1 Samsung 18650-26F ARC test data used for energy calculations for the 50% SOC open canister configuration (S11). Data presented includes the following: (a) cell temperature, (b) gas temperature and (c) average canister temperature.

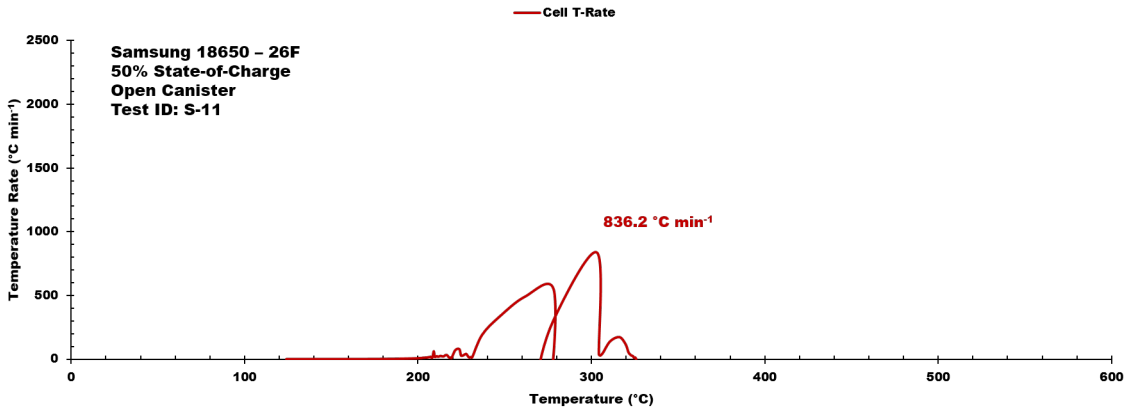

Figure B4-2 Samsung 18650-26F ARC test data used for energy calculations for the 50% SOC open canister configuration (S11). Temp. rate vs. temperature profile is displayed.

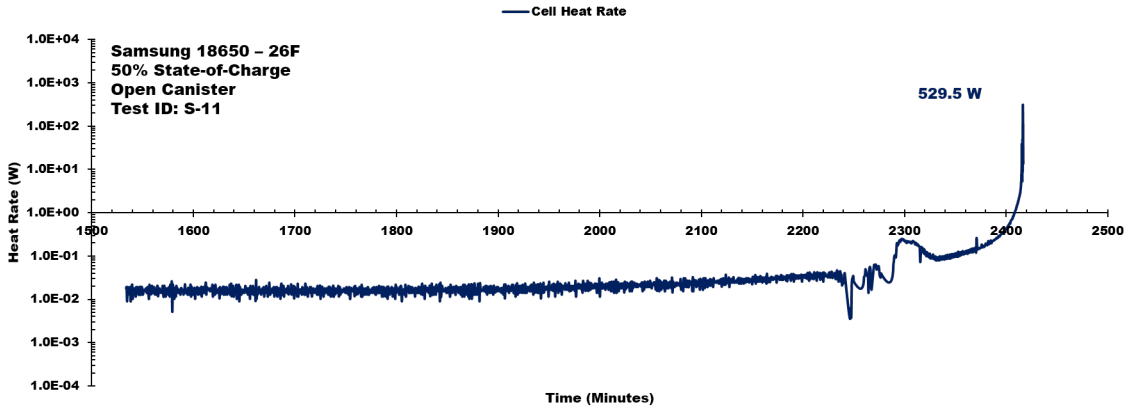

Figure B4-3 Samsung 18650-26F ARC test data used for energy calculations for the 50% SOC open canister configuration (S11). Cell body heat rate profile is displayed.

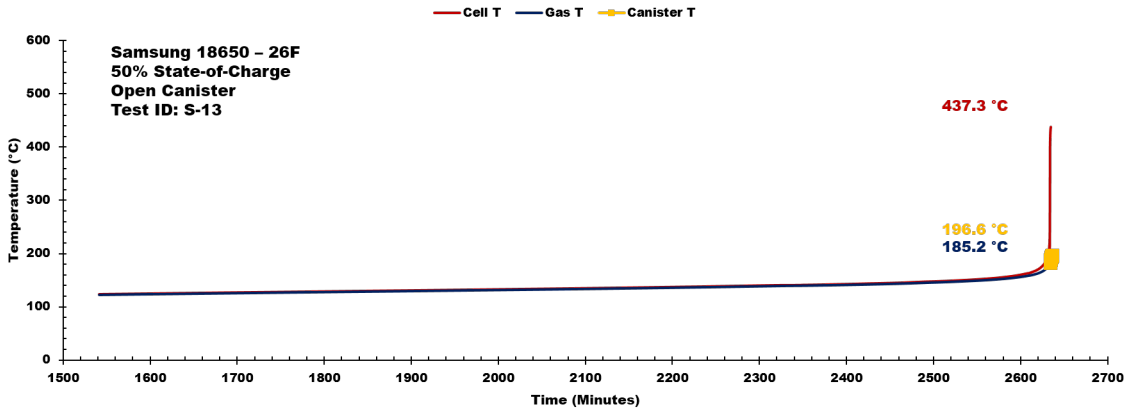

Figure B4-4 Samsung 18650-26F ARC test data used for energy calculations for the 50% SOC open canister configuration (S13). Data presented includes the following: (a) cell temperature, (b) gas temperature and (c) average canister temperature.

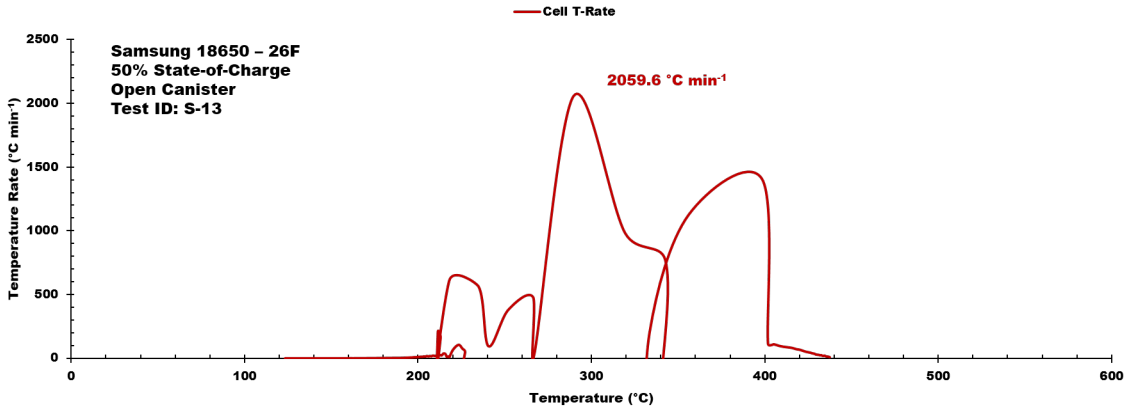

Figure B4-5 Samsung 18650-26F ARC test data used for energy calculations for the 50% SOC open canister configuration (S13). Temp. rate vs. temperature profile is displayed.

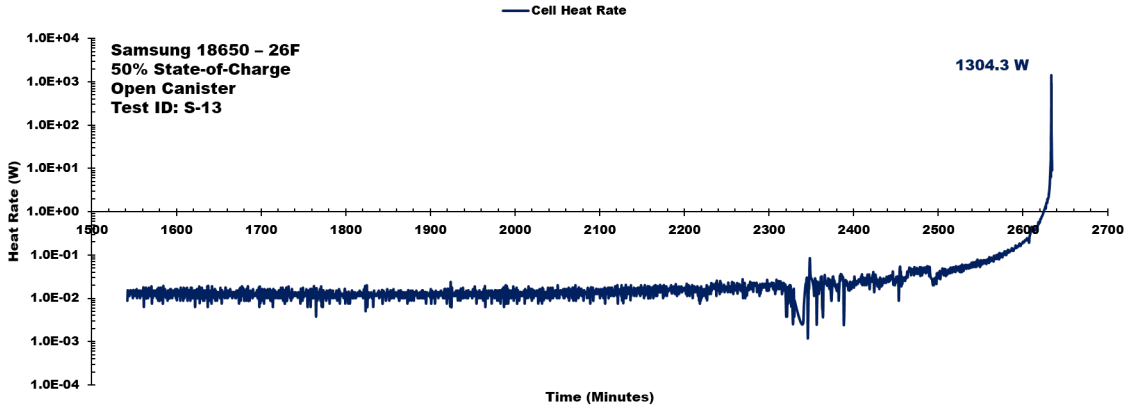

Figure B4-6 Samsung 18650-26F ARC test data used for energy calculations for the 50% SOC open canister configuration (S13). Cell body heat rate profile is displayed.

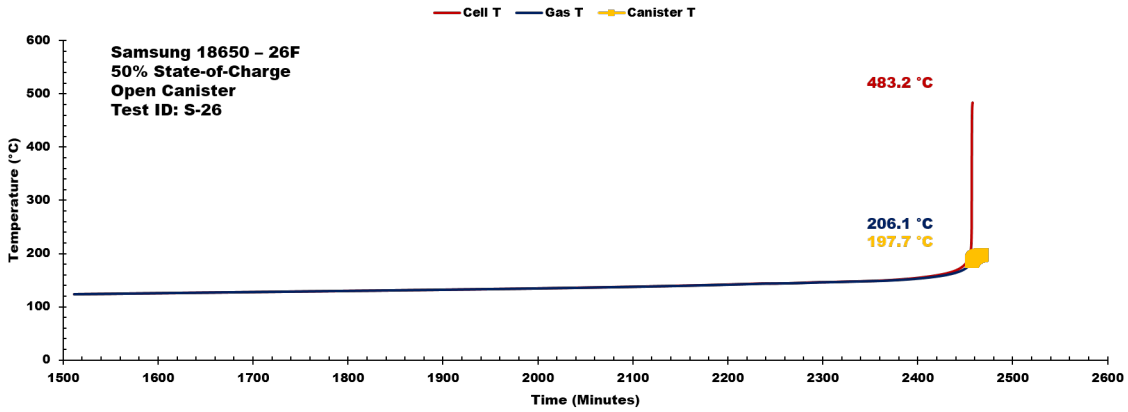

Figure B4-7 Samsung 18650-26F ARC test data used for energy calculations for the 50% SOC open canister configuration (S26). Data presented includes the following: (a) cell temperature, (b) gas temperature and (c) average canister temperature.

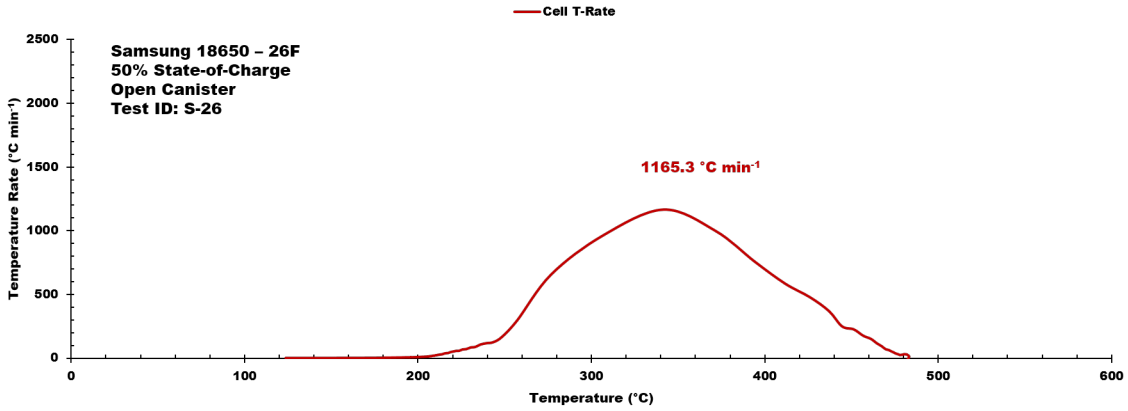

Figure B4-8 Samsung 18650-26F ARC test data used for energy calculations for the 50% SOC open canister configuration (S26). Temp. rate vs. temperature profile is displayed.

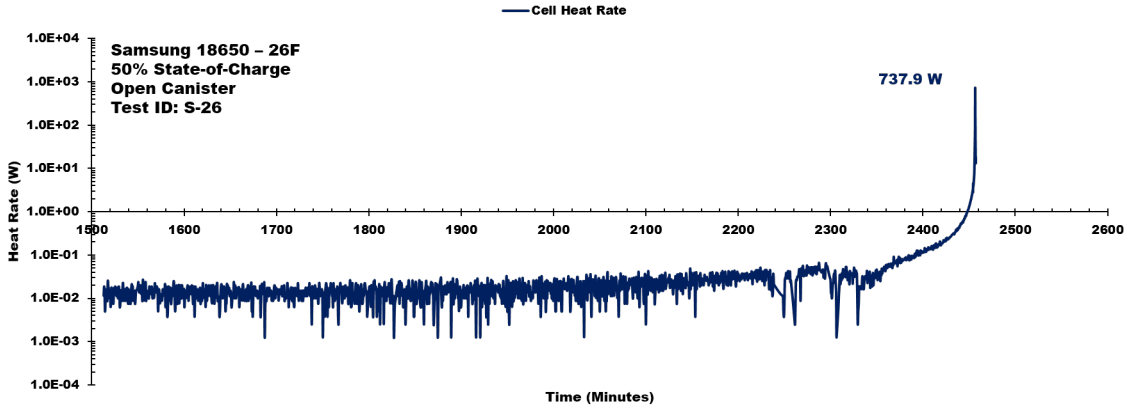

Figure B4-9 Samsung 18650-26F ARC test data used for energy calculations for the 50% SOC open canister configuration (S26). Cell body heat rate profile is displayed.

Appendix C1: MoliCel 18650-J ARC Data (100%-C)

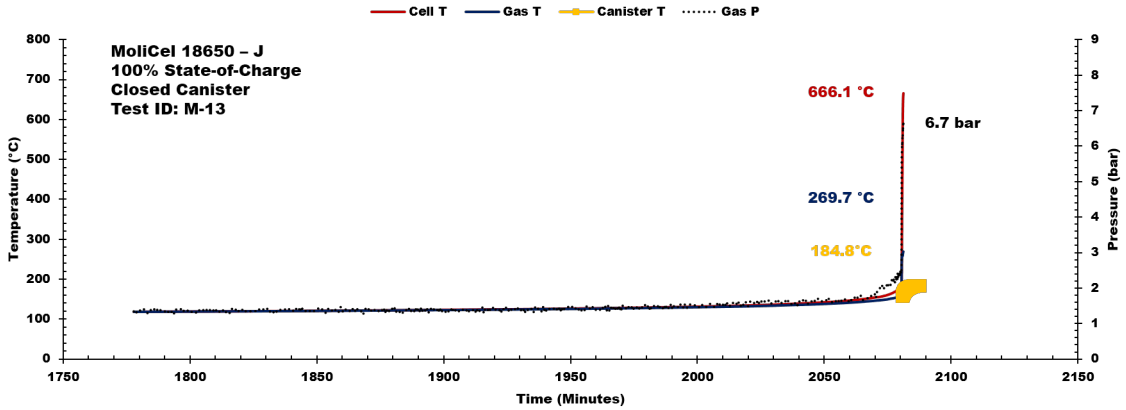

Figure C1-1 MoliCel 18650-J ARC test data used for energy calculations for the 100% SOC closed canister configuration (M13). Data presented includes the following: (a) cell temperature, (b) gas temperature, (c) average canister temperature and (d) pressure.

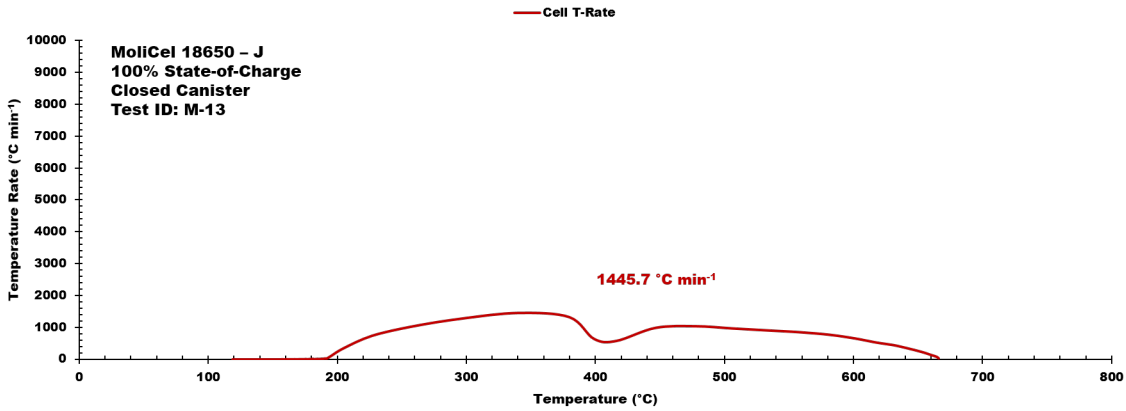

Figure C1-2 MoliCel 18650-J ARC test data used for energy calculations for the 100% SOC closed canister configuration (M13). Temp. rate vs. temperature profile is displayed.

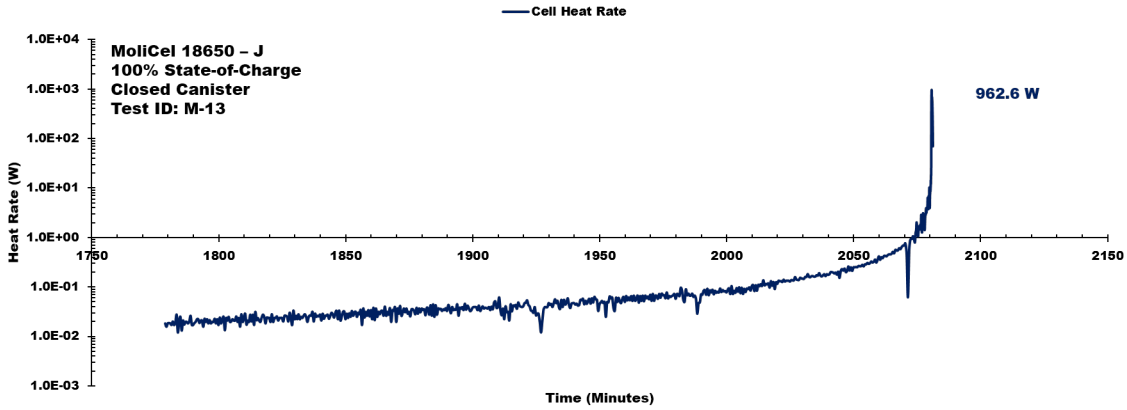

Figure C1-3 MoliCel 18650-J ARC test data used for energy calculations for the 100% SOC closed canister configuration (M13). Cell body heat rate profile is displayed.

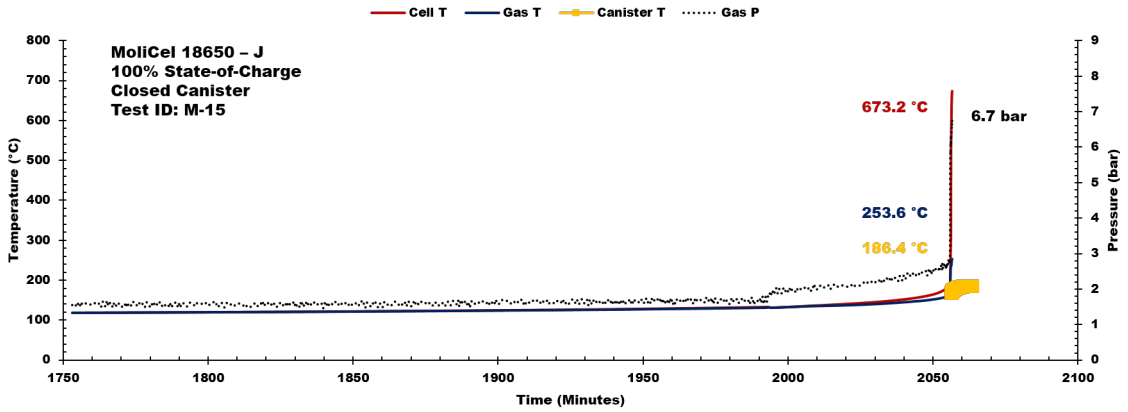

Figure C1-4 **MoliCel 18650-J ARC test data used for energy calculations for the 100% SOC closed canister configuration (M15). Data presented includes the following: (a) cell temperature, (b) gas temperature, (c) average canister temperature and (d) pressure.**

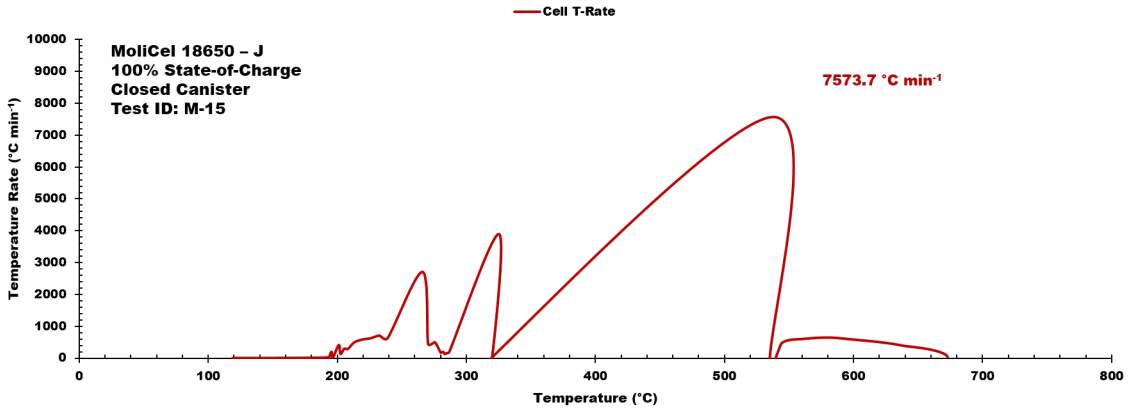

Figure C1-5 **MoliCel 18650-J ARC test data used for energy calculations for the 100% SOC closed canister configuration (M15). Temp. rate vs. temperature profile is displayed.**

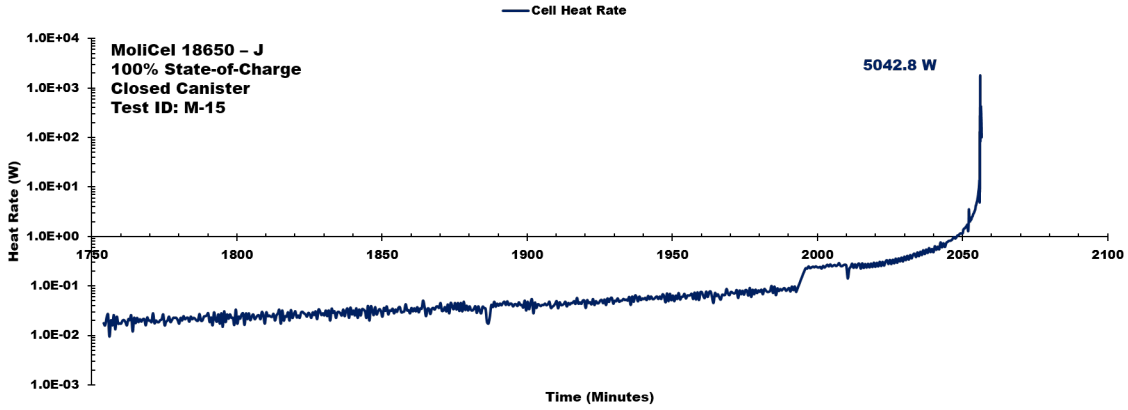

Figure C1-6 **MoliCel 18650-J ARC test data used for energy calculations for the 100% SOC closed canister configuration (M15). Cell body heat rate profile is displayed.**

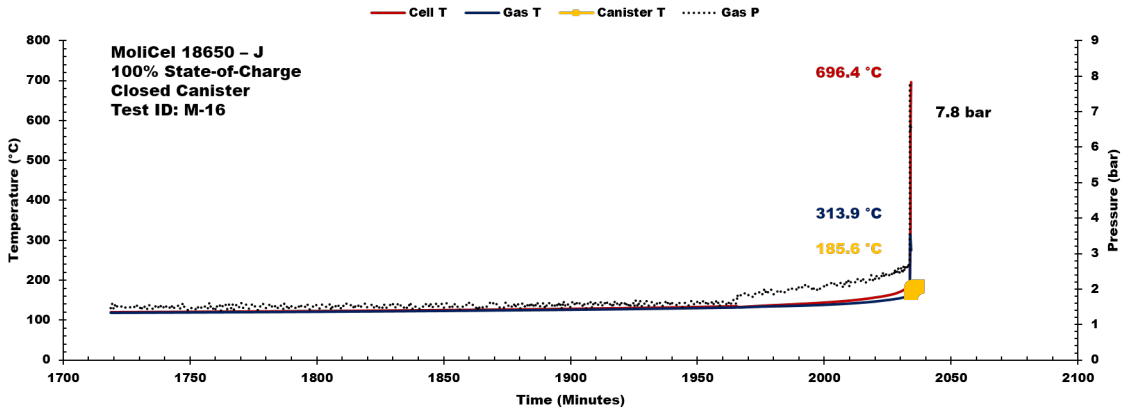

Figure C1-7 MoliCel 18650-J ARC test data used for energy calculations for the 100% SOC closed canister configuration (M16). Data presented includes the following: (a) cell temperature, (b) gas temperature, (c) average canister temperature and (d) pressure.

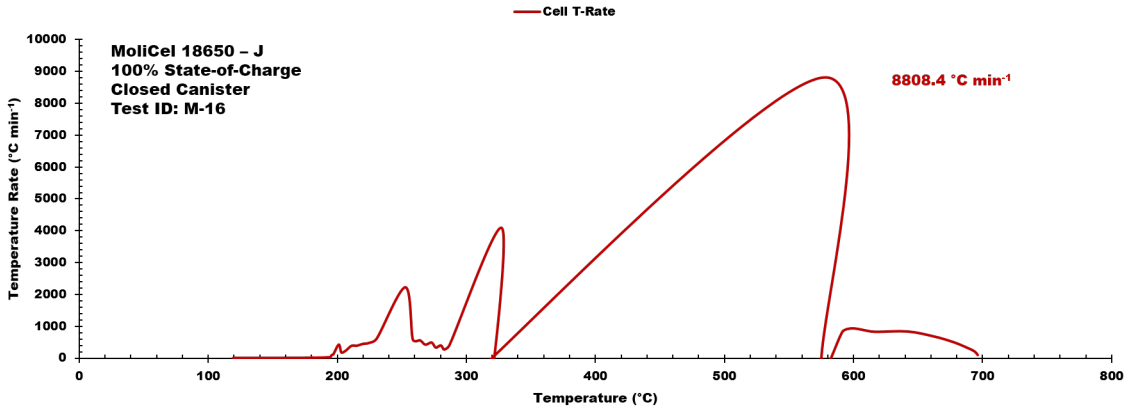

Figure C1-8 MoliCel 18650-J ARC test data used for energy calculations for the 100% SOC closed canister configuration (M16). Temp. rate vs. temperature profile is displayed.

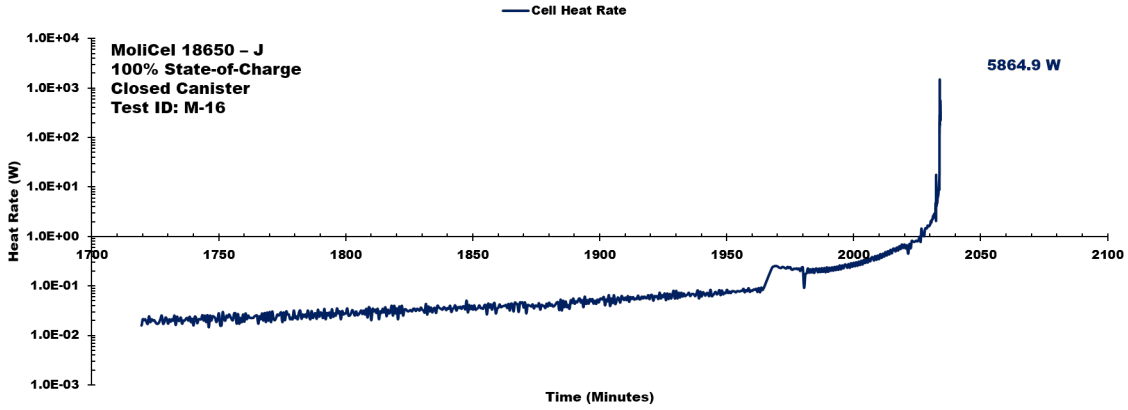

Figure C1-9 MoliCel 18650-J ARC test data used for energy calculations for the 100% SOC closed canister configuration (M16). Cell body heat rate profile is displayed.

Appendix C2: MoliCel 18650-J ARC Data (50%-C)

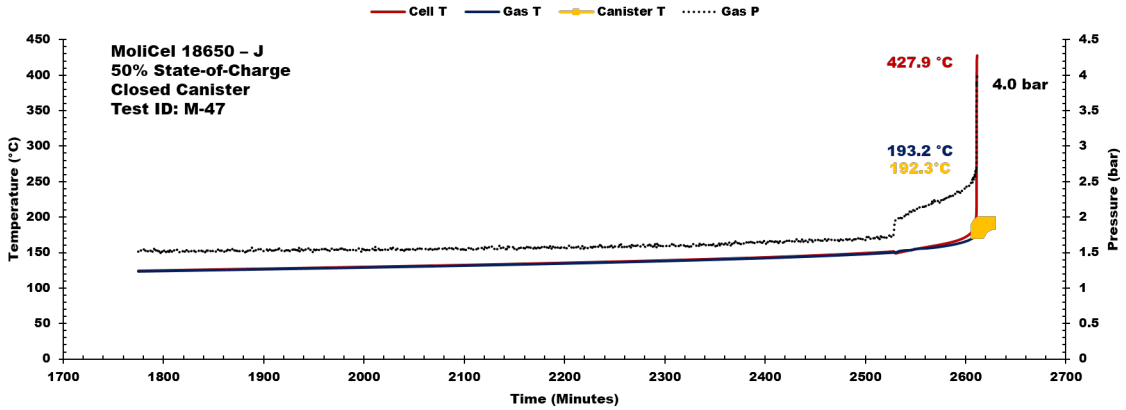

Figure C2-1 MoliCel 18650-J ARC test data used for energy calculations for the 50% SOC closed canister configuration (M47). Data presented includes the following: (a) cell temperature, (b) gas temperature, (c) average canister temperature and (d) pressure.

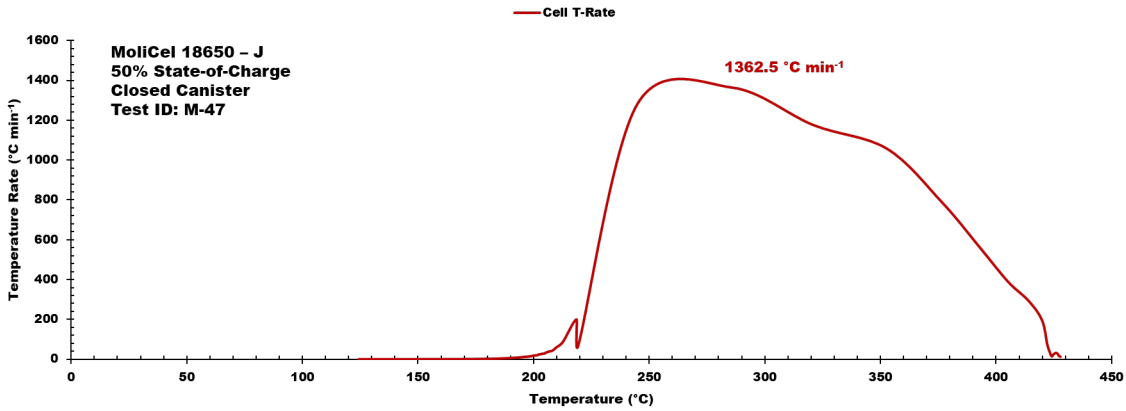

Figure C2-2 MoliCel 18650-J ARC test data used for energy calculations for the 50% SOC closed canister configuration (M47). Temp. rate vs. temperature profile is displayed.

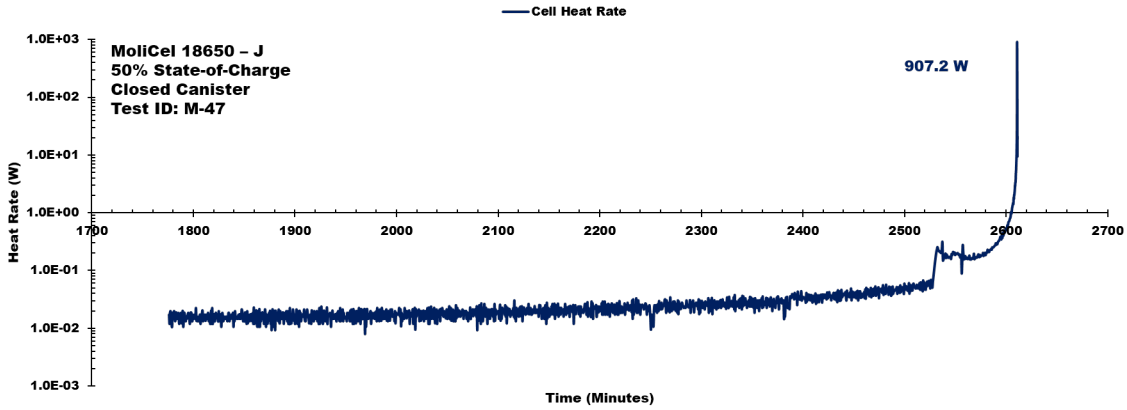

Figure C2-3 MoliCel 18650-J ARC test data used for energy calculations for the 50% SOC closed canister configuration (M47). Cell body heat rate profile is displayed.

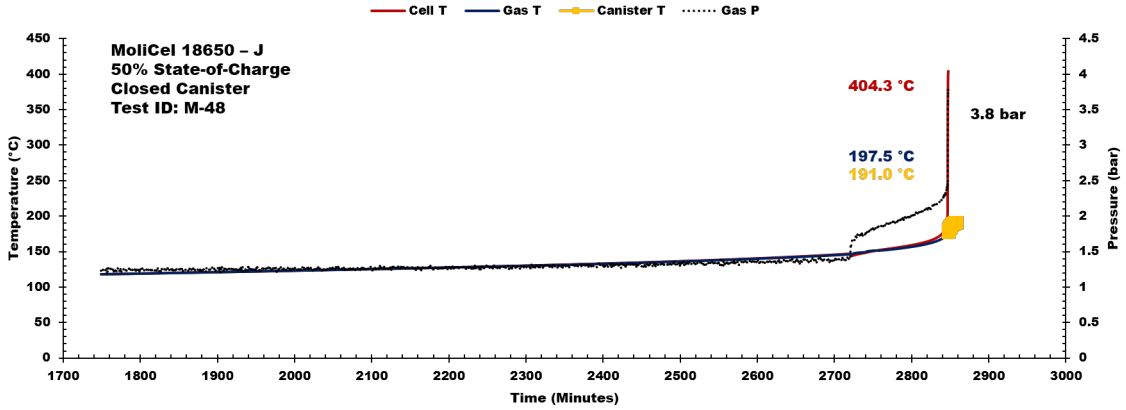

Figure C2-4 **MoliCel 18650-J ARC test data used for energy calculations for the 50% SOC closed canister configuration (M48). Data presented includes the following: (a) cell temperature, (b) gas temperature, (c) average canister temperature and (d) pressure.**

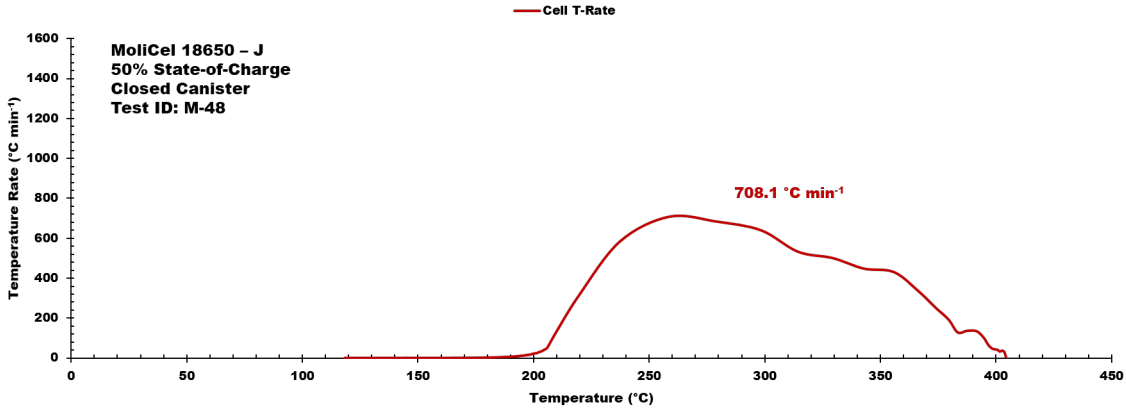

Figure C2-5 **MoliCel 18650-J ARC test data used for energy calculations for the 50% SOC closed canister configuration (M48). Temp. rate vs. temperature profile is displayed.**

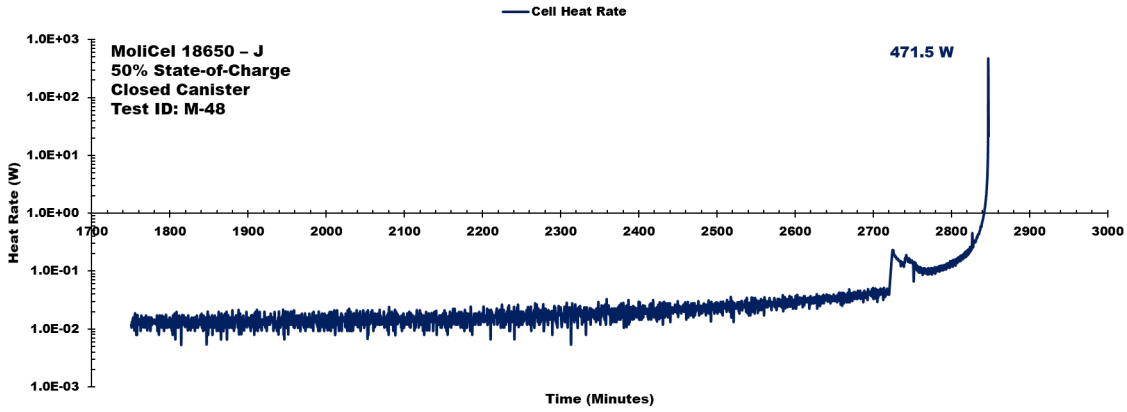

Figure C2-6 **MoliCel 18650-J ARC test data used for energy calculations for the 50% SOC closed canister configuration (M48). Cell body heat rate profile is displayed.**

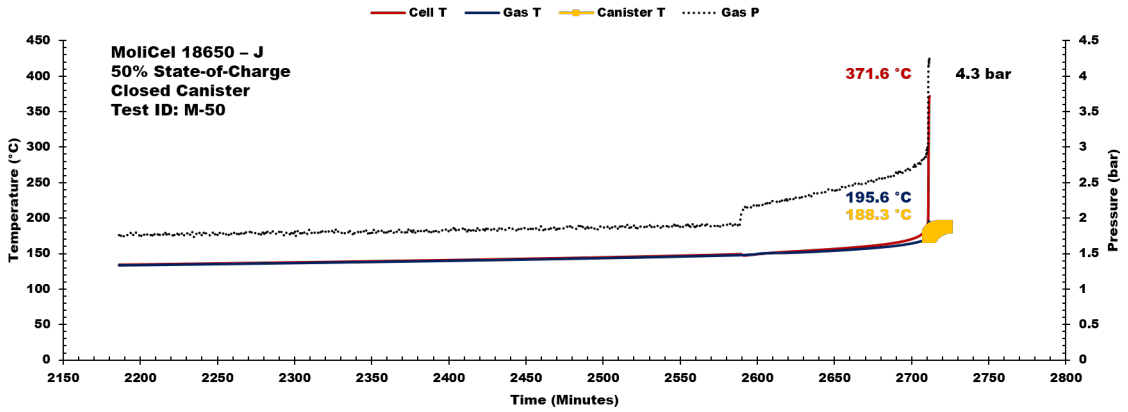

Figure C2-7 MoliCel 18650-J ARC test data used for energy calculations for the 50% SOC closed canister configuration (M50). Data presented includes the following: (a) cell temperature, (b) gas temperature, (c) average canister temperature and (d) pressure.

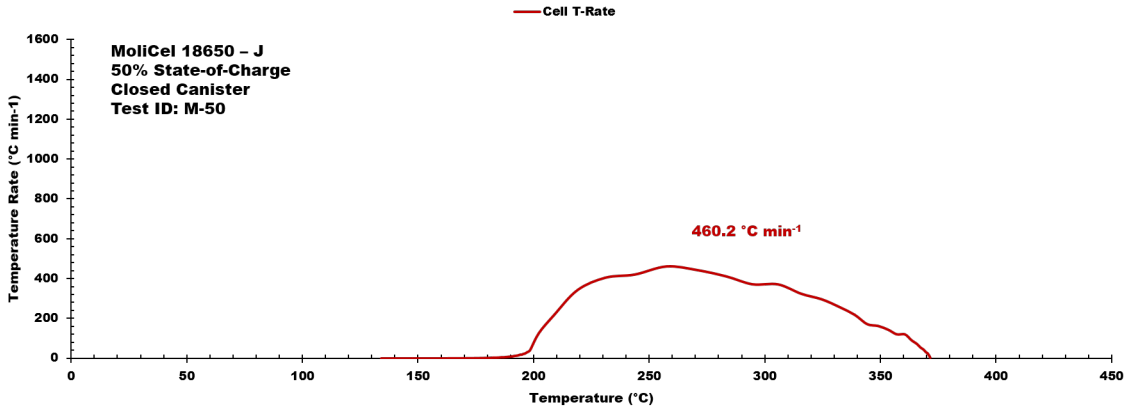

Figure C2-8 MoliCel 18650-J ARC test data used for energy calculations for the 50% SOC closed canister configuration (M50). Temp. rate vs. temperature profile is displayed.

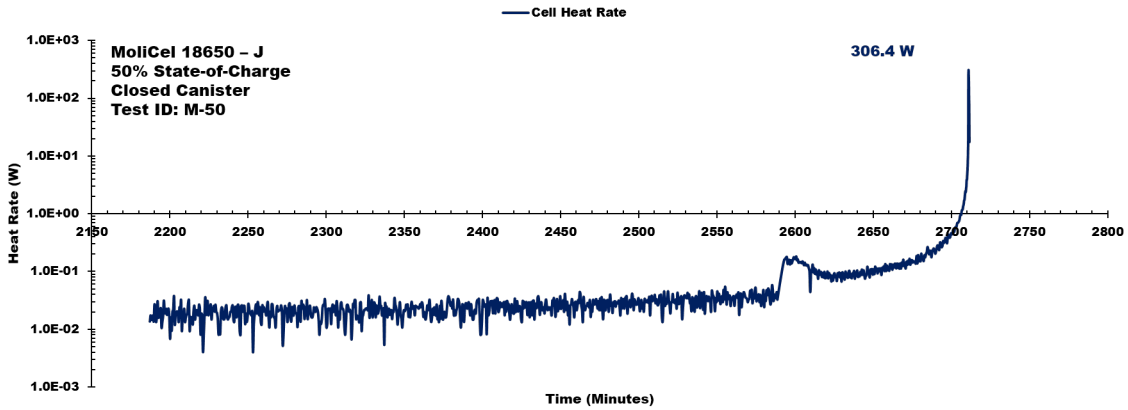

Figure C2-9 MoliCel 18650-J ARC test data used for energy calculations for the 50% SOC closed canister configuration (M50). Cell body heat rate profile is displayed.

Appendix C3: MoliCel 18650-J ARC Data (100%-O)

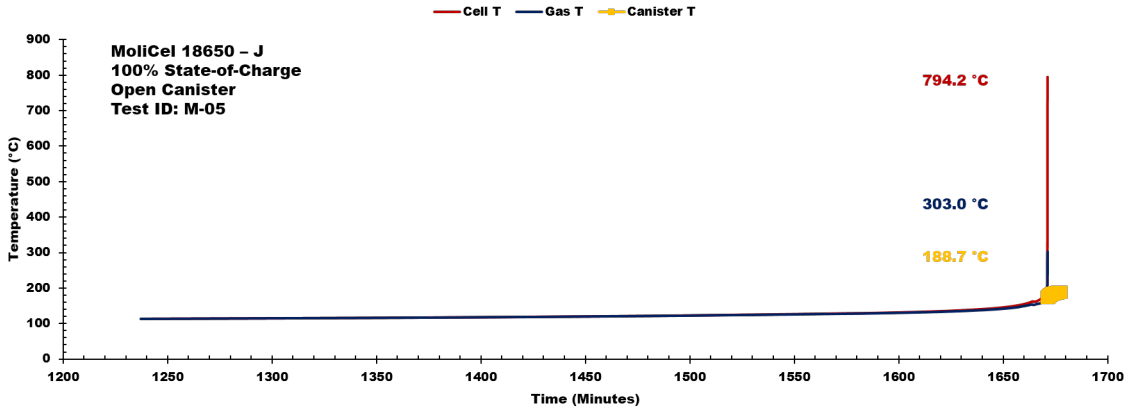

Figure C3-1 MoliCel 18650-J ARC test data used for energy calculations for the 100% SOC open canister configuration (M05). Data presented includes the following: (a) cell temperature, (b) gas temperature, (c) average canister temperature and (d) pressure.

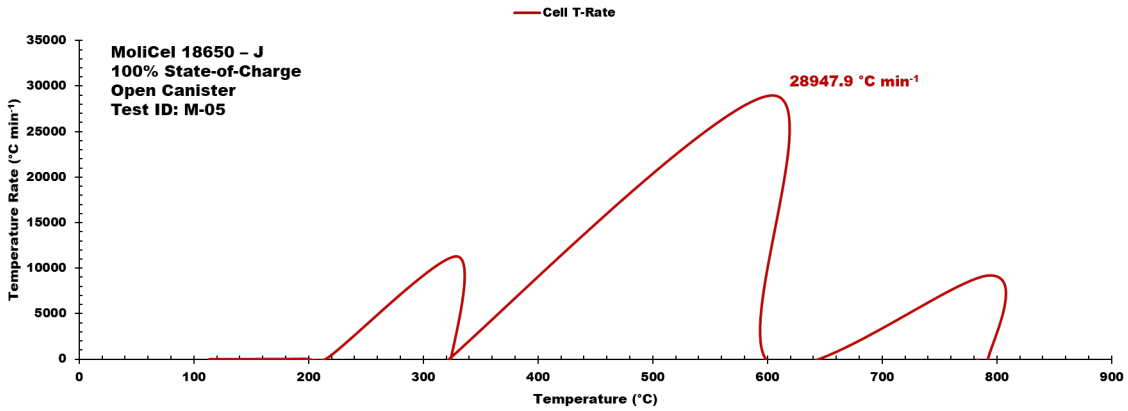

Figure C3-2 MoliCel 18650-J ARC test data used for energy calculations for the 100% SOC open canister configuration (M05). Temp. rate vs. temperature profile is displayed.

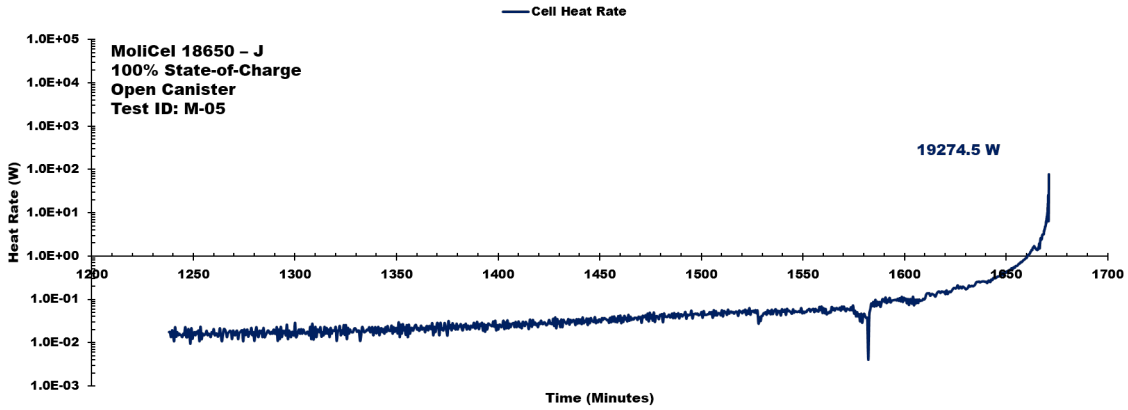

Figure C3-3 MoliCel 18650-J ARC test data used for energy calculations for the 100% SOC open canister configuration (M05). Cell body heat rate profile is displayed.

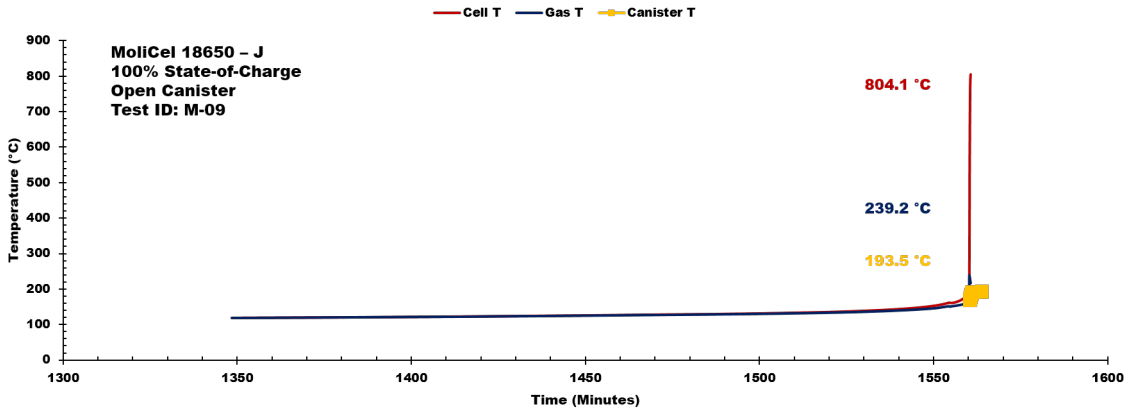

Figure C3-4 MoliCel 18650-J ARC test data used for energy calculations for the 100% SOC open canister configuration (M09). Data presented includes the following: (a) cell temperature, (b) gas temperature, (c) average canister temperature and (d) pressure.

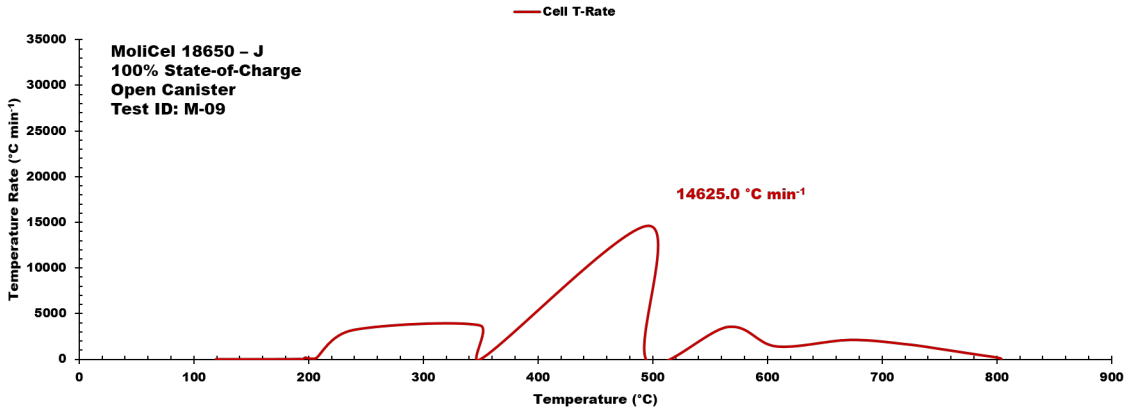

Figure C3-5 MoliCel 18650-J ARC test data used for energy calculations for the 100% SOC open canister configuration (M09). Temp. rate vs. temperature profile is displayed.

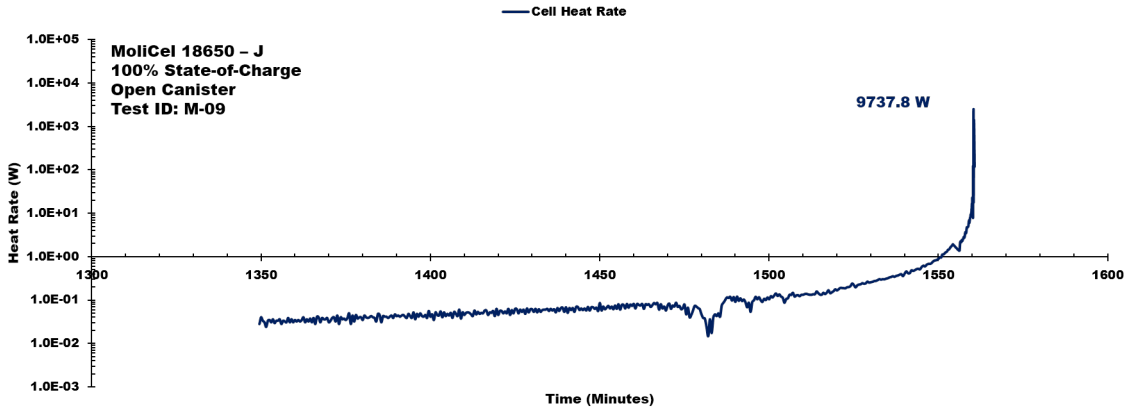

Figure C3-6 MoliCel 18650-J ARC test data used for energy calculations for the 100% SOC open canister configuration (M09). Cell body heat rate profile is displayed.

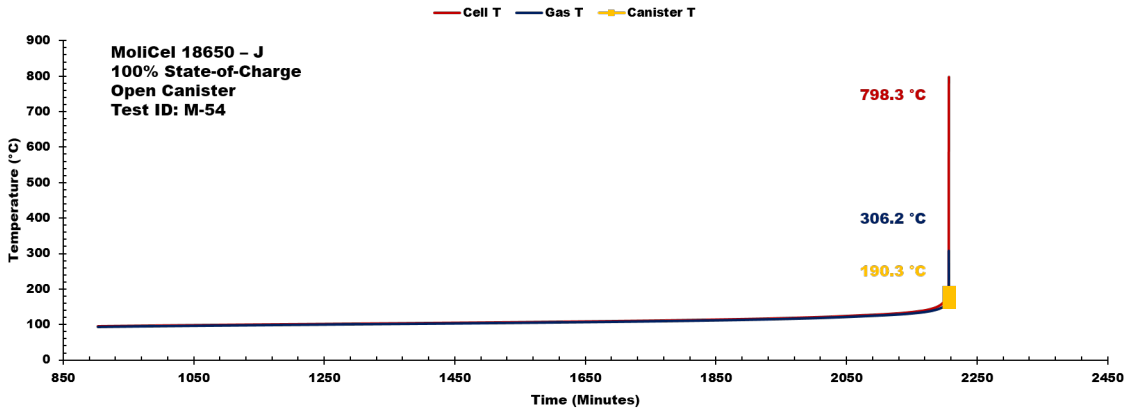

Figure C3-7 MoliCel 18650-J ARC test data used for energy calculations for the 100% SOC open canister configuration (M54). Data presented includes the following: (a) cell temperature, (b) gas temperature, (c) average canister temperature and (d) pressure.

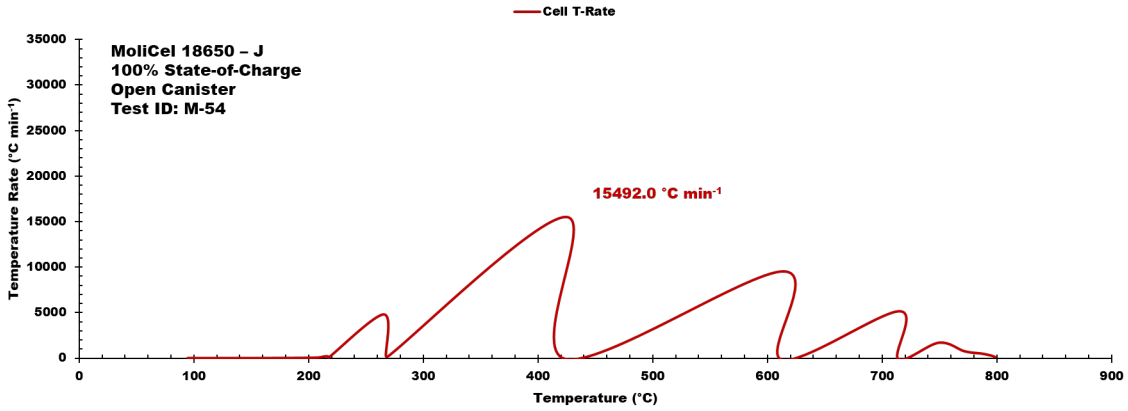

Figure C3-8 MoliCel 18650-J ARC test data used for energy calculations for the 100% SOC open canister configuration (M54). Temp. rate vs. temperature profile is displayed.

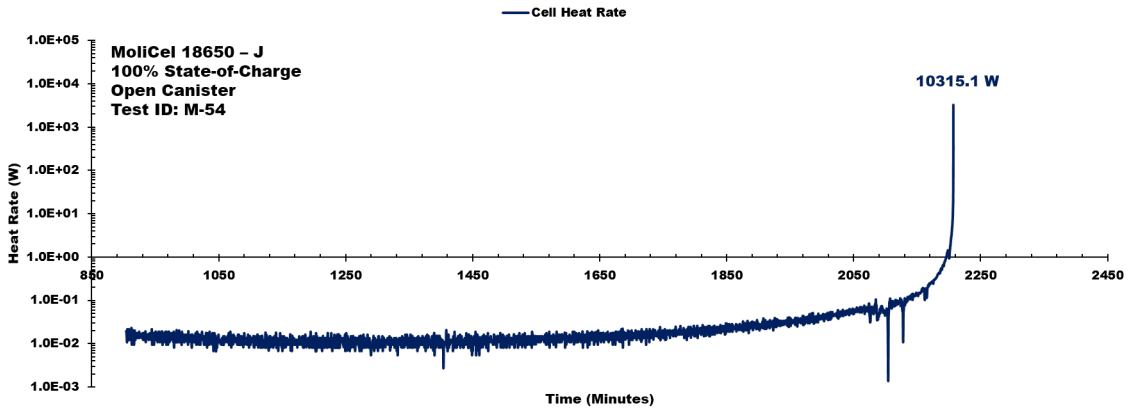

Figure C3-9 MoliCel 18650-J ARC test data used for energy calculations for the 100% SOC open canister configuration (M54). Cell body heat rate profile is displayed.

Appendix C4: MoliCel 18650-J ARC Data (50%-O)

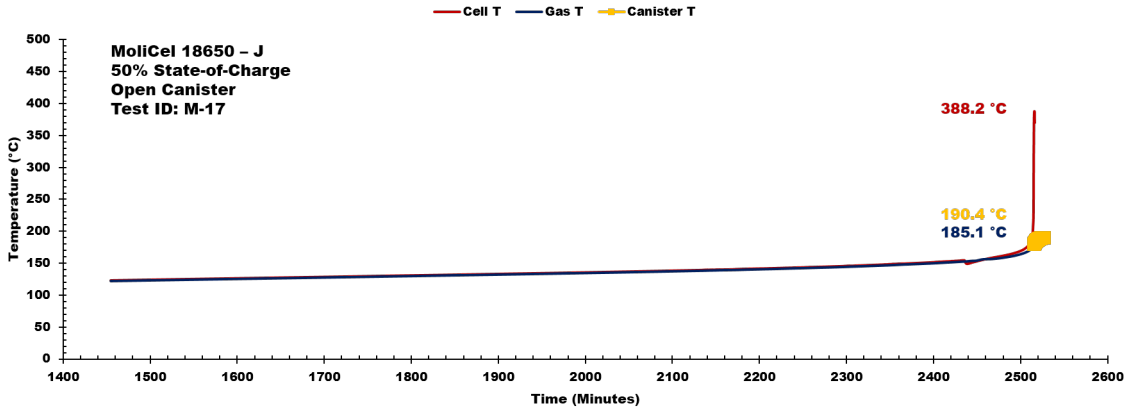

Figure C4-1 MoliCel 18650-J ARC test data used for energy calculations for the 50% SOC open canister configuration (M17). Data presented includes the following: (a) cell temperature, (b) gas temperature, (c) average canister temperature and (d) pressure.

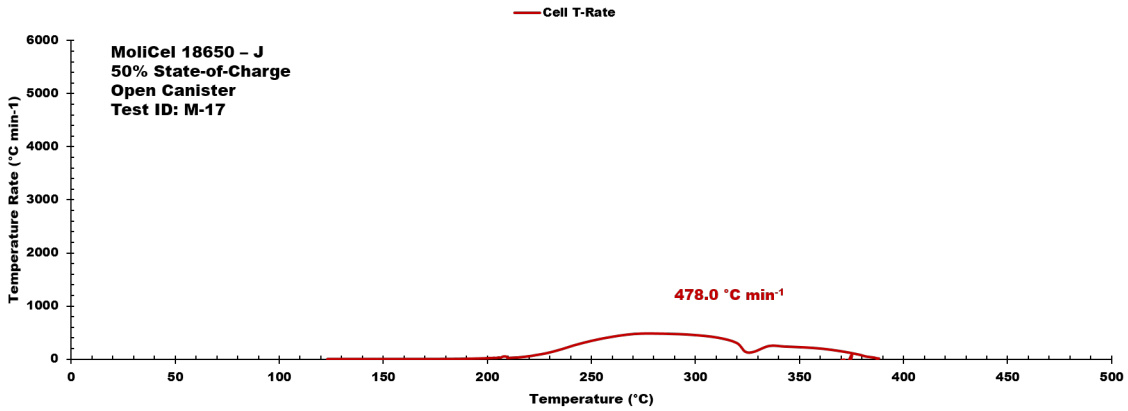

Figure C4-2 MoliCel 18650-J ARC test data used for energy calculations for the 50% SOC open canister configuration (M17). Temp. rate vs. temperature profile is displayed.

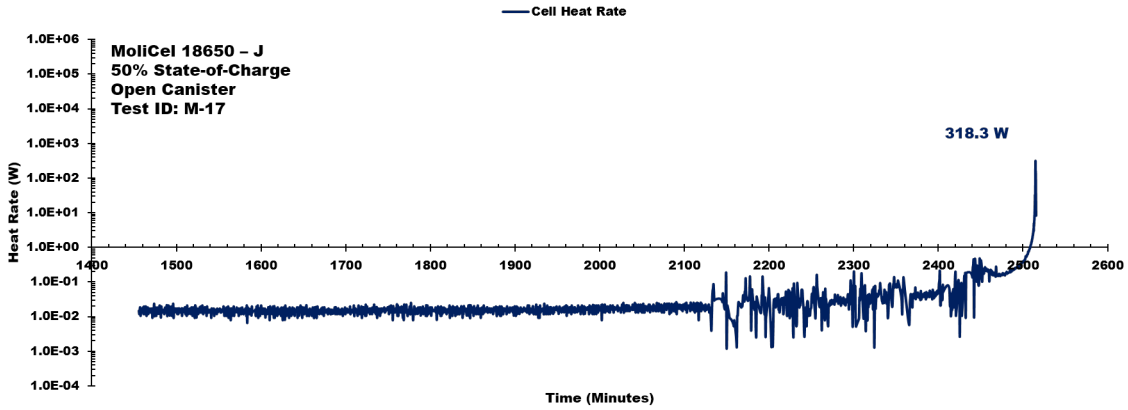

Figure C4-3 MoliCel 18650-J ARC test data used for energy calculations for the 50% SOC open canister configuration (M17). Cell body heat rate profile is displayed.

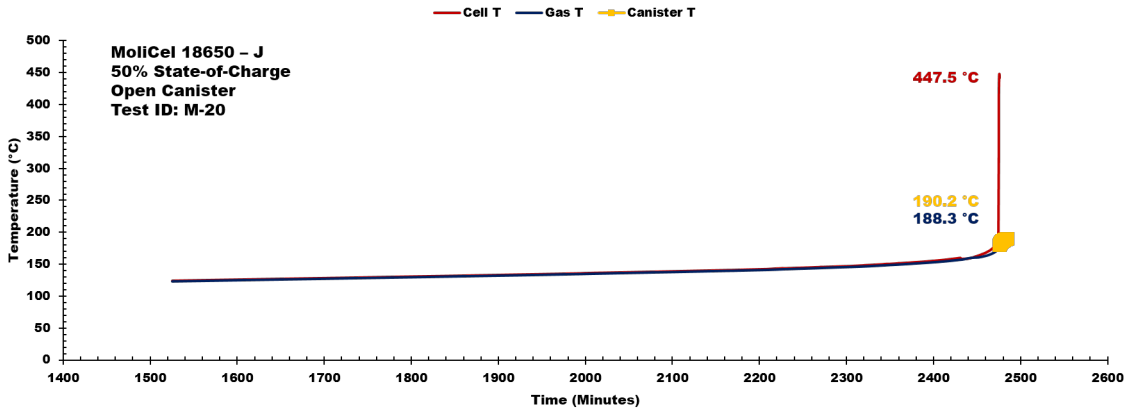

Figure C4-4 **MoliCel 18650-J ARC test data used for energy calculations for the 50% SOC open canister configuration (M20). Data presented includes the following: (a) cell temperature, (b) gas temperature, (c) average canister temperature and (d) pressure.**

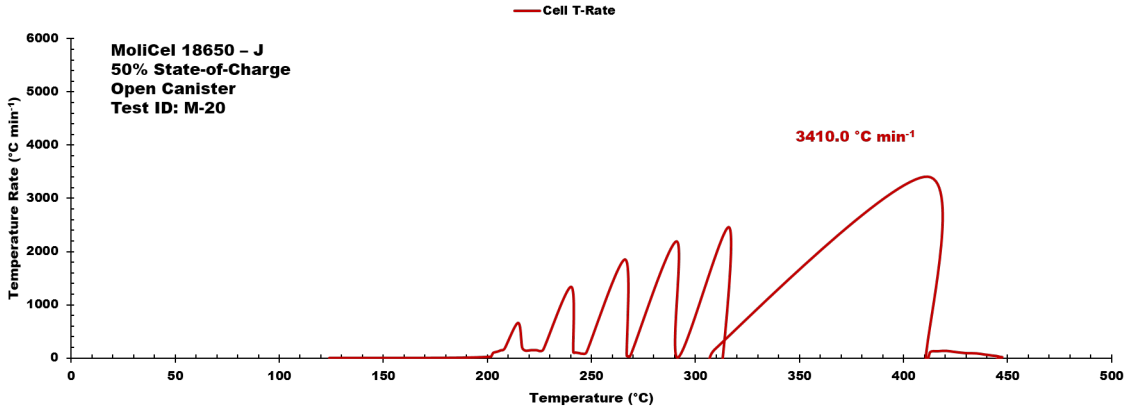

Figure C4-5 **MoliCel 18650-J ARC test data used for energy calculations for the 50% SOC open canister configuration (M20). Temp. rate vs. temperature profile is displayed.**

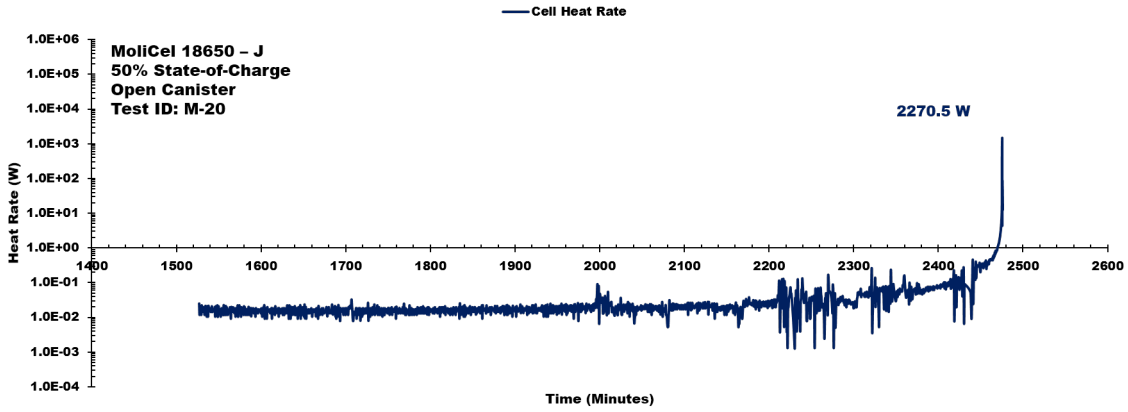

Figure C4-6 **MoliCel 18650-J ARC test data used for energy calculations for the 50% SOC open canister configuration (M20). Cell body heat rate profile is displayed.**

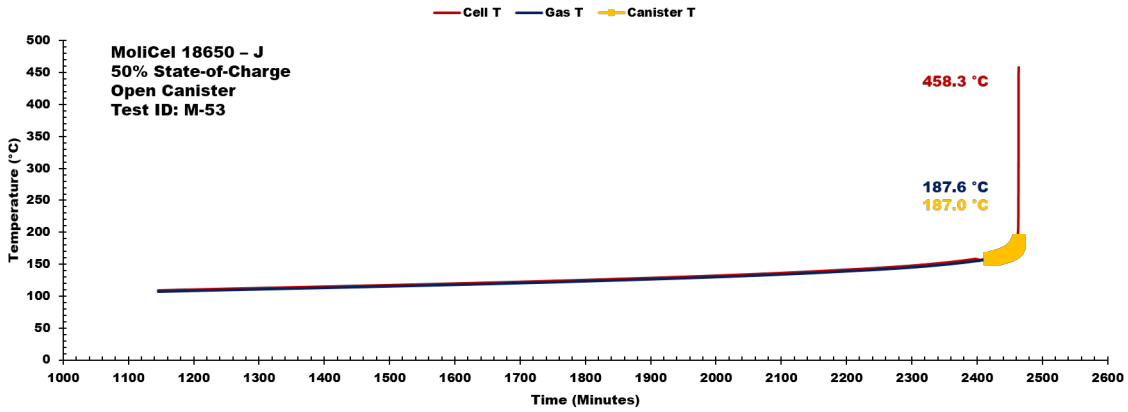

Figure C4-7 **MoliCel 18650-J ARC test data used for energy calculations for the 50% SOC open canister configuration (M53). Data presented includes the following: (a) cell temperature, (b) gas temperature, (c) average canister temperature and (d) pressure.**

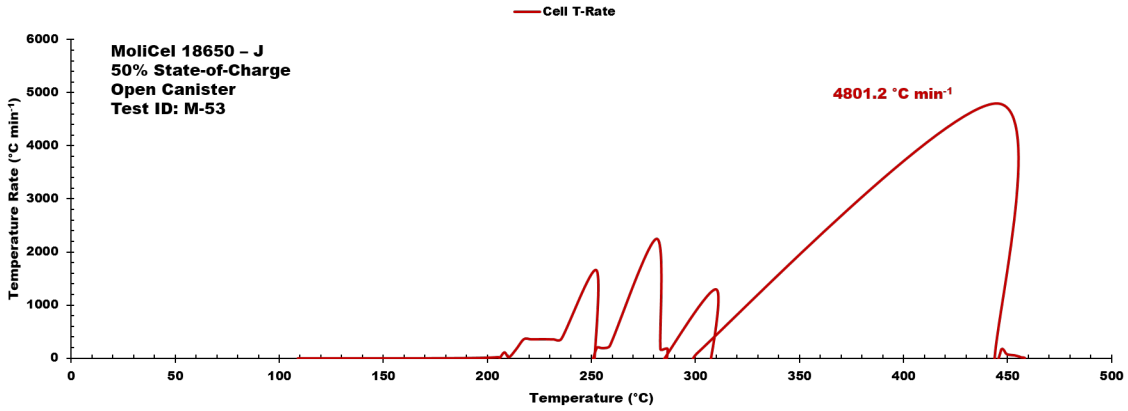

Figure C4-8 **MoliCel 18650-J ARC test data used for energy calculations for the 50% SOC open canister configuration (M53). Temp. rate vs. temperature profile is displayed.**

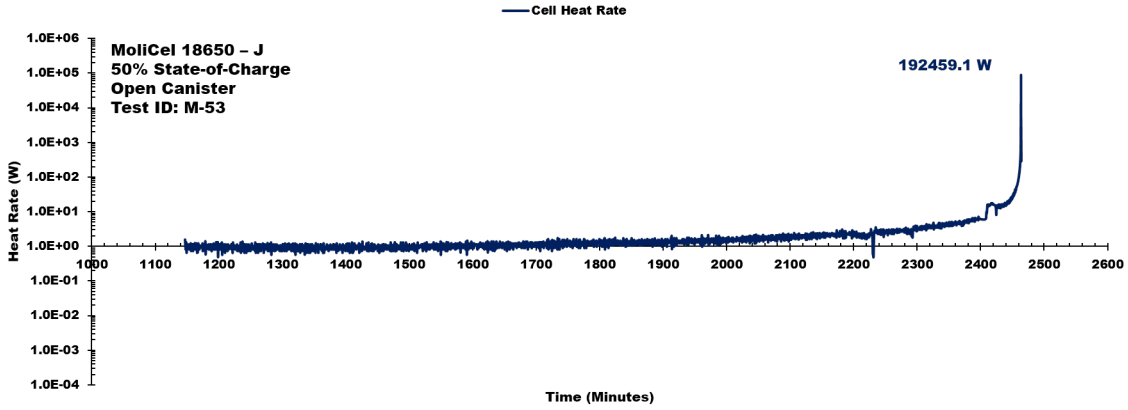

Figure C4-9 **MoliCel 18650-J ARC test data used for energy calculations for the 50% SOC open canister configuration (M53). Cell body heat rate profile is displayed.**